Reconfigurable Metasurfaces for Beamforming and Sensing

by

Bharath Gundappa Kashyap

A Dissertation Presented in Partial Fulfillment
of the Requirements for the Degree
Doctor of Philosophy

Approved November 2023 by the
Graduate Supervisory Committee:

Georgios C. Trichopoulos, Chair
Constantine A. Balanis
James T. Aberle
Ahmed Alkhateeb
Seyedmohammedreza Faghih Imani

ARIZONA STATE UNIVERSITY

December 2023

ABSTRACT

Reconfigurable metasurfaces (RMSs) are promising solutions for beamforming and sensing applications including 5G and beyond wireless communications, satellite and radar systems, and biomarker sensing. In this work, three distinct RMS architectures – reconfigurable intelligent surfaces (RISs), meta-transmission lines (meta-TLs), and substrate integrated waveguide leaky-wave antennas (SIW-LWAs) are developed and characterized.

The ever-increasing demand for higher data rates and lower latencies has propelled the telecommunications industry to adopt higher frequencies for 5G and beyond wireless communications. However, this transition to higher frequencies introduces challenges in terms of signal coverage and path loss. Many base stations would be necessary to ensure signal fidelity in such a setting, making bulky phased array-based solutions impractical. Consequently, to meet the unique needs of 5G and beyond wireless communication networks, this work proposes the use of RISs characterized by low-profile, low-RF losses, low-power consumption, and high-gain capabilities, making them excellent candidates for future wireless communication applications. Specifically, RISs at sub-6GHz, mmWave and sub-THz frequencies are analyzed to demonstrate their ability to improve signal strength and coverage.

Further, a linear meta-TL wave space is designed to achieve miniaturization of true-time delay beamforming structures such as Rotman lenses which are traditionally bulky. To address this challenge, a modified lumped element TL model is proposed. A meta-TL is created by including the mutual coupling effects and can be used to slow down the

electromagnetic signal and realize miniaturized lenses. A proof-of-concept 1D meta-TL is developed to demonstrate about 90% size reduction and 40% bandwidth improvement.

Furthermore, a conformable antenna design for radio frequency-based tracking of hand gestures is also detailed. SIW-LWA is employed as the radiating element to couple RF signals into the human hand. The antenna is envisaged to be integrated in a wristband topology and capture the changes in the electric field caused by various movements of the hand. The scattering parameters are used to track the changes in the wrist anatomy. Sensor characterization showed significant sensitivity suppression due to lossy multi-dielectric nature tissues in the wrist. However, the sensor demonstrates good coupling of electromagnetic energy making it suitable for on-body wireless communications and magnetic resonance imaging applications.

ಈ ಕೃತಿಯನ್ನು ನನ್ನ ತಾಯಿ, ತಂದೆ, ಸುಜನಾ ಮತ್ತು ನನ್ನ ಪ್ರೀತಿಯ ವಿಂಧ್ಯಾಗೆ ಅರ್ಪಿಸುತ್ತೇನೆ

ACKNOWLEDGMENTS

I would like to express my deepest gratitude to my Ph.D. advisor, Prof. Georgios C. Trichopoulos, for his unwavering support, guidance, and encouragement throughout my doctoral research. His expertise, patience, and dedication have been invaluable to me, and I am truly honored to have had the opportunity to work under his mentorship. I am thankful for the countless hours Prof. Trichopoulos spent discussing research ideas, providing feedback on my work, and challenging me to think critically. His passion for the subject matter and commitment to excellence have inspired me to push the boundaries of my knowledge and capabilities.

I would also like to extend my sincere appreciation to the members of my dissertation committee, Prof. Constantine A. Balanis, Prof. James T. Aberle, Prof. Ahmed Alkhateeb, and Prof. Seyedmohammedreza Faghih Imani, for their insightful feedback, expert advice, and encouragement. Each committee member's unique perspective and expertise significantly enhanced the quality of this dissertation.

This Ph.D. research journey has been both challenging and rewarding, and I am profoundly grateful for the constant support of my family. Their love and encouragement have been the cornerstone of my academic journey, providing me with the strength to persevere through the challenges and uncertainties that often accompany doctoral research. I thank my mom, Usha, dad, Gundappa, sister, Sujana, and the rest of my family for their unwavering belief in my abilities. I also want to offer my most special thanks to Vindhya, for her endless patience and love.

Additionally, I am grateful to Subramanian Ramalingam and Panagiotis Theofanopoulos, for their continued mentorship, stimulating discussions, and friendship throughout my doctoral journey.

I am also indebted to my fellow lab mates, Yiran Cui, Aditya Shekhawat, Mohammed Aladsani, Russell Raldiris Torres, and Syam Prakash, for fostering a pleasant academic environment and quality discussions.

Last, but not the least, I would like to thank my friends, Parijat Sengupta, Abhishiktha Tummala, and Jude Pereira for their companionship and fun filled moments that made this journey worthwhile.

TABLE OF CONTENTS

Page

CHAPTER Page

CHAPTER Page

LIST OF TABLES

Table Page

LIST OF FIGURES

Figure Page

Figure Page

Figure Page

Figure Page

Figure Page

Figure Page

Figure Page

Figure Page

CHAPTER 1

INTRODUCTION TO BEAMFORMING AND SENSING WITH RECONFIGURABLE METASURFACES

1.1 Introduction

Reconfigurable metasurfaces (RMSs) are two-dimensional (2D) structures consisting of subwavelength-sized elements that are designed to manipulate the properties of electromagnetic waves, such as their amplitude, phase, polarization, and direction. RMSs offer several advantages for beamforming and sensing applications due to their compact size, low cost, and ease of fabrication. They also offer greater flexibility and control over the properties of electromagnetic waves such as perfect absorption or reflection, beam steering, polarization conversion, etc., allowing for more precise and efficient manipulation of these waves for a wide range of applications. They have a wide range of potential applications, including telecommunications, radars, sensing, etc. In telecommunications and radar systems, they can be used to improve the efficiency of wireless communication systems by controlling the direction and polarization of electromagnetic waves. Additionally, RMSs can improve sensing applications by enabling multi-static sensing, introducing multiple-input-multiple-output (MIMO) methods, or rapid electric beamscanning.

In this work, the focus is on the design and development of a few novel RMS architectures that are tailor-made for applications in the fields of 5G and beyond wireless communications, radar systems, and biomarker sensing. Specifically, novel designs of planar 2D metasurfaces are developed to realize reconfigurable intelligent surfaces (RISs),

along with 1D RMS designs of *substrate integrated waveguide leaky-wave antennas* (SIW-LWAs), and periodically loaded transmission lines which are called *meta-transmission lines* (meta-TL). The 2D RISs developed in this research could be classified as out-of-plane metasurfaces. Such RMSs either reflect or transmit the incident electromagnetic energy to desired directions. On the other hand, the 1D RMSs investigated in the work could be classified as in-plane metasurfaces. Here, the electromagnetic signal propagates along a transmission line or a waveguide structure and could be employed to modify the propagation characteristics (phase constant, attenuation, group delay) of the wave within the medium. Such metasurfaces provide the benefits of realizing low-profile, low-weight, conformable designs that can significantly reduce the fabrication and implementation costs as well as power requirements. Additionally, they can be designed as passive surfaces offering the advantages of low radio frequency (RF) losses which do not scale with frequency. All these advantages make them well suited for compact beamforming and sensing architectures. In the following sections, an overview of representative beamforming and sensing architectures are provided along with their operating principles and constituent challenges. The challenges of current hardware architectures, thus motivates the design of new RMSs.

1.2 Overview of Traditional Beamforming Architectures

Conventionally, electronic beamsteering has been realized through analog or digital phased array antennas or a hybrid combination of both [1-10]. Such antenna arrays are usually deployed in linear, 2D, or 3D arrangements of individual radiating elements that are fed coherently along with some variable phase or time delays [1]. By modulating these

phase shifts between the radiating elements of the array, the primary direction of radiation can be altered, thereby scanning or steering the antenna beam to a desired direction. Further, by varying the amplitude of the excitation signals, the shape of the radiation pattern of the array can also be modified. Thus, phased arrays provide both beam shaping and beam steering capabilities along with other advantages of improving the directivity, beamwidth, bandwidth etc. This phase shifting mechanism is realized by employing feed networks, which consist of a series of RF devices such as oscillators, power dividers/ combiners, amplifiers, mixers, phase shifters, transmission lines, analog-to-digital and digital-to-analog converters (ADCs and DACs), variable attenuators, etc.

Phased array architectures be broadly classified under analog and digital beamforming schemes [3-17]. The typical architecture of the phased arrays systems consists of a baseband digital beamforming and signal processing unit that generates a codebook needed for beam steering. The digital signals are converted to RF signals suitable to be applied to the transmit/receive (TRX) modules in the feed chain of the array elements [3] [9]. The TRX generally comprises of a transmit amplifier and a receive amplifier, a circulator, and a phase shifter. These amplifiers can significantly lower the RF losses, thus improving the array sensitivity and the range of operation. The circulator or a coupler is usually employed to isolate the transmit and receive channels and protect the equipment from leakage and spurs.

While analog beamformers offer the advantage of low-power consumption, they are usually lossy and bulky due to the use of single high-power transmitters. Although the RF losses could be reduced by using distributed TRX modules, the analog beamforming frameworks can only generate a fixed set of beams and would require a complete hardware

makeover if additional directions are desired. As such, they increase the implementation costs making them impractical for applications that demand flexible and dynamic beamsteering capabilities.

Digital beamforming techniques address some of the concerns seen with the analog techniques such as providing a high degree of flexibility in controlling beam shape and pointing direction, wide instantaneous bandwidth needed for high-speed communications, adaptive beamforming capabilities, and better scalability in terms of handling large high-performance arrays. However, they also suffer from several drawbacks as listed below.

- They use high-resolution ADCs and high-speed digital signal processing (DSP) algorithms that consume a large amount of power and increase system complexity.
- The RF chain constitutes a series of digital circuits including phase locked loops (PLLs), filters, ADCs, DACs, FPGAs, and amplifiers, all of which can increase the implementation costs and space requirements.
- The digitization process can introduce quantization noise and other sources of signal distortion, which can degrade the overall system performance.

1.3 5G Beamforming Challenges and Opportunities

The global communication realm is witnessing an ever-increasing demand to achieve higher data rates and spectral efficiencies, lower latencies, and compact architectures. With the spectrum between 300 MHz to 3 GHz almost fully occupied for all the existing communication applications ranging from AM/FM radio to radars and GPS to cellular and satellite communications, there has been a dramatic rise in the bandwidth requirements. Combined with the need for increased channel capacity for cellular

communications, this has propelled the electromagnetic research towards mmWave and low THz frequencies for upcoming 5G and 6G applications [19-23]. It is expected that the current ~700 MHz bandwidth available from 4G could be increased to over 2.5 GHz with 5G, which translates to over ten-fold increase in the data rates [23]. Consequently, more than 1 Gbps data rates are possible with 5G while the theoretical maximum data rate achievable with 4G is 150 Mbps. Such higher speeds can lead to exciting applications in the fields of virtual and augmented reality, holography, wireless power transfer, smart radio environments, [38], [40-41] etc.

The existing commercial phased array architectures (both analog and digital) presented in the previous section have been predominantly designed to operate at microwave frequencies or lower. This is governed by the fact that most of the commercially available RF components are designed for optimum performance up to microwave frequencies. Although the technology is improving to extend the operations to mmWave frequencies and above, there needs to be a considerable research and development that needs to go into this domain before low-cost, low-loss mmWave RF devices can become easily available. Particularly, most of the cost driving factors mentioned in the earlier discussion can turn out to be detrimental if the existing beamforming architectures are adopted without any modifications for mmWave/ THz operation. Additionally, the operation at mmWave and THz, brings in certain unique challenges in terms of network modeling, manufacturing, analysis, design integration, power handling, implementation cost, optimization schemes, regulatory reforms, etc., that must be carefully addressed for successful adoption of the 5G/6G technologies. A detailed look at some of these challenges which could also serve as interesting design opportunities are presented below.

Propagation loss: It is a well-known fact that the propagation distance is inversely proportional to the wavelength of the electromagnetic wave. As such, with the increase in the frequency of operation (smaller wavelength), the propagation loss also known as free space path loss significantly increases if same number of antenna elements are used as with the designs at lower microwave frequencies. The free space path loss can be derived from the Friis Transmission equation [23], which provides the power available at the receiver P_r in a wireless communication environment relative to the transmitted power P_t as

$$\frac{P_r}{P_t} = \left(\frac{\lambda}{4\pi R}\right)^2 G_t^{re} G_r^{re} \tag{1.1}$$

where

λ is the operating wavelength

R is the distance between the transmitter and the receiver

$G_t^{re} = \epsilon_t^{rad}(1 - |\Gamma_t|^2) \cdot \text{PLF} \cdot D_t$ is the realized gain of the transmitter

$G_r^{re} = \epsilon_r^{rad}(1 - |\Gamma_r|^2) \cdot \text{PLF} \cdot D_r$ is the realized gain of the receiver

ϵ_t^{rad} and ϵ_r^{rad} are the efficiencies of the transmitter and receiver respectively

Γ_t and Γ_r represent the mismatch losses at the transmitter and receiver respectively

$\text{PLF} = |\hat{\rho}_t \cdot \hat{\rho}_r|^2$ is the polarization loss factor between the transmitter and receiver

$\hat{\rho}_t$ and $\hat{\rho}_r$ are unit vectors

D_t and D_r are the directivities of the transmitter and receiver respectively

Consequently, the free space path loss for fully matched, lossless, unity gain communication link is given as

$$Path\ loss = \frac{P_t}{P_r} = \left(\frac{4\pi R}{\lambda}\right)^2 \tag{1.2}$$

The increased path loss according to (1.2) necessitates the array designs to be updated to maintain the aperture sizes which leads to the development of ultra-large arrays packed with more number of antenna elements. A direct consequence of this is the increase in the number of RF components in the feed network, which translates to increased implementation costs. Another consequence of increased path loss is the reduction of cell sizes. While the cells served by microwave base stations could be as large as few square miles for 4G, 3G and older generation cellular systems, they can be as small as few hundreds of meters for 5G and beyond. This has led to the origin of microcells, picocells and femtocells [23], which are used in place of traditional base stations.

Penetration loss: The longer wavelength microwave signals have the capability to penetrate walls, wood, glass etc., much better than mmWaves. Additionally, mmWave propagation is also highly susceptible to atmospheric absorption due to rain and oxygen which further increases the attenuation. The rain drops usually have wavelengths comparable to that of mmWaves and thus, can significantly impact the propagation in this realm, as shown in Fig. 1.1 [24].

Multipath loss: In non-line of sight (NLOS) communication environments, the signals from the transmitter can reach the receiver due to reflections from obstacles. The reflections could be from buildings, trees or even ground, all which can arrive at the receiver and interfere constructively or destructively. This is unlike the line of sight (LOS) propagation scenario, where there exists a direct path between the transmitter and the receiver. A multipath propagation environment is depicted in Fig. 1.2. The multipath propagation gives rise to the requirement of developing smart signal processing techniques at the receivers that can collect and process the impinging energy in a coherent manner.

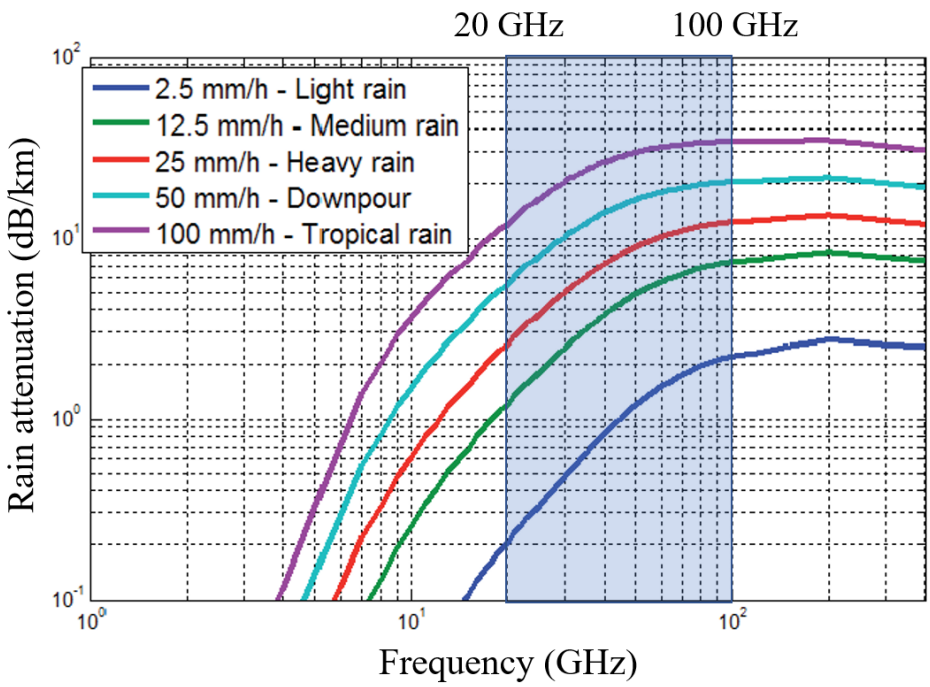

Fig. 1.1: Attenuation of electromagnetic waves in the presence of rain as a function of frequency. The attenuation significantly increases ($> 10\ dB/\ km$) above 30 GHz and pose challenges for the implementation of mmWave communication networks [24].

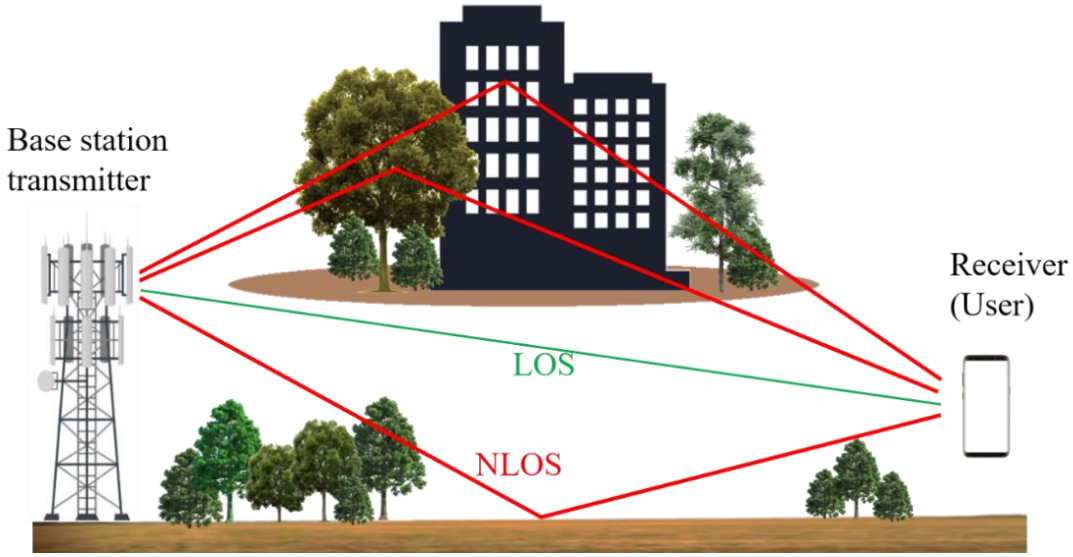

Figure 1.2: Multipath propagation environment showing different paths the transmitted signal can take to reach the receiver.

Limited RF-front-end Electronics Performance: The existing devices employed to realize the phase shifts steer the beam are based on ferrites, true time delay units [11-12], monolithic microwave integrated circuits (MMICs), and micro-electromechanical systems (MEMS). Ferrite based phase shifters are bulky and are not suitable for integration with printed circuit technology. TTDs require careful design considerations to avoid mismatch problems (gain, offset, bandwidth, and timing) which can significantly drive up the cost. MEMS based phase shifters, while are promising in terms of their cost and performance at microwave frequencies, their performance and reliability needs to be evaluated at mmWave frequencies. While conventional Silicon (Si) based MMICs offer excellent phase shifting solutions at microwave frequencies, they tend to become lossy and power hungry at higher frequencies. As such, Gallium Arsenide (GaAs) and Gallium Nitride (GaN) based solutions are currently being explored. On the other hand, there have been several works to develop efficient phase shifting solutions based on PIN diodes, field effect transistors (FET) switches, liquid crystals, as well as varactors. The main drawback with these RF phase shifting techniques are extremely sensitive to manufacturing inaccuracies which can lead to poor isolation and increased insertion loss. A direct consequence is the lack of control on beam pointing accuracy and beam shape. Similarly, the high-resolution ADCs are required in the receiver RF chain of each antenna element to achieve the dynamic range necessary to reduce interference and improve sensitivity. This has already been shown to significantly drive up the cost even in microwave implementations, making them prohibitively expensive for mmWave systems that demand high sensitivity. Additionally, efficient fabrication techniques must be investigated to enable large-scale manufacturing suitable for commercial applications at mmWave frequencies.

Antenna Design and Beamforming challenges: To solve the problems with traditional phased arrays, the 4G and long-term evolution (LTE) systems have focused on the development of single input multiple output (SIMO), multiple input single output (MISO) as well as the now prevalent multiple input multiple output (MIMO) antenna arrays. MIMO systems offer the manifold advantages such as improved signal fidelity, higher data rate and throughput, reduced bit error rate (BER), as well as higher quality of service (QoS) and spectral efficiency. The use of signal processing algorithms on received data along with beamforming can help extend the cell coverage and support more subscribers. Another important feature of MIMO resulting from the use of multiple antennas is diversity reception which can significantly reduce signal fading effects. The spatial multiplexing feature of the MIMO antennas can lead to improvement of channel capacity without requiring additional bandwidth. Moreover, a large number of antennas could be used to create massive MIMO architectures for the base station transmitters [29]. However, to achieve multi-beamforming capability, MIMO phased arrays require a large number of phase shifters in the order of thousands for large mmWave arrays, which consequently increases the implementation cost, power consumption. As such, it is necessary to explore alternate antenna architectures to take better advantage of MIMO [30].

Some of the alternate architectures considered include high gain horn antenna arrays with ferrite phased shifters which provide good channel propagation [25] [31] but can be bulky with slower switching speeds and higher power consumption. Lens-based designs (Rotman, Fresnel, Luneburg, etc.,) as well as reflector-based designs have also been investigated [18] to achieve multibeam capabilities. However, these implementations turn out to be bulky for commercial wireless applications.

In this research, one of the most promising alternate beamforming architectures for 5G and beyond wireless communication applications – *the reconfigurable metasurface* (RMS) – is investigated [32-37]. RMSs are artificial electromagnetic surfaces made up of a large number of passive reflecting elements that can be controlled by integrated electronics to alter the directions of incoming signals and achieve beam control. RMSs employed wireless communications are also colloquially known as reconfigurable intelligent surfaces (RISs), intelligent reflective surfaces (IRSs), reconfigurable reflective surfaces (RRSs), and reflective metasurfaces. RISs have the potential to completely revolutionize the mmWave and THz wireless communications through spectrum and energy efficient communication channels. RISs can be deployed to enhance wireless signal strength and coverage in areas with poor signal quality, such as indoor environments, airport, stadiums, urban canyons, or remote locations. Some of the striking advantages resulting from the implementation RISs, compared to any other existing beamforming architectures, are highlighted below.

- RISs are thin, low-profile, and lightweight structures which makes them suitable for conformal mounting on walls and facades of buildings, ceilings, lamp posts, etc.
- They are usually planar and well-suited for low-cost and scalable manufacturing techniques such as PCB fabrication.
- They can be designed as fully-passive reflectors (no additional components) or as active surfaces (that require only a DC biasing circuitry and no RF feed network), which can lead to cost-effective solutions compared to other existing techniques.
- The absence of RF feed network also leads to ultra-low loss implementations with virtually no RF losses. This is a unique advantage of RISs, because unlike other

array designs the RF losses do not scale with frequency. This makes RIS designs extremely well suited for high frequency 5G and radar applications.

- They offer low-power consumption solutions, of several orders less than the phased array-based implementation, thus can improve energy efficiency and battery life in remote deployment scenarios.
- They can be employed to enhance channel capacity and spectral efficiency in wireless networks through dynamically reconfigurable beams, allowing for higher number of simultaneous connections with higher data rates.

RISs are usually compared with relay-aided transmission [38] and backscatter communications [39]. A distinctive feature of RIS lies in its ability to make the communication channel deterministic and controllable unlike the relay and backscatter techniques currently being used in mmWave wireless communications. This ability of the RIS to intentionally control the propagation environment has led to the emergence of 'smart radio environments' [32]. In such an environment, the communication channel could be reconfigured and optimized using machine learning algorithms to ensure high signal fidelity and quality of service (QoS). Relays typically depend on 'amplify and forward' operational mechanism, and thus can also provide improved gain and signal coverage. Moreover, they offer the advantage of storing and processing the received signals before retransmitting. However, the geometric size of the antennas of relays and backscattering tags is small, which makes them diffusers rather than specular reflectors [32], [38-42]. The smaller sizes would lead to wider beam widths and can increase interference in the channel. Additionally, the use of amplifiers and rest the RF feed chain can lead to higher cost and power consumption. RISs, with their large geometric sizes can provide narrow beamwidth

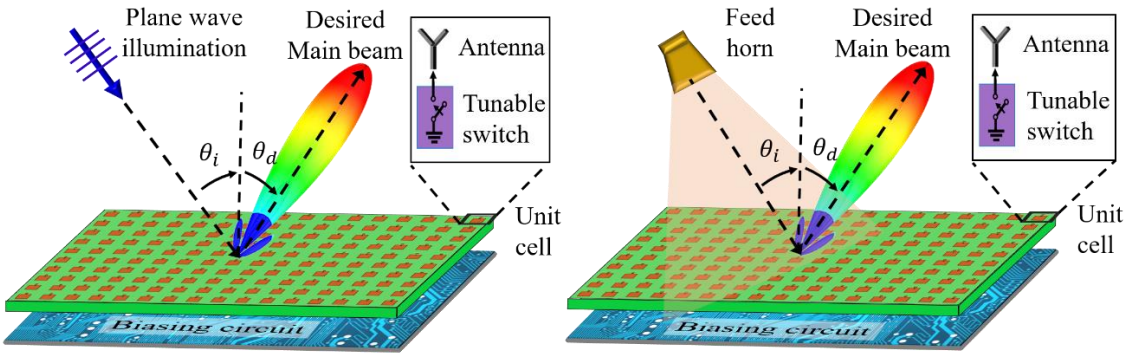

(a) (b)

Figure 1.3: Generic RIS architectures: (a) RIS working with plane wave excitation and (b) RIS working with excitation from a feed horn.

signals to improve the security of the communication link and avoid interference. The RISs also provide remarkable link budget gains compared to relay and backscatter communications. It has also been shown that by careful design of the phase shifts of the radiating elements in the RIS, it is possible to make the multipath signal arrive in phase at the receiver and thus, improve the non-line-of-sight (NLoS) connectivity [32], [43].

The two commonly used implementations of RIS architectures are shown in Fig. 1.3. The primary difference between the two is the mode of excitation. The implementation in Fig. 1.3 (a) employs plane wave illumination to excite the reflecting elements while the one in Fig. 1.3 (b) employs a feed horn illumination. In both cases, the redirected beam obeys the generalized Snell's law, and can be programmed to point towards any desired arbitrary direction. The metasurface elements are usually integrated with a phase shifting mechanism that could be leveraged using PIN diodes, FETs, MEMS switches at mmWaves and 2D materials like graphene and vanadium-di-oxide (VO_2) for THz implementations.

There have been several research efforts to design novel RIS architectures suitable for 5G and beyond wireless communication applications. Numerous state-of the-art RIS

designs are reviewed in [36], [44-45]. In [32], the authors present some mathematical models and optimization algorithms to design RIS-assisted wireless communication systems. [33] considers a multiple-input multiple-output (MIMO) system with multiple IRSs, where the objective is to optimize the system performance in terms of the overall capacity and energy efficiency. The paper also investigates the impact of the IRS size and the number of reflecting elements on the system performance. In [34-35], the authors propose the use of machine learning algorithms to optimize the RIS performance and improve the energy efficiency of the wireless system. [37] presents a path loss model for wireless communications through reconfigurable intelligent surfaces (RIS) based on ray tracing simulations and experimental measurements. There have been approaches to enhance wireless communication systems by using a swarm of unmanned aerial vehicles (UAVs) equipped with reconfigurable intelligent surfaces (RISs). RISs have also been shown to improve security of the communication systems by efficiently modeling power allocation and channel estimation errors.

From the signal processing perspective, RIS systems bring interesting challenges to the design of the large-dimensional passive beamforming matrices at the RIS surfaces. For example, [46] investigates the design of low-complexity and energy-efficient RIS beamforming algorithms, [47] designs robust RIS beamforming solutions, and [48–49] develop techniques for the joint base station-RIS beamforming design problem. To address the challenge of large training overhead, [50] developed RIS architectures where sparse active elements can be leveraged to acquire some knowledge about the channel. This can also enable leveraging compressive sensing and deep learning approaches to efficiently estimate the RIS channels [50]. From the network perspective, prior work has analyzed the

coverage performance in outdoor or indoor settings utilizing the RIS for reflection [51–54], refraction to enhance the outdoor-to-indoor coverage [55], and for joint transmission and reflection [56–57]. The existing works however, are mainly limited to simulation data.

From the circuits and prototyping perspectives, various tuning topologies have been reported in the microwave frequency region using PIN or varactor diodes [58–60]. In [61], an implementation of an RIS was presented where the authors showed an indoor coverage analysis using a 2.4 GHz 3200-element RIS. In [62], the authors presented a sub-6 GHz RIS to enhance received signal in wireless communication systems. However, the RIS prototype uses varactor switches, vias, and multilayered PCB structure, which are not suitable to be scaled for mmWave and THz frequencies. For the RIS to be attractive in wireless systems, the surface needs to be scalable to large areas with thousands of unit cells and switches, low-profile and conformal to fit in various irregular surfaces, consume low-power, and be cost efficient in manufacturing, installation, and maintenance. Although most of these features are inherent in reflective surfaces, switching performance, and manufacturability due to the biasing circuit topologies are some of the challenges that need close attention. In this research, the design, fabrication, and characterization of RISs at sub-6 GHz, mmWave, as well as sub-THz frequencies are presented.

1.4 Overview of Biomarker-Sensing Architectures

Remote sensing is an important application of beamforming systems where the information about the targets is obtained remotely typically through various imaging (optical or microwave) techniques. Some of the beamforming architectures presented in the previous sections are also suited to be employed for remote sensing applications. The

goal is to measure the energy reflected, transmitted, or emitted by the targets to capture unique information related to the target.

The development of microwave, mmWave, THz remote sensing apparatus has led to near field imaging techniques that are particularly focused towards developing efficient biomedical imaging, security screening, and non-invasive imaging methods. Driven by the advantage of better penetration capability than the infrared (IR) and optical methods, the remote sensors are finding increasing number of applications. These involve monitoring vital signs [63–64], cardiac sensing [65], finger print imaging [66], security screening [67], etc. Specifically, the past few years has seen a rapid growth in the hand gesture sensing techniques [68-78]. This is driven by the advances in gaming, virtual reality, robotics, and a plethora of other 5G and internet of things-based applications. Several optical [68], glove-based [69], electromyography-based [70], as well as vision based [71] and radar-based [72–73] techniques have been developed to detect hand gestures and interact with machines. The improvement in the spatial resolution of the sensing images has also enabled the development of several deep learning-based classification techniques which can be used for accurate image and gesture interpretations. The following discussion presents some of the existing gesture sensing techniques in the literature.

Surface Electromyography (sEMG) devices are gaining a lot of popularity in both commercial and medical applications. This is due to the ability of the sEMG sensors to provide abundant information about the muscular deformation that can be used to classify gestures. However, these systems suffer from the dependency on targets, skin color, sweat, and rapid movements [74]. Electrical impedance measurement schemes such as Electrical impedance tomography (EIT) [75], contact resistance sensing [76], and capacitance

sensing [77] techniques use electrodes to sense the changes in impedance caused by various hand/finger motions. However, these systems are susceptible to environmental interferences and even some irrelevant hand motions which can inherently deform the skin. Force electromyography (FMG) [78] is a mechanical sensing method based on monitoring pressure, and in contrast to sEMG has shown higher preference among users in addition to its ability to provide higher accuracy data. However, this method is also vulnerable to changes in subsequent sessions as well as electromagnetic interference. Other mechanical sensing schemes include inertial measurement units (IMU), strain, and flex sensors which have achieved reasonable miniaturization to be suitable for wearable applications [79]. However, these systems are susceptible to one or more of the following problems; sensor shifting, low accuracy, interference from various body motions, as well as expensive implementation schemes.

Ultrasound imaging [80-81] has been gaining interest for gesture recognition as it can simultaneously capture both deep and superficial muscle activity, thus offering higher resolution and accuracy compared to sEMG. However, at present, ultrasound-based techniques are bulky and expensive making them unsuitable for wearables. There are also mechanomyography [82] and bone conducted sound sensing schemes that capture the vibrations from skeletal muscles either directly or using actuators. However, these schemes suffer from background noise, motion artifacts, and low signal levels. Optical sensing schemes [83] offer the advantage of lightweight, portable, cheap, and miniature devices that are suitable for consumer electronics. Photo plethysmography, near-infrared spectroscopy, and time-of-flight (ToF) techniques have been used to classify gestures. The

primary drawbacks of the optical techniques include susceptibility to ambient light noise, very high sensitivity to sensor location, skin type, and even rapid body movements.

The SIW-LWA gesture sensor developed in this work operates by illuminating the human wrist with non-ionizing electromagnetic signals that get reflected by various tissues within the hand and return to the detector. These reflected signals possess diverse spatial information resulting from the changes in the positions of the tissues such as tendons and nerves, due to various hand gestures. The sensor is designed to operate in the microwave region to combine the advantageous features of both the existing low-frequency sensing schemes and the optical techniques. Thus, sufficient miniaturization suitable for wearable electronics (smartwatches, wristbands, etc.,) is realized ($8cm \times 2cm$), while also achieving necessary penetration depth requirements.

1.5 Scope of this Work

This dissertation focuses on the design and characterization of reconfigurable metasurfaces (RMSs) for beamforming and sensing applications. Specifically, the analysis of RISs for 5G and beyond wireless communications, meta-TL structures aimed at miniaturizing Rotman lenses suitable for satellite and radar communications, and SIW-LWAs for gesture sensing applications are presented.

Both implementations of RISs (horn illumination and plane wave illumination) are considered for analysis in this work. The use of horn antenna has the advantage of imparting an inherent pseudorandom profile to the phase modulation of the reflecting elements, thereby nullifying the impact of phase errors resulting from quantization. As such, RISs excited by horn antennas do not suffer from the problem of quantization lobes

seen with the implementations that employ plane wave as the source of illumination. However, the RISs with horns suffer from feed blockage issues, limiting the scan range. As such, RISs with plane wave illumination are usually preferred. However, when low-bit (e.g. single bit) quantization schemes are utilized to minimize the cost and complexity of the design, they lead to the generation of grating lobes in undesired directions known as quantization lobes. These quantization lobes usually tend to have the same amount of energy as the main lobe of the surface and thus, can be detrimental to the performance in wireless communication applications where low-interference is desired. Motivated by this requirement, a quantization lobe mitigation technique is developed using phase randomization. Through random phasing, the symmetry of the periodic errors resulting from quantization can be broken and the quantization lobe levels could be reduced.

Rotman lenses are true-time delay structures as the phase delays needed for beamsteering are due to the actual time of travel within the lens. This leads to the advantage of high beam pointing accuracy and minimizes beam squints across the frequency of operation. Rotman lenses are well-suited of the design of amorphous arrays (arrays which do not have all the radiating elements in a single plane and have non-uniform spacing between them). Such requirements are posed by arrays mounted on satellites and aircrafts where the antennas of the array might be located on different locations of the fuselage, wings, etc., but need to be fed coherently. While Rotman lenses offer an excellent low-cost solution for they are usually bulky making them unsuitable for airborne applications. As such, a miniaturization technique based on meta-TLs to model the wave space within the Rotman lens is developed. Specifically, the research focuses on developing a feasibility model using a 1D rendition of a meta-TL to demonstrate the bandwidth and linearity

improvements that can be achieved by deviating from the conventional transmission line (TL) models used in the literature.

Touchless human computer interaction (HCI) is a fast-growing domain particularly with the advent of various virtual and augmented reality applications. It involves the design and development of gesture-based devices that can detect and interpret human gestures such as hand and body movement or facial expressions. The gesture sensors need to be capable of detecting gestures with high accuracy and compact to be integrable with commercial wearable electronic devices such as smartwatches. Additionally, they need to be low-cost, customizable, and consume low power. To address these needs a near-field SIW-LWA based gesture sensor is developed in this research which works on the principles of the near-field radar. Specifically, the sensor is designed to capture the variations in the reflected signals from different tissues within the human wrist resulting from various hand movements and map them to various gestures.

1.6 Outline of the Dissertation

- Chapter 2 presents the basic theory of reconfigurable metasurfaces with an emphasis on the design principles for the analysis of RISs and LWAs.
- In Chapter 3, the design and development of a sub-6 GHz RIS for non-standalone 5G applications is presented. Both passive and active RIS designs employing horn antenna for excitation are considered for analysis in this chapter. The improvement of signal strength and coverage due the presence of RIS in a shadow region of a real-world wireless communication network is demonstrated. This section is largely compiled from the material in [84-85].

- In Chapter 4, a novel technique for addressing the quantization lobe issue witnessed in non-randomized RISs is presented. The quantization lobes are undesired grating lobes which can degrade privacy and raise interference in communication systems. A phase randomization technique is outlined in this chapter, which can be used to mitigate quantization lobes. Two passive RIS designs – one designed for operation in the sub-THz (222.5 GHz) region [86-88] and another in the mmWave (28 GHz) region [89-90] are considered. The design, analysis, and fabrication of both the designs are presented. Additionally, the characterization of both the prototypes using a quasi-optical measurement setup is also detailed along with the demonstration of ability to mitigate quantization lobes.
- Chapter 5 presents the design and evaluation of a 1D prototype meta-TL that serves as a proof-of-concept design for achieving a super-miniaturized Rotman lens suitable for airborne antenna applications. The evaluation of the prototype is presented to demonstrate its ability to improve the dispersion-free frequency range of operation compared to the conventional lumped element TL design. This section derives its material from [91-93].
- In Chapter 6, the ongoing research and remaining steps to conclude this research is presented. Specifically, the development of an SIW-LWA based gesture sensor is detailed. The approach used for designing the near-field SIW-LWA antenna that can efficiently couple electromagnetic energy into biological tissues (particularly human wrist) is also presented. Some of the preliminary results published in [94] are employed to compile this chapter.

CHAPTER 2

THEORY AND PRINCIPLES OF SELECTED ELECTROMAGNETIC METASURFACES

2.1 Introduction

Metasurfaces are engineered two-dimensional (2D) metamaterials made up of electrically small, periodic structures that are designed to control the propagation of electromagnetic waves in ways not found in nature [95–103]. They are made up of sub-wavelength size structures also called *meta-atoms*. They can be made from a variety of materials, including metals, dielectrics, and semiconductors. When the size and shape of the meta-atoms are carefully tuned, they can interact with electromagnetic waves in a way that allows for precise control over their properties. Thus, by manipulating the geometry, orientation, and composition of these structures, it is possible to create a metasurface that can alter the amplitude, phase, and/or polarization of an incoming wave.

Metasurfaces are electrically thin (typically <λ) structures that could be considered as the 2D counterparts of the 3D volumetric metamaterials which are characterized by effective permittivities (ϵ_{eff}) and permeabilities (μ_{eff}) negative or close to zero. They have been termed as double-negative (DNG) materials, negative refractive index materials, and left-handed materials (LHM) [99-101]. While the earliest occurrences of metamaterial descriptions could be traced back to Lamb [104], who suggested the existence of backward waves (waves which travel in the opposite direction of the energy flow), in the electromagnetic sense, the artificial dielectrics could be considered as first examples.

Although Veselago [99] presented a theoretical analysis of the electromagnetic properties of left-handed materials in the 1960s, it was only after the practical realization of such structures by Pendry [100], Smith [101] *et.al.*, that the research on metamaterials started picking pace. The primary advantage of 2D metasurfaces is that their low-profile, planar and flexible nature, and less bulky architectures makes them better suited for design and fabrication compared the 3D metamaterial structures. Additionally, the significant losses and space requirements involved with the 3D metamaterials have led to the increased research interest towards metasurfaces since the beginning of 21st century.

Metasurfaces have gained a lot of popularity in the recent years owing to their ability to offer significant advantages and a wide range of potential applications from microwave to optical frequencies. They can be used to develop novel antenna architectures to achieve dynamic beamforming, reconfigurability, and polarization conversion. By controlling the phase and amplitude of the electromagnetic waves interacting with the metasurface, it is possible to steer the beam to a desired direction. Moreover, the low-profile, lightweight, and conformal nature of the metasurfaces make them well suited to be integrated with other structures such as vehicles, aircrafts, buildings etc., in communications and automotive radar applications. They can also be implemented as frequency selective surfaces (FSS), impedance matching surfaces (IMS), checkerboard surfaces, superlenses with perfect reflection properties, and cloaking devices. While the conventional FSS, IMS, and checkerboard surfaces could be completely designed as passive surfaces, the RISs studied in this work are integrated with active elements to achieve beam reconfigurability. As such, we trade off complexity and versatility to inflexibility but simplicity. Overall, metasurfaces offer a promising approach for

manipulating electromagnetic waves with unprecedented control and flexibility, opening new possibilities for applications in areas such as communications, sensing, imaging, etc.

2.1.1 Metasurface Types

There are several types of 2D metasurfaces, each with its unique properties and applications. Some of the most common types of 2D metasurface designs are listed below.

Dielectric metasurfaces: These are metasurfaces made of dielectric materials, such as silicon or silicon dioxide [105]. They are lightweight, low-loss, and can be used to control the phase, amplitude, and polarization of electromagnetic waves.

Metallic/Plasmonic metasurfaces: These are metasurfaces made of metallic nanostructures, such as gold or silver [106]. They can confine and manipulate light at the nanoscale, leading to enhanced nonlinear effects, strong field confinement, and enhanced light-matter interactions.

Hybrid metasurfaces: These are metasurfaces made of a combination of dielectric and metallic nanostructures [107]. They can offer a balance of low loss and high field confinement, leading to unique properties and applications.

Chiral metasurfaces: These are metasurfaces that have a chiral structure, meaning they do not have mirror symmetry [106] [108]. They can exhibit strong circular dichroism, which is useful for applications such as biosensing and optical communication.

Non-linear/ Active metasurfaces: These metasurfaces can dynamically control their properties using external stimuli, such as electric or magnetic fields, or by integrating active materials, such as liquid crystals or graphene [105] [108–109]. Some manifestations could also include RF amplification or frequency multiplication.

2.1.2 Metasurface Fabrication Techniques

Metasurface fabrication techniques vary depending on the specific application, material, and desired properties of the metasurface. Some commonly used fabrication techniques include:

Electron beam lithography: It is a high-resolution patterning technique that involves using a focused electron beam to create a pattern on a substrate. This technique can produce feature sizes of nanometer scale, making it useful for fabricating high frequency subwavelength structures

Photolithography: Photolithography is a widely used patterning technique that uses light to transfer a pattern from a photomask to a substrate. The process involves exposing the photoresist to ultraviolet light through a photomask, which contains the desired pattern, and then developing the photoresist to remove the unexposed areas. Photolithography can be used to fabricate metasurfaces with feature sizes down to a few hundred nanometers.

Nanoimprint lithography: A technique that involves pressing a stamp with a patterned relief structure into a thermoplastic material to create the desired pattern. This technique is useful for large-area patterning and can produce high-resolution features.

Chemical vapor deposition (CVD): This technique involves depositing a thin film of material onto a substrate using a chemical reaction between vaporized precursor molecules and a heated substrate. The deposited material can then be patterned using lithographic techniques.

Focused ion beam milling: FIB milling is a direct write technique that uses a focused beam of ions to mill a pattern into a substrate. This technique is useful for creating complex 3D structures and can produce sub-10 nm features.

Chemical etching: A process that uses chemical agents to selectively remove material from a substrate to create the desired pattern. This technique is useful for creating large-area patterns and can produce sub-micron features.

Laser ablation: A technique that uses a high-energy laser to selectively remove material from a substrate to create the desired pattern. This technique is useful for creating high-aspect-ratio features and can be used to fabricate metasurfaces on non-planar surfaces.

3D printing: 3D printing is a rapidly evolving technique that can be used to fabricate complex structures with high precision. 3D printing can be used to fabricate metasurfaces with subwavelength features and can be used to fabricate structures with complex geometries.

In this work, planar metasurfaces are designed using a combination of some of the above design approaches and fabrication techniques to realize reconfigurable intelligent surfaces (RISs), meta-transmission lines (meta-TLs), and substrate integrated leaky wave antennas (SIW-LWAs) suitable for 5G and beyond wireless communications, satellite and radar applications, and gesture sensors. Specifically, PCB manufacturing and chemical etching techniques are used to create RISs at sub-6 GHz and mmWave frequencies, meta-TL, and the gesture sensor prototype. On the other hand, the sub-THz RIS is realized using nanofabrication techniques. In the following sections, the analysis techniques for each of the metasurface architectures developed in this work are discussed in detail.

2.2 Analysis of Reconfigurable Intelligent Surfaces

An RIS, typically designed using printed circuit technology, consists of an array of radiating elements integrated with a phase shifting mechanism to redirect the impinging

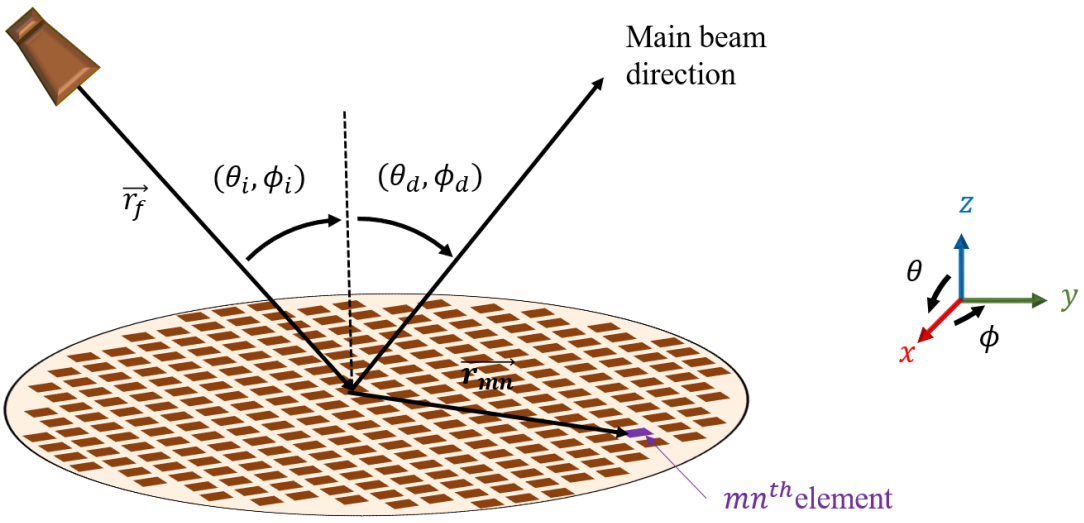

Figure 2.1: A typical feed horn illuminated RIS surface.

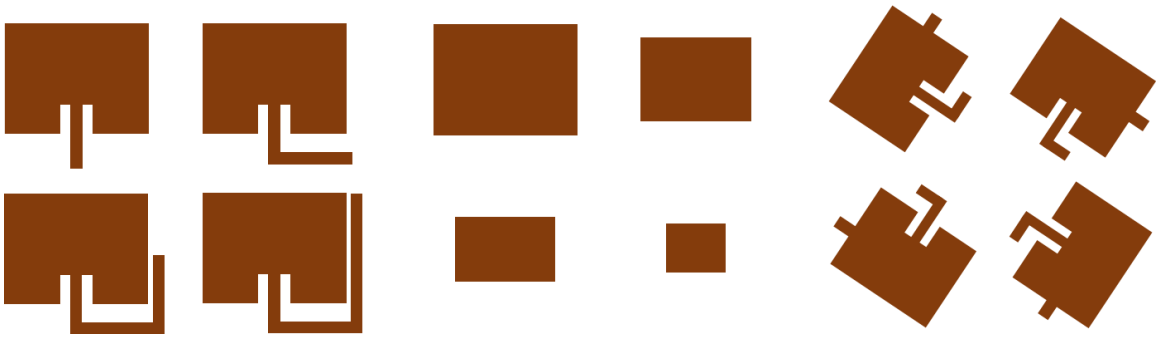

(a) (b) (c)

Figure 2.2: Commonly used phase tuning schemes (a) varying length of phase delay lines, (b) varying element sizes, and (c) varying element rotation angles.

electromagnetic signals from a feed horn or plane waves to a desired direction [110-113]. RISs combine the unique features of planar printed arrays and parabolic reflectors to create hybrid beamforming architectures. A microstrip patch based reflective surface (also known as reflectarray) employing feed horn excitation is shown in Fig. 2.1. The phase shift required to achieve a focused beam could be realized by varying the geometrical parameters of the individual elements such as employing different lengths of phase delay

lines, element sizes (patches, loops, dipoles etc.), or element rotation angles as shown in Fig. 2.2 (a), (b), and (c), respectively. The designs employing patches with variable delay line lengths, transfer the electromagnetic energy impinging on the patch along the transmission line (TL). The TL could be terminated in a short or open. As such, the signal accumulates a phase shift equal to twice the length of the line, gets reflected and radiates towards a chosen direction. Further, by employing active tuning circuitry such as PIN diodes, varactors, etc., along the lengths of the delay lines, dynamic tuning capabilities can be realized. The important design considerations in this approach include the accurate design of the patch for a desired resonant frequency and good match between the patch and the TL. The use of phase shifting lines can lead to dissipative losses as well as spurious radiation at the bends. The mismatch between the TL and patch can lead to phase errors. On the contrary, the designs that use variable element sizes offer better performance in terms of lower dissipative losses and cross polarization levels. However, they suffer from non-linear phase variations due to the high Q resonant nature of the patches, which also leads to narrow bandwidths. Another approach leverages the variation of element rotation to achieve desired phase tuning. The phase shift of the reflected wave can be adjusted by rotating the elements about their origin. This technique however, is limited to RIS designs employing circular polarization.

The design and analysis of RISs requires accurate characterization of the reflective elements, including phase shift and dissipative losses for each polarization, which can be obtained either from circuit models or electromagnetic analysis techniques. Evaluation of radiation patterns, including co- and cross-polarization components, also requires considering the feed model, typically modeled as a $\cos^q(\theta)$ function, but more accurate

simulations or measurements can be used. Radiation patterns can be computed by dividing power patterns by the total power in the feed-horn.

Radiation analysis of RISs is an important design consideration that is used to effectively characterize the performance of the surface. Most approaches approximate the elements on the array aperture as identical elements and use array summation or far field transformation to calculate the radiation pattern. While full wave simulations can provide accurate results, they also require significant computational time and resources. As such, array theory or aperture field techniques [110] can be used as initial evaluation of the radiation performance of RISs. In this work, the array theory method is adopted owing to its simplicity and fast computational time.

Let us assume a feed horn source illuminating the RISs. The radiation pattern of the feed can be modeled to be a rotationally symmetric using cosine q function, and is given by [110]

$$E^{feed}(\theta_i, \phi_i) = \begin{cases} \cos^{q_f}(\theta_i) & for\ 0 \le \theta_i \le \dfrac{\pi}{2} \\ 0 & elsewhere \end{cases} \tag{2.5}$$

where

θ_i, ϕ_i corresponds to the feed pointing direction as shown in Fig. 2.1

q_f is the power pattern of the feed (usually chosen to be between 6 and 8)

Although (2.5) does not include the polarization and reflection effects, it provides a good physical understanding and fast computational time.

Similarly, the radiation pattern of the RIS elements could be modeled using the cosine q function as

$$E^{ele}(\theta_d, \phi_d) = \begin{cases} \cos^{q_e}(\theta_d) & for\ 0 \le \theta_d \le \frac{\pi}{2} \\ 0 & elsewhere \end{cases} \tag{2.6}$$

where

θ_d, ϕ_d corresponds to the direction of the main beam as shown in Fig. 2.1

q_e is the power pattern of the radiating element (usually chosen as 1 to model radiating elements with wide beamwidth)

Consider a 2D planar RIS consisting of $M \times N$ elements arranged on an xy plane. When employing a plane wave illumination, the phase modulation experienced by each radiating element due to the impinging electromagnetic signal from an arbitrary direction (θ_i, ϕ_i) is given by

$$\Phi_{mn}^{illum} = -k_0(x_m \sin\theta_i \cos\phi_i + y_n \sin\theta_i \sin\phi_i) \tag{2.7}$$

where

(x_m, y_m) correspond to the position of the mn^{th} element of the array

k_0 is the free space propagation constant

For the feed horn illumination, with the feed located at (x_f, y_f, z_f) above the plane of the surface, the phase of the illuminating signal can be obtained by using Euclidean distance between the feed and the surface as

$$\Phi_{mn}^{illum} = -k_0 d_{mn} \tag{2.8}$$

where

$$d_{mn} = \sqrt{(x_m - x_f)^2 + (y_m - y_f)^2 + z_f^2}$$

From the classical array theory, the phase shift required by each element of an array to produce a collimated beam in the desired direction (θ_d, ϕ_d) is given by [93]

$$\Phi_{mn} = -k_0(x_m \sin\theta_d \cos\phi_d + y_n \sin\theta_d \sin\phi_d) \quad (2.9)$$

Further, it is to be noted that the phase of the reflected field at each RIS element could also be modeled as the sum of the phase of the incident field from the feed and the phase shift introduced by each individual cell, and is given by

$$\Phi_{mn} = -k_0 d_{mn} + \Phi_{mn}^{\text{ele}} \quad (2.10)$$

where

Φ_{mn}^{ele} is the phase shift due to mn^{th} element

d_{mn} is the distance between the phase center of the feed and the mn^{th} element

From (2.7) and (2.8), the phase shift due to the mn^{th} element of the RIS can be obtained by

$$\Phi_{mn}^{ele} = k_0 d_{mn} - k_0(x_m \sin\theta_d \cos\phi_d + y_n \sin\theta_d \sin\phi_d) \quad (2.11)$$

The incident fields from the feed induces a current distribution on the individual elements of the RIS. These induced currents, together with the phase distribution of the elements leads to radiation with the main beam in the desired direction, which can be modeled effectively using the array theory [110]. Such scattered fields from an $M \times N$ RIS can be computed using

$$E(\hat{u}) = \sum_{m=1}^{M}\sum_{n=1}^{N} \vec{A}_{mn}(\hat{u}) \cdot \vec{I}_{mn}(\vec{r}_{mn}) \quad (2.12)$$

$$\hat{u} = \hat{x}sin\theta cos\phi + \hat{y}sin\theta sin\phi + \hat{z}cos\theta$$

where

A is the element pattern vector function

I is the element excitation vector function

$\vec{r}_{mn}$ is the position vector of the mn^{th} element

Scalar approximations of the field patterns could be used to simplify the analysis. As such, the element pattern and the element excitation pattern could be obtained using cosine q function as

$$A_{mn}(\theta, \phi) = \cos^{q_e}(\theta_d) \cdot e^{jk(\vec{r}_{mn} \cdot \hat{u})} \tag{2.13}$$

and

$$I_{mn} = \frac{\cos^{q_f}\left(\theta_i\ (m,n)\right)}{\left|\vec{r}_{mn} - \vec{r}_f\right|} \cdot e^{-jk(|\vec{r}_{mn} - \vec{r}_f|)} \cdot |\Gamma_{mn}| e^{j\Phi_{mn}} \tag{2.14}$$

where

$|\Gamma_{mn}|$ is the receive mode pattern of the mn^{th} element which can also be modeled using cosine q function as $|\Gamma_{mn}| = \cos^{q_e}(\theta_d(m,n))$

$\vec{r}_f$ is the position vector of the feed

Thus, by using (2.11) and (2.12), the approximate scattered fields of the RIS could be obtained using the traditional array summation technique as

$$E(\theta, \phi) = \sum_{m=1}^{M} \sum_{n=1}^{N} \cos^{q_e}(\theta_d) \cdot \frac{\cos^{q_f}\left(\theta_i\ (m,n)\right)}{\left|\vec{r}_{mn} - \vec{r}_f\right|} \cdot e^{-jk(|\vec{r}_{mn} - \vec{r}_f| - \vec{r}_{mn} \cdot \hat{u})} \cdot \cos^{q_e}(\theta_d(m,n))\, e^{j\Phi_{mn}} \tag{2.15}$$

The array theory approach provides a computationally efficient method to generate the general RIS scattered fields and model the main beam direction and the beamwidth.

For accurate analysis of RISs, usually electromagnetic simulators are employed which serve as powerful tools to understand the full-wave behavior of the surfaces'

scattering properties, polarization, and mutual coupling effects. Some of the commonly used computational techniques include finite element method (FEM), finite difference time domain (FDTD), and method of moments (MoM). Infinite array approach with Floquet ports and periodic boundary conditions can minimize the simulations resources by reducing the model to a single periodic unit cell. A simple simulation model is shown in Fig. 2.3. Floquet ports are generally used in electromagnetic simulators to excite periodic structures like gratings and metasurfaces. The Floquet port applies periodic boundary conditions to the structure by using the Floquet theorem. The Floquet modes which arise from the mathematical concept of Floquet theorem are the solutions to Maxwell's equations in periodic structures, where the field profile repeats itself with a certain period. They can be used to analyze the propagation of waves in these structures and to determine their dispersion relations, which describe how the waves propagate in space and frequency. As such, by specifying the excitation or termination coefficients for each Floquet mode, the user can accurately model the behavior of the periodic structure under different scan angles. The number of Floquet modes (TE_{00}, TM_{00} etc.,) to be employed for analysis could also be specified to get a comprehensive understanding of the array behavior. It allows for a more efficient simulation of these structures since only one-unit cell needs to be modeled, rather than the entire structure. The Floquet port is placed on the boundary of the unit cell (typically at a distance of $\lambda/2$) and provides an excitation signal that represents the incident wave on the periodic structure. The reflected fields can be obtained at the port for characterizing the RIS elements. The other techniques involve metallic waveguide simulators and analytical circuit models [110].

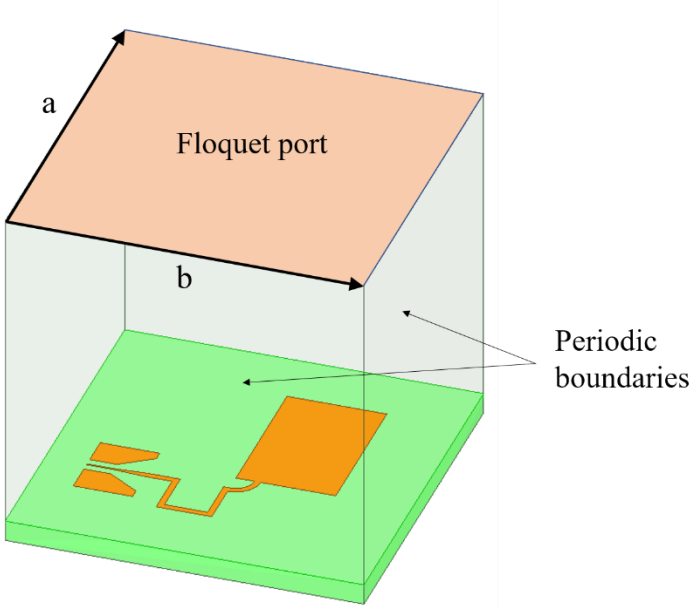

Figure 2.3: Unit cell of an array analyzed using infinite array approach, employing Floquet port excitation and periodic boundary conditions.

The analysis techniques must also consider different sources of errors in the desired phase shifts arising from the employed design techniques, fabrication limitations, and approximations in the analysis. Three primary sources of phase inaccuracies are quantization errors, phase range errors, and infinite array approximations. To reduce the design and fabrication complexities, it might be necessary to use quantized phase values instead of continuous phases. This difference between the ideal phase values and the quantized phases results in quantization errors that lead to the generation of grating lobes in undesired directions. The entire phase range ($0 - 360°$) might not be available due to design limitations which would then lead to limited values of quantization levels and consequently quantization errors.

RISs using printed microstrip elements offer advantages such as low-profile, small mass, and low manufacturing cost. They can achieve high efficiency and wide-angle beam

scanning without the need for complex beamforming networks or expensive T/R amplifier modules. The flat structure of reflectarrays allows for simpler and reliable deployment mechanisms. They can also be fabricated with low-cost chemical etching processes and can achieve accurate contour beam shapes through phase synthesis techniques. Multibeam capability can also be achieved using switches or by placing multiple feed elements at the focal area.

Despite its numerous capabilities, a distinct disadvantage of RISs is their narrow bandwidth, typically not exceeding much beyond ten percent. This limitation is influenced by factors such as element design, aperture size, and focal length. They also require precisely calibrated phase shifters which can drive up the cost in mmWave implementations. In the future chapters, 3 RIS implementations employing patch antenna as the primary scattering element are analyzed to evaluate their potential to be adopted for upcoming 5G and beyond wireless communication applications. The design techniques presented in this section will be leveraged to develop the surfaces. Following sections below will focus on the design and analysis techniques of other metasurface architectures employed in this work.

2.3 Analysis of Meta-Transmission Lines

In this section, the design procedure for meta-TLs is outlines which belong to the class of in-plane metasurface based delay lines. Electromagnetic delay lines are devices that use electromagnetic waves to introduce a time delay in a signal path. They are used in applications that require precise time delays such as phased array antennas, radar systems, and analog signal processing circuits. Coaxial cable delay lines, microstrip delay lines, and

waveguide delay lines are the most commonly used types of delay lines. Such electromagnetic delay lines are characterized by high-power handling capabilities, wide bandwidth, and low noise, which can be advantageous for beamforming and sensing applications. Additionally, since the delay properties are based on the actual time of travel along the line, they provide true time delays (TTDs) that could be used to steer the signal to a specific direction or achieve accurate phase compensations. However, they also have some limitations, such as the loss and dispersion of the signal over long distances and the need for careful design and calibration to ensure precise time delays. Particularly, when used for low-frequency applications such as long-range radars and satellite communications, the physical dimensions of the transmission lines and waveguides become prohibitively large while also increasing losses. As such, usually lumped element circuit model of the TLs is employed to achieve the phase or time delays required for beamforming in these applications. The lumped TL models provide the great degree of miniaturization compared to the physical cables and thus, are preferred at low frequencies (below ultra-high frequency (UHF) range). The conventional lossless model of the TL could be implemented using the LC ladder network shown in Fig. 2.4. Such an arrangement provides a low-pass filter response with the upper cut-off frequency (f_c) determined by the constituent L (inductance) and C (capacitance) values and is given by the following expression.

$$f_c = \frac{1}{\pi\sqrt{LC}} \tag{2.16}$$

The corresponding time delay T that could be achieved by this implementation is

$$T = \sqrt{LC} \tag{2.17}$$

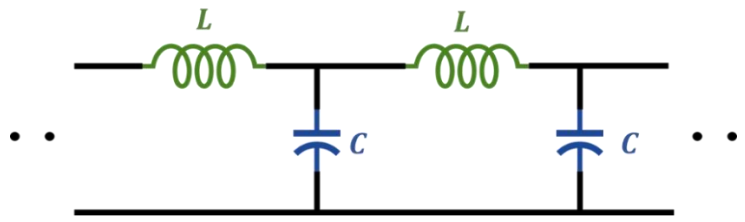

Figure 2.4: Conventional lumped LC ladder network used to model a lossless TL.

A primary drawback of this simplified representation of a TL is that it does not include the mutual coupling between the adjacent elements of the line. Additionally, another characteristic of such a periodic arrangement is that the TL becomes dispersive below the cut-off region. Thus, the dispersion ($\omega - \beta$) diagram becomes highly non-linear near the cut-off and consequently, a constant velocity of propagation cannot be maintained in the entire frequency range of operation. Several attempts, both theoretical and experimental, were carried out in the early part of 20th century [114-116] to improve the usable frequency range by improving the linearity of the dispersion diagram. It was first noted in [113] that by introducing some mutual inductance in a standard low-pass filter, the β curve could be straightened, and a constant velocity of propagation could be achieved. This technique is adopted in this work to improve the accuracy of modeling a traditional lumped LC ladder network and the resulting TL is referred to as *meta-transmission line* (meta-TL). This definition deviates from that of the more colloquial metamaterial TLs where either left handed (LH) medium (with capacitors in series and inductors in shunt) or a combination of left and right-handed media (also known as the conventional TL model) are used to realize LH-TLs or Composite right/left handed transmission lines (CRLH TLs). However, it is important to note that the approach used in this work uses sub-wavelength structures which can engineer the behavior of

electromagnetic signal propagation and achieve enhanced performance in terms of size reduction and bandwidth improvement. This justifies the use of the term meta-TL to describe the structure developed in the work.

In [115], L. Brillouin presents a comprehensive analysis of the effect of introducing mutual inductances in the LC ladder network. Mutual inductance terms are not only introduced between the first nearest neighbors, but also between the farther elements of the line. As such, a constant velocity of propagation could be maintained all the way up to cut-off. Fig. 2.5 represents the LC ladder network with mutual inductance terms. For brevity, only the mutual inductances between the first nearest neighbors are depicted. The voltage across the n^{th} unit cell of the meta-TL is given by

$$L\frac{d}{dt}(i_n) + M_1\frac{d}{dt}(i_{n-1} + i_{n+1}) + \cdots + M_p\frac{d}{dt}\left(i_{n-p} + i_{n+p}\right) + \cdots = V_{n-1} - V_n \tag{2.18}$$

where

M_1 is the mutual inductance between the first nearest neighbors

M_2 is the mutual inductance between the second nearest neighbors

M_p is the mutual inductance between the p^{th} nearest neighbors

$V_n = Q_n/C$

By simplifying (2.18), the required values of the mutual inductance terms can be obtained. It was discovered that the by using the mutual inductance between the first two nearest neighbors, a sufficient degree of linearity improvement could be achieved that leads to a constant velocity TL model all the way up to cut-off. The required mutual inductance values are found to be

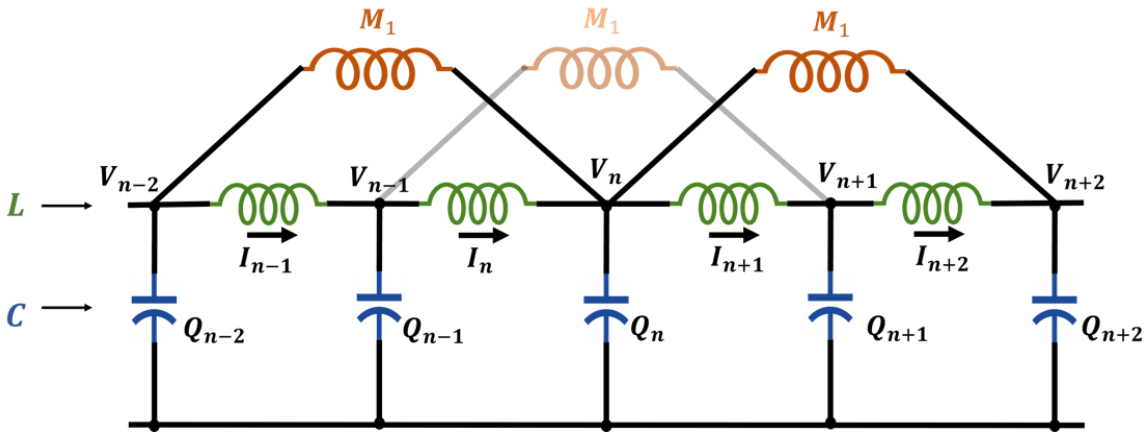

Figure 2.5: LC ladder network with the mutual inductance term introduced between the first nearest neighbors to improve the accuracy of the TL model and extend the frequency range with constant velocity of propagation.

$$M_1 = 0.171\,L$$

$$M_2 = -0.0485\,L$$

$$M_3 = M_4 = \cdots = 0 \tag{2.19}$$

Further, it will be shown in Chapter 5 that even by using only the M_1 term, the achieved linearity improvement is satisfactory for practical implementations. The meta-TL developed in this work is targeted towards miniaturizing Rotman lens architectures at low VHF/ UHF frequencies. Rotman lenses provide the unique capability of achieving excellent beam pointing accuracy needed for satellite communications and radars over a wide bandwidth, because of their true time delay properties. The existing solutions of Rotman lens implementations however, are extremely bulky (of the order of 5λ in the VHF/ UHF bands) making their deployments challenging on airborne platforms. As such, miniaturization techniques are highly sought after. The meta-TL approach developed in this work to realize a hyper-compact Rotman lens will be detailed in Chapter 5.

2.4 Analysis of Leaky-Wave Antennas

Leaky-wave antennas (LWAs) are a type of directional antenna that radiates an electromagnetic wave with a controlled radiation pattern. LWAs work by exciting a guided wave mode in a transmission line that is intentionally made to be lossy or leaky. The energy of the guided wave propagates along the structure and is radiated into space through the leakage openings. The radiation pattern can be controlled by varying the spacing and size of the openings along the length of the structure. LWAs have several advantages over traditional antennas. For example, they offer continuous scanning of the radiation pattern without requiring any moving parts, which makes them suitable for applications that require rapid beam steering, such as radar and satellite communication systems. They also have a lower profile and can be made to be conformal to a curved surface, which makes them ideal for applications that require low-profile or conformal antennas, such as aircraft and spacecraft. LWAs are used in a variety of applications, including satellite communication, radar, and wireless communication systems. In the recent years, they are also extensively used in biomedical imaging and sensing applications.

LWAs have been studied for several decades, with significant progress made in terms of understanding their behavior, design, and performance [97–98]. The earliest work on LWAs dates to the 1940s [117], when they were initially proposed as a means of guiding and radiating electromagnetic waves in microwave circuits. Most of the initial LWAs were based on closed waveguides with long uniform slits along the length of the waveguide. However, these long slits lead to high attenuation constant (α) along the line making it difficult to achieve narrow beams. To counter this and achieve narrow beams, by controlling α, the single slit designs were later replaced by multiple holes or slots along

the length of the waveguide. While early LWA designs were based on closed waveguides, most of the current LWAs employ open waveguide structures. LWAs are predominantly classified as uniform and periodic based on the type of the modulation that leads to radiation. Uniform LWAs have no variation along the length of the waveguide. The dominant mode is a fast wave which is the source of radiation. While they boast simplistic designs, such implementations can only radiate in the forward quadrant and have wide beamwidth. The beamwidth and the sidelobes could be reduced by introducing some taper along the waveguide. On the other hand, periodic LWAs possess some periodic modulation along the length of the waveguide. In these implementations, the dominant waveguide mode is a slow wave. As such, the radiation is through the space harmonics resulting from the periodic modulation. Consequently, they can radiate in both forward and backward quadrants. In this work, both uniform and periodic LWAs designed in a substrate integrated waveguide environment are employed to develop a radio-frequency (RF) gesture sensor that can detect hand signals. Both the designs are evaluated for their ability to capture the reflected signals from various tissues in the human wrist. The inherent frequency scanning capabilities of the LWAs are exploited to obtain unique tissue specific information corresponding to various hand gestures. A typical representation of a uniform and a periodic LWA is shown in Fig. 2.6 (a) and (b), respectively.

Fast and Slow Waves: The wave traveling within a waveguide can have a phase velocity (v_p) that is either higher or lower than the speed of the light. When v_p is higher than the speed of light, the wave is called a fast wave, i.e.,

$$v_p > c \ \rightarrow \beta < k_0 \tag{2.20}$$

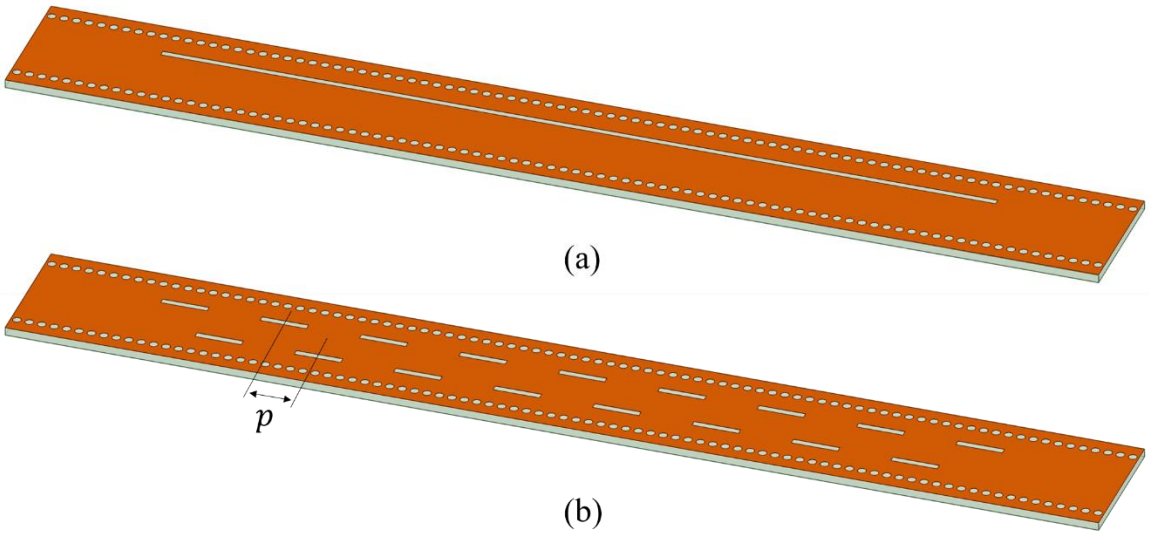

Figure 2.6: Typical LWA implementations: (a) uniform LWA and (b) periodic LWA with a modulation period p.

where

c is the speed of light = $3 \times 10^8\ m/s$

β is the phase constant in the medium

k_0 is the free space propagation constant

On the other hand, when v_p is lower than the speed of light, the wave is called a slow wave ($\beta > k_0$) and is bound to the medium. Such waves are generally seen in dielectric filled waveguides and do not radiate. As such, most periodic LWAs designed using dielectric filled waveguides radiate using space harmonics or Floquet modes. These harmonics are generated by the periodic modulation introduced by adding grooves, metallic strips, etc., along the walls of the waveguide. Each space harmonic is characterized by a phase constant given by [79-80]

$$\beta_n p = \beta_0 p + 2n\pi \tag{2.21}$$

where

$\beta_0 = \beta$ is the same phase constant of the slow wave

p is the modulation period

$n = \pm 1, \pm 2, \pm 3, \ldots$ is the order of the space harmonic ($n \neq 0$ for radiation to occur)

Forward and Backward Leaky Waves: The leaky-waves could be classified as forward or backward leaky waves. Forward leaky-waves (FLWs) have their group and phase velocities in the same direction and radiate in the first quadrant, while the backward leaky-waves (BLWs) have their group and phase velocities in the opposite directions, leading to radiation in the second quadrant. Additionally, FLWs are represented by $\beta > 0$ (electromagnetic wave propagates along $+z$ direction) and $\alpha > 0$ (wave attenuates as it propagates). Consequently, the phase constant of the space harmonic above the LWA plane β_x must be positive as the leaky wave is propagating in the $+x$ direction. However, $\alpha_x < 0$ for FLWs indicating that the field strength increases as the above the surface as indicated by Fig. 2.7 (a). To that end, FLWs are also known as 'improper' or 'non-spectral' waves. On the contrary, the BLWs have $\beta < 0$ (wave propagation is along $-z$ direction) while $\alpha > 0$. Additionally, both β_x and α_x are positive, thus making the BLWs 'proper' waves. The forward and backward leaky-waves propagating in a substrate medium and contributing to radiation are depicted in Fig. 2.7 (a) and (b), respectively.

The condition required for radiation is $\beta_n < k_0$ which is readily confirmed by the existence of dominant fast waves in air-filled waveguides. For substrate-based waveguides, $\beta_n > k_0$ as the dominant mode is a slow wave. Consequently, the constraint for the existence of space harmonic could be obtained by modifying (2.21) as

$$\frac{\beta_n}{k_0} = \frac{\beta}{k_0} + \frac{2n\pi}{k_0 p} \tag{2.22}$$

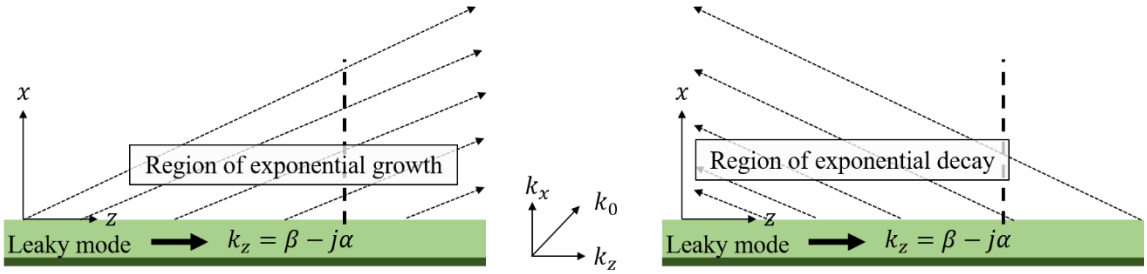

(a) (b)

Figure 2.7: Leaky wave generation in a substrate medium (a) forward leaky-waves and (b) backward leaky-waves.

It follows that $\beta_n/k_0 < 1$ can only be achieved if n is negative $(-1, -2, ...)$. Further, to ensure there is only one main beam, at a given frequency, it is also necessary to make sure that $n = -2$ fast wave mode does not radiate. This can be ensured by properly designing the modulation period p of the LWA. The desired main beam direction is dependent on the phase constant of the radiating mode and is given by

$$\theta_m = \sin^{-1}\left(\frac{\beta_n}{k_0}\right) \tag{2.23}$$

It should also be noted that the attenuation constant α controls the beamwidth of the main beam and is dependent of the length of the LWA, L as

$$\Delta\Theta = \frac{1}{\left(\frac{L}{\lambda_0}\right) sin\theta_m} \tag{2.24}$$

The above design equations could be employed to tailor the performance of both uniform and periodic LWAs. Usually α is chosen such that at least 90% of the input power is radiated before reaching the end of the waveguide. This ensures that the entire aperture contributes to the radiation and there are no significant reflections from the edge of the waveguide.

In this work, 1D substrate integrated waveguide leaky-wave antennas (SIW-LWAs) are designed for gesture sensor applications. The sensor works on the near-field radar principles to illuminate the human wrist region with non-ionizing microwave radiation and capture the gesture specific information resulting from the shift in the positions of various tissues within the wrist due to different hand motions. As the LWA is designed to operate in the near field to illuminate the wrist tissues, the general design approach presented above will be optimized to model the quadratic phase distribution required for near-field operation. The design equations together with the full wave simulations will be employed to optimize the geometry of the LWA to improve the radiation efficiency and achieve uniform tapering of the attenuation constant. Care is taken to ensure that the developed LWAs are also relatively compact compared to other types of directional antennas. This feature of the LWAs together with their ability to provide inherent frequency scanning capability makes them well-suited for integration with commercial wearable electronics such as smartwatches and wristbands.

2.5 Conclusion

In this chapter, the theory and design principles of some of the selected metasurfaces – RISs, meta-TLs, and LWAs are presented. While RISs represent the out-of-plane metasurfaces that reflect the impinging plane waves to desired directions, the meta-TLs and LWAs belong to the class of in-plane metasurfaces. The principles of operation presented in this chapter provide the foundation for developing the different metasurface architectures presented in the following chapters. Specifically, the phase control of the RIS plays a critical role in developing multibeam capabilities. In this work,

TL-based phase tuning method will be employed to achieve both fixed beam and multibeam RIS implementations. The effect of including the mutual coupling into the conventional TL model has been shown to create accurate TL models – called the met-TLs – that can be utilized to achieve miniaturization. Finally, the basic leaky wave theory was presented that will be leveraged to develop near-field LWA that can efficiently couple electromagnetic energy into human wrist to develop a novel gesture recognition technique.

CHAPTER 3

RECONFIGURABLE INTELLIGENT SURFACES FOR WIRELESS COMMUNICATIONS

3.1 Introduction

Reconfigurable Intelligent Surfaces (RISs) have attracted significant interest in the recent years from both academia and industry motivated by their promising gain and signal coverage improvements for both millimeter wave (mmWave)/terahertz (THz) and sub-6 GHz wireless communication systems. RISs comprise reconfigurable reflective surfaces that employ tunable subwavelength structures (e.g. antennas) to modulate the phase and/or amplitude of reflected waves. A smooth flat surface (e.g. mirror) reflects signals in the specular direction (incident angle = angle of reflection) because of the predetermined constant phase delay induced as the wave traverses the surface. On the other hand, RISs are capable of anomalous reflection (angle of reflection ≠ incident angle) by artificially modulating the phase and/or amplitude of the reflected wave. Besides redirecting the signal to desired directions in the far-field, RISs can also focus the energy when the user (or BS) is in the radiating near-field of the RIS. The sub-wavelength unit cell receives the incident signal and re-radiates it back into free space with a different amplitude and/or phase. Such modulation can be achieved by tuning the electromagnetic properties of the unit cell. For example, a switch placed at the feed of a patch antenna can alter the path of the electric current (open/short termination) and modulate the amplitude and phase of the re-radiated field. More switches can allow multi-bit wave front

modulation with improved beam control and efficiency. Several topologies can be found in the literature using single or multiple active devices as well as single or multi-layered substrates [118]. In all approaches, a biasing circuit and control unit (e.g. microcontroller) is required to be integrated within the RIS to control the state of the tunable devices by varying the biasing voltage across the device terminals. RISs are considered two-dimensional structures because the lateral dimensions are multiple wavelengths and thickness only a fraction of a wavelength. Such geometrical properties could allow for seamless installation on building surfaces (indoors or outdoors) even on curved surfaces.

At mmWave/THz bands, RIS surfaces provide a potential solution for the critical coverage challenge by intelligently reflecting the wireless signals to the receiver direction. At sub-6GHz bands, RIS systems could be leveraged to enhance the propagation characteristics and increase the spatial multiplexing gains. RISs also find interesting applications such as security and sensing. They can be used to enhance the security and privacy of wireless communication by creating signal-blocking barriers. Unless the user is near the specular direction, signal strength is impacted drastically and enabling anomalous reflection can provide viable propagation paths and boost the strength of received signal. As such, the use of RIS in sub-6 GHz communication systems has the potential to significantly improve wireless signal strength, coverage, and reliability. With all this potential, it is important to accurately evaluate the performance of the RIS. Based on this motivation, this work considers designing a low-power and portable proof of concept prototype for RIS-integrated wireless communications systems and leveraging it to validate the potential sub-6 GHz RIS gains in realistic communication environments.

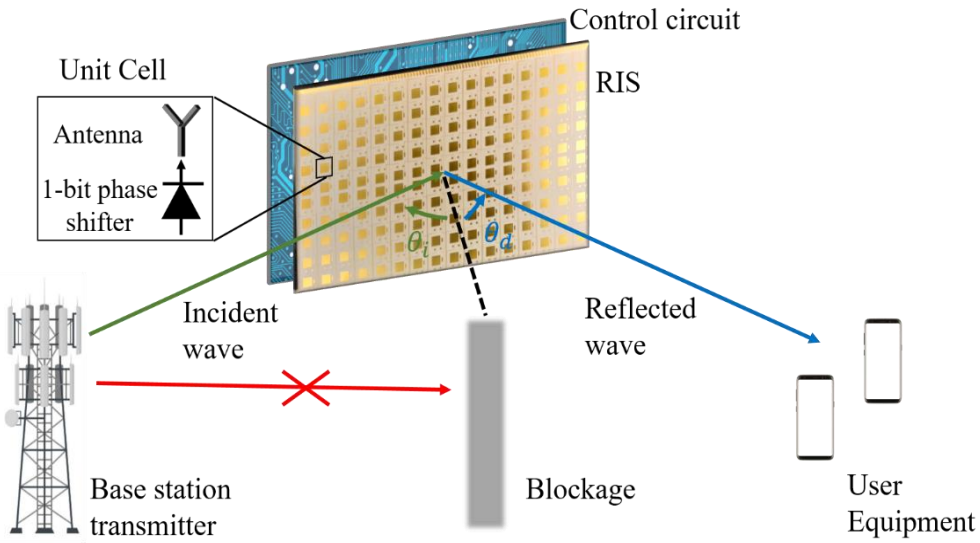

Figure 3.1: Overview of the proposed reconfigurable intelligent surface (RIS). A control circuit provides the necessary excitation (beamforming weights) to the unit cells and redirects the incident wave to the desired direction.

Using the bistatic radar equation, it is possible to estimate the received power P_r when an RIS is placed between the user equipment (UE) and the base station (BS), as illustrated in Fig. 3.1, as

$$P_r = \sigma \frac{P_t G_{BS} G_{UE}}{4\pi} \left(\frac{\lambda}{4\pi R_1 R_2} \right)^2 \tag{3.1}$$

where

P_t is the power transmitted by the BS

G_{BS} and G_{UE} are the gains of BS and UE antennas respectively

R_i and R_d are the distances between BS and RIS, and RIS and UE respectively

The radar cross section σ of the RIS can be approximated as a rectangular, flat conductive surface with losses. As such, the monostatic RCS of the an electrically large RIS with area A, efficiency η, and wavelength λ is

$$\sigma = \frac{4\pi\eta A^2}{\lambda^2} \tag{3.2}$$

In a bistatic scenario, common with the deployments in wireless communications, the RIS is viewed with an angle θ_i from the BS and θ_d from the UE (as shown in Fig. 3.1), assuming BS and UE are on the same plane. Then, the bistatic RCS of the RIS can be approximated by

$$\sigma = \frac{4\pi\eta cos\theta_i cos\theta_d A^2}{\lambda^2} \tag{3.3}$$

It should be noted that the received power increases quadratically with the size of the RIS. Namely, a ten-fold increase in the area A provides 20 dB stronger signal for the same propagation scenario. Similarly, using RISs in higher frequencies, the received power will increase inversely proportional to the square of the wavelength. Such signal improvement is also crucial when considering that higher frequency signals suffer more losses (e.g. free path loss, penetration loss). For example, a window glass or a brick wall can have attenuation that exceeds 25 dB and 91 dB respectively at 38 GHz [119].

Consider the RIS beamforming design problem, if the incident and desired reflection directions are (θ_i, ϕ_i) and (θ_d, ϕ_d), respectively, then the optimal RIS phase shifting configuration for each element ϕ_{mn} is given by

$$\Phi_{mn} = \Phi_{mn}^{illum} - \Phi_{mn}^{d} \tag{3.4}$$

where Φ_{mn}^{illum} and Φ_{mn}^{d} are respectively the phase of the incident wave and phase for the desired reflection direction on the mn^{th} RIS unit cell.

For a two-dimensional planar RIS with unit cells arranged on the xy plane, these phases are given by

$$\Phi_{mn}^{illum} = k_0(x_m \sin\theta_i \cos\phi_i + y_n \sin\theta_i \sin\phi_i) \tag{3.5}$$

$$\Phi_{mn}^{\mathrm{d}} = -k_0(x_m \sin\theta_d \cos\phi_d + y_n \sin\theta_d \sin\phi_d) \tag{3.6}$$

where

k_0 is the free space wavenumber

(x_m, y_m) are the coordinates of the mn^{th} element

For practical implementation purposes, the continuous phases in ϕ_{mn} are quantized using 1-, 2- or 3- bit quantization schemes. In this work, a single-bit phase quantization scheme is adopted owing to its simplicity and lower cost when compared to higher bit quantization methods. As such, all the phase values in the range $[-90°, +90°]$ are rounded off to $0°$ (designated as state '0'/OFF) and the rest of the phase values are rounded off to $180°$ (designated as state '1'/ON). The two states are realized using PIN diodes with state '0' representing the OFF state of the diode and state '1' corresponding to the diode's ON state, as will be explained in detail in the following sections. Thus, the quantized phase shift at the mn^{th} RIS unit cell is

$$\Phi_{mn}^{q} = \left| 180° \cdot floor\left(\frac{\Phi_{mn}}{180°} + 0.5\right)\right| \tag{3.7}$$

With this RIS beamforming design, the resulting scattered fields of the RIS at a direction (θ, ϕ) can be approximated by the array factor

$$AF_{RIS}(\theta, \phi) = \sum_{i=1}^{m}\sum_{j=1}^{n} e^{-j\Phi_{mn}^{illum}} e^{-j\Phi_{mn}^{q}} e^{-jk_0(x_m u + y_n v)} \tag{3.8}$$

where $k_0(x_m u + y_n v)$ corresponds to the phase modulation due to Green's function, $u = \sin\theta\cos\phi$, and $v = \sin\theta\, sin\phi$.

3.2 RIS Design and Prototyping

This section details the design and characterization of the RIS, including the unit cell layout, measurement of the radiation pattern of both a fixed-beam (no switches) and a multi-beam RIS prototype (integrated PIN switches), and integration of the control circuitry. The RIS is designed at a center frequency of 5.8 GHz which is part of the unlicensed spectrum used in wireless local area networks (WLANs). The goal of this work is to design a single layer topology (besides the ground plane) without requiring the use of vertical components (e.g. vias). As such, the RIS is comprised of the ground plane, the substrate, and the top metallization layer. Such topology is attractive for future mmWave and THz RISs where multilayer structures increase losses and fabrication complexity.

3.2.1 Unit Cell Design

Both the fixed-beam and the multi-beam sub-6 GHz RISs designed in this work comprise 160 (16×10) unit cells. While each unit cell of the fixed-beam RIS consists only a resonant metallic patch designed to radiate at 5.8 GHz, the patch in the multi-beam RIS unit cell is integrated with a radio-frequency (RF) PIN diode (switch), and biasing lines, as shown in Fig. 3.2 and Fig. 3.3. The resonant patch re-radiates the received signal with a phase difference that depends on the current distribution. Typically, such a phase shift is enabled either by changing the resonant frequency of the patch (variable size patches) or by providing extra path to the current on the feed of the patch (integrated open/short TLs) [110-113]. The latter approach requires a short transmission line terminated to the ground. Such topology would require a via, thus, to minimize fabrication complexity, the resonance approach adopted by adding a parasitic patch next to the main

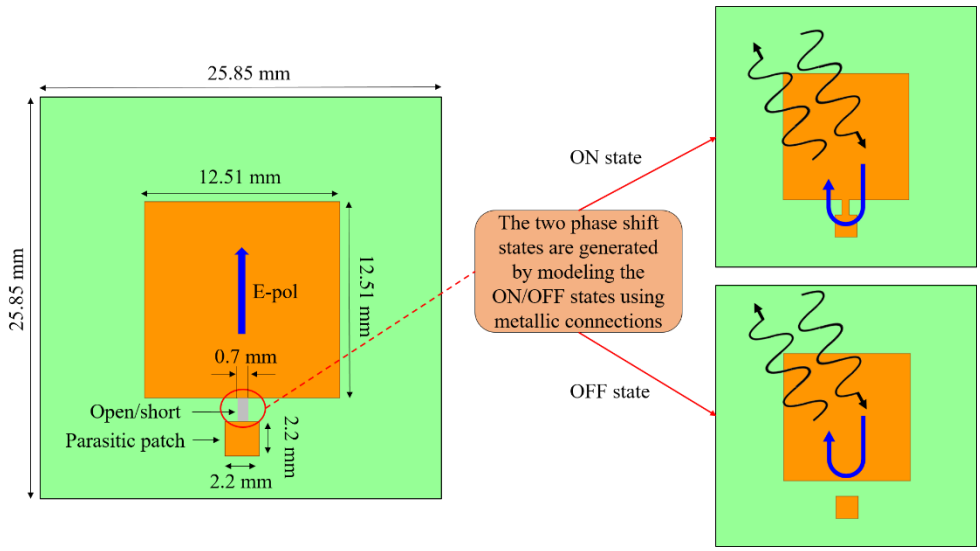

Figure 3.2: Layout of the fixed-beam RIS unit cell. (a) The unit cell consists of a resonant metallic patch and a parasitic patch either connected by a permanent metallic connection during fabrication or left open, and (b) the presence or absence of the metallic connection altering the current path and providing a desired phase modulation.

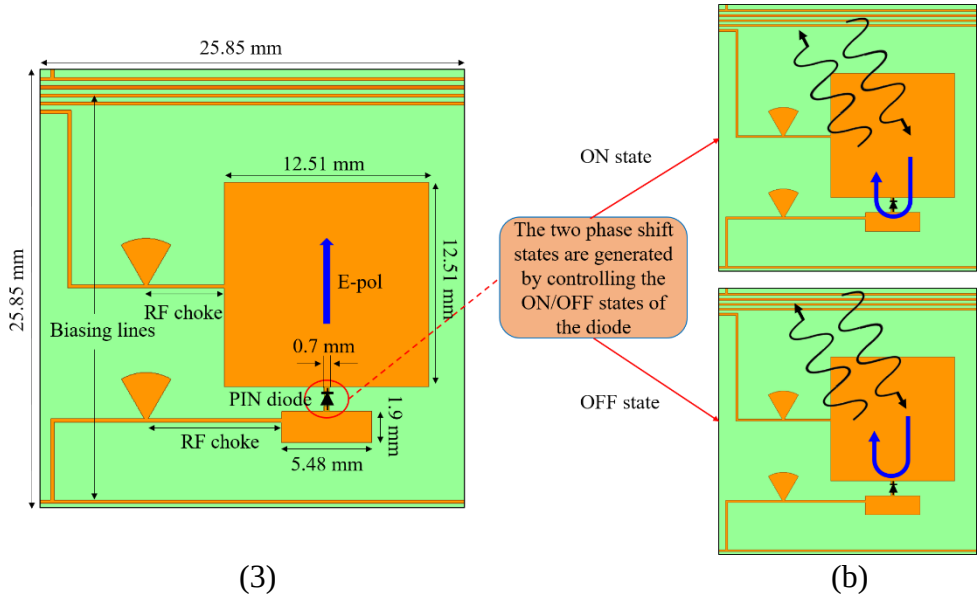

Figure 3.3: Layout of the multi-beam RIS unit cell. (a) The unit cell consists of a main resonant metallic patch connected to a parasitic rectangular patch through an RF PIN diode (switch). The necessary biasing lines and RF chokes are integrated for switch activation (ON/OFF), (b) Activation of the RF PIN diode alters the current distribution, resulting in phase modulation of the reflected signal (180 degrees) without a significant modulation of the magnitude within the bandwidth of interest.

Resonant patch connected through the metallic bridge or the PIN diode. Additionally, biasing lines are needed for both diode terminals, therefore, two narrow lines are connected to the main patch and the parasitic patch respectively, as depicted in Fig. 3.3. To isolate the RF signal from the biasing lines, a radial stub is used in each one of the lines. As opposed to current multi-beam approaches in the literature, the proposed topology i) requires only a single tuning device (switch) and ii) comprises a single-layer with no vertical connections to the ground. Although single switch approaches result in quantization sidelobes, in this study, the RIS is used only in limited scanning range to avoid sidelobe interference. Nevertheless, using pre-coded, phase randomization methods, it is possible to eliminate the undesired side lobes using practical topologies. This technique for mitigating quantization lobes will be treated in detail in Chapter 4. Phase quantization can also limit the minimum step in beam scanning. For the 1-bit topology presented here, beam step is limited to approximately one half-power beamwidth (HPBW). As such, for a 1-bit RIS with a HPBW of 6°, the beam scanning step is also 6° when scanning close to boresight. The step will increase when scanning at wider angles close to the horizon. The response of the unit cell under different biasing states is evaluated using the commercial electromagnetic (EM) software, Ansys HFSS. As such, an infinite array approach is employed to design the unit cells using periodic boundary conditions on each primary direction. Although this process omits radiation effects at the edge of the aperture, it is considered reliable in estimating the EM response of an individual unit cell. The substrate used in this work is the Rogers RT/ Duroid 6002 RF laminate with dielectric constant, height and loss tangent of 2.94, 2.54 mm, 0.0012, respectively. The microstrip patch/switch (BAR50-02V) co-design is carried out using the measured S-parameters provided by the manufacturer (MACOM).

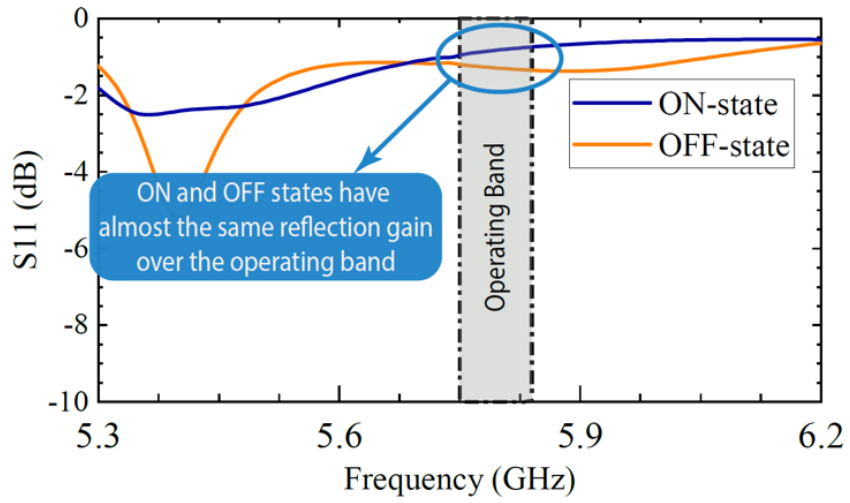

(a)

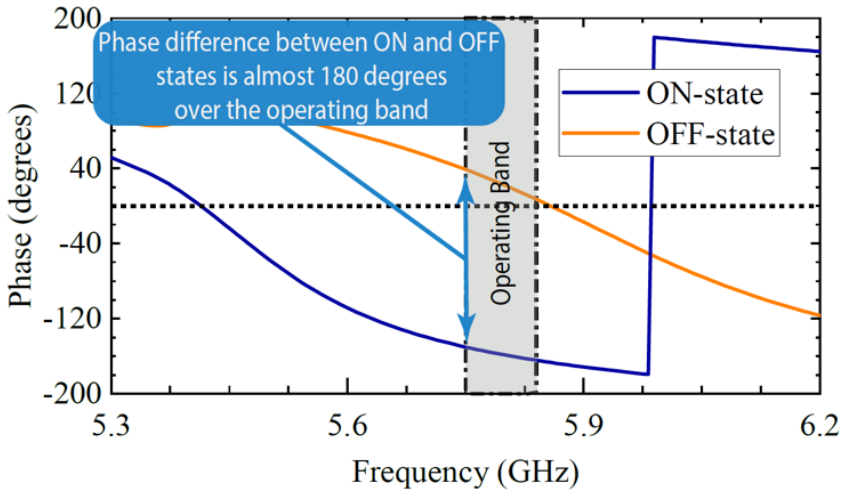

(b)

Figure 3.4: Numerical analysis (periodic boundary conditions) of the unit cell response under boresight illumination ($\theta_i = 0$) for two switch states (ON/OFF).

Employing the infinite array model, the reflected signals on the Floquet port under broadside illumination ($\theta_i = 0$) are obtained. The unit cells are optimized to achieve a reflection magnitude difference $< 1dB$ and a reflection phase difference $\approx 180°$, between the ON and OFF states. For an acceptable phase modulation range of $180° \pm 20°$ between

the two states, the achieved bandwidth is approximately 150 MHz for the multi-beam design, as shown in Fig. 3.4. Similar results are achieved for the fixed-beam RIS. It is also important consider the effect of different angles of incidence and mutual coupling between the radiating elements on the reflection magnitude and phase response, as they determine the overall scanning and bandwidth performance of the RIS. This will be evaluated in the following sections utilizing with the full array design.

3.2.2 Array Design

The radiation characteristics of the RISs have been studied using both the analytical expression in (3.8) as well as the full-wave numerical method. Both fixed- and multi-beam RISs were designed in HFSS and to account for the electrically large model, finite element boundary integral (FE-BI) method was used, which reduces the computational complexity. The designed arrays have overall dimensions of $414\ mm \times 259\ mm$, as shown in Fig. 3.5. For the multibeam RIS, the biasing lines used to control the PIN diodes are routed in groups of five-unit cells to ensure minimum wiring complexity, as shown in the inset of Fig. 3.5 (b). A feed horn antenna located at $\theta_i = -27.5°$ is used to excite the surfaces. The fixed-beam RIS is designed to reflect the incident beam to $+60°$ direction. The normalized RCS patterns obtained from the analytical equations and HFSS simulations are plotted in Fig. 3.6, which shows a good agreement between the two.

For the multi-beam RIS, the RCS patterns for three different reflection angles ($0°, 17°$, and $60°$) are computed. The three excitations result in different switching states of the PIN diodes, leading to three distinct main lobes at the desired directions, as shown in the analytical and full-wave simulation results of Fig. 3.7. Additionally, to evaluate the

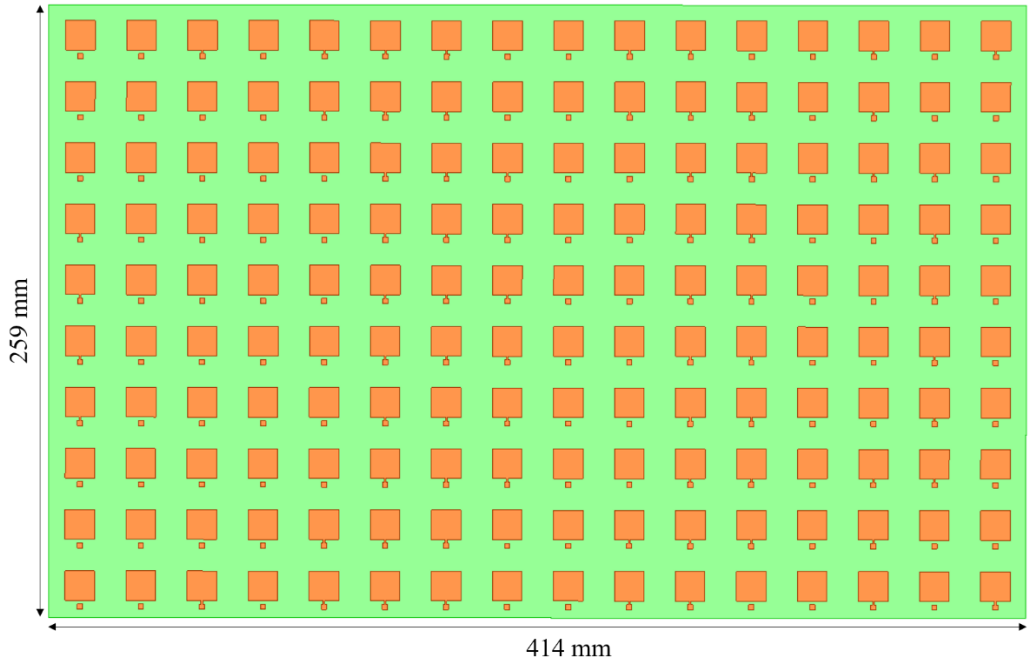

(a)

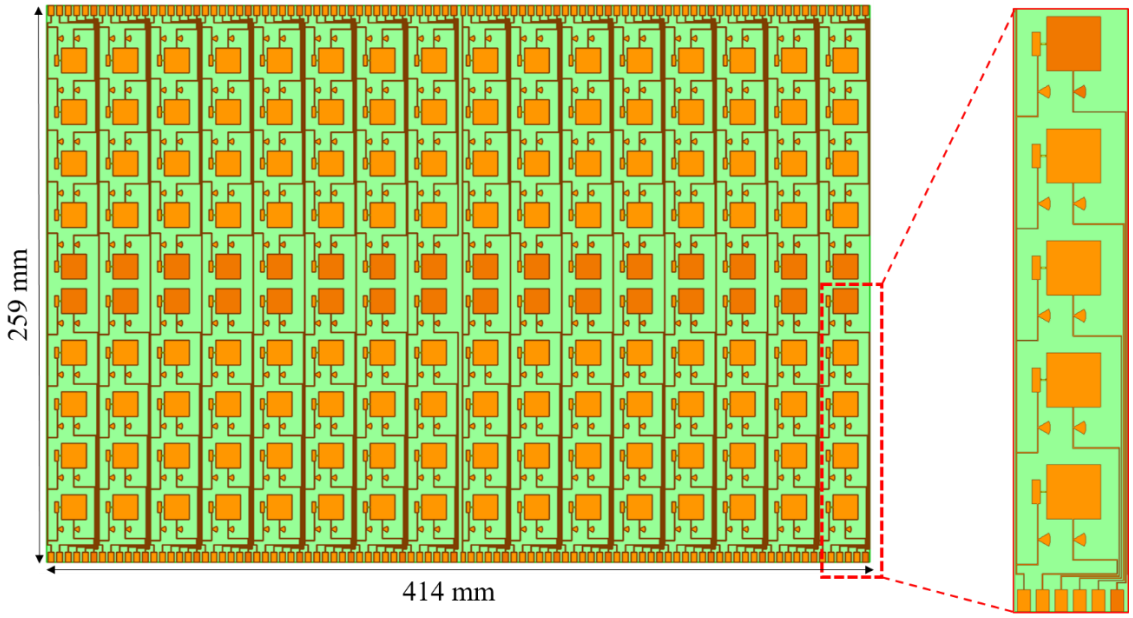

(b)

Figure 3.5: The layout of the 160-element (16 × 10) array used in the proposed RIS. (a) Fixed-beam RIS and (b) multi-beam RIS. The inset shows the routing of the biasing lines for 5-unit cells (no vias).

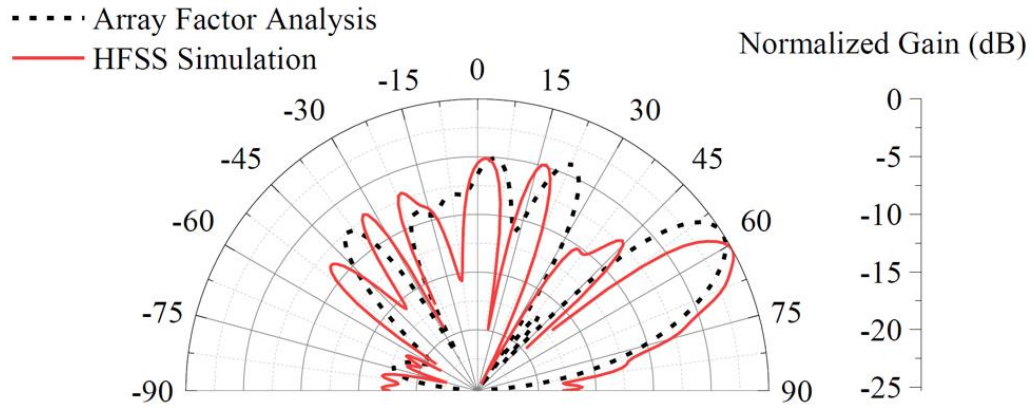

Figure 3.6: Comparison between the analytical and full-wave simulation results of the RCS patterns obtained for the fixed beam RIS designed to reflect the incoming EM signal towards $+60°$.

beamforming characteristics when the feed is in the far-field (plane wave illumination), as expected in several wireless communications scenarios, the feed horn antenna is replaced with a plane wave source in HFSS. The normalized radar cross section (RCS) pattern for three arbitrarily chosen reflection angles ($22.5°$, $40°$, and $60°$) are also computed using both array factor analysis and full-wave simulations. This again leads to three distinct switching states of the PIN diodes. The resulting plots are compared in Fig. 3.8. Due to the phase quantization error (due to 1-bit quantization), the reflected beam presents a second grating lobe at a direction opposite to that of the desired direction, as shown in Fig. 3.8. The grating lobe has the same energy as the main beam and may not be desirable for some applications. Further, it should also be noted that the discrepancy between the patterns with respect to the sidelobe levels is attributed to the diffraction and surface wave phenomena that are not accounted for in the array factor analysis.

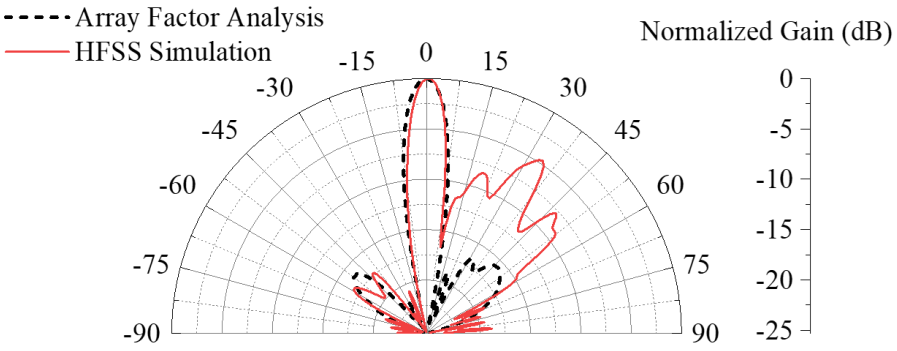

(a)

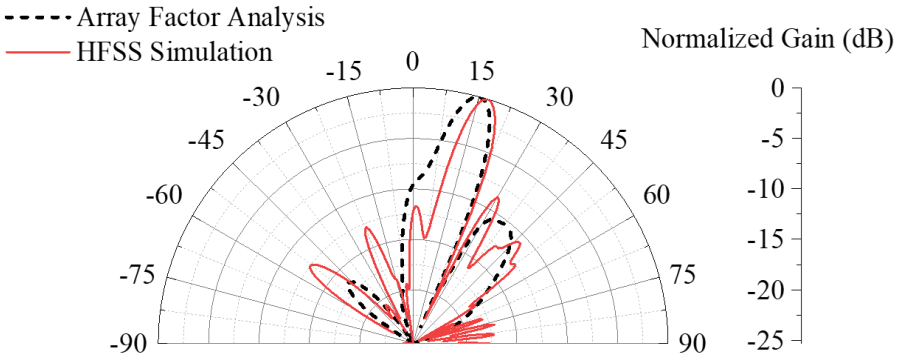

(b)

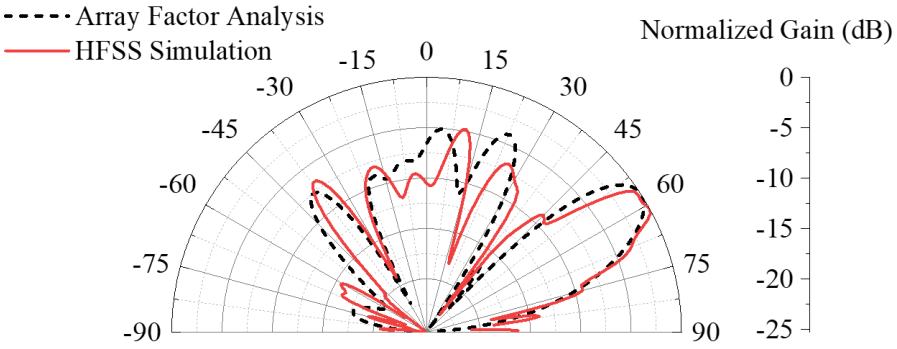

(c)

Figure 3.7: Comparison between the analytical and full-wave simulation results of the RCS patterns obtained for the fixed beam RIS with a feed horn excitation from $\theta_i = -27.5°$: (a) main beam at 0°, (b) main beam at 17°, and (c) main beam at 60°.

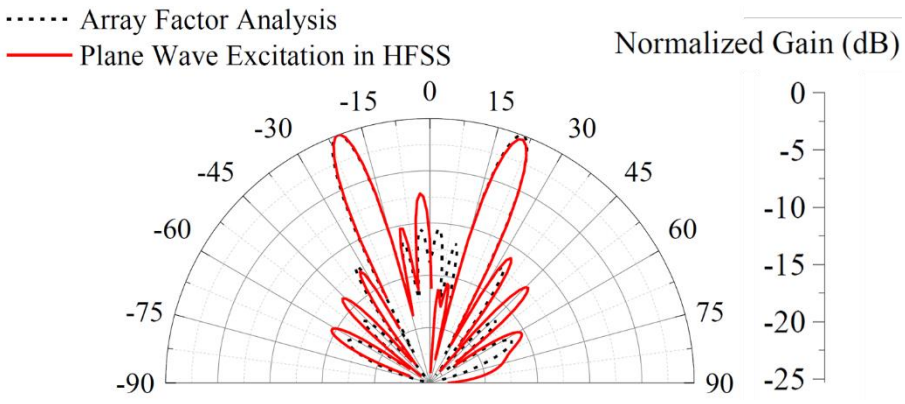

(a)

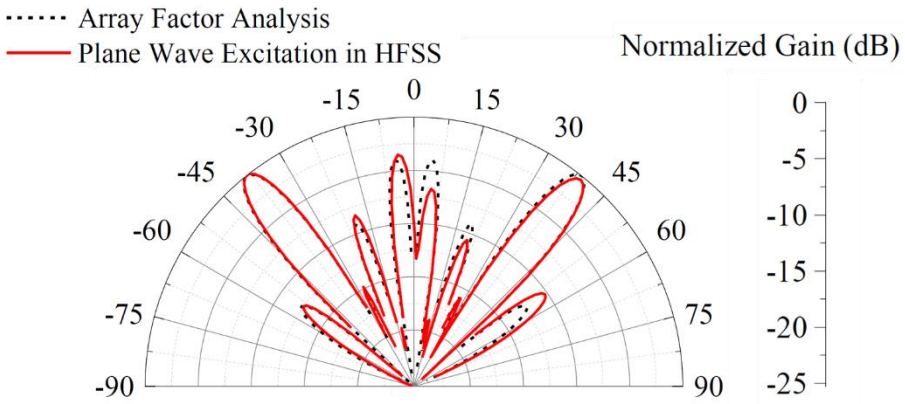

(b)

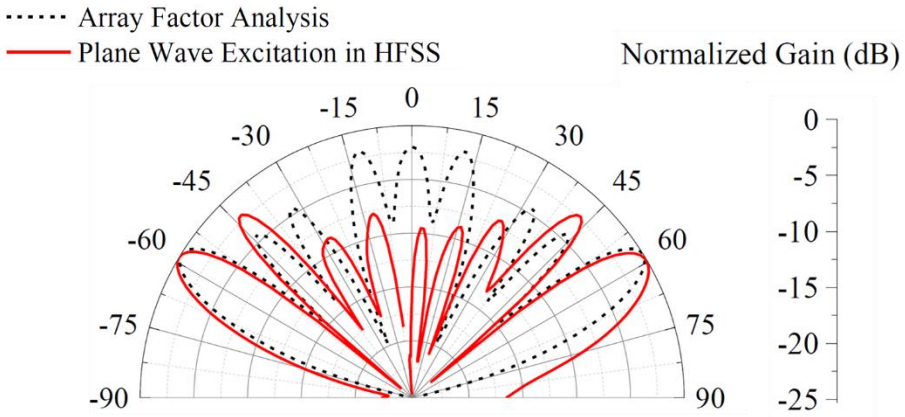

(c)

Figure 3.8: Comparison between the analytical and full-wave simulation results of the RCS patterns obtained for the fixed beam RIS with plane wave excitation from broadside. (a) main beam at 22.5°, (b) main beam at 40°, and (c) main beam at 60°.

3.2.3 Sub-6 GHz RIS Fabrication

The fixed beam RIS was fabricated using a chemical etching process on a $2.54\ mm$ thick Rogers RT/Duroid 6002 substrate. First, the array layout is printed on a thermal sheet using an inkjet printer and then heat pressed on the substrate at $400°\ F$ using a pneumatic heat transfer machine. Afterward, the substrate with the imprinted mask is immersed into sodium persulphate ($Na_2S_2O_8$) solution, and mechanical agitation is used to etch out the unwanted copper. Finally, the mask is removed using acetone to obtain the array pattern. The fabrication process is highlighted in Fig. 3.9.

The smaller feature sizes of the multi-beam RIS leads to difficulties with chemical etching. As such, standard PCB manufacturing techniques were employed to fabricate a prototype multi-beam RIS board. The BAR50 PIN diodes are first evaluated using a test bench to effectively characterize their reflection magnitude and phase responses in the 150 MHz band around 5.8 GHz. The multi-beam RIS requires a control circuitry to bias the 160 PIN diodes and control their states to steer the impinging signals to desired directions. The control circuitry comprising the biasing network and a microcontroller, designed in this work to achieve beamsteering, is depicted in Fig. 3.10. The microcontroller (Arduino MEGA2560) is used to push the beamforming codeword serially to 20 8-bit shift registers. With this biasing circuit design, the bit sequence of each codeword determines the unit cell induced phased delay (0° or 180°) across the 160-element array, and thus steering the beam to the corresponding direction. An LED and a resistor are connected in series with each output pin of the shift register to supply the 0.8 V to turn on the PIN diodes and limit the current to 3 mA. A power consumption analysis is carried out to characterize the total

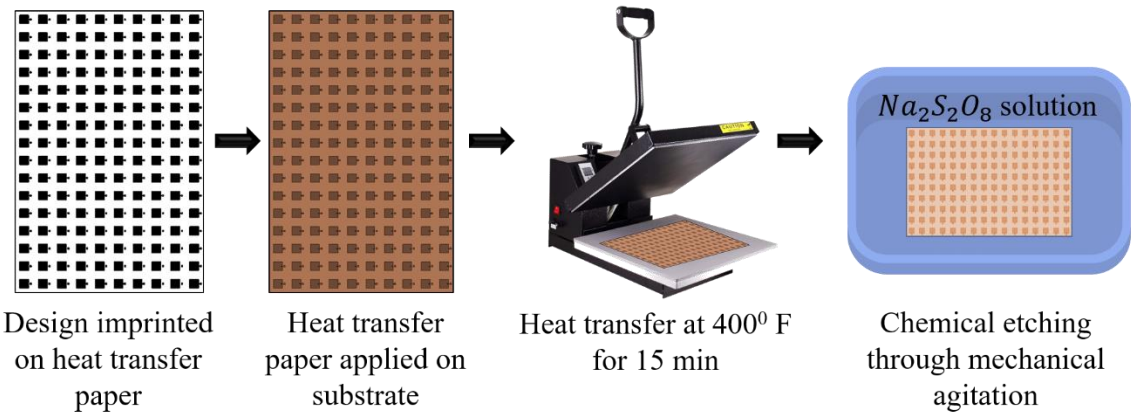

Figure 3.9: Fabrication flow used for creating the fixed-beam RIS.

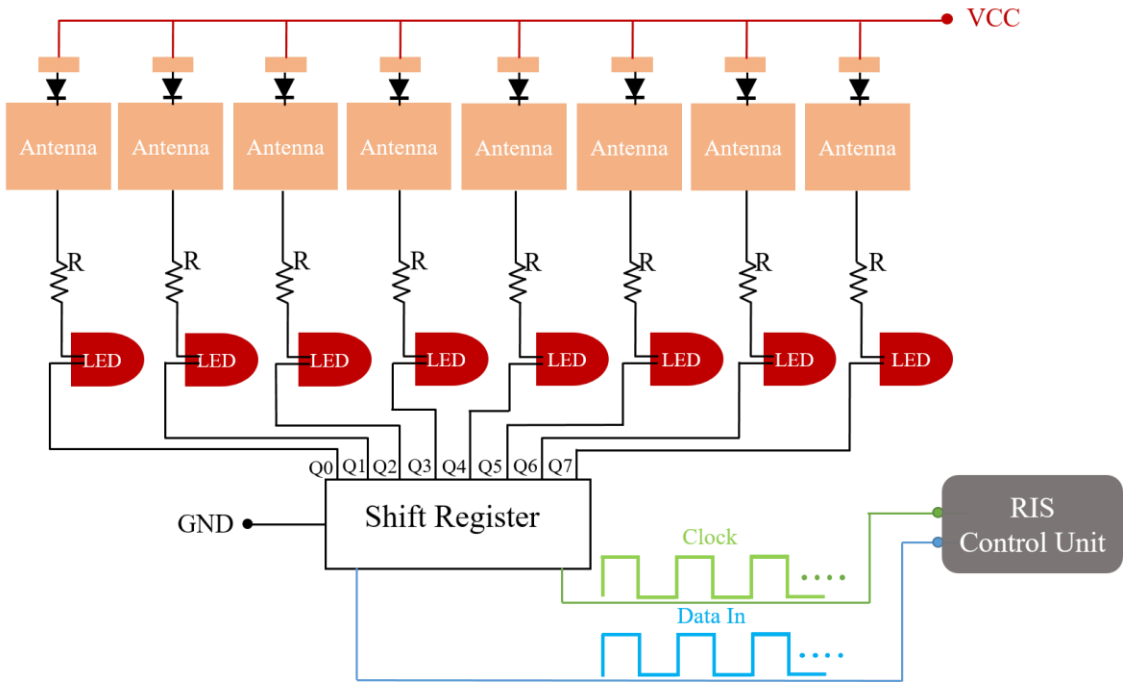

Figure 3.10: Schematic of the RIS control circuit. A codeword is generated and parsed to the RF PIN diodes through a microcontroller and 20 8-bit shift registers (LEDs are only needed for troubleshooting).

DC power requirements of the multi-beam RIS. It was found that each LED consumes 3 mW and each PIN diode consumes 1.58 mW, leading to a total DC power consumption of 560 mW for the worst-case situation (when all diodes are ON). Additionally, the

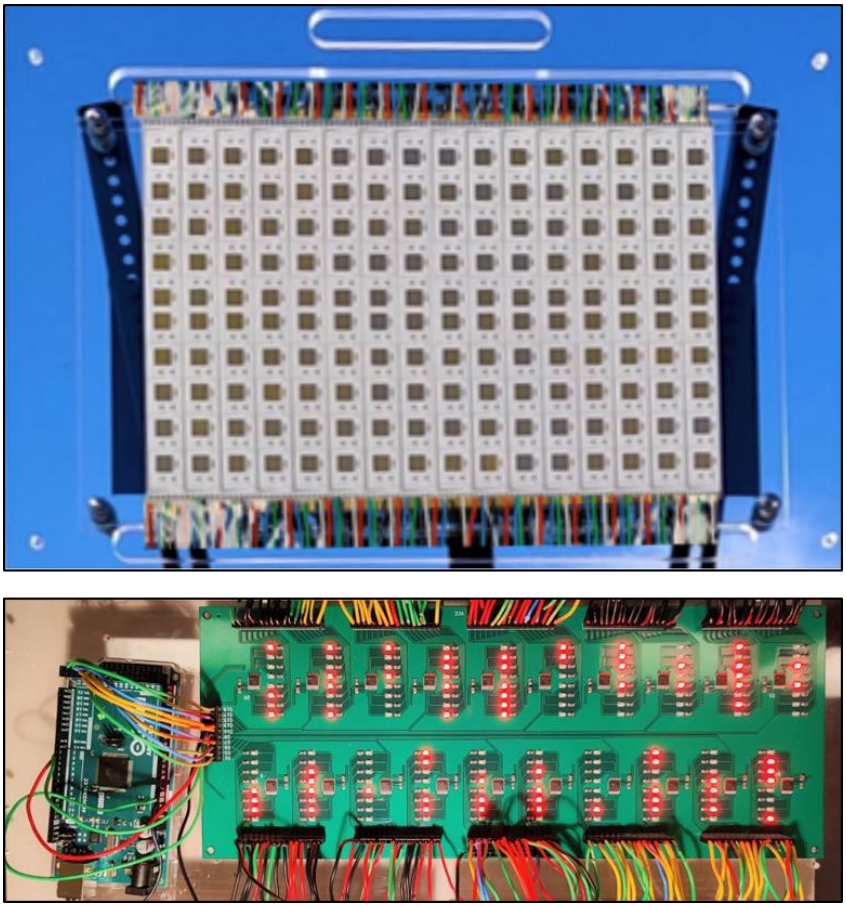

Figure 3.11: The fabricated prototype of the multi-beam RIS mounted on a fixture (top) and the RIS control circuit consisting of a microcontroller and a biasing network (bottom).

Microcontroller also consumes an average power of about $100\ mW$. However, it must be noted that only about 50% of the diodes are ON at any time for the typical operation of RIS. As such, the total power consumption is usually less than $400\ mW$. Additionally, the LEDs used in this control circuit are purely for easier testing and debugging purposes and are not necessary for actual commercial implementations. Since LEDs contribute a significant amount to the total power consumption, it follows that the power requirements could be reduced by omitting the LEDs from the control circuit design. The fabricated multi-beam RIS mounted on a fixture along with the control circuit is shown in Fig. 3.11.

3.3 RIS Characterization and Field Measurements

To demonstrate the potential of reconfigurable intelligent surfaces, the fabricated prototype is employed to carry out targeted measurement campaigns for characterizing beamforming capabilities and resulting improvement in signal coverage. Further the multi-beam RIS is integrated with a wireless testbed to evaluate the beamforming codebook.

3.3.1 Indoor Beamforming Measurements

The beamforming capabilities of both fixed- and multi-beam RISs are first evaluated in an anechoic chamber (Arizona State University's Compact Antenna Test Range). Both the surfaces are illuminated with a 12.5 dBi gain horn antenna fixed at an angle $\theta_i = -27.5°$ in front of the surfaces, as depicted in Fig. 3.12 (a) and (b). Being in the near- field, the feed horn impresses a Gaussian field distribution on the RIS aperture, generating an inherent pseudorandom phase profile. As such, even with 1-bit quantization a single main beam without any quantization lobes could be obtained. A single tone RF signal at 5.8 GHz is used to excite the surfaces and the normalized gain is measured in the $[-90°, +90°]$ range (E-plane). The fixed-beam RIS is designed to reflect towards $+60°$ direction and the normalized gain obtained from the measurements are plotted together with the simulation results, in Fig. 3.13, showing a good agreement between the two.

The measurements are repeated with the multi-beam RIS prototype. The recorded radiation patterns for 4 reflection directions ($\theta_d = 0°, 15°, 30°, and\ 45°$) show very good agreement with the full-wave simulations, as plotted in the left column of Fig. 3.14. The right column in Fig. 3.14 shows the quantized phase distribution used to set the switch

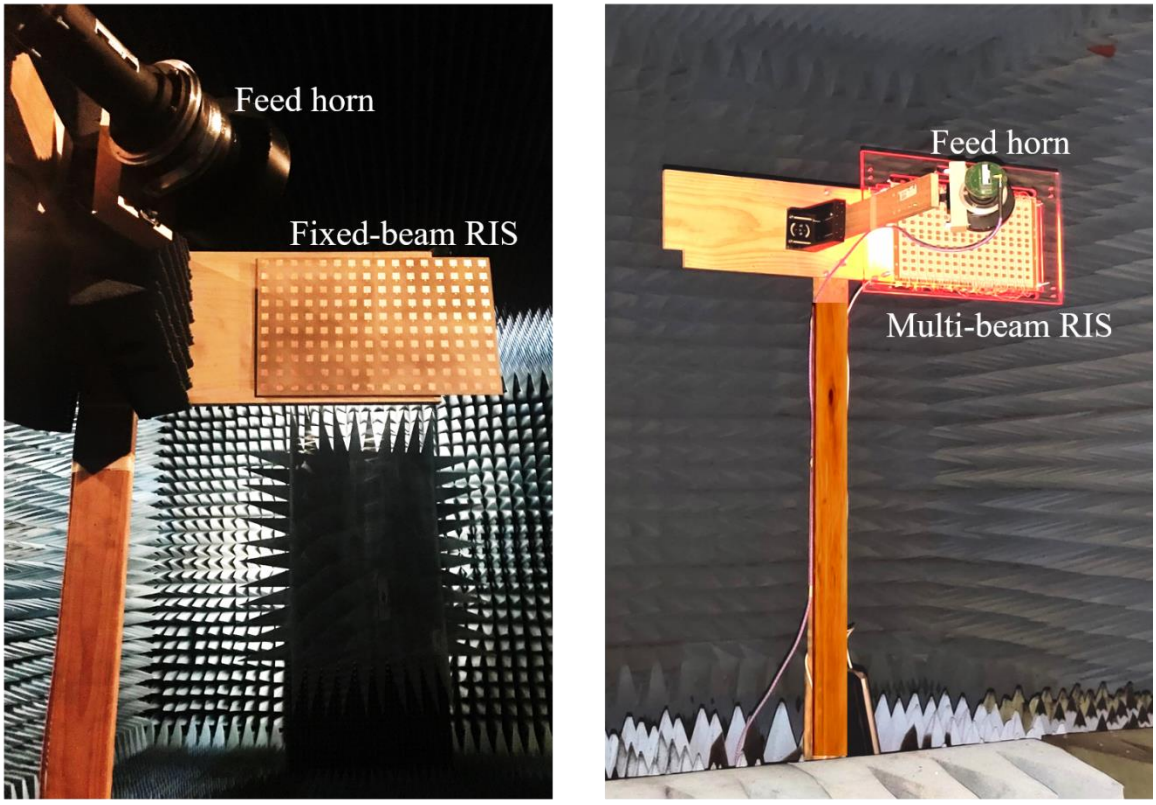

(a) (b)

Figure 3.12: Anechoic chamber measurement setup used for characterizing the RIS prototypes. (a) Fixed-beam RIS and (b) multi-beam RIS.

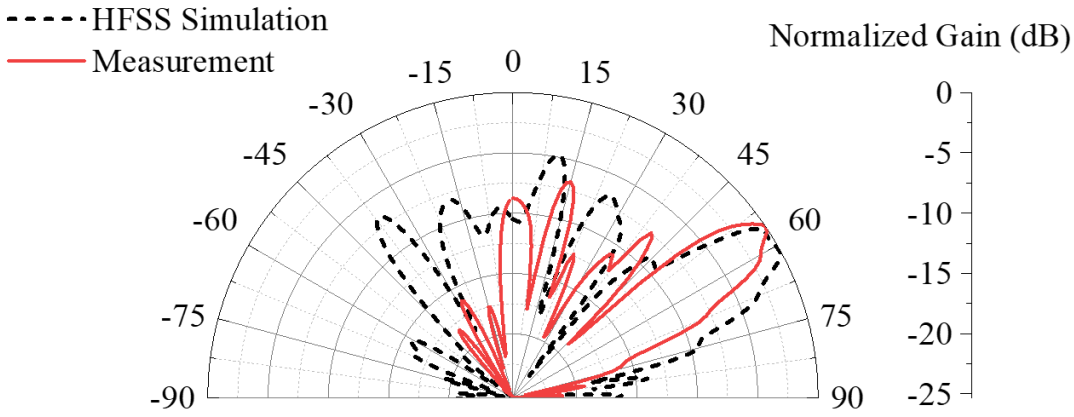

Figure 3.13: This figure shows a comparison between the measured (in the anechoic chamber) and computed radiation patterns of the 5.8 GHz fixed beam (passive) RIS prototype, which confirms the agreement between the designed and actual beams.

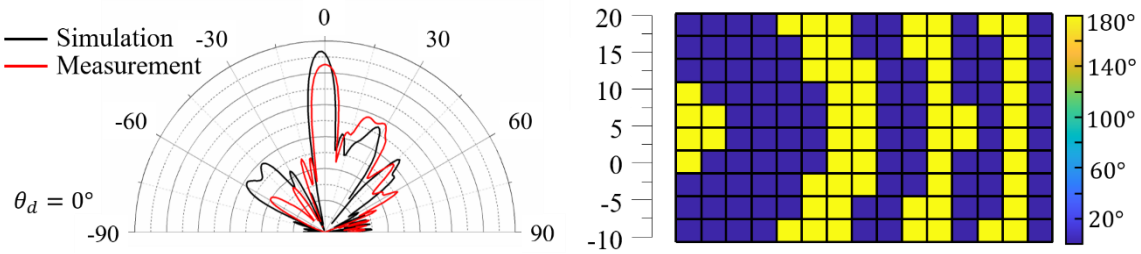

(a)

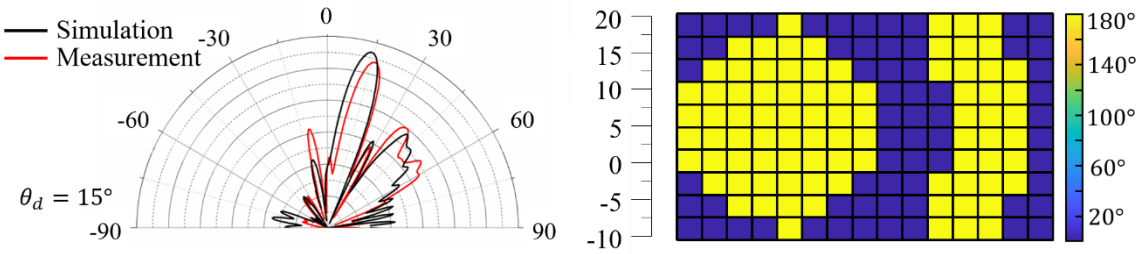

(b)

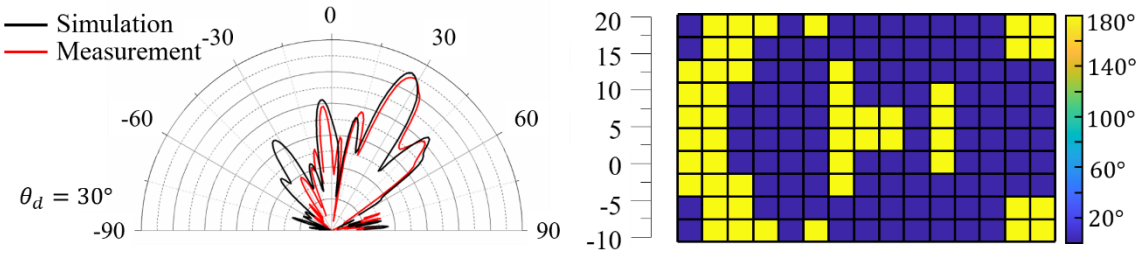

(c)

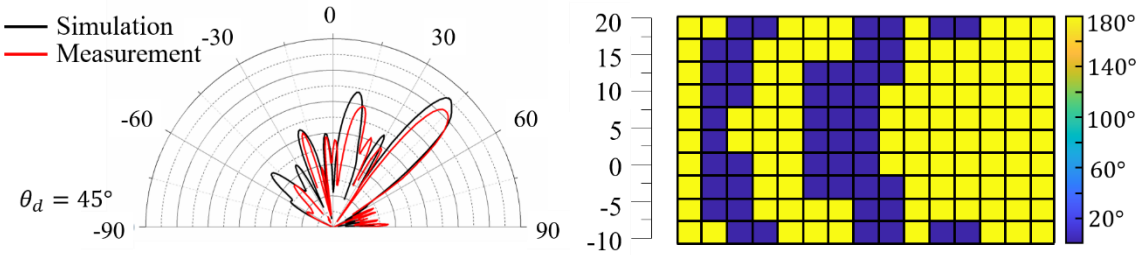

(d)

Figure 3.14: Anechoic chamber measurement results characterizing the beamforming capabilities of the multi-beam RIS designed in this work. Four arbitrary reflection angles ($\theta_d = \ 0°, 15°, 30°, and\ 45°$ in (a) to (d) respectively) are chosen at 5.8 GHz with the feed horn illuminating the surface from $\theta_i = -27.5°$. Left column: Comparison between computed and measured radiation patterns. Right column: Quantized (1-bit) phase shift distribution Φ^q on the RIS to generate the respective radiation patterns.

states and thereby redirect the incoming beam to desired directions. The measurements confirm the capability of the RIS to scan in the $\pm 60°$ range maintaining a single main lobe. It should be noted that the beam scanning resolution is limited by the 1-bit phase quantization. As such, the beam step (angular distance between successive main lobes) is approximately equal to the beam's half-power beamwidth (HPBW). In this work, the HPBW is approximately $6°$ resulting in a beam step of $6°$ when beam steering is close to the broadside. The step increases when the scanning to wider angles according to the HPBW. Additionally, the side lobe level (SLL) is maintained below 7 dB for more than 100 MHz bandwidth ($5.75 - 5.85$ GHz) and below 5 dB for more than 400 MHz for $\theta_d = 30°$. Finally, the maximum gain has a variation of less than 2.5 dB between $5.7 - 5.9$ GHz for all measured reflection angles.

3.3.2 Field Measurements to Characterize Beamforming Capabilities of Multi-beam RIS

This section details the measurement campaigns employed to evaluate the performance of the RIS through real-world field measurements. It is worth mentioning that all the measurement campaigns are conducted outdoors to account for wave propagation phenomena that occur in real-world scenarios, including scattering from the terrain, posts, and edge diffraction. Therefore, the results of these campaigns draw important insights into the actual performance of RISs in realistic wireless communication deployments. The RIS is integrated with a wireless communication testbed that consists of a (i) a single-antenna transmitter, (ii) a single-antenna receiver, and (iii) the RIS, as shown in Fig. 3.15. The developed RIS-integrated wireless communication system operates at the sub-6 GHz band with a center frequency of 5.8 GHz and a 20 MHz bandwidth. The systemadopts an

OFDM transmission/reception with 64 subcarriers. Some of the key aspects of the testbed are described below.

Transmitter: A single-antenna transmitter is implemented using an NI USRPs 2901 operating at 5.8 GHz. The USRP is connected to a horn antenna with an 18.5 dBi gain, emulating the antenna gain of a BS. As will be explained shortly, the transmitter operation is controlled by a Raspberry Pi that is wirelessly controlled (over a 2.4 GHz channel).

Receiver: The communication receiver is also implemented using an NI USRP 2901 operating in the 5.8 GHz band. The USRP is connected to either a dipole antenna or a horn antenna with 12.5 dBi gain. The receiver is controlled by a laptop that manages the overall operation of the RIS-integrated wireless communication system.

RIS: The developed RIS, consisting of 160 elements, is leveraged for reflecting the transmitted signal towards the receiver.

The main objective of the developed testbed is to evaluate the coverage gains when using an RIS. At first, for given locations of the transmitter and receiver, the central controller triggers the transmitter to send OFDM-based pilot sequences. During this transmission, the controller wirelessly orders the Raspberry Pi that is controlling the RIS configurations to switch between all the available beams in the codebook. The receiver measures the power in the received signal to select the optimal RIS configuration that can provide best gain improvement. The beamforming measurements are carried out in a parking lot on ASU campus. The satellite image of the parking lot where the beamforming measurements are carried out, with the measurement setup overlaid, is shown in Fig. 3.16. The tripod-mounted-RIS is depicted in the inset of Fig. 3.16.

Figure: 3.15: The RIS-assisted wireless communication system consisting of an RIS, a transmitter (BS), and a receiver (UE). The transmitter and receiver are portable and can be placed in the far-field of the RIS surface.

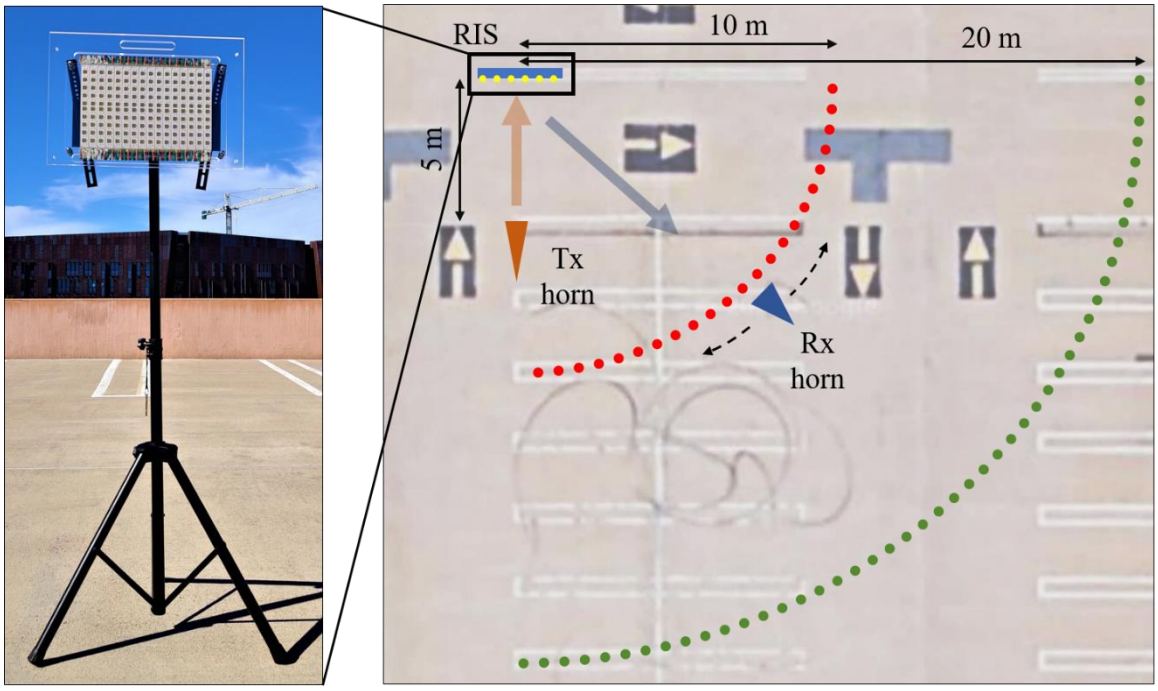

Figure 3.16: Measurement setup in ASU Campus Parking Lot. To test the RIS' electronic beamscanning capabilities in the field, the RIS is illuminated from the boresight direction ($\theta_i = 0°$) and the reflected signal is recorded at various angles and distances. (Inset: RIS mounted on a tripod).

The measurements are carried out in a parking lot to effectively characterize the beamforming codebook in an LoS real-world scenario. The setup consists of the prototype-RIS mounted on a tripod, a C-band corrugated conical horn antenna with a gain of 12.5 dBi used as the feed, and a C-band pyramidal horn with a gain of 18.5 dBi used on the receiver. The feed and the receiver horns were respectively connected to transmitting and receiving USRP modules. The feed horn is positioned in front of the RIS at 5 m distance from the surface. The receiver is positioned at a distance of $10\,m$ in front of the RIS and rotated in a circular arc from $0° - 60°$ to capture the deflected signals from the RIS. The 20 MHz bandwidth OFDM signal centered around 5.8 GHz is coupled to the feed horn from the transmitting USRP module. The feed horn is aligned in front of the RIS such that it illuminates the RIS from broadside. The reflected signals are recorded using a receiver horn antenna along a $10° - 60°$ arc with a radius of $10\,m$, at every 2.5°. After beamscanning at every point, a reception pattern is formed for every RIS scanning angle.

The 3D surface plot of Fig. 3.17 shows the beamforming capability of the RIS proposed in this work. As the beams from the RIS are scanned from $0° - 60°$ employing the beamforming codebook, the peak power is received at the corresponding receiver location. A 5° offset between the receiver positions and RIS beam directions, noticed in the figure, is attributed to localization errors in the measurements setup due to the large distances between the RIS, transmitter, and receiver. The received power at an example arbitrary angle of 40° from the broadside is shown in the inset of Fig. 3.17. For receiver angles less than 20°, coupling is noticed between the transmitter and the receiver. This is primarily due to the transmitter's back lobes as well as its proximity to the receiver for directions near broadside. This is an artifact due to the limitations of the measurement

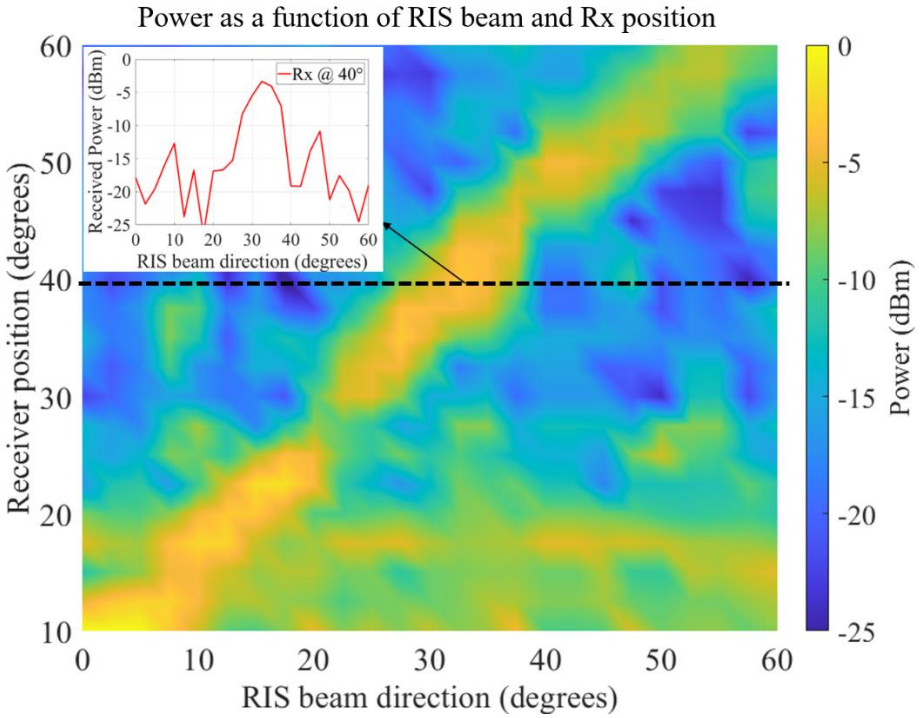

Figure 3.17: Evaluating the RIS' electronic beamscanning (azimuth plane). The high receive power at the diagonal line confirms the agreement between the codebook beam directions and the receiver location (which is moving along a circular path, as shown in Fig. 3.16). (Inset: 2D plot of the received signal when the receiver is oriented at 40° from broadside).

setup and would not be present in a deployment where the transmitter is much farther or blocked by an occlusion. Nevertheless, the power corresponding to the desired direction is still sufficiently high to offset this coupling effect and the receiver can detect the RIS beam. Using as a reference the SNR of the signal when the receiver is not aligned with the RIS beam, Fig. 3.17 shows that it is possible to achieve around $18 - 20$ dB SNR gain in the considered deployment scenario. It is worth mentioning here that these beamforming gains can potentially be improved if these codebooks are further optimized to match the RIS hardware impairments and the surrounding environment [120-121]. It is also important to note here that due to the 1-bit phase quantization, there is a symmetric beam that appears

around the specular direction. In Fig. 3.17 however, the effect is not seen as the measurements only utilizes the RIS beam that is the desired direction (towards the blocked users).

3.3.3 Pathloss Characterization

Further, to characterize the pathloss, similar beamforming measurements were repeated at distances of $20\ m$ and $40\ m$ from the RIS. Fig. 3.18 depicts the change in the received power levels, at few nominal angles ($10°, 20°, and\ 30°$) from broadside, as a function of distance from the RIS. As expected, the pathloss increases as the distance from the RIS increases as well as when the beam deviates away from the broadside direction.

3.3.4 Field Measurements to Characterize Signal Coverage Improvement with RIS

To emulate a user environment with significant signal degradation, the coverage measurements are carried out around the entrance of ASU's Gammage Memorial Auditorium, shown in Fig. 3.19. Here, the base station is modeled using a 18.5 dBi horn antenna placed on one side of a tall ($5\ m$) and thick ($2\ m$) concrete wall, covering the north and eastern side of the outdoor area of the venue. On the other side of the wall, the receiver uses an omnidirectional antenna and moves in the area in front of the venue entrance. The concrete wall serves as an occlusion between the transmitter and the receiver, thus providing an effective mechanism to examine the level of the received signal with and without the use of the RIS.

The goal of the signal coverage measurements is to evaluate the improvement of the received signal power for a mobile user that employs an omnidirectional antenna. In

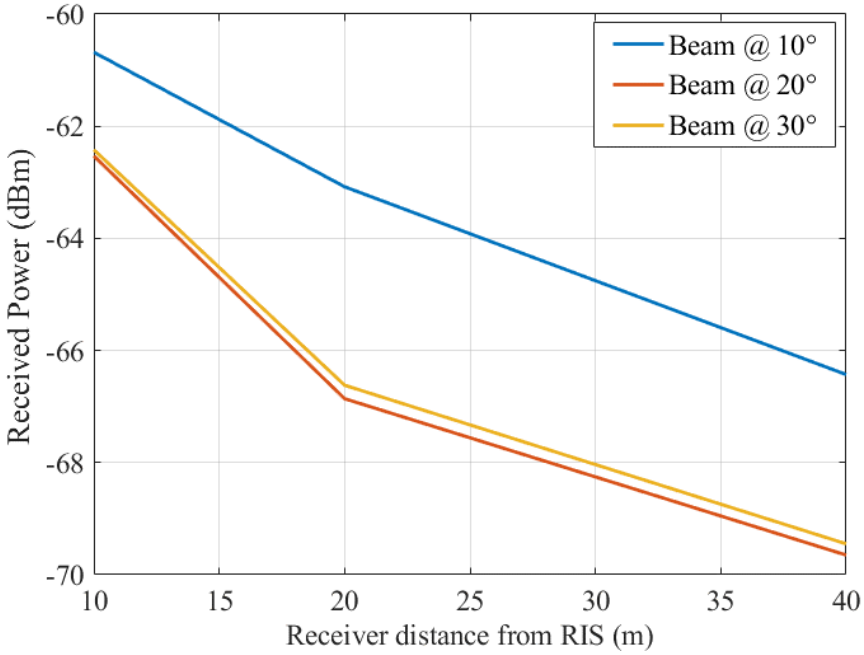

Figure 3.18: Path loss as a function of distance: The receiver is fixed at various directions ($\theta_d = 10°, 20°, and\ 30°$) from broadside and the distance between the RIS and the receiver is increased from $10\ m$ to $40\ m$.

the absence of RIS, the received signal on a 28-point grid is low due to the occlusion (signal blockage) from the large wall, as shown in the coverage map in Fig. 3.20 (a). To evaluate the potential of the RIS in expanding the signal coverage, the RIS is placed at a strategic location such that the RIS is in LoS of both the base station and the occluded area (in front of the venue entrance). As such, the RIS intercepts the signal from the base station and redirects it to the mobile user. In this scenario, the path from the base station to the RIS to the UE ranges between $30 - 40$ meters depending on the grid position. As the user moves to each grid position, the RIS scans the codebook beams horizontally to find the optimum signal reception. The second coverage map in Fig. 3.20 (b) shows the improved received signal levels achieved using the RIS beamscanning. The SNR improvement along

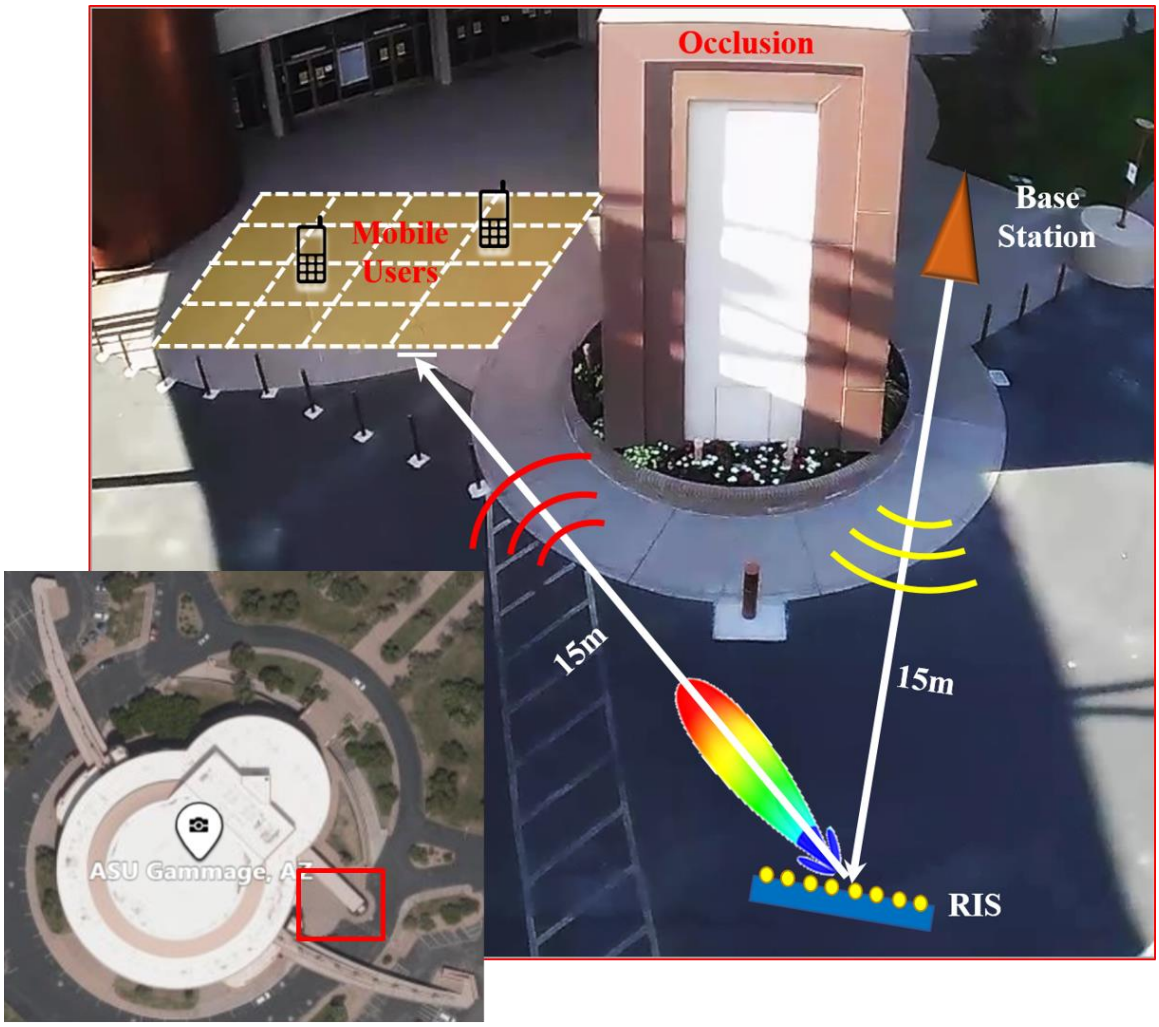

Figure 3.19: Measurement Setup at ASU's Gammage Memorial Auditorium. In this field test, a strong occlusion (blockage) exists between the BS and the mobile user. The RIS is strategically placed to leverage its beamscanning capabilities in extending the coverage to the LoS-obstructed mobile users.

the occluded/blocked region is up to 8 dB with an average of 6 dB. It should be noted that the SNR improvement is a function of the RIS size, thus a reasonably 10 times larger aperture (1600 elements) would result in 28 dB SNR improvement for the same coverage scenario. The 20 dB improvement is due the fact that the received signal depends on the square of the RIS area, as derived from (3.1) and (3.3).

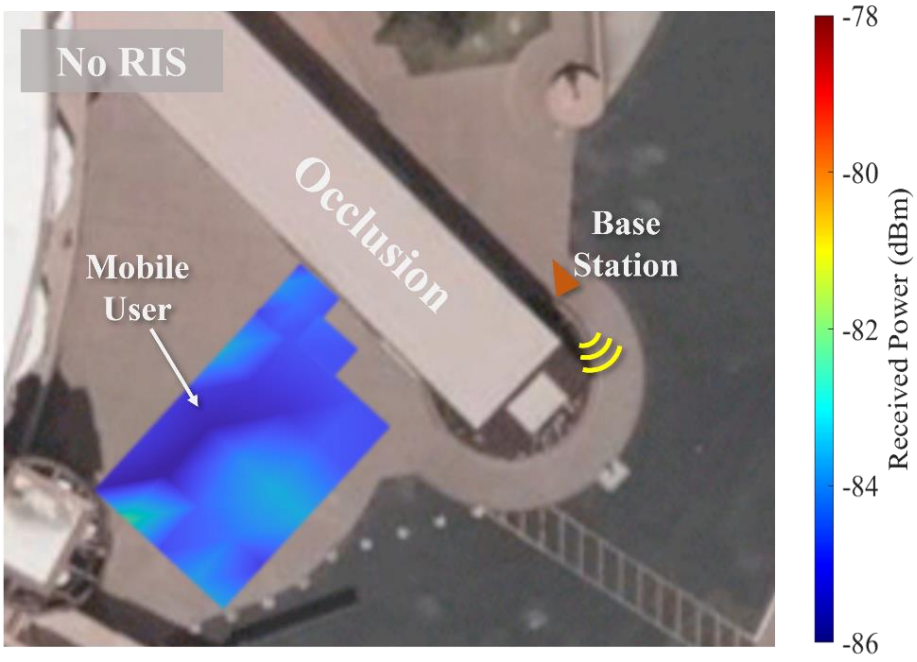

(a)

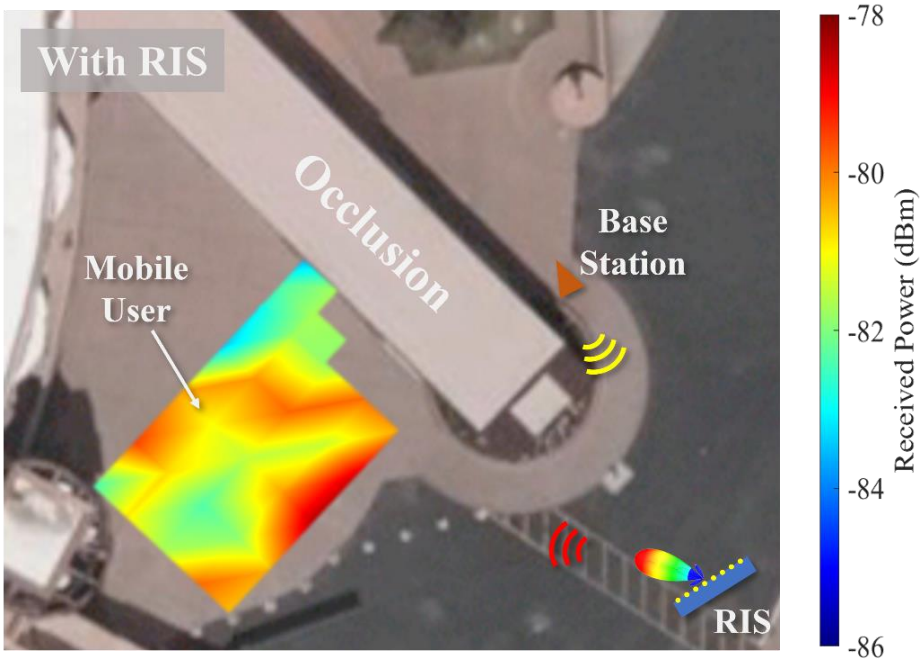

(b)

Figure 3.20: Field test with strong occlusion between the base station and the mobile user. (a) Coverage map without the RIS and (b) Coverage map using the RIS. The field measurement indicates an average SNR improvement of ~6 dB (with max. of 8 dB) when the RIS is deployed.

3.4 Conclusion

In this chapter, proof-of-concept prototypes for fixed- and multi-beam RISs were developed and characterized to evaluate their potential gains in real-world environments and practical settings. Specifically, the design and fabrication techniques of a sub-6 GHz $160-$element RIS prototype, which relies on a planar single layer reconfigurable reflectarray (no vias) capable of scanning in both azimuth and elevation planes, was detailed. Thanks to the simplicity of the geometry and the capability to operate with single-bit switches, the proposed design can be directly scaled to higher frequencies such as mmWave and THz systems using either RF PIN switches, transistor-based switches (e.g., CMOS-based), or tunable materials (e.g., graphene). Both prototypes were first characterized in an anechoic chamber. Then, field measurements were carried out to characterize the SNR gain and signal coverage improvements that could be achieved by deploying RISs in commercial communication networks.

A primary drawback of employing the 1-bit quantization is the appearance of grating lobes which have the same amount of energy as the main lobe, but in some undesired direction. This can be serious concern for security applications where it is necessary to avoid eavesdropping as wells as in high-density communication systems to avoid interference. This motivates the research to develop techniques to mitigate quantization lobes. One such effective novel technique is studied in the following chapter.

CHAPTER 4

MITIGATING QUANTIZATION LOBES IN LOW – BIT RECONFIGURABLE INTELLIGENT SURFACES

4.1 Introduction

The general mechanism of achieving beamforming be it phased array antennas or RISs ideally involves applying a series of continuous progressive phase shifts to individual array elements. Consequently, the main reflected beam can be steered to the desired direction. However, the implementation of continuous phase shifts significantly increases the design complexity or requires continuous phase modulators, such as varactors, that exhibit very poor performance at mmWaves and above [122]. As such, the continuous phases are usually quantized by rounding them off to discrete values through 1-, 2-, or 3-bit quantization schemes [123]. The 1-bit quantization scheme is commonly used owing to its design simplicity and lower implementation cost when compared to the higher-bit quantization schemes. A primary drawback of such single-bit RISs was identified in Chapter 3. Under plane wave illumination, the quantized coding techniques introduce grating lobes due to the periodicity of the errors resulting from the limited number of bits used in the phase rounding quantization [124]. These undesired grating lobes are known as *quantization lobes* and appear in addition to the main lobe, as shown in Fig. 4.1(a). The issue is particularly aggravated in a 1-bit quantization scheme where the quantization lobe has the same power as the main lobe [125-127]. Thus, to exploit the advantages of a 1-bit quantization scheme, it is critical to break the periodicity of the phase rounding quantization error and suppress the quantization lobes.

In this chapter, a technique to mitigate the quantization lobes, in planar, single-layer 1-bit RISs, that appear when illuminated with plane waves is presented. Specifically, the principles of random phasing originally proposed in multi-bit phased array systems [124] to break the periodicity of the phase rounding quantization error is adopted to mitigate the quantization lobes in RISs. The technique is realized by incorporating a randomized phase delay in each unit-cell of the RIS, as shown in Fig. 4.1(b). A similar procedure was recently employed to mitigate the quantization lobes in 1-bit designs using a two-layer reflective metasurface excited by normally incident plane waves at 39 GHz [128]. A stacked-layer implementation with two substrate layers and three metal layers is employed with one metal layer acting as the tunable antenna element and the other as the delay. However, such multi-layer implementation can result in increased design complexity and possibly more losses when scaling to higher frequencies. The conductor losses due to the presence of vias and the dielectric losses resulting from the use of multiple substrates constitute the main sources of loss. In addition, the bonding materials and possible airgaps at the substrate interfaces can introduce undesired signal loss at mmWave and THz frequencies. With multiple dielectric layers, the fabrication complexity also increases due to misalignment between layers, airgaps, and bows and/or warpages in the individual wafers.

The proposed technique for mitigating quantization lobes is based on introducing random phase delays in a single layer RIS with 1-bit quantization. Some of the preliminary simulation results were presented in [129], where a 20-element linear RIS is designed on a 20 μm thick high-resistivity Si ($\epsilon_r = 11.9$) at 275 GHz. In this work, the study is extended by focusing on the design, fabrication as well as characterization of the 2D RISs – one targeted for the future 6G applications and designed at 225.5 GHz and the second

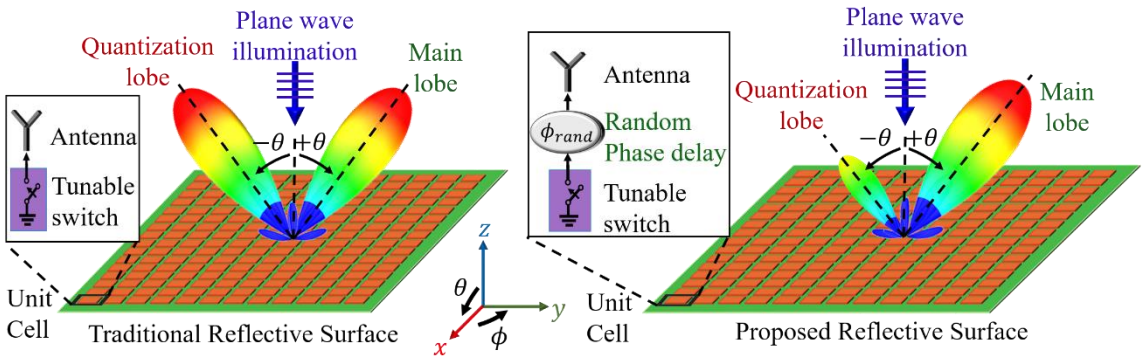

(a) (b)

Figure 4.1: Beamsteering with (a) 1-bit non-randomized RIS results in parasitic quantization lobe. Adding random phase delays in the unit-cells (b) suppresses the undesired lobe.

design targeted for the more imminent mmWave 5G applications and designed at 28.5 GHz. The sub-THz RIS is designed on an alumina ribbon ceramic wafer ($\epsilon_r = 10, tan\delta = 0.8 \times 10^{-3}$, thickness = 40 μm), while the mmWave RIS is designed using a Rogers RO4003 ($\epsilon_r = 3.55$, $tand = 0.0027$, thickness = 0.508 mm) substrate.

4.2 Mitigating Quantization Lobes Using Random Phasing

In this section, a comprehensive study of the random phasing technique employed to suppress the quantization lobes appearing in 1-bit RIS designs is presented.

4.2.1 Theory of Random Phasing

Let us consider a two-dimensional planar 1-bit RIS consisting M×N radiating elements arranged on the *x*-*y* plane and illuminated by a plane wave from (θ_i, ϕ_i) direction. To steer the reflected main beam to the desired direction (θ_d, ϕ_d), the excitation phase induced on the currents of the mn^{th} element is given by

$$\Phi_{mn} = \Phi_{mn}^{o} - \Phi_{mn}^{illum} \tag{4.1}$$

where Φ_{mn}^{o} is the phase delay required by the reflective elements to deflect the main beam in the (θ_d, ϕ_d) direction when the RIS is illuminated from broadside ($\theta_i = 0°$). Φ_{mn}^{illum} is the phase distribution of the element currents induced by a plane wave impinging from (θ_i, ϕ_i). These phase distributions are given by

$$\Phi_{mn}^{o} = -k_0(x_m \sin\theta_d \cos\phi_d + y_n \sin\theta_d \sin\phi_d) \tag{4.2}$$

$$\Phi_{mn}^{illum} = k_0(x_m \sin\theta_i \cos\phi_i + y_n \sin\theta_i \sin\phi_i) \tag{4.3}$$

where k_0 is the free space wavenumber and (x_m, y_n) represents the row and column indices of the mn^{th} element.

Considering the 1-bit quantization scheme, all the phase values are rounded off to $0°$ or $180°$ and the periodicity of the errors resulting from this quantization scheme leads to the generation of quantization lobes in traditional RISs. To suppress such lobes, random phase delays, Φ_{mn}^{rand} are added at every unit-cell using physical delay lines. Thus, the continuous excitation phase of the mn^{th} element given by (1) becomes

$$\Phi_{mn} = \Phi_{mn}^{o} - \Phi_{mn}^{illum} - \Phi_{mn}^{rand} \tag{4.4}$$

The random phase delays in (4) are obtained from a uniform pseudorandom number generator using

$$\Phi_{M\times N}^{rand} = rand(M, N) \cdot 180^{o} \tag{4.5}$$

where, $\Phi_{M\times N}^{rand}$ is the M×N matrix of random phases. The pseudorandom number generator produces random integer values between 0 and 1 and they are multiplied by $180°$ to obtain the phase values in the $[0, 180°]$ range. A uniform distribution is considered in this work

to generate random phase delays and not a gaussian or a triangular distribution as the former gives the maximum achievable SLL when compared to the latter two distributions [124]. As such, the resultant quantized phase delay of each RIS element is a binary $[0, 180°]$ distribution:

$$\Phi_{mn}^{q} = \left| 180° \cdot \text{floor}\left(\frac{\Phi_{mn}}{180°} + 0.5\right)\right| \tag{4.6}$$

All the phase values between $[-90°, +90°]$ are assigned to $0°$ (state "0"/OFF), and the remaining values are assigned to $180°$ (state "1"/ON). Consequently, the array factor of the randomized RIS is given by

$$AF_{RRS}(\theta, \phi) = \sum_{i=1}^{m}\sum_{j=1}^{n} e^{-j\Phi_{mn}^{total}} e^{-jk_0(x_m u + y_n v)} \tag{4.7}$$

where $\Phi_{mn}^{total} = \Phi_{mn}^{\mathrm{q}} + \Phi_{mn}^{illum} + \Phi_{mn}^{rand}$ corresponds to the total phase profile of each radiating element, $k_0(x_m u + y_n v)$ corresponds to the phase modulation due to Green's function, $u = \sin\theta\cos\phi$, and $v = \sin\theta\, sin\phi$.

4.2.2 Effect of Random Phase Delays

To study the effect of introducing random phase delays into the unit cells of RISs, a 20-element linear 1-bit RIS is considered. It is illuminated by a plane wave from broadside ($\Phi_{M\times N}^{illum} = 0$). The geometry of the designed randomized 20-element RIS is shown in Fig. 4.2. The surface is designed to redirect the incident plane wave towards $20°$.

The case of 'no randomization' ($\Phi_{M\times N}^{rand} = 0$) as shown in Fig. 4.3(a), is first considered for analysis. In this case, the quantization errors due to phase rounding exhibit a periodic phase distribution across the RIS elements, leading to a periodic quantized phase

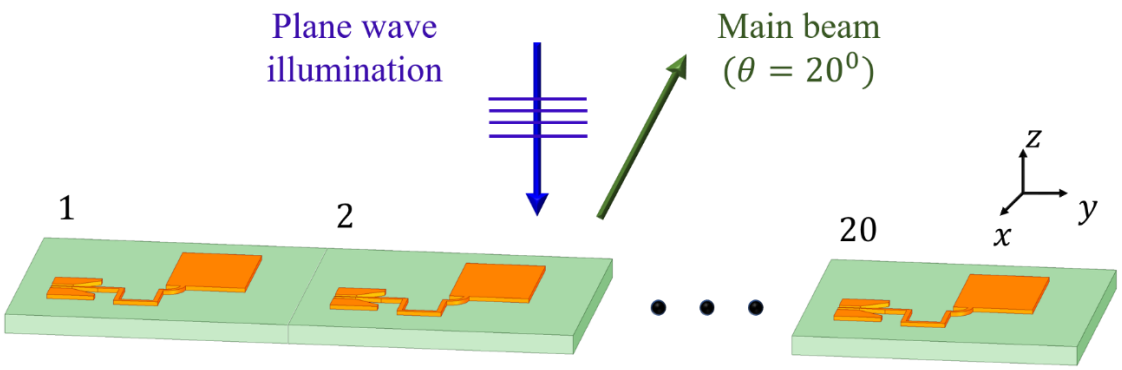

Figure 4.2: A 20-element (linear) 1-bit RIS illuminated by a plane wave from broadside and designed to radiate at $\theta = 20°$.

($\Phi^q_{M\times N}$) profile, as shown in Fig. 4.3(b). This spatial wave component results in a secondary undesired lobe called the quantization lobe, as shown in the radiation pattern of Fig. 4.3 (c). For the 20-element RIS example considered here, the main lobe is designed to be at $+20°$, while the undesired quantization lobe appears at $-20°$. In other words, (4.7) gives the same phase modulation for the radiation towards $+20°$ as well as $-20°$. In general, under plane wave illumination from broadside, the quantization lobe level (QLL) is equal in magnitude to the main lobe and appears at a direction symmetrically opposite to that of the specular reflection angle ($\theta_i = 0^0$ for this example). The same is not true of oblique incidences as it shall be seen in the following sections.

When a small range of randomization is introduced, for example, $0 - 90°$, then $\Phi^{rand}_{M\times N} \neq 0$, the random phase delays obtained from (4.5) are between 0° and 90° , as shown in Fig. 4.3 (d). Such a phase range is insufficient to break the periodicity of the quantization error. As such, the errors maintain a quasi-periodic distribution in $\Phi^q_{M\times N}$, as shown in Fig. 4.3 (e). This is significantly more pronounced in smaller arrays due to a limited number of elements, and thus, there a slight reduction in the QLL (-4.15 dB), as

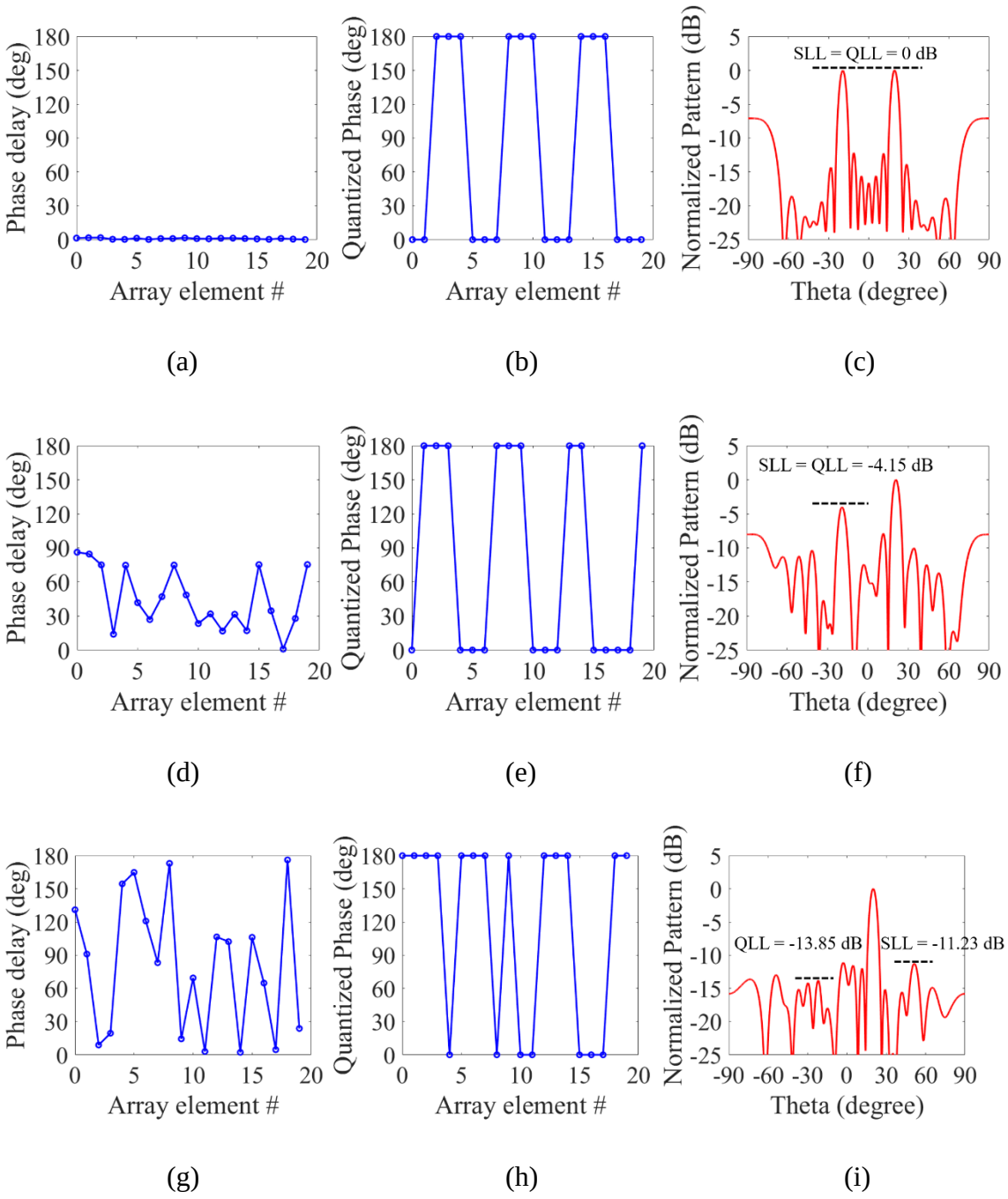

Figure 4.3: Effect of phase randomization on the radiation pattern of the RIS illuminated by a plane wave from broadside. Case 1 – No randomization: (a) randomly generated phase delays (everything is 0° for this case), (b) quantized phase values obtained using 1-bit quantization scheme, and (c) the normalized radiation pattern showing quantization lobe (at $-20°$) with the same energy as the main lobe (at 20°). Case 2 – $0 - 90°$ randomization: (d) random phase delays, (e) quantized phases, and (f) radiation pattern showing QLL reduction of -4.15 dB. Case 3 – Full randomization ($0 - 180°$): (g) random phase delays, (h) quantized phases, and (i) radiation pattern showing QLL reduction of -13.85 dB.

shown in Fig. 4.3 (f), is witnessed. This indicates that 1-bit RISs require a large degree of randomization. Evidently, when the full range of randomization ($0 - 180°$) is utilized to randomize the coding scheme, as shown in Fig. 4.3 (g) and 4.3 (h), the quantization lobe reaches a minimum value (QLL = -13.85 dB) as shown in Fig. 4.3 (i). The overall side lobe level achieved is about -11.23 dB for this surface. It should be noted that even with full randomization range, a sufficient QLL reduction (e.g. $<$ 10 dB) might not be achieved for all sets of random phase delays generated. Although the impact is more significant on small arrays, it could also be noticed occasionally in the large 2D arrays. As such, a MATLAB script is developed, that takes the array size and desired side lobe level (SLL) as inputs and runs the script iteratively to generate the random phase delays that can guarantee a low SLL along with a low QLL.

To illustrate the capability of the design to redirect the incident signal effectively in other directions, the performance of the design for different main beam directions are also evaluated, and a couple of representative plots for two main beam directions of $\theta = +15^0$ and -55^0 are represented in Fig. 4.4 (a) and (b), respectively. When randomization is introduced, the quantization lobe gets suppressed for both the designs. Consequently, a QLL of -18.4 dB and an SLL of -11.12 dB is achieved for the design with the main beam at $+15°$, and a QLL of -14.89 dB and an SLL of -10.72 dB is achieved for the design with the main beam at $-55°$. On the other hand, for the non-randomized design, it can be noticed that the quantization lobe appears in the symmetrically opposite direction of the main beam ($at\ -15°$ for the design with $15°$ main beam, and at $+55°$ for the $-55°$ main beam), as the plane wave illumination is from the broadside direction.

Further, to demonstrate the robustness of the proposed randomization technique, RISs are excited by obliquely incident plane waves. A couple of example incidences of $20°$ and $45°$ are chosen for this analysis. The same two main beam directions of $\theta = +15^0$ and $-55°$ are again considered. The respective plots for these designs are depicted in Fig. 4.4 (c), (d), (e), and (f), respectively. From the radiation pattern plots, it is again confirmed that the proposed randomization technique has excellent quantization lobe reduction capabilities irrespective of the directions of the incident or reflected waves. Consequently, SLL < -10 dB is achieved for all the designs. An interesting phenomenon with the oblique incidence is that the quantization lobe does not appear at a symmetrically opposite direction of the main lobe. For example, for the main beam direction of $+15°$, the quantization lobe is at $-70°$, when the plane wave incident is from $+20°$ direction as depicted in Fig. 4.4 (c), and it is at $+25°$, when the incidence is from $+45°$ direction, as seen from Fig. 4.4 (e). Similarly, for the $-55°$ main beam design with the same angles of plane wave incidence as before, the quantization lobes are at $10°$ and $-40°$, respectively. It is also worth mentioning that all the radiation patterns in Fig. 4.3 and 4.4 are obtained by evaluating (4.7). The element pattern is assumed to be omnidirectional; thus, the radiation pattern depends mainly on the array factor. As such, the total radiation pattern is approximately same as the array factor pattern. It should be noted that the beam broadening effect for higher main beam directions is also seen in RISs. As such, as the main beam direction increases, the beamwidth also increases.

To generalize the effect of introducing random phasing, the design process is extended to 2D RISs. The large number of elements in the 2D surfaces could pose a similar design and fabrication challenges as with the continuous phasing approach. This because a

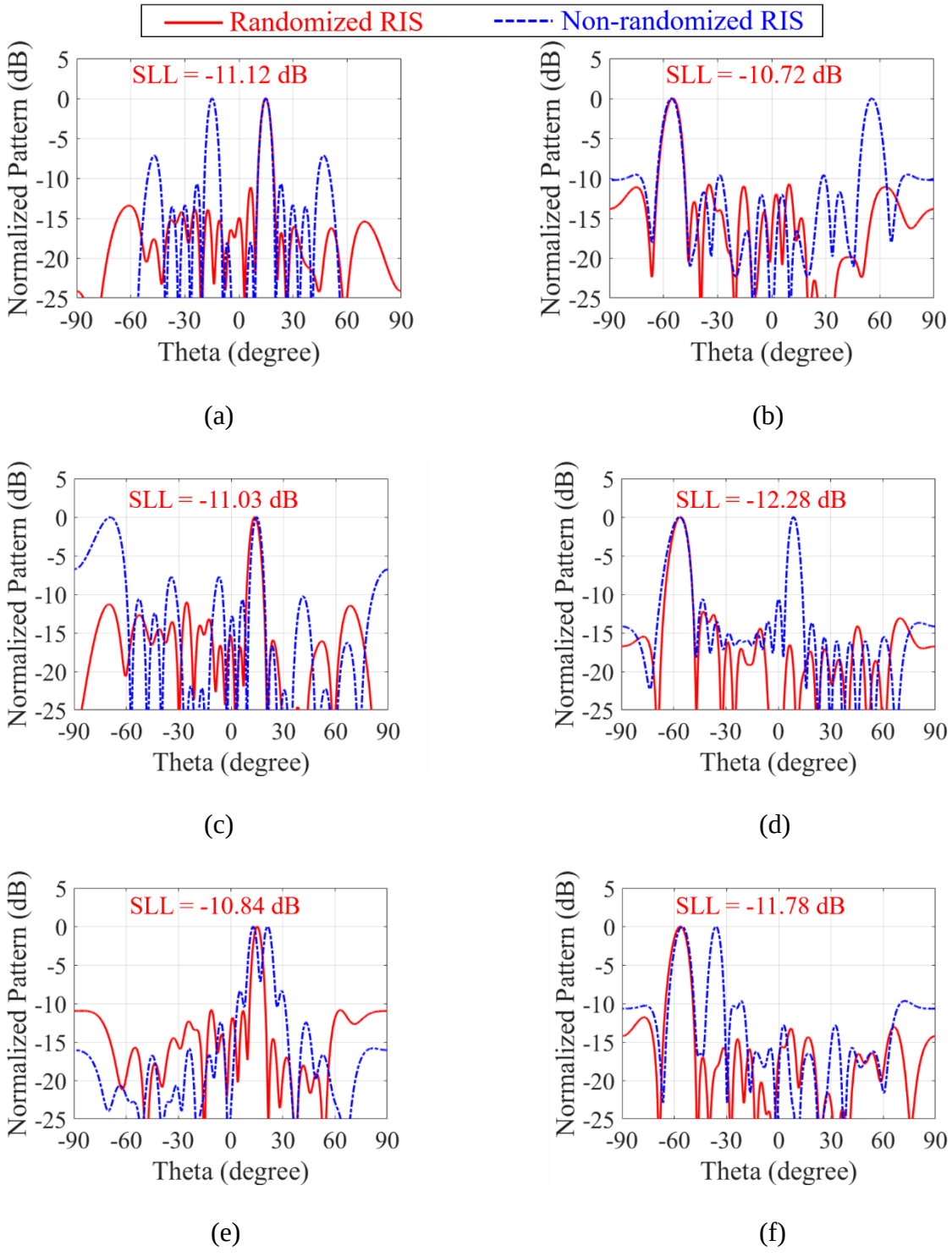

Figure 4.4: Normalized radiation patterns of 20-element (linear) 1-bit randomized RIS excited by a plane wave from (a) 0° with main beam at 15°, (b) 0° with main beam at −55°, (c) 20° with main beam at 15°, (d) 20° with main beam at −55°, (e) 45° with main beam at 15°, and (f) 45° with main beam at −55°.

$M \times N$array might need as many as MN (total number of elements in the array) different random phases. To counter this challenge and reduce the fabrication overhead, a study is carried out to determine the minimum number of different random phases (e.g. delay line lengths in this work) necessary to break the periodicity of the quantization error and reduce the QLL below a desired threshold. This additional design step called the pre-quantization process involves quantizing the MN random phases in $\Phi_{M\times N}^{rand}$ in (4.5) to q uniformly distributed phase values using

$$\Phi_{M\times N}^{rand(pre\_q)} = \left|\Delta \cdot \text{floor}\left(\frac{\Phi_{M\times N}^{\text{rand}}}{\Delta} + 0.5\right)\right| \tag{4.8}$$

where

$\Phi_{M\times N}^{rand(pre\_q)}$ is the $M \times N$ matrix of pre-quantized random phases

q is the desired number of random phase delays (q >2)

$\Delta = \frac{\pi}{q-1}$ is the quantization step-size

The quantized set of random phases obtained from (4.8) can be substitutes in (4.4) and the rest of the design process could follow the procedure detailed in Section 4.2.1.

To evaluate the validity of the pre-quantization technique, a comparative study is carried out using four 2D RISs of sizes 5×5, 10×10, 20×20, and 30×30. A main beam direction of $-30°$ is chosen for all the four surfaces. Both broadside and oblique incidences are considered for a comprehensive evaluation of the proposed methodology. At first, the case of plane wave incidence from the broadside direction is considered to obtain the corresponding radar cross section (RCS) patterns for the following cases: no randomization, full randomization employing all available random phase delays, and pre-quantizing to- 2 and 6 unique phase delays. The corresponding RCS patterns for a 900-

element array are shown in Fig. 4.5. As expected, when no randomization is employed, the parasitic quantization lobe appears in the RCS pattern making the SLL = 0. On the other hand, when full randomization is employed, an SLL of -12.54 dB is achieved. Further, as pre-quantized phase delays with 2 and 6 unique phases are used, the SLL changes to -12 dB, and -11.89 dB, respectively. Although the increase in SLL is barely noticeable for broadside illumination, a significant increase in the SLL will be witnessed at oblique incidences. As such, various oblique angles of incidence in the range $-60°$ to $+60°$ (with a step of 1° increments) are considered for analysis using the above-mentioned array sizes. The corresponding SLLs obtained for the cases of- no randomization, full randomization employing all available random phase delays, and pre-quantizing to 2 and 6 phase delays, are plotted in Fig.4.6 (a-d). When no randomization is employed, SLL below -10 dB is achieved only for the specular incidence. Consequently, since a main beam direction of $-30°$ is considered here, a dip in the SLL is observed around $\pm 30°$ incidence.

Further, to devise a set of guidelines for choosing the least number of unique phase delays required to design a randomized RRS, a statistical analysis is carried out by finding the average SLLs for all angles of incidence and the corresponding variances for each case. The results are tabulated in Table 4.1. When only 2 phase states are used, spikes are observed in the SLL, as shown in Fig. 4.6. This leads to a larger value of variance and thus, higher SLLs at certain incident angles. Although, the SLL improves noticeably when only 4 unique random phase states are employed, the variance still stays high. However, when 6 unique phase delays are employed, both mean and variance of the SLLs approach those of the fully randomized design employing no pre-quantization. As such, 6 random phase delay states uniformly distributed in the range $(0,180°)$ can be used for designing a

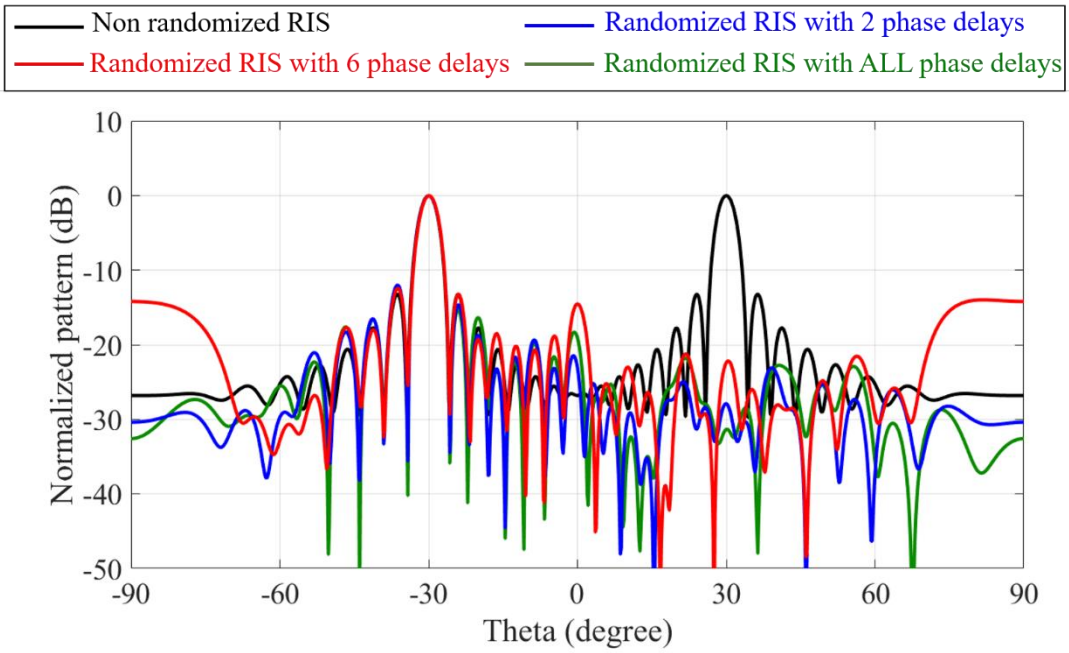

Figure 4.5: RCS patterns of 30×30 RIS employing different levels of pre-quantization levels compared with non-randomized design. Under broadside incidence, even 2 unique random phase delays are sufficient to break the periodicity of quantization error and achieve an SLL < -10 dB. However, under oblique incidences, more random phases are needed to break the symmetry.

randomized RRS in lieu of all the phase delays. Although, this pre-quantization method is not employed in the design of the 2D RISs developed in this work, owing to the sophisticated fabrication techniques, the study serves as an excellent guide when extremely low fabrication costs are desired.

Furthermore, to understand the effect of the range of the random phase delays on the achieved SLL, a comparison is carried out for apertures of various sizes and bit configurations. As such, the results obtained based on (4.7) for 200-element and 900-element linear RISs, are depicted in Fig. 4.7, for 1-, 1.5-, and 2-bit quantization schemes. It is observed that the range of randomization required for minimum SLL should be at least $[0, 180°]$ for 1-bit quantization, $[0, 120°]$ for 1.5-bit, and $[0, 90°]$ for 2-bit, as summarized

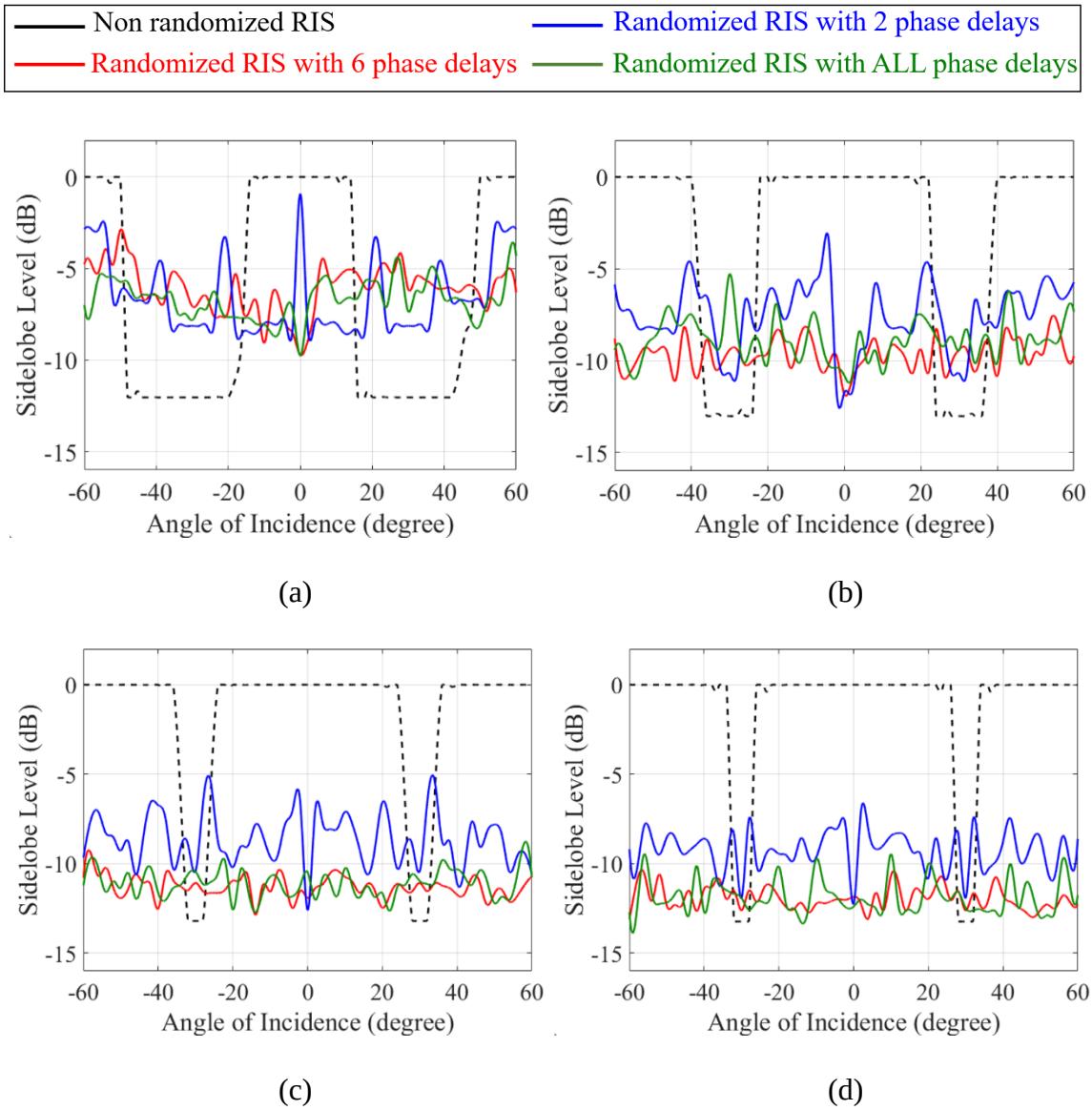

Figure 4.6: SLL v/s incident angle:(a) 5×5, (b) 10×10, (c) 20×20, and (d) 30×30 RISs. Incident angles are scanned from $-60°$ to $+60°$.

in Table 4.2. This range of randomization also guarantees the lowest SLL achievable for each configuration. Moreover, it is noticed from the radiation patterns of Fig. 4.3 and 4.4 that the average SLL is also impacted by the random phase delays. Namely, as randomization is increased, the average SLL also increases. This is attributed to the random redistribution of the quantization lobe power to other directions.

Table 4.1: Mean sidelobe levels and variances for different RISs under oblique incidences with various pre-quantization levels

# of Phase delays/ Array size	Mean SLL (dB) / Variance ($\boldsymbol{\sigma^2}$)			
	$\mathbf{5 \times 5}$	$\mathbf{10 \times 10}$	$\mathbf{20 \times 20}$	$\mathbf{30 \times 30}$
2	6.6 / 4.3	7.6 / 3.5	8.6 / 2.1	9.2 / 1.2
4	6.5 / 2.4	8.8 / 2.1	10.9 / 0.9	11.5 / 1.2
6	6.7 / 1.1	8.9 / 1.3	11.1 / 0.6	11.9 / 0.9
All	6.1 / 1.6	9.7 / 0.7	11.3 / 0.4	12.0 / 0.4

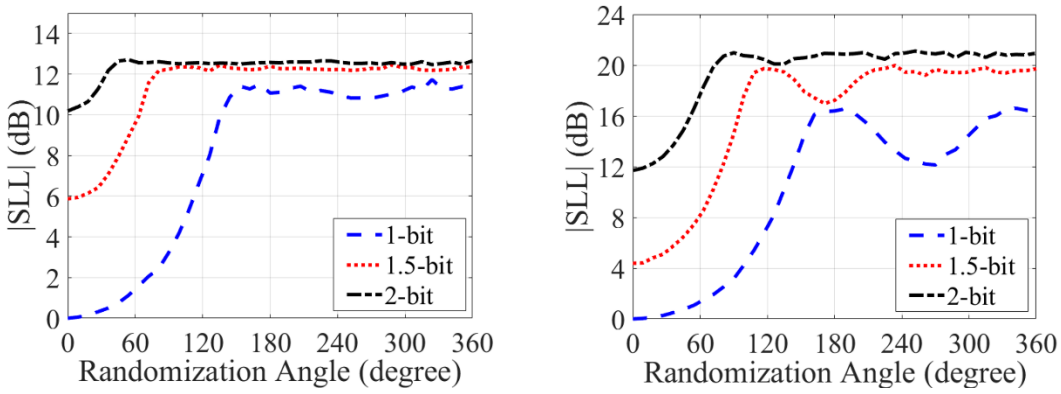

(a) (b)

Figure 4.7: Variation of the |SLL| v/s the range of randomization for (a) 200-element linear RIS and (b) 900-element linear RIS.

Table 4.2: Required range of phase delay randomization (Φ_{rand_range}) for various quantization schemes

Quantization scheme	Φ_{rand_range}
$1-$ bit	0 to 180°
$1.5-$ bit	0 to 120°
$2-$ bit	0 to 90°

4.3 RIS Design

In this section, the design procedure for the sub-THz 30×30 2D RIS is described. A single layer design is considered for less fabrication complexity and reduced losses

arising from the use of multilayered structure, both of which are typically exacerbated at THz frequencies. Additionally, a parallel design procedure for an $800-$element (25×32) mmWave RIS is also detailed. A four-layer design is adopted for the mmWave RIS to enable integration with active switches (PIN diodes, FETs etc.,) and control circuitry in the future implementations. Both the designs employed to evaluate the proposed random phasing technique are fixed beam RIS designs. Future works will focus on extending the technique to multi-beam RISs.

4.3.1 Sub-THz Unit Cell Design

The design of the randomized RIS developed in this work for mitigating quantization lobes is shown in Fig. 1 (b). Each unit-cell consists of an antenna integrated with a switch and an additional randomized phase delay implemented through microstrip lines. The implementation of the randomized single-bit unit-cell is depicted in Fig. 4.8 (a), with a linearly polarized patch antenna and a transmission line feed with an embedded switch integrated at the non-radiating edge. To ensure maximum signal coupling and minimize mismatch loss, the feed position y_0 is optimized at $40\ \mu m$ from the radiating edge of the patch. The transmission line width is also optimized to obtain a characteristic impedance of $Z_0 = 80\ \Omega$ to achieve a good impedance match. The non-radiating edge of the patch is used for feeding the antenna to reduce the metal structure footprint and facilitate the development of higher-bit RIS designs in the future. The patch is designed to radiate at 222.5 GHz and has the dimensions of $284\ \mu m \times 185\ \mu m$. The necessary random phase delays for each unit-cell can be implemented by varying the length of the feed line branch Δl.

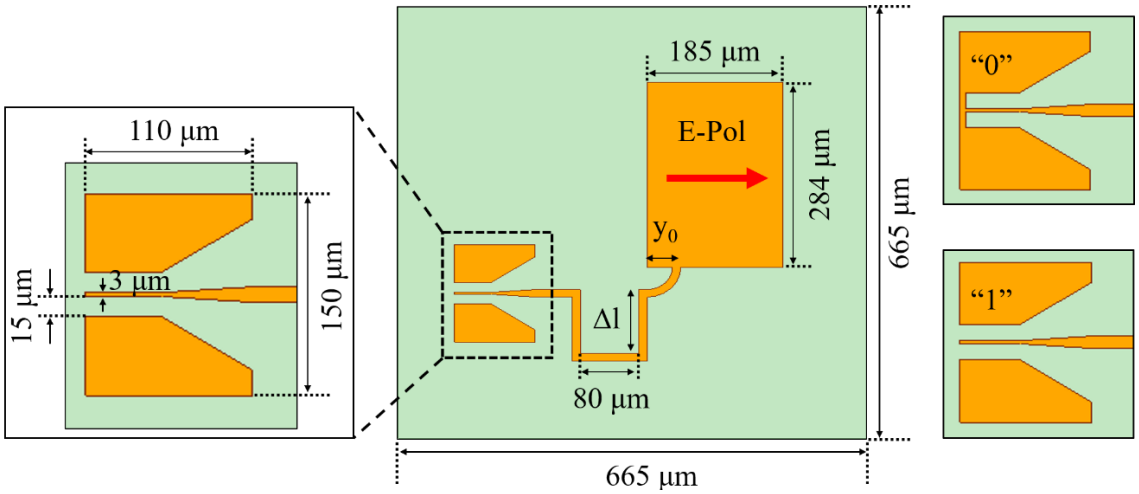

Figure 4.8: (a) A unit-cell of the designed RIS and (b) the two states of the switch.

The switch is implemented in a coplanar waveguide (CPW) with a Z_0 of $80\,\Omega$ [131], as shown in the inset of Fig. 4.6 and the two states of the switch are depicted in Fig. 4.8 (b). This configuration is favorable in terms of RF performance for switches that utilize planar, tunable 2D materials (e.g., graphene), as discussed in [132]. Herein, to demonstrate the proof-of-concept of the proposed technique, open and short transmission line terminations are employed to emulate the on/off states of ideal switches. To maintain a planar topology and avoid the use of complex and high inductance vias, a microstrip to CPW transition is employed. The total size of the unit-cell is $665\ \mu m \times 665\ \mu m$, which is approximately $\lambda_0/2$ at 222.5 GHz.

4.3.2 MmWave Unit Cell Design

For the mmWave RIS, a four-layer design is adopted to optimize the radiation performance and to enable future integration of the multi-beam RIS with a control circuitry.

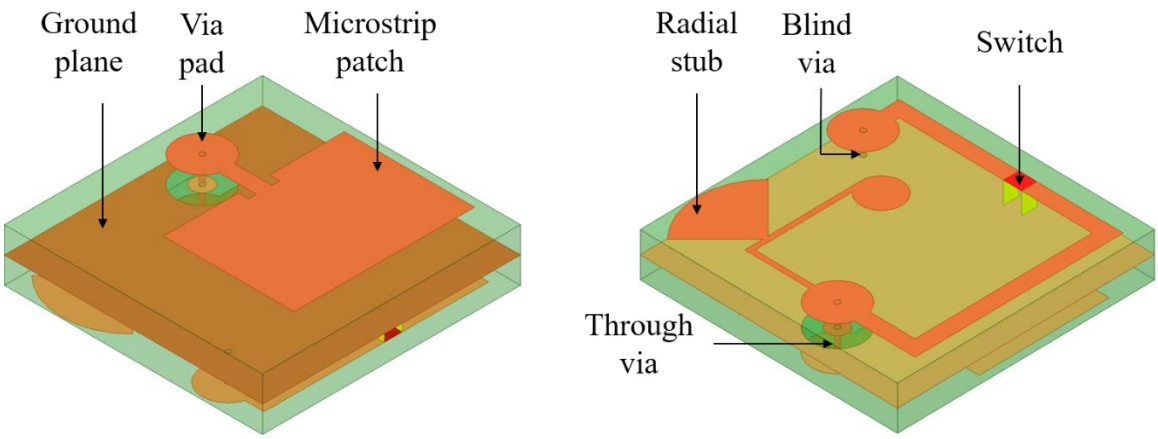

(a) (b)

Figure 4.9: 3D perspective views of the mmWave RIS unit cell with the key components labelled: (a) top view and (b) bottom view.

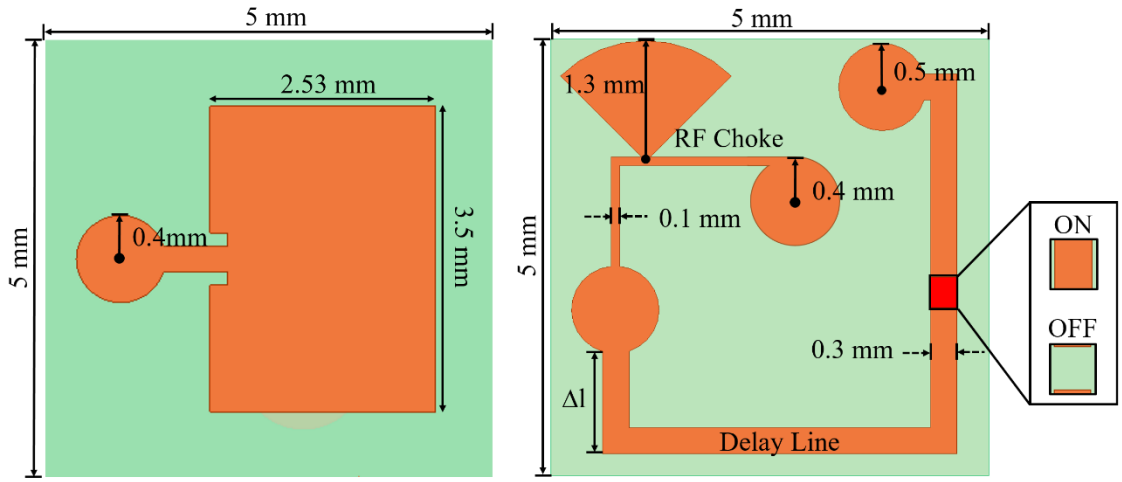

(a) (b)

Figure 4.10: 2D views of the mmWave unit cell with the optimized design dimensions: (a) top view and (b) bottom view (Inset: Two states of the single-bit switch).

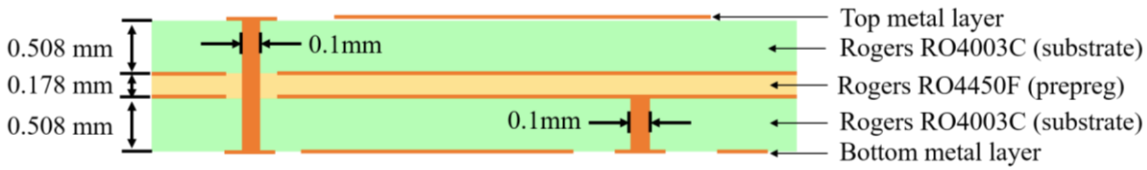

Figure 4.11: Stack up of the 4-layer mmWave RIS unit cell.

The 3D view of the unit cell of the proposed design is shown in Fig. 4.9, and the corresponding 2D view with all the design dimensions is depicted in Fig. 4.10. The top layer consists of an inset fed patch antenna and the bottom layer is used to implement the delay line and switch. Two Rogers RO4003C substrates are bonded together using a Rogers RO4450F prepreg material as shown in the stack-up in Fig. 4.11. Both the top and bottom substrates are $0.508\,mm$ thick while the prepreg is $0.178\ mm$ thick to ensure structural stability as well as PCB design symmetry. The unit cells are $5\ mm \times 5\ mm$ in size with the radiating patch size of $3.5\ mm \times 2.53\ mm$. The patch antenna is linearly polarized and designed to radiate at 28.5 GHz. A $0.1\ mm$ diameter through via is designed to access the delay line and achieve the desired phase shift needed to redirect the impinging beam to a chosen direction. The ON and OFF states of the single-bit switch are realized by either connecting the delay line to the ground (ON) through the quarter-wave section or leaving the gap between the delay line and the quarter wave section (OFF), as shown in in the inset of Fig. 4.10 (b). The switch is connected to the ground through a blind via. As with the sub-THz RIS, the branch length Δl could be varied to control the random phase values. An RF choke is introduced into the unit cell of the mmWave RIS. This is to facilitate the implementation of an integrated biasing board through ball grid array (BGA) technology in the future works.

4.3.3 2D RIS Design

In this section, both randomized and non-randomized RIS designs are compared through numerical analysis. For the non-randomized case, $\Phi_{M\times N}^{rand} = 0$, and thus, the random phase delays are zero, as shown in Fig. 4.12 (a). Consequently, the corresponding

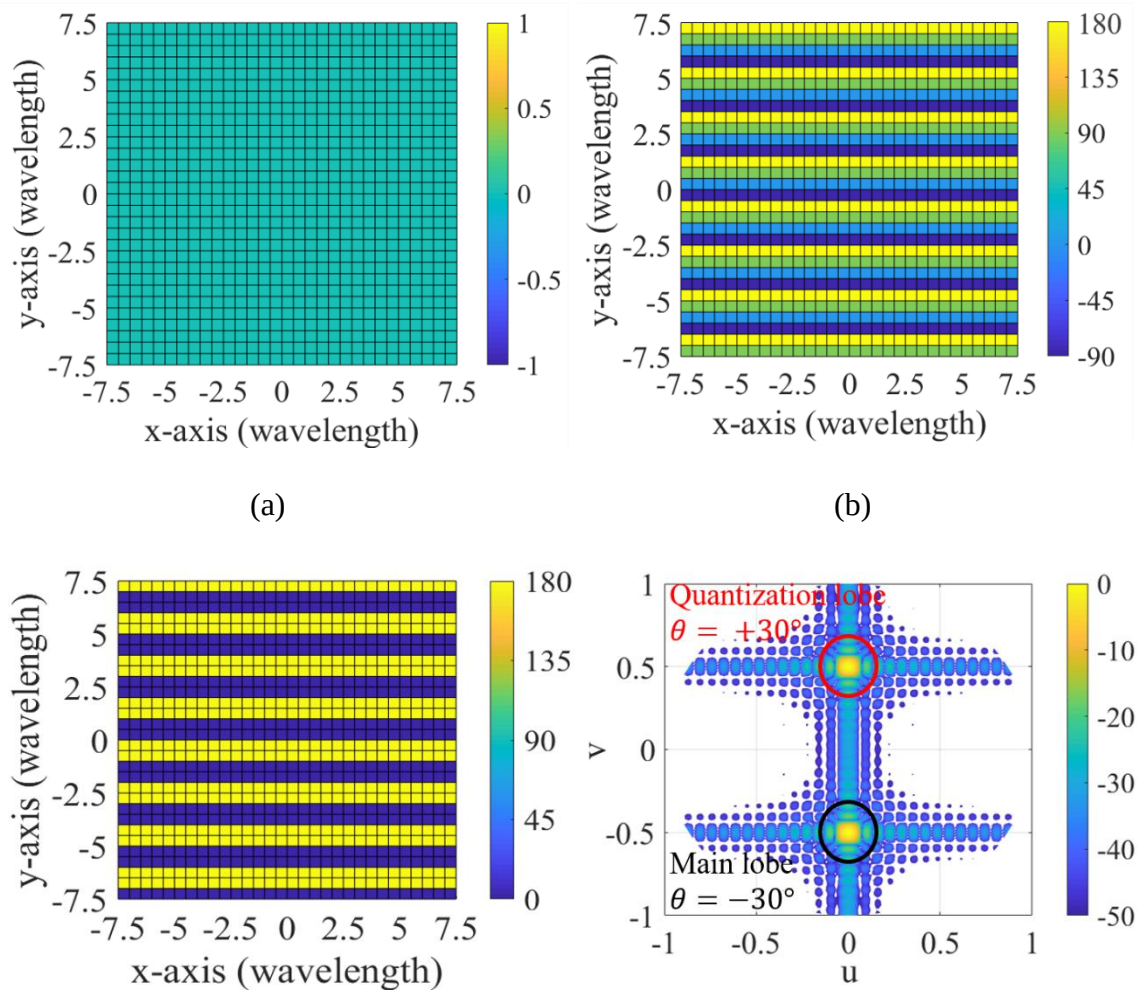

Figure 4.12: 30×30 2D non-randomized RIS design: (a) delay phase $\Phi_{30\times30}^{rand} = 0$, (b) excitation phase $\Phi_{30\times30}$ obtained from (1), (c) total phase $\Phi_{30\times30}^{total}$ based on 1-bit quantization scheme obtained from (6), and (d) normalized scattered fields obtained from (7) and plotted in the u-v plane ($u = \sin\theta\cos\phi$, and $v = \sin\theta\, sin\phi$).

continuous element phases obtained from (1) and shown in Fig. 4.12 (b) result in a repetitive quantized coding scheme. This repetitive coding scheme is caused by the periodicity of the phase rounding quantization error which makes the total phase, $\Phi_{M\times N}^{total}$ periodic, as shown in Fig. 4.12 (c). The resulting radiation pattern obtained from (7) has both the desired main lobe along the $-30°$ direction, and an undesired quantization lobe at

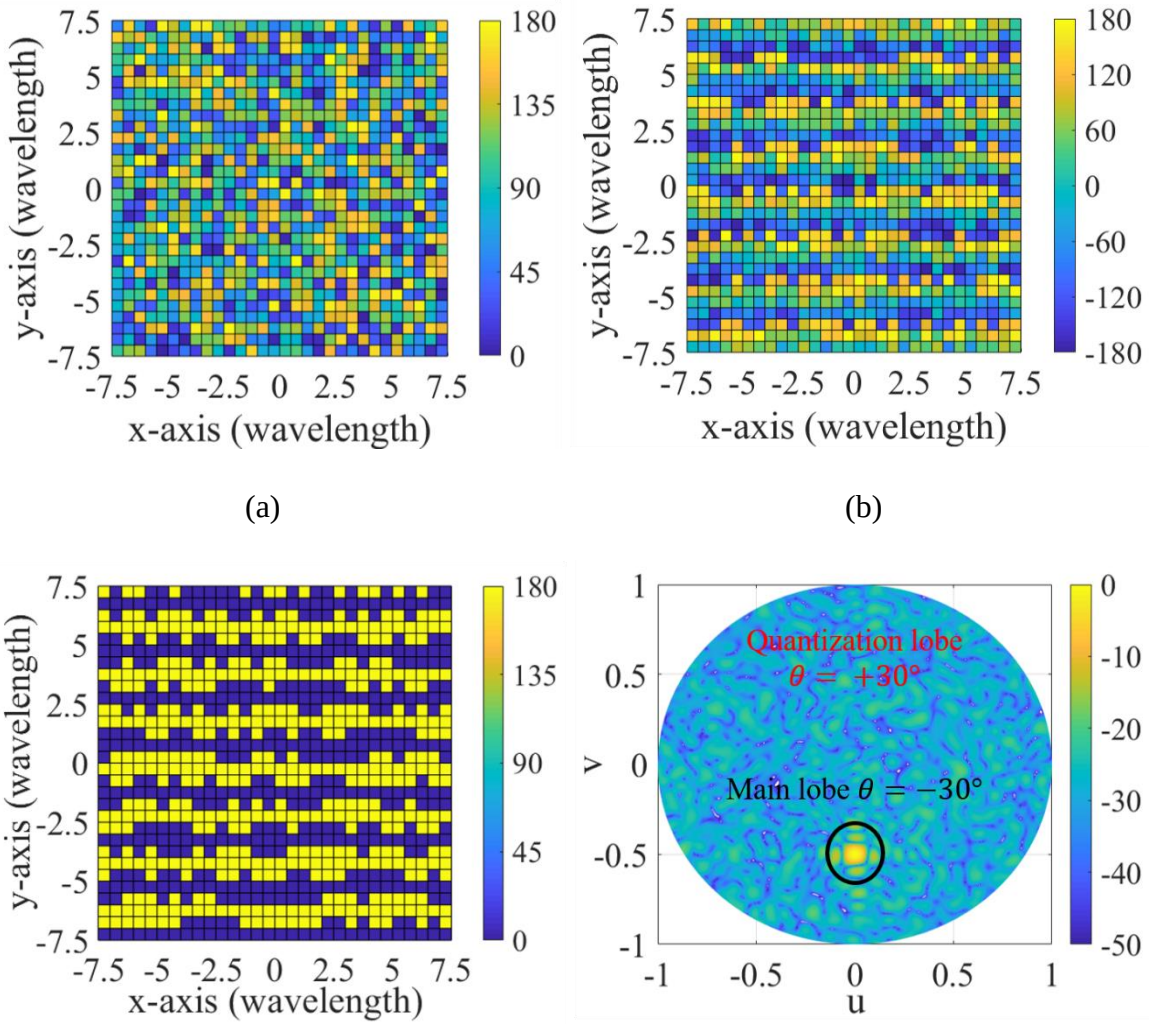

Figure 4.13: 30×30 2D randomized RIS design: (a) randomly generated phase delays $\Phi_{30\times30}^{rand}$ obtained from (5), (b) excitation phase $\Phi_{30\times30}$ obtained by adding random phase delays as in (4), (c) total phase $\Phi_{30\times30}^{total}$ based on 1-bit quantization scheme obtained from (6), and (d) normalized scattered fields obtained from (7) and plotted in the u-v plane ($u = \sin\theta\cos\phi$, and $v = \sin\theta\, sin\phi$).

$+30°$, as shown in Fig. 4.12 (d). This quantization lobe has the same magnitude as the main lobe, and thus, the QLL is 0 dB.

In contrast, for the case of randomized RISs, $\Phi_{M\times N}^{rand} \neq 0$; the pseudorandom phase delays are generated from (5) and given in Fig. 4.13 (a). These phase delays correspond to

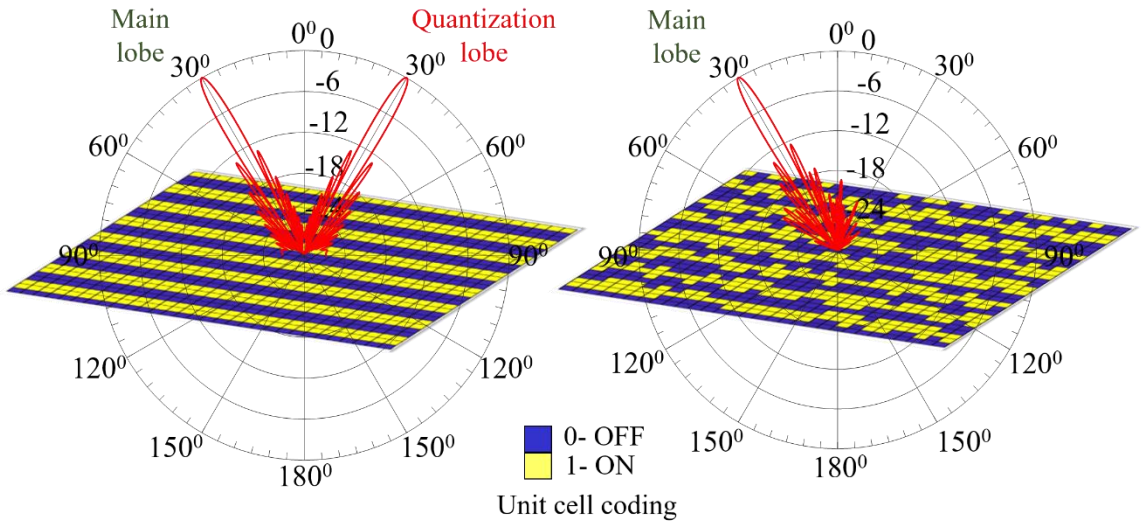

Figure 4.14: Normalized 2D radiation pattern of the 30×30 sub-THz RIS in the $\phi = 90^0$ plane, comparing the designs with no randomization (left) and full randomization ($0 - 180^0$) – (right). The main beam is along $\theta = -30°$ and the quantization lobe is along $\theta = +30°$, as highlighted.

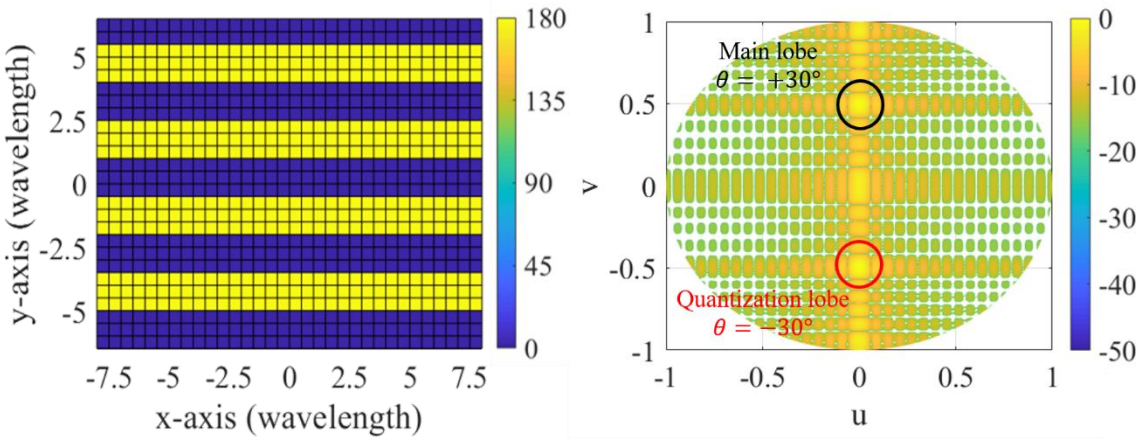

(a) (b)

Figure 4.15: 25×32 mmWave RIS design: (a) the quantized binary phase pattern ($\Phi_{25\times32}^{total}$) obtained based on the 1-bit quantization scheme and (b) the normalized scattered field pattern obtained from obtained from (7) and plotted in the u-v plane.

the physical lengths implemented by varying the branch length, Δl of the microstrip feed line. phase delay scheme eliminates the quantization lobe and achieves a QLL of -18 dB.

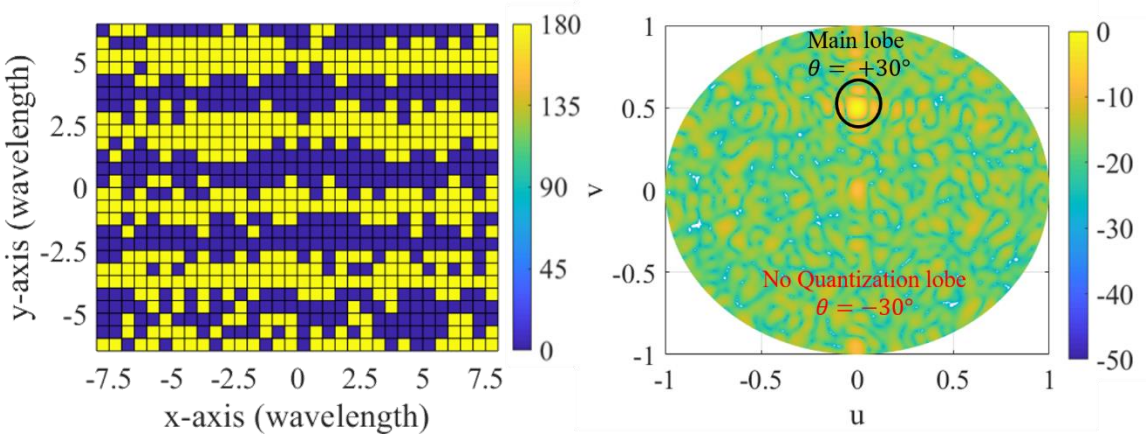

(a) (b)

Figure 4.16: 25×32 mmWave RIS design: (a) the quantized binary phase pattern ($\Phi_{25\times32}^{total}$) obtained based on the 1-bit quantization scheme and (b) the normalized scattered field pattern obtained from obtained from (7) and plotted in the u-v plane.

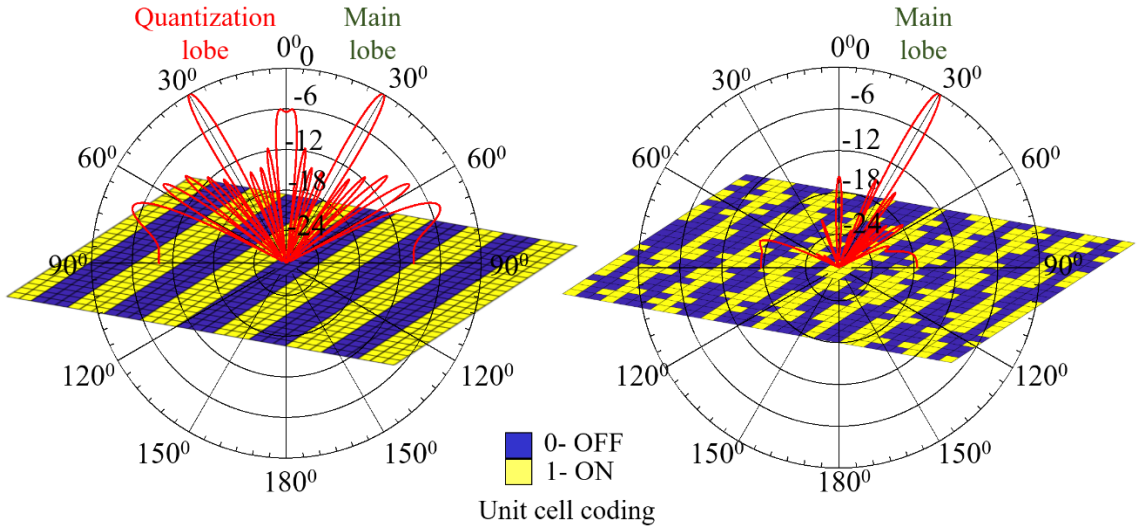

Figure 4.17: Normalized 2D radiation pattern of the 25×32 mmWave RIS in the $\phi = 90^0$ plane, comparing the designs with no randomization (left) and full randomization ($0 - 180^0$) – (right). The main beam is along $\theta = +30°$ and the quantization lobe is along $\theta = -30°$, as highlighted.

The resulting continuous element phases are calculated using (4) and shown in Fig. 4.13 (b). Consequently, the error periodicity of the corresponding total phase, $\Phi_{M\times N}^{total}$ is

perturbed as shown in Fig. 4.13 (c), resulting in a single main lobe at $-30°$, as depicted in Fig. 4.13 (d). Finally, the comparison of 2D scattered fields of the non-randomized and randomized RIS topologies in the $\phi = 90^0$ elevation plane is shown in Fig. 4.14.

A similar design procedure is employed to develop the 800-element mmWave 2D RIS. A main beam direction of $+30°$ is chosen for this design. For the non-randomized RIS under plane wave illumination the quantization lobe appears at $-30°$. With randomization, the QLL can be reduced to -20.64 dB. The overall SLL achieved with this design is -11.29 dB. The total quantized binary phase pattern and the surface plot of the fields scattered by the non-randomized mmWave RIS are shown in Fig. 4.15 (a) and (b). The corresponding plots for the randomized RIS are shown in Fig. 4.16 (a) and (b) respectively, where the periodicity of the quantization error is broken, and the quantization lobe is suppressed. Further, the comparison of the 2D cut of the scattered fields in the $\phi = 90°$ plane for both the non-randomized and the randomized RISs is shown in Fig. 4.17.

4.4 RIS Fabrication Methods

Both the sub-THz RIS and the mmWave RIS have been fabricated to characterize their performance. Owning to their frequency of operation and resulting feature sizes, two distinct fabrications processes are employed, and both are detailed in this section. To carry out a comparative analysis, both randomized and non-randomized designs of the sub-THz RIS are fabricated using nanofabrication techniques. On the other hand, for the mmWave RIS, a standard multi-layer PCB fabrication method is employed. The sub-THz RIS was fabricated at ASU's cleanroom facility while the mmWave RIS was fabricated through external PCB vendor.

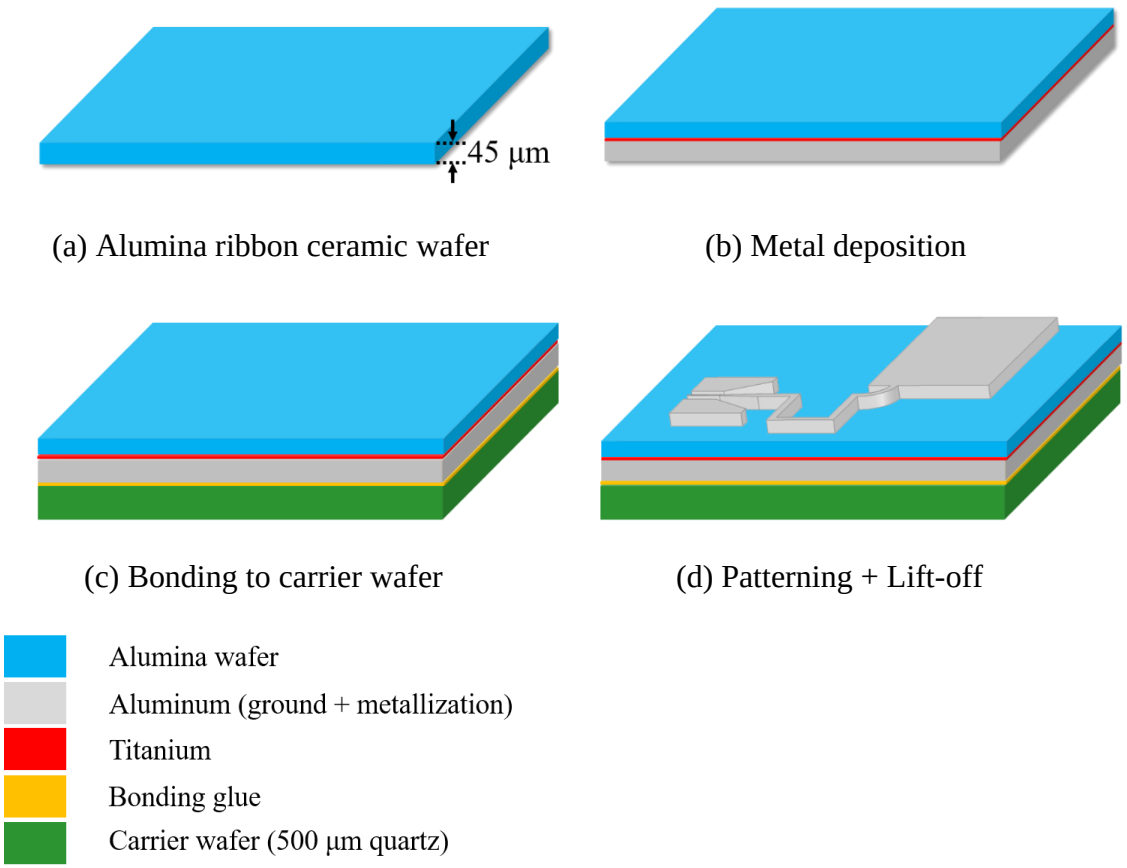

Figure 4.18: Fabrication process flow for the on-wafer development of the proposed RIS (a) 45 µm thick, 2" diameter alumina ribbon ceramic substrate used as the base wafer in the fabrication, (b) Ti/Al deposition to form the ground plane for the RISs, (c) 500 µm thick, 2" diameter quartz wafer bonded to the metalized side of the wafer to impart sturdiness to the alumina ribbon ceramic wafer, and (d) device formation through spin coating, photolithography, patterning, and lift-off processes.

4.4.1 Sub-THz RIS Fabrication

The single-layer implementation reduces the fabrication complexities when compared to the existing methodologies used for fabricating RISs that produce single beam radiation patterns. Both the non-randomized and the randomized RISs are fabricated side-by-side on a 2" diameter, 45 μm thick alumina ribbon ceramic wafer from Corning [133]. The wafer has an $\epsilon_r = 10$ and $tan\delta = 0.8 \times 10^{-3}$ obtained from quasi-optical reflectometer

measurements at ASU. The alumina ribbon ceramic wafer is semi-transparent and flexible owing to its fine grain, dense microstructure and low thickness of $45\ \mu m$, so it was bonded to a 2" diameter, $500\ \mu m$ thick quartz wafer to impart the sturdiness required by the alumina wafer for further fabrication steps. Initially, a $30\ nm$ thick titanium (Ti) layer followed by a $300\ nm$ thick aluminum (Al) layer was deposited on one side of the alumina ribbon ceramic wafer. This layer serves as the ground plane for the radiating structures. Then the metalized side of the alumina ribbon ceramic wafer was permanently bonded with the carrier quartz wafer. The bonding process was carried out in the Flexible Electronic Display Center (FEDC) at ASU.

The bonded wafer was spin-coated with photoresists and exposed to UV through the photolithography step to develop the antenna patterns. Then a second metallization step is used to deposit Al for radiating structures, followed by a lift-off process, to obtain the final patterns as shown in Fig. 4.18 (d). The steps used in the fabrication process are illustrated in Fig. 4.18. Fig. 4.19 (a) depicts the finished alumina ribbon ceramic wafer with fabricated RIS. The randomized RIS is on the left, and the non-randomized RIS is on the right. A high-magnification image of the individual unit-cell is shown in Fig. 4.19 (b).

4.4.2 MmWave RIS Fabrication

Standard multilayer PCB manufacturing process was employed to fabricate the mmWave RIS prototype. The 2D RIS designed in HFSS is exported into Altium designer to generate the gerber and drill files needed for fabrication. Two $0.508\ mm$ thick Rogers RO4003C substrates are attached back-to-back using a prepreg material (Rogers RO4450F: $\epsilon_r = 3.52, tan\delta = 0.004$). The prototype board has the dimension of $168\ mm \times 129\ mm$

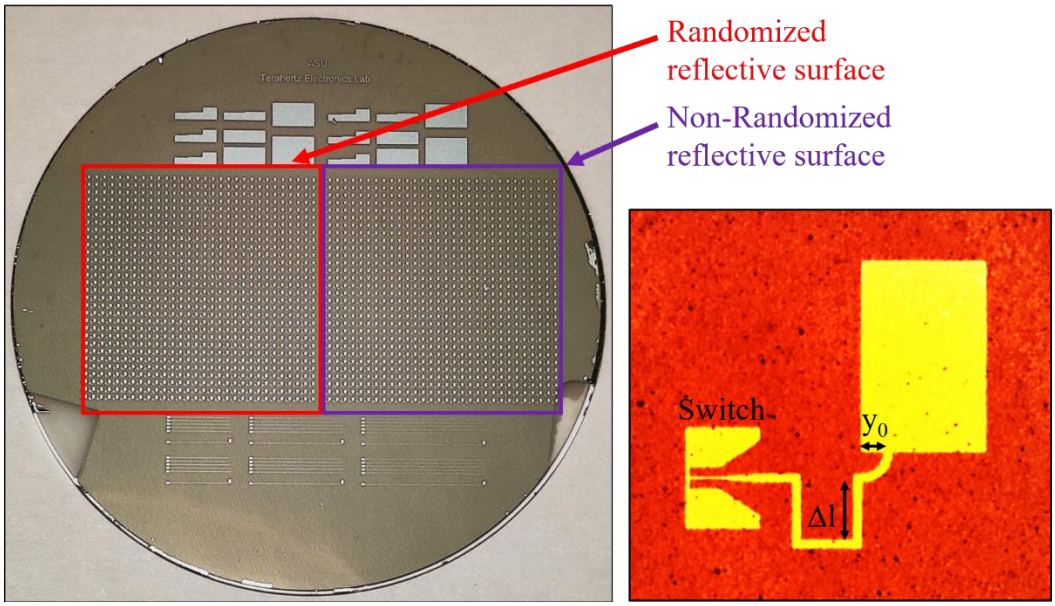

(a) (b)

Figure 4.19: Fabricated sub-THz RIS on the alumina ribbon ceramic wafer with (a) randomized (left) and non-randomized RIS sections, and (b) high-magnification image of a unit-cell of the fabricated RISs.

and is only 1.2 mm thick. This small thickness leads to challenges in terms of warpage of the board which can alter the radiation and loss properties. To compensate for this, the four-layer design was adopted for fabricating the mmWave RIS. It should be noted that a three-layer design with a shared ground plane (for the top layer patch and the bottom layer microstrip geometry) could also be utilized, the addition of the prepreg bonding layer created an imbalance in the metal distribution about the center of the board stack-up, and this was identified to have a significant impact on the warpage (particularly for thin designs). Additionally, the Rogers RO4003C is also flexible, thus aggravating the warpage problem. As such, two-separate ground planes are used for top and bottom layers on either side of the prepreg as shown in Fig. 4.11. The warpage was considerably reduced with is approach. The top and bottom views of the fabricated prototype are shown in Fig. 4.20.

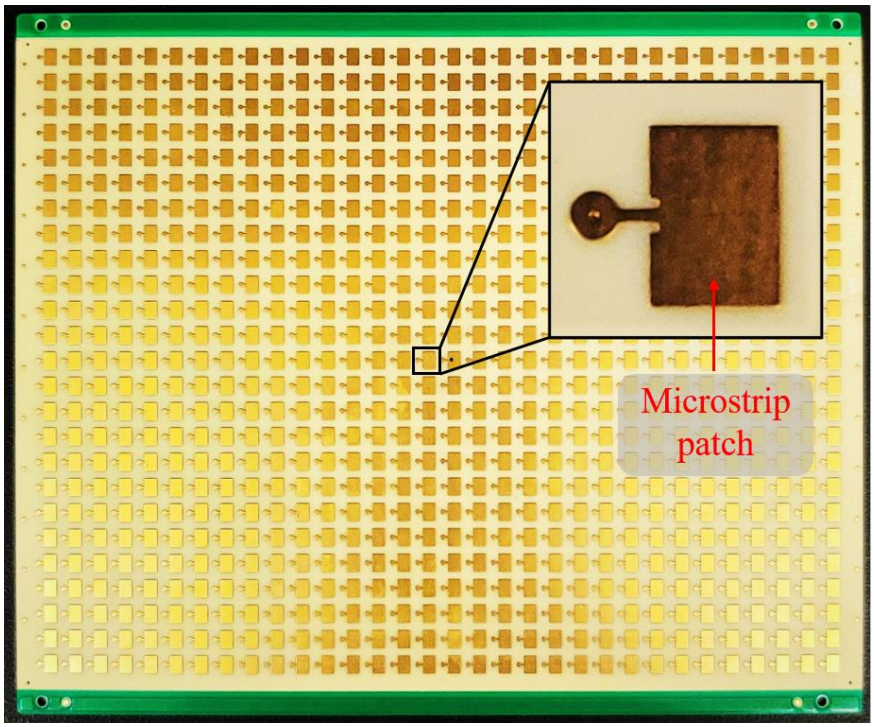

(a)

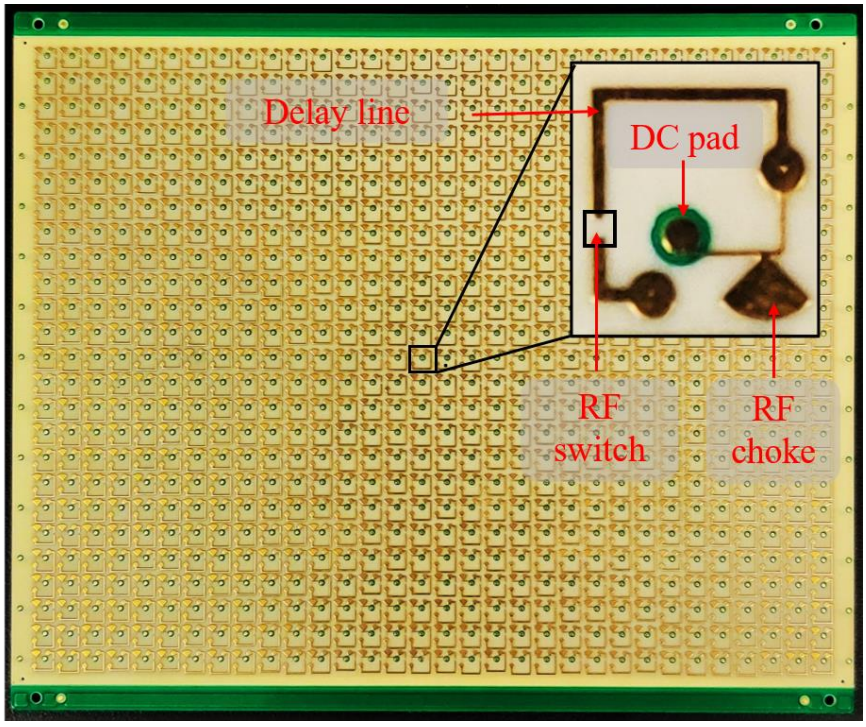

(b)

Figure 4.20: Fabricated prototype of mmWave RIS: (a) top view, and (b) bottom view.

4.5 RCS Characterization

Quasi-optical measurement setups as shown in Fig. 4.20, are used to measure the RCS characteristics of the fabricated RIS prototypes. Particularly, Fig. 4.21 (a) illustrates the measurement setup utilized for sub-THz RIS characterization. This setup includes two vector network analyzer (VNA) extenders, a transmitting and a receiving horn antenna, two collimating lenses, and the prototype wafer containing both randomized and non-randomized RISs. All the components are mounted on an optical breadboard. The VNA signal is upconverted to 222.5 GHz using the VNA extender on the transmitter side and directed towards the wafer. The collimating lens situated in front of the transmitting horn antenna is used to collimate the diverging beam from the horn and provides an illumination beam of radius 1 cm on the RISs. The wafer is mounted on a sliding pedestal so that the RIS under test is aligned with the transmitter beam at boresight (θ_i = 0). To measure the scattered fields, the receiver is rotated radially around the center of each RIS covering the $[-20°, -80°]$ and $[+20°, +80°]$ angle ranges, only restricted by the geometrical limitations of the setup. Nevertheless, a single point monostatic RCS measurement at $\theta_d = 0^0$ is carried out to ensure that there is no significant radiation in the broadside direction.

The measured 2D RCS patterns of the non-randomized and randomized RISs at 222.5 GHz have been plotted along with the analytical results, for both the surfaces in Fig. 4.22 (a) and (b), respectively. A good agreement is achieved between the analytical and measured results. The non-randomized RIS radiates at both $-30°$ and $+30°$, indicating the presence of an undesired quantization lobe, while the randomized RIS radiates only at $-30°$, which confirms that the quantization lobe is eliminated by incorporating of phase

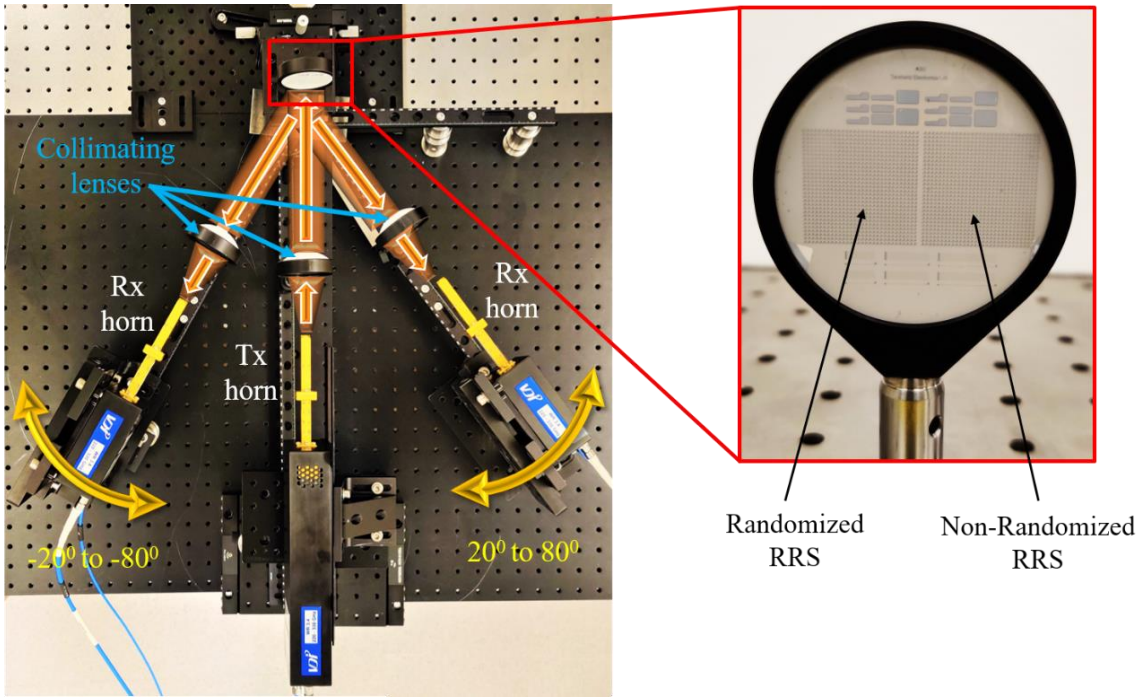

(a)

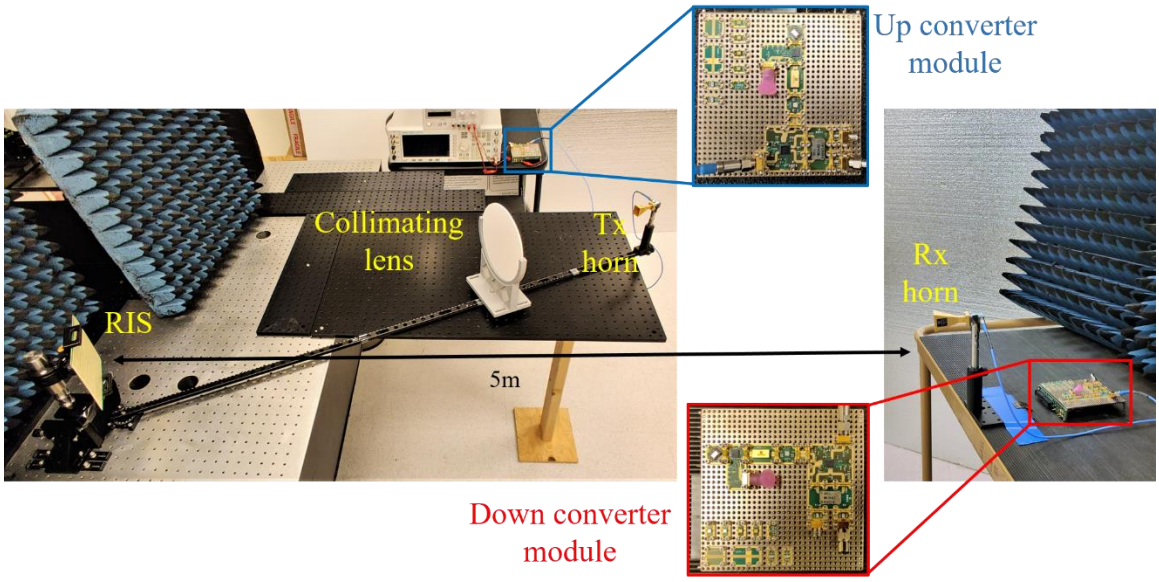

(b)

Figure 4.21: Quasi-optical measurement setups used for the characterization of the fabricated RIS prototypes: (a) Sub-THz (222.5 GHz) RIS measurement setup and (b) mmWave (28.5 GHz) RIS measurement setup.

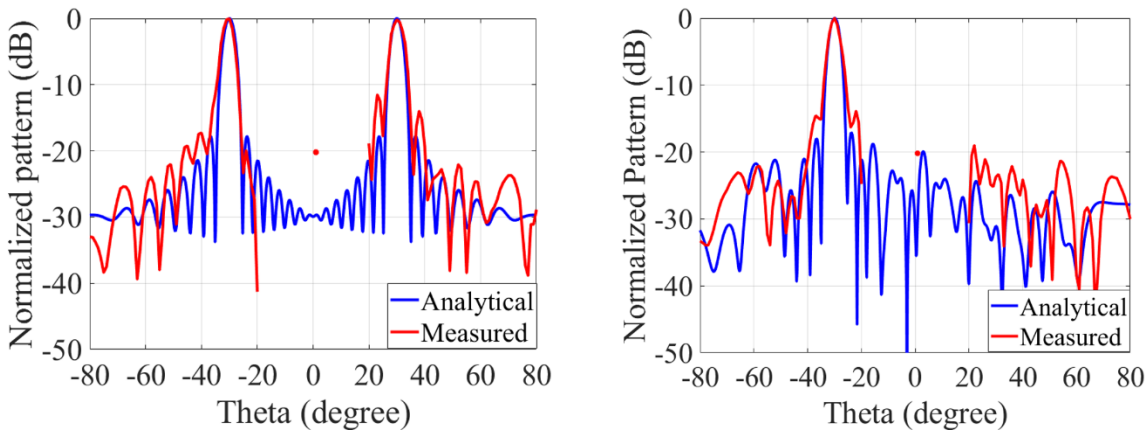

(a) (b)

Figure 4.22: Normalized RCS as a function of the scan angle theta at 222.5 GHz for (a) non-randomized RIS and (b) randomized RIS.

randomization in the feed network of the RIS unit-cells. From the measurements, a QLL below -18 dB is achieved. The analytically computed and measured radiation patterns of both the RISs are conformal demonstrating that the element pattern has minor impact on the total radiation pattern. Furthermore, to evaluate the bandwidth of operation, the RCS is plotted as a function of frequency and scan angle theta, as shown in Fig. 4.23 (a) and (b). For both non-randomized and randomized RISs, the 3 $-$dB bandwidth is approximately 8.5 GHz, which corresponds to a fractional bandwidth of 3.8 %.

A slightly modified setup is used for characterizing the mmWave RIS as shown in Fig. 4.21 (b). Here, the receiving horn antenna is fixed and placed in front of the RIS, at a distance of $5m$. The receiver is positioned such that it is in the far-field of the RIS and along the broadside direction. The lens is only used in front of the transmitting horn antenna unlike the sub-THz setup where collimating lenses are used in front of both transmitter and receiver. The Teflon lens collimates the diverging beam from the horn and

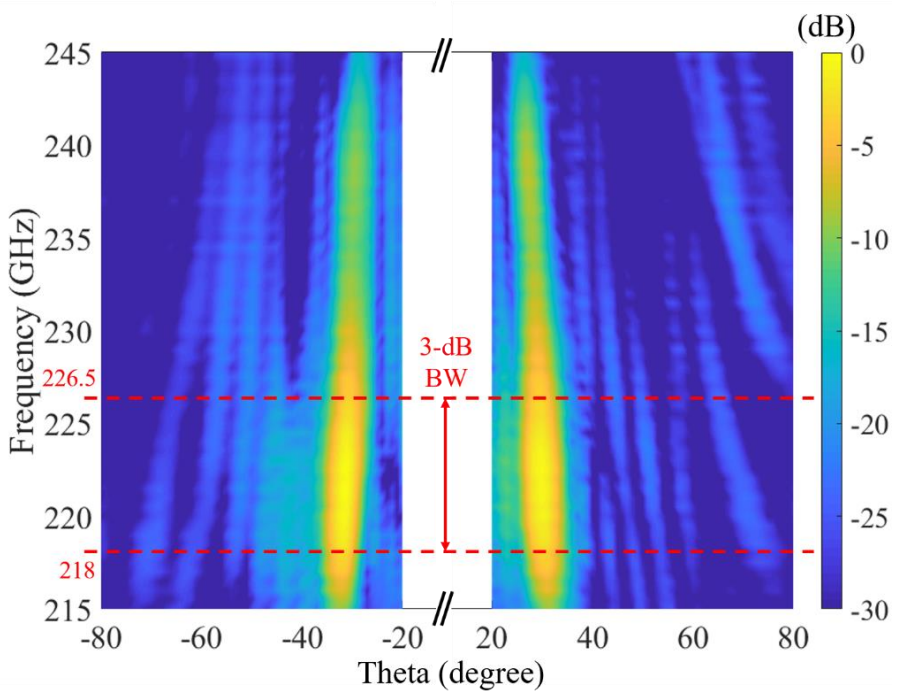

(a)

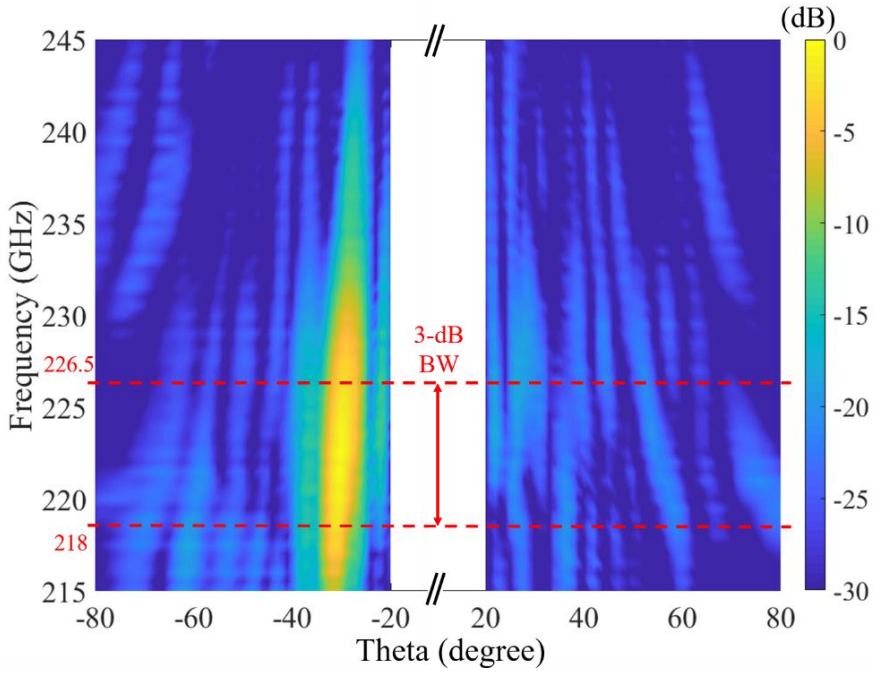

(b)

Figure 4.23: Normalized RCS as a function of frequency and scan angle theta for (a) non-randomized RIS and (b) randomized RIS.

focuses it on the reflective surface. The distance between the lens and the surface is adjusted to ensure maximum illumination and to avoid any spillover. The collimated beam has a waist of radius $75mm$, which covers the entire surface of the RIS. To measure the RCS characteristic of the RIS, the transmitter is rotated radially (instead of receiver as with the sub-THz system) around the center of the RIS from $[-20°, -70°]$ and $[+20°, +70°]$, with the scan angle range again limited by the geometrical limitation of the setup. The RIS, lens, and transmitting horn are all mounted on an optical breadboard, which helps keep the whole measurement setup stable to provide accuracy and repeatability.

X-microwave ADMV1013 upconverter and ADMV1014 downconverter are used to generate the signals necessary for operation in the mmWave band. Two local oscillator signals – 26 GHz and 31 GHz are set up respectively on the frequency upconverter and downconverter using a Raspberry Pi based controller. The generated signal of 2.5 GHz is upconverted to provide the 28.5 GHz signal using the X-microwave upconverter on the transmitting end. The transmitted beam from the horn is reflected from the RIS, captured by the receiving horn, and is down converted to 2.5 GHz at the receiving end using the X-microwave downconverter. The down converted signal is then fed into a spectrum analyzer, and the received power is determined.

The measured RCS patterns of the randomized RIS at 28.5 GHz have been plotted in Fig. 4.24. The randomized RIS radiates only at $+30°$ which confirms that the quantization lobe is eliminated by incorporating the random phases in the feed network of the RIS unit-cells. A good agreement is achieved between the analytical and measured results. From the measurements, a QLL of below -16.5 dB and an SLL of below -10 dB were achieved.

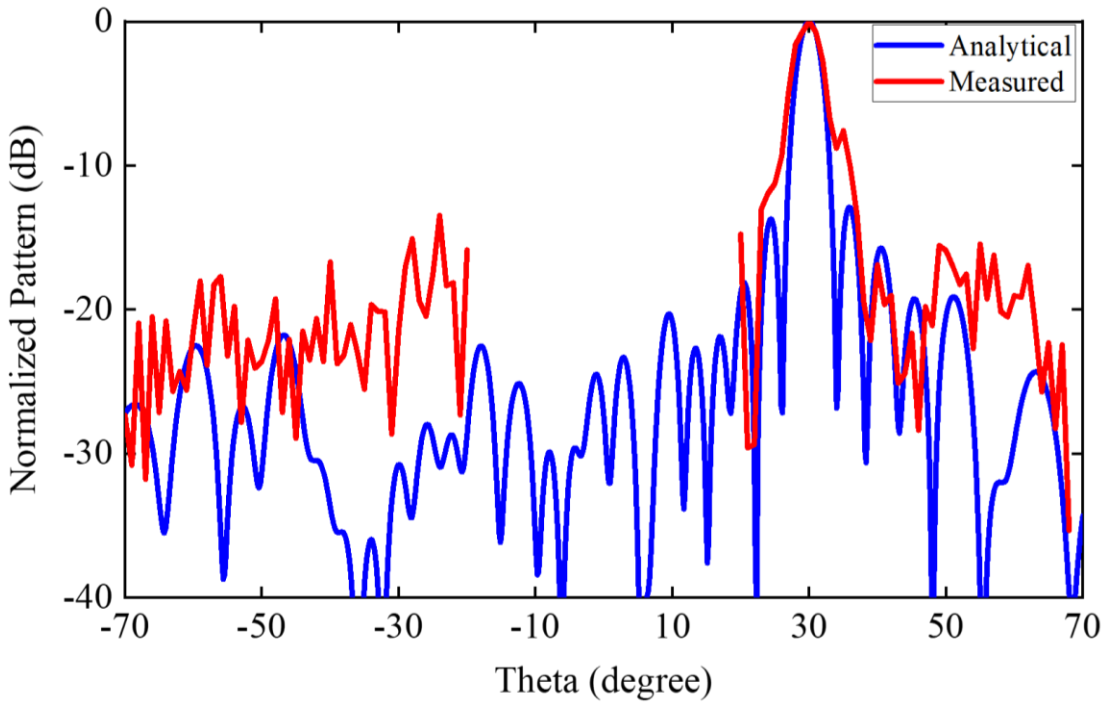

Figure 4.24: Normalized RCS as a function of the scan angle theta at 28.5 GHz for a RIS implemented with randomization.

Table 4.3: Comparison of the proposed 1-bit RIS with the state-of-the-art

Ref.	Illumination	Frequency	Design	Quantization lobe level
[20]	Plane wave	10.0 GHz	Single-layer	0 dB
[21]	Plane wave	11.1 GHz	Single-layer	0 dB
[22]	Plane wave	90.0 GHz	Single-layer	0 dB
[23]	Plane wave	39.0 GHz	Multi-layer	−13 dB
This work	Plane wave	222.5 GHz	Single-layer	−18 dB
This work	Plane wave	28.5 GHz	Multi-layer	−16.5 dB

Table 4.3 provides a comparison of the performance of the proposed design with the existing state-of-the-art designs in the literature that employ plane wave illumination and 1-bit phase quantization. [125], [126], and [127] utilize a single layer design but consist of one or more quantization lobes. Pre-phasing technique is employed in [128] to suppress the quantization lobes and achieve an SLL of about −13 dB. However, as multi-layer

design is adopted, it is unsuitable for sub-THz implementations. In contrast, the single layer design proposed in this work is well suited for sub- THz implementations and achieves a single beam pattern with a QLL of -18 dB (sub-THz). Additionally, the mmWave multi-layer design achieves a much better QLL reduction of -16.5 dB (mmWave RIS).

4.6 Conclusion

In this chapter, a robust technique was presented for mitigating quantization lobes in sub-mmWave single-layer 1-bit RISs under plane wave illumination using random phase delays. Specifically, the technique is realized by introducing randomized physical delay lines in the feed network of the individual unit-cells to break the periodicity of the quantization error and mitigate the quantization lobes. A comprehensive study explaining the effect of introducing varied degrees of randomization in a traditional RIS is presented along with the analytical results. Leveraging these results, the condition for choosing the range of randomization required to achieve the lowest SLL was formulated for the first time. Adopting the stipulated range of randomization, two RIS designs were evaluated: (i) a 30×30 single-layer 1-bit randomized RIS was designed at 222.5 GHz to radiate along $-30°$ direction and (ii) a 25×32 four-layer 1-bit randomized RIS designed at 28.5 GHz to radiate along $+30°$ direction. To carry out a comparative analysis, a non-randomized RIS with similar specifications was also designed. Both sub-THz and mmWave RIS prototypes were fabricated. The RCS of the fabricated RISs was characterized by a quasi-optical measurement setup, and the results confirm that the quantization lobes in randomized RIS are suppressed with QLLs below -18 dB (sub-THz) and -16.5 dB (mmWave RIS). To demonstrate the proof-of-concept of the proposed technique, the

fabricated prototype is implemented with permanent, ideal switches using open and short terminations. Future work will focus on realizing the proposed topology with tunable switches (e.g., PIN diodes, FETs, graphene, vanadium dioxide etc.).

CHAPTER 5

LINEAR META-TRANSMISSION LINE DESIGN FOR MINIATURIZATION OF ROTMAN LENSES

5.1 Introduction

Electronic beamforming is a key enabler in wireless communications, radars, and sensing applications. Generally, phased arrays are employed in such applications to realize the necessary beamsteering using complex feed networks consisting of phase shifters, mixers, amplifiers, oscillators etc. These components lead to reduced operating bandwidth, increased losses, cost, and power consumption, as well as beam squinting issues [1], [23], [134-139]. To counter these problems, usually true time delay (TTD) systems are preferred. TTD beamformers are the structures where the phase shift is determined by the actual propagation time between the input ports and the array elements [140-142]. TTD units can provide variable phase shift that is frequency dependent, thus providing a constant group delay over the entire operating band. As such, they do not suffer from the beam squinting problems witnessed in the conventional phased array systems and inherently provide wideband capabilities [141]. TTD units can be designed using passive transmission lines as well as active circuits based on complimentary metal-oxide-semiconductor (CMOS)/ Gallium Arsenide (GaAs) technologies. Consequently, the TTD units could be employed in analog, digital, or hybrid beamforming architectures [136-139], [143]. In this work, the focus is on designing analog beamforming architectures owing to their advantages of low power consumption, low losses, and wider bandwidth. The most common TTD analog

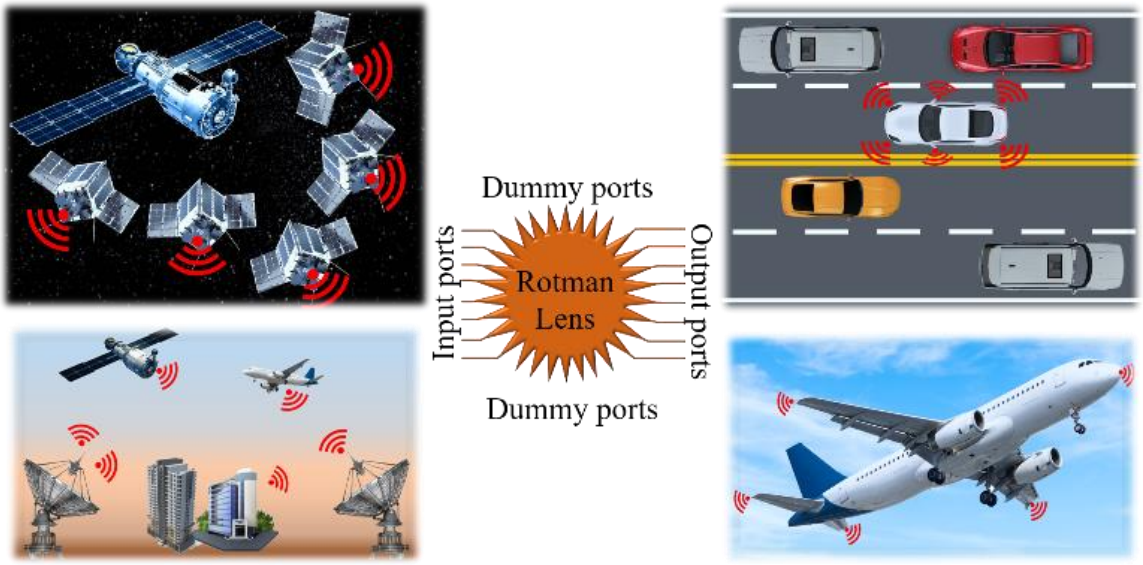

Figure 5.1: Applications of miniaturized Rotman lenses as beamforming structures for long-range low-frequency phased array antenna systems.

beamformers are based on Butler [144-145] and Blass [146] matrices, Rotman lenses [142], [147-155], and tree type transmission line network [140]. Particularly, Rotman lenses are excellent candidates for amorphous arrays where the radiating elements could be placed at strategic locations with non-uniform spacings, as shown in Fig. 5.1, while achieving the desired phase shifts to realize the optimal array performance. Rotman lenses could be implemented as metallic plate waveguides [142], dielectric loaded waveguides [152-155], as well as in microstrip [147-150] and substrate integrate waveguide [150] environments. Additionally, these lenses also offer the advantages of dynamic beamforming, multibeam capabilities, and low cost of operation [148-149].

A primary drawback of Rotman lenses is their large size at low frequencies. Due to their TTD nature, the Rotman lenses need to be $5-6$ wavelengths long which when designed using conventional techniques, corresponds to sizes of the order of $5-15m$ in the very/ultra-high frequency (VHF/ UHF) bands. As such, most of the existing Rotman

lens-based beamforming solutions are restricted to microwave and mmWave bands [148-152]. Consequently, to exploit the advantages of Rotman lenses at lower frequency bands, it is necessary to devise methods to reduce their size. Most common techniques employed for achieving size reduction involve employing high dielectric constant (ϵ_r) materials. By loading the lens wave-space with high ϵ_r materials, the wave can be slowed down, and lens size can be reduced. In [147], a microstrip based Rotman lens was designed in the lower UHF band ($450 - 1000\ MHz$) for the first time using a substrate with $\epsilon_r = 10.9$. There have also been efforts to employ ceramics with $\epsilon_r > 100$ [153-154], artificial dielectric based on mushroom metasurface ($\epsilon_r \approx 80$) [155] etc., to achieve miniaturized designs. However, there is a price paid in dielectric loss, the potential for non-linear behavior at high powers, and temperature variability. Moreover, the lenses developed using these approaches would still need to be at least $2m$ long at $100\ MHz$. As such, the size reduction achieved is inadequate for most practical deployments.

An alternate technique to achieve phase retardation is to model the Rotman lens wave-space as a periodic grid of transmission lines (TLs). Particularly, the parallel plate region between the input and output ports of the lens could be replaced by distributed (microstrip, strip line etc.,) or lumped TL structures to achieve the desired delay behavior. This research work outlines a novel technique for miniaturizing the Rotman lenses by employing modified lumped element TLs, which are referred to as meta transmission lines (meta-TLs). Specifically, the design and analysis of a proof-of-concept 1D meta-TL is presented along with the fabrication and measurement results. A 2D rendition of such a meta-TL wave-space will be employed in the future works to realize a hyper-compact Rotman lens.

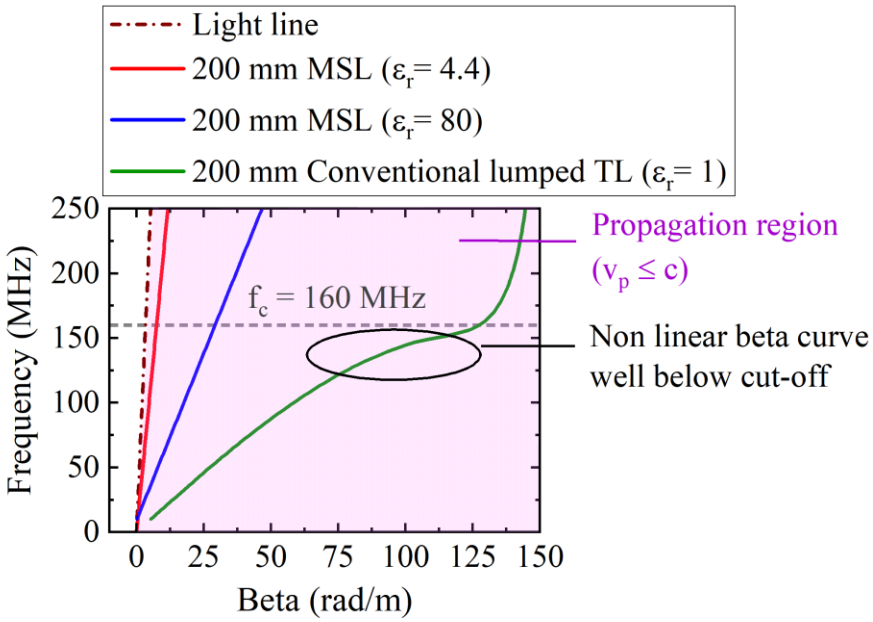

Figure 5.2: Dispersion diagram depicting higher beta values (higher degree of miniaturization) achievable using lumped TL networks.

5.2 Meta-Transmission Line Design

This section presents the design procedure and the simulation results of the proposed 1D meta-TL. The first step toward this goal is to demonstrate that a dispersionless wave-space based on a periodic grid of meta-TLs can be constructed at an arbitrarily small scale. The achievable degree of miniaturization can be effectively examined using the dispersion diagram – with the higher value of beta (β) indicating greater size reduction. Further, the linear region of the $\omega - \beta$ curve determines the bandwidth of operation. While distributed TLs (microstrip, strip, or coax) offer excellent linearity, sufficient size reduction cannot be achieved even with ϵ_r of the order of 80. This is depicted in the dispersion diagram plots of Fig. 5.2 by employing $200\,mm$ microstrip lines (MSL) designed using substrates with $\epsilon_r = 4.4$ and 80. On the other hand, it is also possible to model the lens wave-space by employing lumped LC ladder networks which provide the best possible size

reduction at low frequencies. With this approach, the inductor (L) and capacitor (C) values could be chosen to achieve a desired cut-off frequency, f_c. While the size of such a periodic system is only constrained by the fabrication limitations, the structure becomes strongly dispersive as it approaches f_c, thereby reducing the usable range of frequencies, as shown in Fig. 5.2 ($200\ mm$ Lumped TL curve). Consequently, the conventional lumped element TL model needs to be modified to improve the linearity of the dispersion diagram and extend the operating bandwidth. In this research, technique is introduced to extend the linear region of the dispersion diagram by modifying the classical TL model to include the effects of mutual inductance between the neighboring inductor elements. The addition of mutual inductance terms can potentially increase the dispersion-free region all the way up to the cut-off.

Herein, the 1D meta-TL is designed to prove the feasibility of construction of a 2D meta-TL wave-space. In [116], [156] it was demonstrated that by introducing mutual coupling terms between the neighboring elements of a conventional lumped LC ladder network, it is possible to change the shape of the dispersion diagram and thereby increase the linearity of the $\omega - \beta$ curve. The solution for achieving a constant velocity over the entire band leads to the requirements on the mutual coupling between the inductors of the LC ladder to be: $M_1 = 0.171\ L$ (between the first nearest neighbors) and $M_2 = -0.0485\ L$ (between the second nearest neighbors). All further mutual coupling terms are small enough to be ignored. In this work, only the first mutual inductance term (M_1) is employed to design the meta-TL and demonstrate that it is possible to achieve a remarkably linear dispersion diagram. The TLs are designed for a VHF cut-off frequency f_c of $160\ MHz$ using

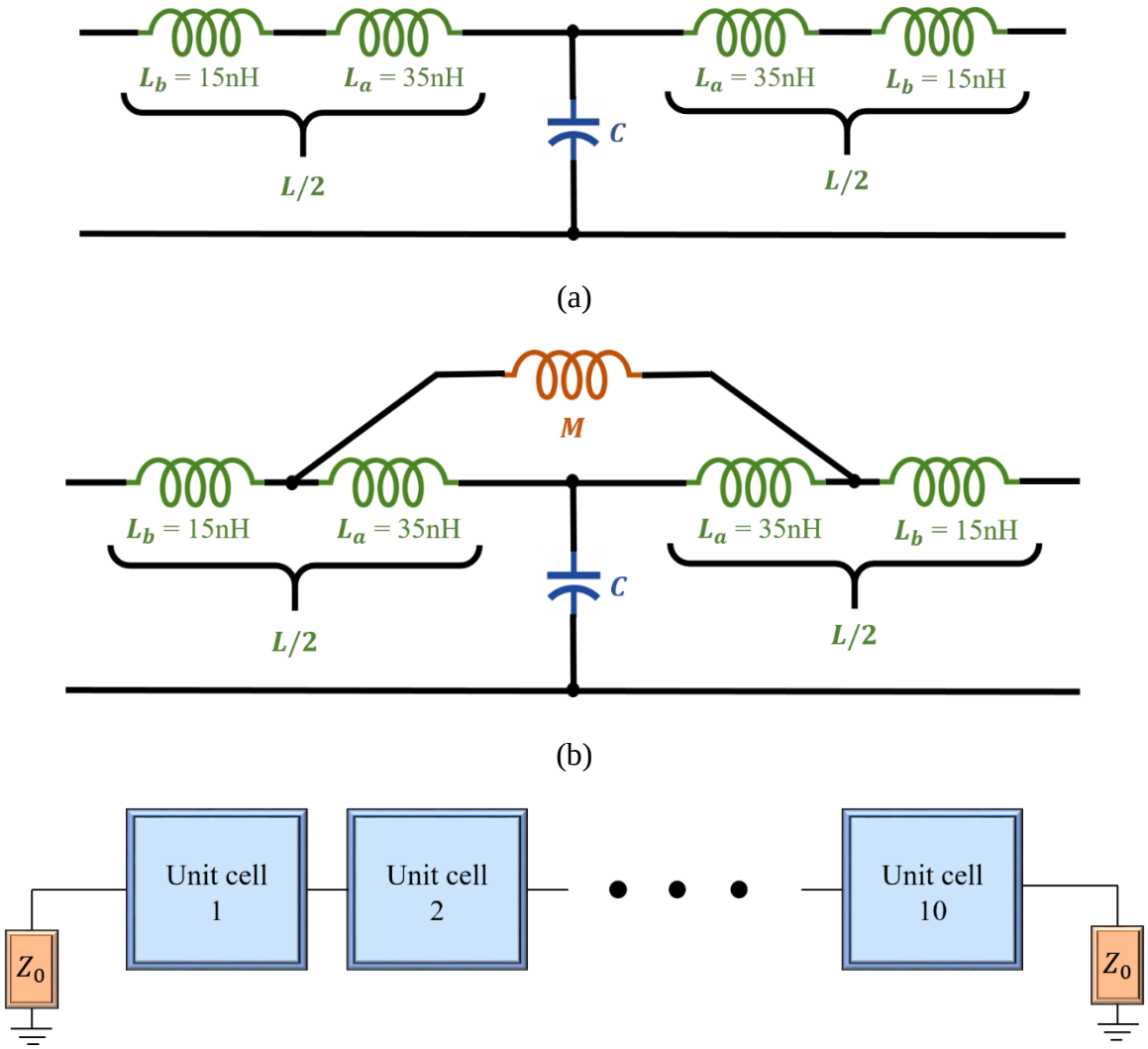

Figure 5.3: Circuit schematics for the comparative study of the meta-TL: (a) conventional TL model, (b) meta-TL model with a single mutual inductance between first nearest neighbors, (c) 1D rendition of the TLs obtained by cascading 10-unit cells.

$$\omega_c = \frac{2}{\sqrt{LC}} \tag{5.1}$$

where $\omega_c = 2\pi f_c$, $L = 2Z_0/\omega_c$, $C = 2/\omega_c Z_0$, and Z_0 is the characteristic impedance of the TL. The L and C values are found to be approximately $L = 100\,nH$ and $C = 40\,pF$, respectively. The circuit schematics of the unit cells of the conventional and the meta-TLs

are depicted in Fig. 5.3 (a) and (b), respectively. The $100\ nH$ inductance is split into two pairs of $L_a = 35\ nH$ and $L_b = 15\ nH$ series inductors arranged in parallel with the $40\ pF$ capacitor to form the LC ladder network. A comparative analysis is carried out by simulating 1D arrays of both the conventional lumped element LC ladder network and the meta-TL designed with mutual inductance terms ($M_1 \approx 17\ nH$), as shown in Fig. 5.3 (c). The TL behavior is evaluated by comparing the scattering (S) parameters and dispersion diagrams of the two transmission lines. The return (S_{11}) and insertion (S_{21}) losses are compared in Fig. 5.4 (a) and (b). While the conventional TL exhibits S_{11} better than $-8\ dB$ and S_{21} better than $-1\ dB$ up to $130\ MHz$, the meta-TL shows a remarkable improvement by extending this passband to $180\ MHz$, well beyond cut-off. This is further confirmed by the dispersion $(\omega - \beta)$ diagrams in Fig. 5.4 (c). The meta-TL design remains linear with a constant propagation delay up to $180\ MHz$, while the conventional TL model becomes non-linear around $130\ MHz$. The severe deviation of the β curve from the light line near cut-off makes the conventional LC ladder network strongly dispersive in this frequency range, thus reducing the usable range of frequencies to be much lower than the cut-off frequency. As such, the meta-TL design provides an overall bandwidth improvement of about $50\ MHz$ (~38.5 %).

In addition, to fully appreciate the bandwidth improvement and miniaturization achieved using the proposed meta-TL designed with $f_c = 160\ MHz$, another comparative study is carried out using two additional conventional lumped TL and meta-TL pairs designed with $f_c = 300\ MHz$ and $600\ MHz$. As seen from the plots in Fig. 5.5 (a), the TLs designed with higher f_c exhibit a wider operational bandwidth, as expected. But this must not be mistaken for higher degree of miniaturization. The degree of miniaturization

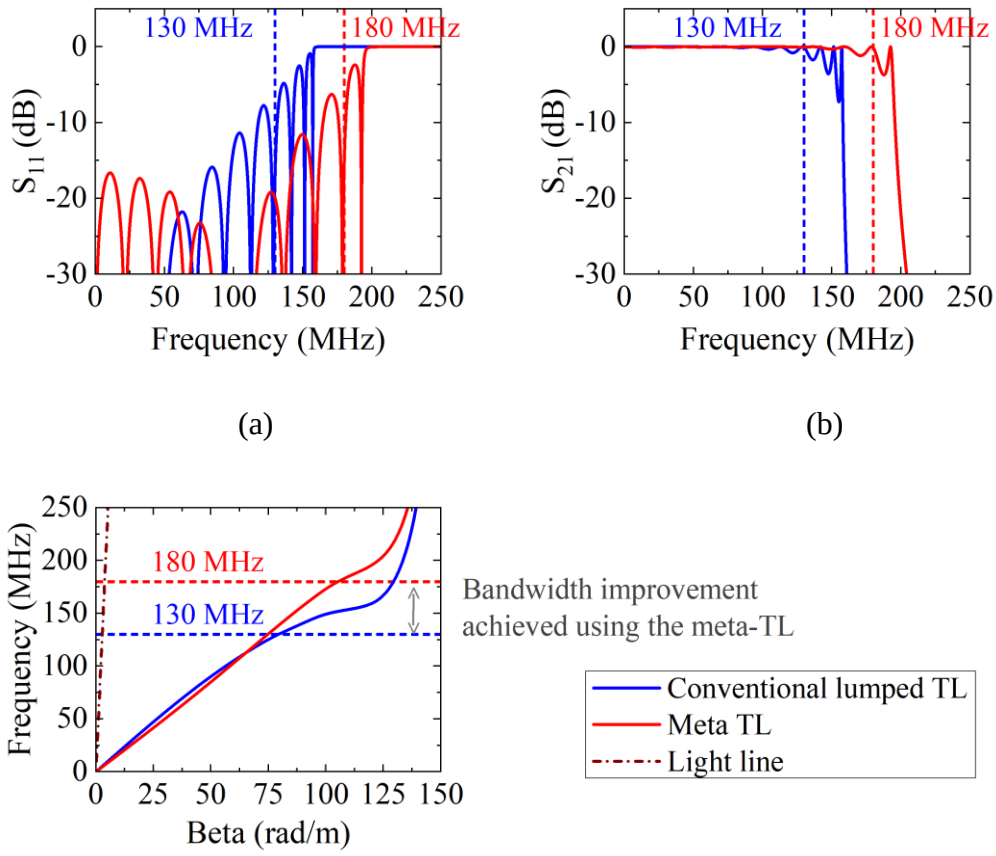

Figure 5.4: Circuit analysis results of the proposed lumped and meta-TL designs: (a) S_{11}, (b) S_{21}, and (c) dispersion diagram plots showing bandwidth and linearity improvement with the meta-TL design.

is determined by the slowing factor of the electromagnetic signal in the medium, which could be represented by (i) higher value of β in the dispersion diagram and (ii) higher value of group delay. From Fig. 5.5 (a), the TL designs with $f_c = 160\ MHz$ exhibit higher β compared to the other two designs. Moreover, for each TL pair, adopting the meta-TL design improves the bandwidth by approximately 40 %. Further, the group delay plots in Fig. 5.5 (b) show that the proposed design achieves a constant group delay in the entire operating band of about $22\ ns$, whereas the other two designs exhibit $11\ ns$ ($f_c =$

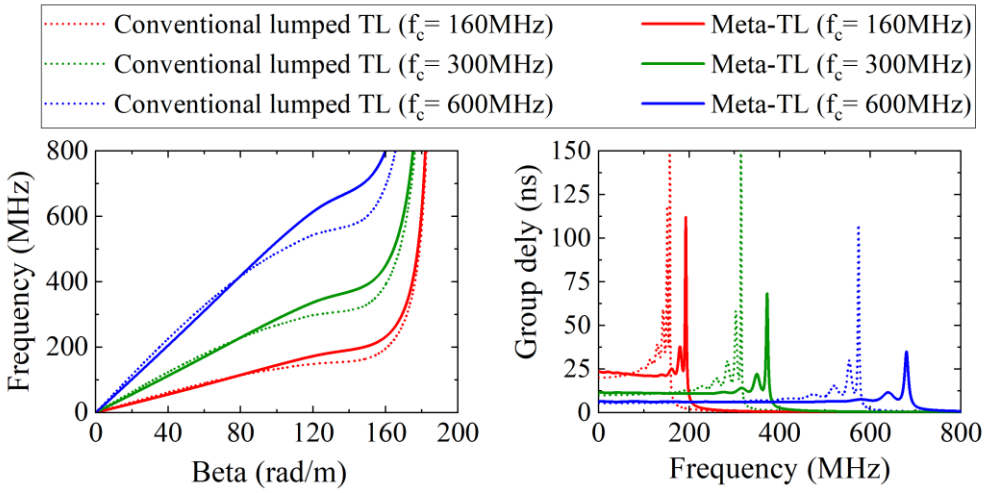

Figure 5.5: Comparison of the proposed VHF TLs with TLs design at higher cut-off (f_c) frequencies. (a) Dispersion diagram plots showing bandwidth improvement with meta-TL designs and (b) group delay plots depicting the higher degree of miniaturization achievable using low f_c designs.

$300\ MHz$) and $6\ ns$ ($f_c = 600\ MHz$) delays, respectively. This shows that the slowing factor approximately gets halved as f_c is doubled. It is also observed from the plots that, in each instance, by employing the meta-TL design, the dispersion can be significantly reduced as witnessed by the flat group delay curve, extending the bandwidth up to cut-off.

Furthermore, to understand the full-wave behavior of the TLs, both the designs are modeled in the 3D electromagnetic solver, Ansys HFSS. A two-wire transmission line model is adopted in this work to implement the HFSS design of both the TLs. The L and C values are realized using RLC boundary conditions for the conventional TL. To model the mutual inductance between the first nearest neighbors, a center tapped two- turn loop inductor is chosen. The loop inductor is designed and optimized in Ansys Maxwell. The loop radius and the spacing between the turns are tuned to achieve the required inductance of $\sim 70\ nH$ and a mutual inductance of $\sim 17\ nH$ ($\approx M_1 = 0.171\ L$). The optimized loop radius is 4.5 mm, and the spacing between the turns is $0.508\ mm$. The remaining $30\ nH$

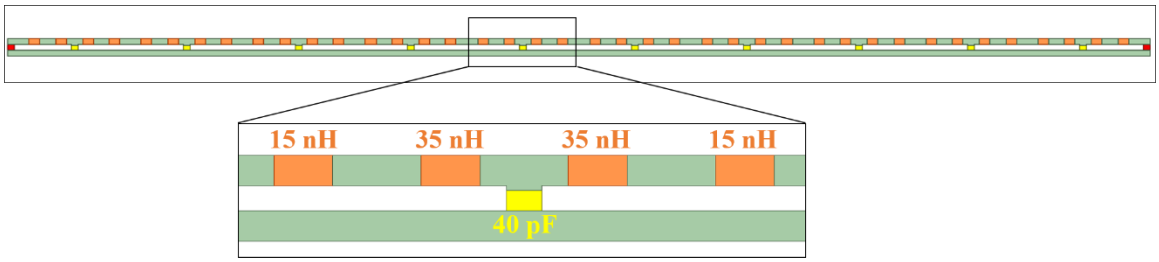

(a)

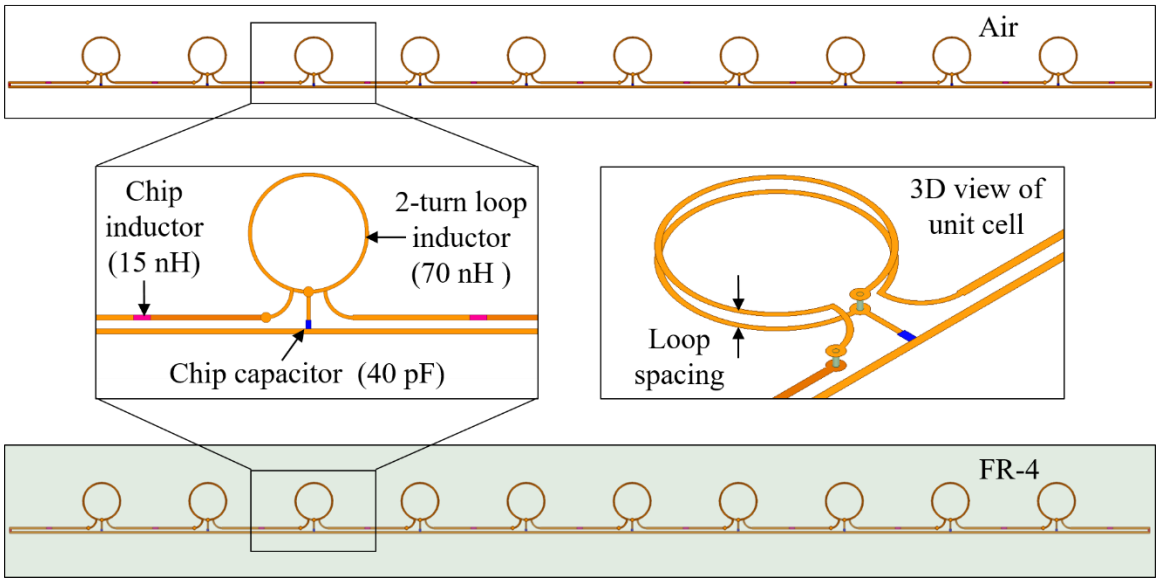

(b)

Figure 5.6: Simulation models of the conventional lumped TL (no mutual coupling) and the proposed meta-TL for the comparative study: (a) conventional lumped element LC ladder network (inset: unit cell with the inductor and the capacitor values annotated), (b) meta-TL in air medium (top) and meta-TL in FR-4 medium (bottom) (inset: unit cell with the inductor and capacitor values annotated (left) and 3D view showing the 2-turn loop inductor (right)).

inductance is split into two 15 nH chip inductors arranged in series with the loop inductors, while the 40 pF shunt capacitances are realized using ceramic chip capacitors. Both the TLs, designed as 10-element linear arrays in the 3D electromagnetic solver employing the two-wire transmission line model, are shown in Fig. 5.6 (a) and (b), respectively. As with the circuit analysis, a comparative study is carried out here as well to compare the S-

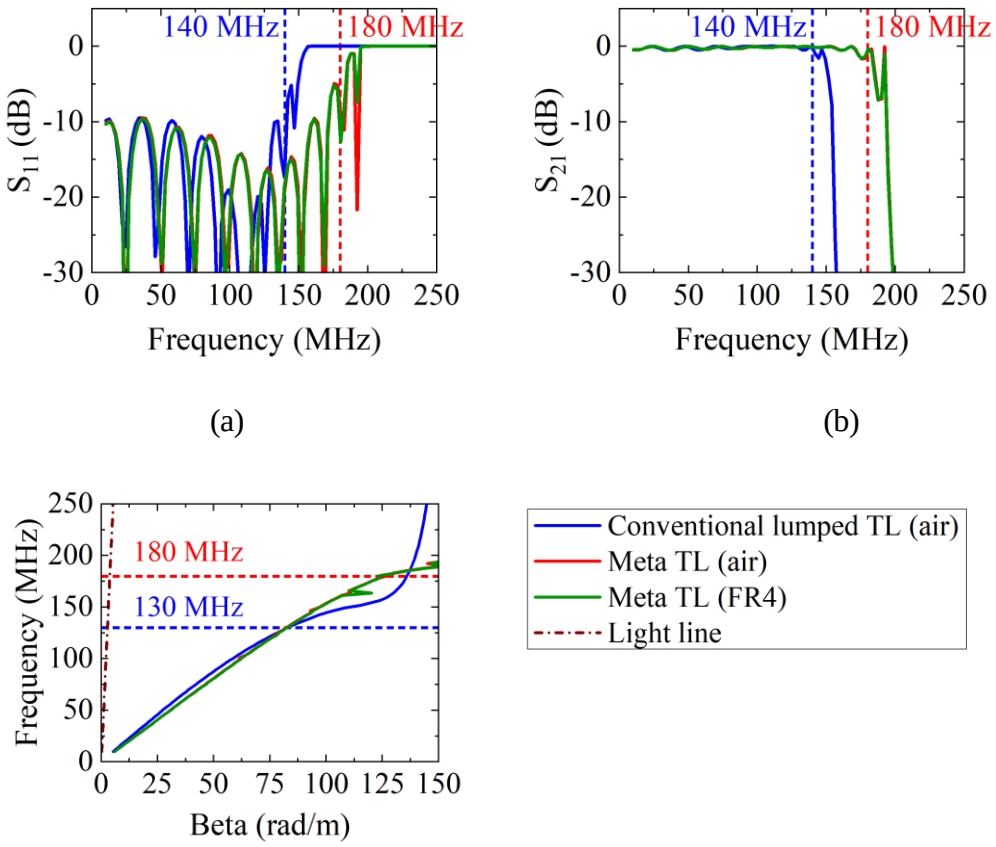

Figure 5.7: Full-wave characterization of the conventional lumped LC ladder and meta-TL structures designed in a 3D electromagnetic solver (Ansys HFSS): (a) S_{11}, (b) S_{21}, and (c) dispersion diagram.

parameters and the dispersion diagrams. At first, the TLs are designed in an air medium, and then a $0.508\,mm$ thick substrate (FR-4: $\epsilon_r = 4.4$) is introduced to effectively investigate the impact of substrate on the meta-TL performance. The results are plotted in Fig. 5.7 (a), (b) and (c), respectively. The S-parameter plots demonstrate that the LC ladder exhibits good passband characteristics up to $140\ MHz$ ($10\ MHz$ more than circuit analysis results), while the meta-TL results are on par with the circuit analysis. However, the dispersion diagram in Fig. 5.7 (c) shows that the LC ladder becomes non-linear around

$130\ MHz$, thereby restricting the dispersion-free frequency range to $130\ MHz$. As such the operational bandwidth is determined as a combination of passband performance and linearity of the structure. Consequently, a similar bandwidth improvement of $\sim 50\ MHz$ (38.5 %) is witnessed with the full wave simulations as well. Further, it should also be noted that the addition of the substrate has virtually no impact on the performance of the meta-TL, as seen from the green curves (meta-TL structure designed in FR-4) in the plots.

5.3 Time Domain Analysis

In this section, the time domain analysis of the designed TL structures is presented. Specifically, the dispersion and delay properties of the proposed 1D meta-TL are examined along with those of the lumped LC ladder and microstrip lines designed in FR-4 substrate. Similar to the previous section, transient simulations are carried out in both a circuit analysis tool (Keysight ADS) and a 3D electromagnetics solver (Ansys HFSS). In the circuit analysis, a $1\ V$ square pulse with a pulse width of $5\ ns$ and a rise time of $0.1\ ns$ was used as the source of excitation to carry out the simulations. The amplitude of the voltage at the output port of the transmission lines are plotted as a function of time to examine the delay achieved, as shown in Fig. 5.8 (a). The $200\ mm$ long meta-TL and the lumped TL are compared with conventional microstrip lines (MSLs) designed in substrates with $\epsilon_r = 4.4$ and 80, as was done on Section 5.2.

A parametric analysis was carried out for MSLs with different TL lengths to determine the exact length of the line required to achieve the delay response obtained from the proposed meta-TL. It can be seen, that the $200\ mm$ MSL (same length as that of the

meta and lumped TLs) does not give enough delay. As such, to achieve similar delay properties, it is necessary to employ a $4\ m$ long MSL designed in a substrate with $\epsilon_r = 4.4$ or a $1.1\ m$ long MSL designed in a substrate with $\epsilon_r = 80$. It should also be highlighted that the circuit simulations do not account for all the losses, especially the increased dielectric losses witnessed with high ϵ_r substrates. As such, even though the length of the microstrip line can be reduced to $1.1\ m$ using a substrate with $\epsilon_r = 80$, there might be additional challenges (attenuation, dielectric breakdown etc.,) that could impact the practical implementation. Nevertheless, the proposed meta-TL structure achieves about $\sim$95 % size reduction compared to the $4\ m$ MSL and $\sim$82 % size reduction compared to the $1.1\ m$ line. Another important observation that can be made from the plots is the presence of dispersion in the lumped TL structure, witnessed by the spreading of the pulse. On the other hand, the dispersion is significantly minimized for the meta-TL which has similar response as the microstrip lines in the entire operating band.

An identical approach was employed to evaluate the time domain behavior in the electromagnetic solver (HFSS). A broadband pulse was used to excite the TL structures and the amplitude of the output voltage obtained from the full-wave simulations are plotted in Fig. 5.8 (b). As with the circuit analysis, it is observed that the delay achieved using the lumped and meta TL structures is on par with the $4\ m$ (with $\epsilon_r = 4.4$) and $1\ m$ (with ϵ_r= 80) MSLs. Additionally, the full wave simulations also confirm that the dispersion can be significantly reduced by employing the proposed meta TLs.

Finally, to compare the slowing down of the wave with respect to the MSL designs, the corresponding group delays are also plotted across the operating bandwidth for all the TLs studied. The plots in Fig. 5.8 (c) show that the $200\ mm$ meta-TL provides a constant

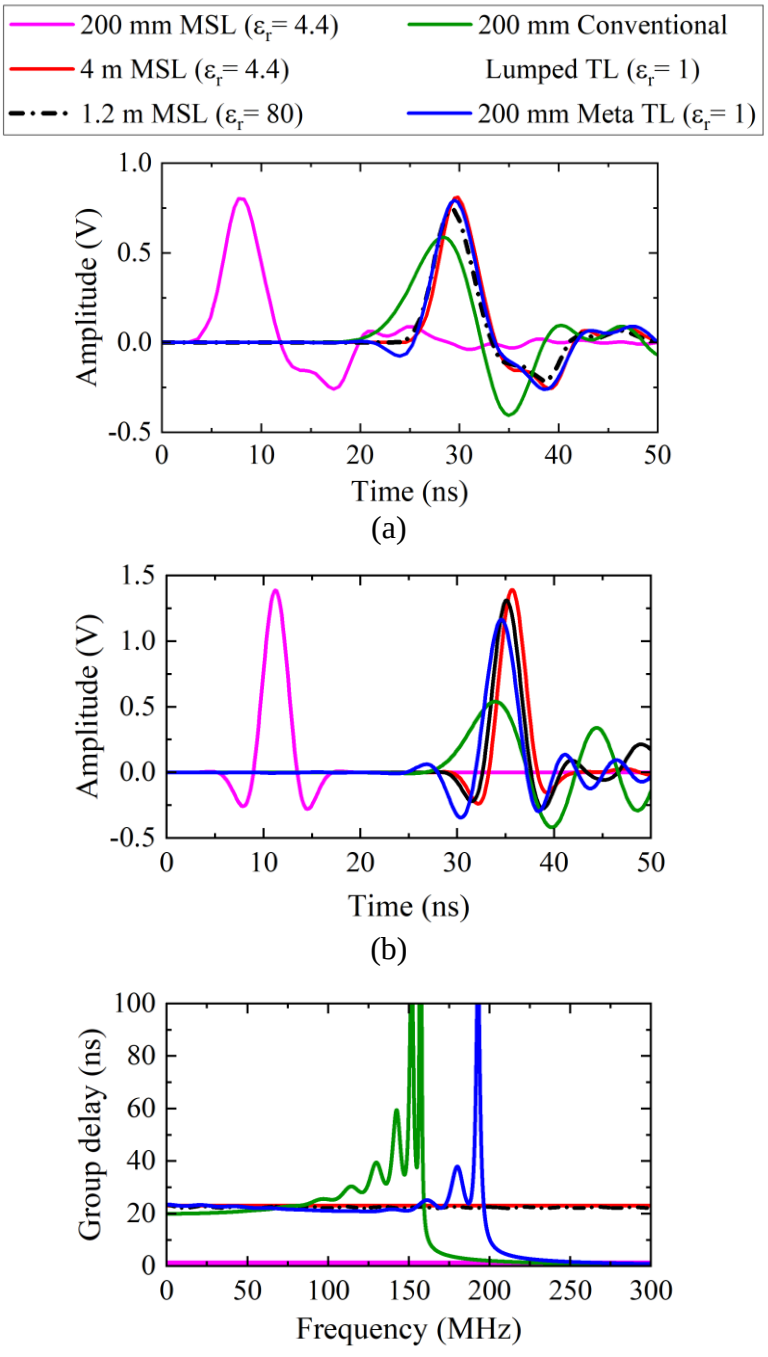

Figure 5.8: Time domain analysis of the TL structures studied in this work: (a) Circuit analysis results depicting the dispersion and delay characteristics of the 200 mm meta-TL to be on par with that of the microstrip lines of lengths 4 m ($\epsilon_r = 4.4$) and 1.1 m ($\epsilon_r = 80$), (b) Full wave simulation results from the 3D electromagnetic solver showing a similar comparison, and (c) group delay plots depicting the slowing down of the wave obtained from lumped TL designs along with the linearity and bandwidth improvement achievable from the meta-TL design.

group delay of $\sim 22\,ns$ which is on par with the $4\,m$ ($\epsilon_r = 4.4$) and $1.1\,m$ ($\epsilon_r = 80$) MSLs. In comparison, the $200\,mm$ MSL only exhibits a group delay of $1.2\,ns$ which corresponds to about 18 times slower wave.

5.4 Characterization of Meta-TL Prototype

The two-wire TL model employed in this work is a balanced line. However, for measurement purposes, the fabricated meta-TL prototype would need to be integrated with a coaxial type connector. Since the coaxial connector is an unbalanced transmission line, it can lead to unintended radiation loss when directly connected to a balanced line. This necessitates the design of a balun to facilitate the transition from the unbalanced coaxial line to the balanced two-wire meta-TL. In this prototype, a simple LC balun is chosen owing to its ease of design, fabrication, and minimal space requirements.

5.4.1 Balun Design

The schematic of the LC balun used in this work is shown in Fig. 5.9 (a). The inductor and the capacitor values of the balun are obtained using the following equations.

$$X = \sqrt{Z_{balanced} \cdot Z_{unbalanced}} \tag{5.2}$$

$$L_{balun} = \frac{X}{\omega_c}; \qquad C_{balun} = \frac{1}{X\omega_c} \tag{5.3}$$

where

X is the geometric mean of the impedances of the balanced ($Z_{balanced}$) and unbalanced ($Z_{unbalanced}$) sections of the meta-TL with balun and

ω_c is the cut-off frequency

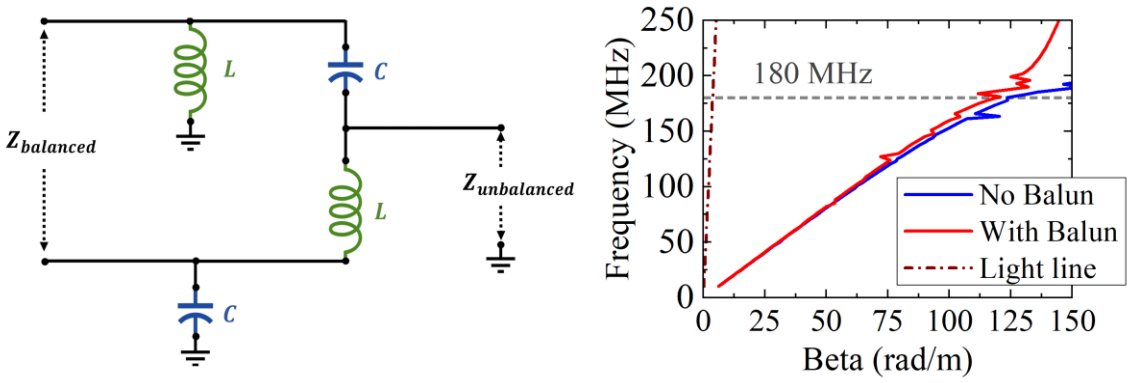

(a) (b)

Figure 5.9: (a) Circuit model of the LC balun employed to connect the two-wire meta-TL (balanced section) to an SMA (sub-miniature A) connector (unbalanced) and (b) dispersion diagram plots demonstrating that the balun does not adversely affect the linear region and bandwidth of the meta-TL.

The balun inductance was obtained to be $47\ nH$ and the capacitance $25\ pF$. The balun design was also first carried out in ADS, and it was found that the dispersion diagram stays linear throughout the frequency range while S_{11} stays below $-18\ dB$ and S_{21} at $\sim 0\ dB$. Additionally, two baluns were put back-to-back to evaluate the effect on S-parameters and dispersion diagrams. It was again verified that the dispersion diagram stays linear throughout the frequency range of interest. The return loss stays below $-10\ dB$, while the insertion loss is above $-2\ dB$ in this frequency range. Further, the balun design was also included in the 3D electromagnetic model of the meta-TL, and the composite effect of the structure on the dispersion diagram was verified. The dispersion diagram plots shown in Fig. 5.9 (b) confirm that the inclusion of balun does not adversely impact the linearity of the line or its passband behavior. As such, the dispersion-free frequency range is maintained at $180\ MHz$ for the meta-TL with a balun.

5.4.2 Loss Characterization

The 3D electromagnetic model of the optimized meta-TL structure with balun is shown in Fig. 5.10 (a) and (b). Microstrip environment is chosen to implement the balun to facilitate the feeding using a $50\,\Omega$ edge mount SMA (sub-miniature A) connector (Amphenol RF 132357-11). To evaluate the effect of actual component losses, additional simulations were carried out where the ideal components were replaced with real-world components, and the results are presented in Fig. 5.10 (c) and (d). Particularly, the impact of substrate losses (FR-4: $\epsilon_r = 4.4,\ tan\delta = 0.002$) and ohmic losses due to DC resistances of the inductors are characterized. The DC resistances were obtained from the component datasheets and included in the simulation model employing lumped RLC boundary conditions in HFSS. Additionally, to investigate the losses introduced by the SMA connector, a 3D HFSS model of the SMA connector was also imported from the supplier website.

It was noticed that the S_{21} monotonically decreases across the frequency range with the introduction of losses. The S_{11} and S_{21} plots of Fig. 5.10 (c) and (d) show that for the lossless meta-TL, the insertion loss stays around $0\ dB$ for the entire dispersion-free frequency range. On the other hand, the S_{21} of the meta-TL with ohmic and substrate losses reduces to $-3.2\ dB$, while that of the meta-TL with losses + SMA connector reduces to $-3.6\ dB$. However, the impact on S_{11} is minimal, with S_{11} staying below $-10\ dB$ up to cut-off, as seen in Fig. 8 (c). It was found that the DC resistance of the high inductance series inductors primarily results in the lowering of S_{21}. Consequently, the $8\ dB$ bandwidth ($|S_{21}| - |S_{11}|$) of the meta-TL is reduced to $155\ MHz$ due to the losses. A similar impact is also witnessed on the lumped TL structure. In fact, the losses are more pronounced due to increased number of

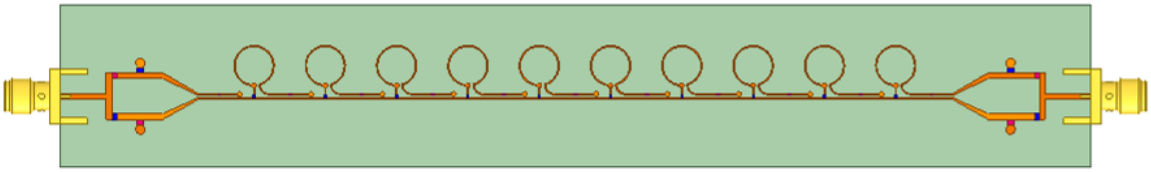

(a)

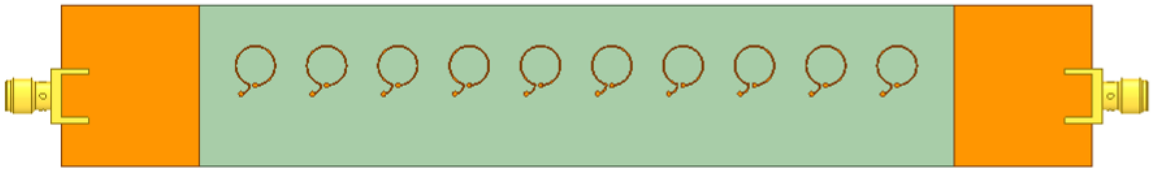

(b)

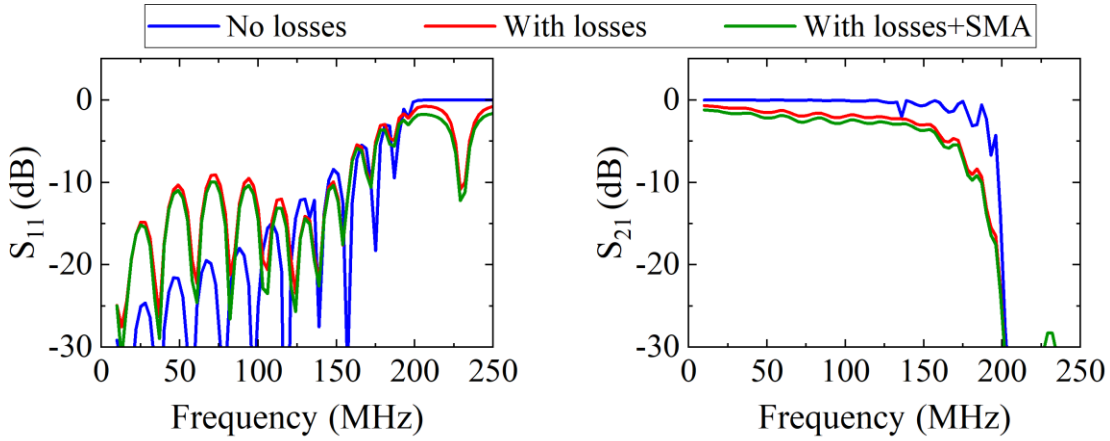

(c) (d)

Figure 5.10: Full wave simulation model of the 1D meta-TL designed on an FR-4 substrate with SMA connectors used for excitation: (a) top view and (b) bottom view, (c) S_{11}, and (d) S_{21} plots characterizing the effect of various losses that lead to degradation of meta-TL performance.

series chip inductors. As such, although the useable frequency range is reduced, the overall bandwidth improvement due to the meta-TL does not change. Further, it should be noted that these additional losses might not be present in the actual 2D implementation of the meta-TL wave space as no baluns and SMAs would be needed there. Nevertheless, these losses have

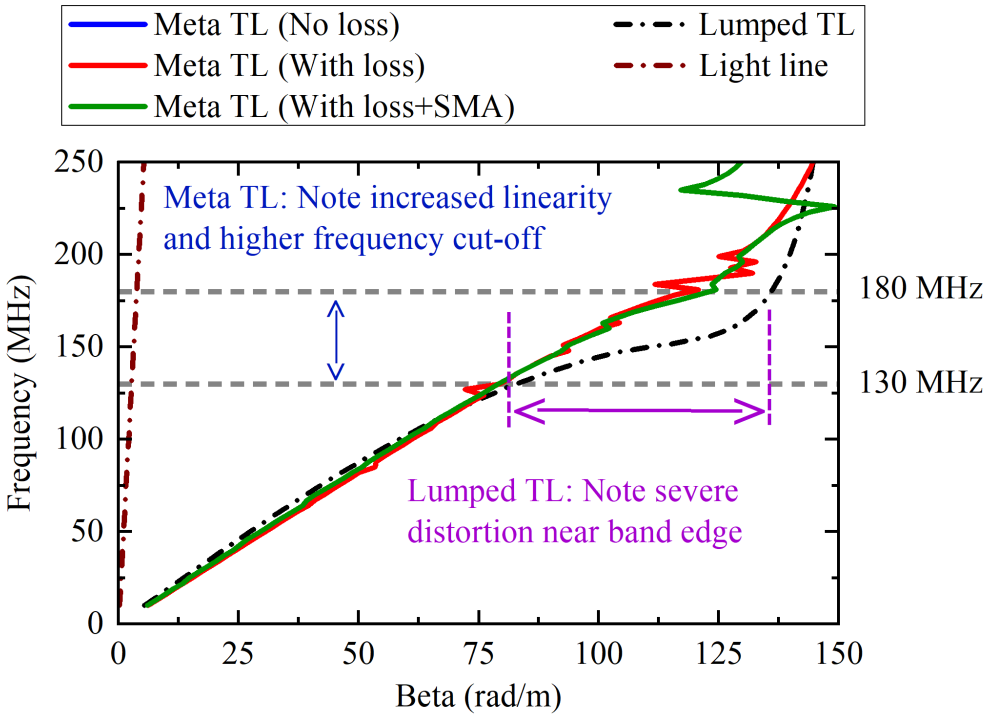

Figure 5.11: Dispersion diagram plots demonstrating the improvement of the dispersion free frequency range with meta-TL.

minimal impact on the dispersion diagram, as seen in Fig. 5.11, where the linear region is still up to 180 MHz for the designed meta-TL. On the other hand, as expected, the dispersion-free frequency range of the conventional lumped LC ladder stays restricted to 130 MHz.

5.4.3 Meta-TL Fabrication and Characterization

The 3D electromagnetic model of the meta-TL was exported into Altium designer to generate the Gerber and assembly files needed for fabrication. The meta-TL was fabricated on a 0.508 mm thick FR-4 substrate using a standard two-layer printed circuit board (PCB) manufacturing process. The fabricated prototype was characterized using a vector network analyzer (VNA) through two-port S-parameter measurements. The prototype, along with the

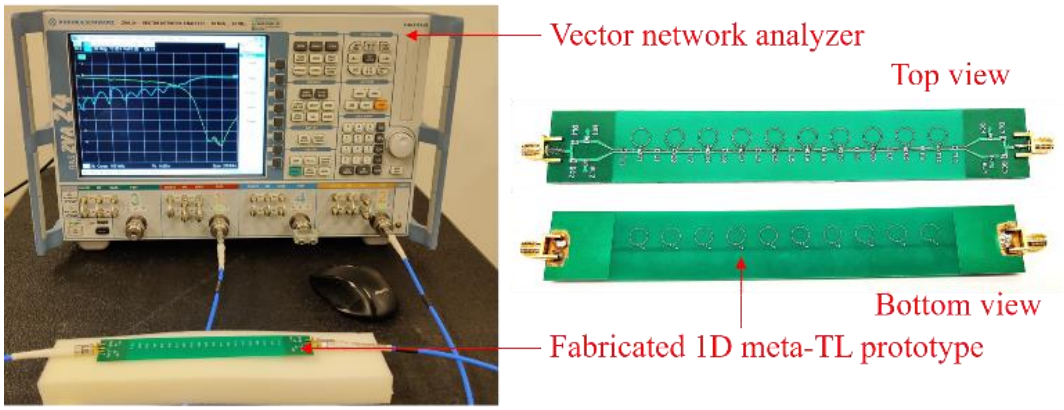

Figure 5.12: Fabricated meta-TL with the measurement setup.

measurement setup used to characterize the meta-TL, is shown in Fig. 5.12. The measured S-parameters are compared with the simulation model with all the losses in Fig. 5.13 (a) and the dispersion diagram plots are compared in Fig. 5.13 (b). A good agreement is seen between the two. Although measurements show a lower S_{21} near the cut-off frequency (about $-5.4\ dB$ as compared to $-3.6\ dB$ in simulations), the return loss also gets lowered by about $2\ dB$ in the measurements and stays below $-11\ dB$, thus maintaining the overall usable frequency range at $155\ MHz$. The additional $2\ dB$ of losses witnessed in the measurements could be attributed to the accuracy of modeling the SMA connectors and the lumped elements (no tolerances considered) used in HFSS, as well as fabrication uncertainties. It should also be noted that by using lower values of series inductances (especially in baluns), the losses could be significantly reduced.

5.5 Conclusion

In this chapter, a 1D meta transmission line design is presented, which can be employed to improve the time delay properties by achieving a slowdown factor of 18 and

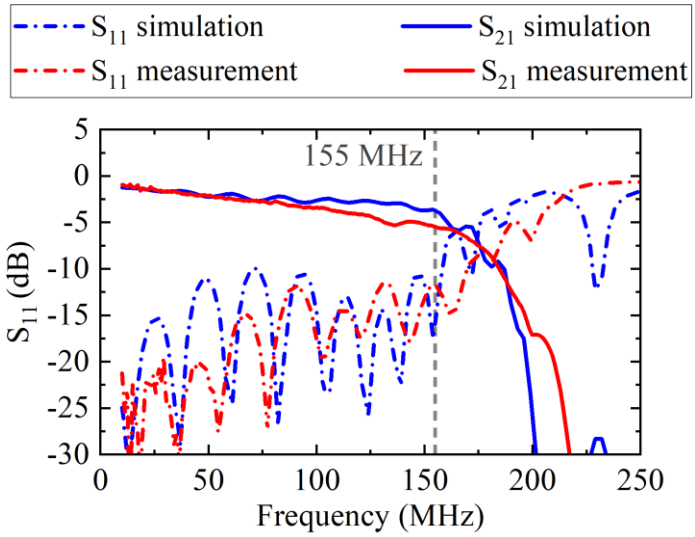

(a)

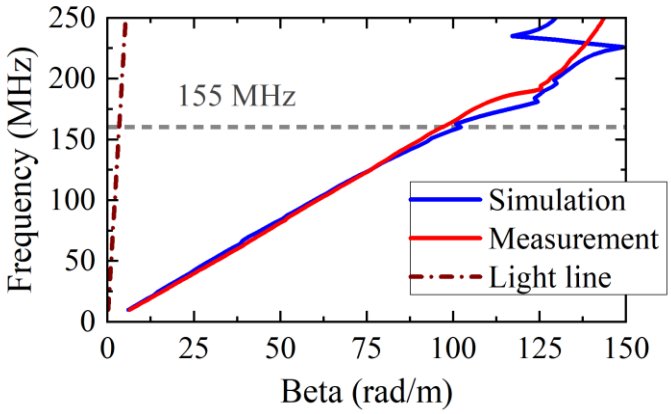

(b)

Figure 5.13: Comparison of simulation and measurement results of the designed meta-TL prototype demonstrating good performance up to cut-off. (a) S-parameter results and (b) dispersion diagram.

an overall bandwidth improvement of about 40 %. Consequently, it is possible to deploy such solutions minimize the space requirements for the low-frequency implementations of true time delay (TTD) beamformers. Specifically, by incorporating mutual inductance between the first nearest neighbors in the conventional TL model, dispersion-free

frequency range was shown to be extended up to the cut-off frequency. Both circuit and full-wave electromagnetic analyses are presented to demonstrate the ability of the proposed technique to improve the linearity of the dispersion diagram. Additionally, time domain analysis was utilized to demonstrate the slowing down of the signal within the meta-TL. A prototype was also fabricated to evaluate the performance of the meta-TL, and a good agreement is achieved between the simulations and the measurements. Consequently, by introducing the mutual inductance, a bandwidth improvement of approximately $50\ MHz$ is realized. Future works will focus on the design and development of 2D meta-TL wave spaces that could be used to realize hyper-compact Rotman lenses for dynamic TTD beamforming applications.

CHAPTER 6

METASURFACES FOR RADIO FREQUENCY BASED GESTURE SENSING

6.1 RF Gesture Sensor Development for Human Computer Interaction

Hand gestures have been integral parts of non-verbal communication throughout human history to elegantly convey information with little effort. As such, there has been an increasing interest in recent years to adopt this mode of information delivery to interact with machines. The design and development of touchless interaction systems have garnered a lot of interest in the past few years, particularly gesture-based interaction. Gesture recognition forms an integral part of human – computer interaction (HCI) technologies that deal with recognizing various movements of the human body and interpreting them as commands to interact with a machine. Specifically, different hand motions could be associated with gestures that can be interpreted by a computer as commands to carry out specific tasks. Such hand gesture recognition techniques using wearable devices finds prominent applications in the fields of robotics, medicine, sign language detection, augmented/virtual reality, gaming, [157] etc., as shown in Fig. 6.1.

Several gesture recognition techniques in different regions of the frequency spectrum ranging from acoustics to optical frequencies have been developed with the key objectives of achieving better accuracy, ease of usage, low- power and cost, and miniaturization suitable for commercial wearable devices. While some of the vision-based methods have reached a mature state and demonstrated very good accuracies (> 90%), the usage can be limited in conditions with strong ambient lighting and in cases when obstacles are present in the field-of-view. Microsoft Kinect and Leap Motion controllers that use 3D

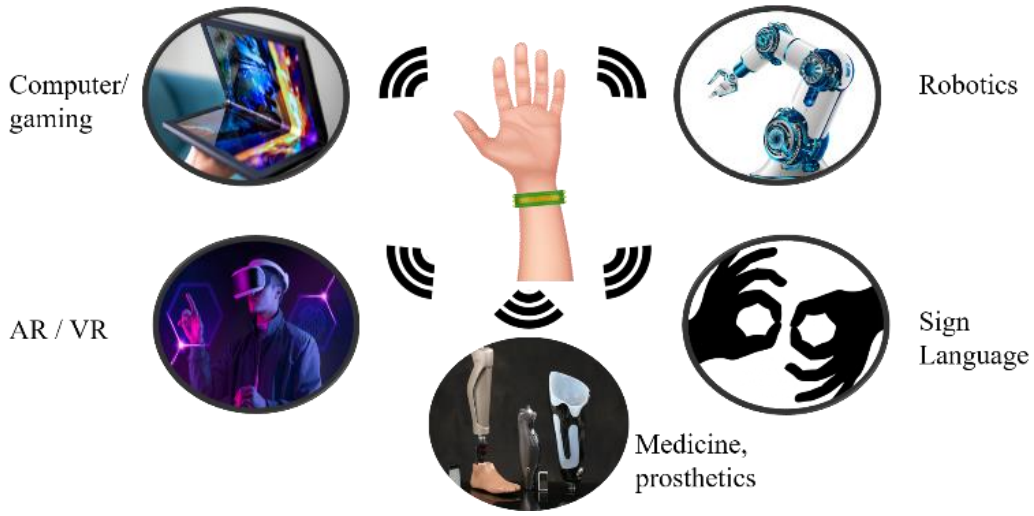

Figure 6.1: Applications of wearable gesture sensors.

cameras form the examples of this method. On the other hand, the techniques based on radars, electromyography (EMG), ultrasound, and optics, use sensors that can be directly attached to hands/ fingers using electrodes, antennas, gloves, etc., and extract information using electromechanical methods. They have been shown to successfully solve most of the issues experienced by vision-based methods. But, they do come with their own unique challenges such as the drifting of the sensor position, sensitivity to the type of skin, sweat, environmental interferences, etc., all of which reduce the accuracy of the gesture recognition. Additionally, the techniques based on ultrasound are still bulky and power consuming to be adopted for wearable devices.

From the gesture interpretation perspective, while most of these techniques can faithfully capture motion-specific information, there is usually an additional block needed to associate the obtained data to individual gestures, and this is typically achieved through machine learning algorithms. Thus, any gesture sensor primarily consists of two elements – a signal detection block and a classification block. With an increase in the number of

wearable electronics, the focus on the development of wearable gesture sensors has also expanded.

In this work, radio frequency (RF) based gesture sensing technique is proposed that uses microwave signals to illuminate the human hand and extract the gesture related information from changes within the hand resulting from various motions. At first, a single open-waveguide based sensor is developed to evaluate the validity of the proposed idea. Then a substrate integrated waveguide leaky-wave antenna (SIW-LWA) based sensor prototype is developed to improve the sensitivity of gesture recognition. Further, the ability of the proposed gesture sensor to solve some of the shortcomings in the existing state-of-the-art gesture sensors –such as– sensitivity to skin color, rapid hand movements, and other environmental interferences, is also evaluated. The proposed approach also has excellent potential to be integrated with machine learning algorithms for efficient and automated gesture sensing.

6.2 Single Probe Sensitivity Analysis

This section presents the operating principles of the proposed gesture recognition technique. Human hand has several different tissues (tendons, blood vessels, nerves, muscles, bones, etc.,), the anatomy and relative positions of which can change when a person performs different hand/ finger motions. As it has been shown with other gesture recognition methods, the anatomy of the wrist can provide unique information for several hand-gestures. Here, the goal is to understand how sensitive RF signals are in recognizing the correct gestures by discerning the backscattered signals emanating from the wrist area. To examine this hypothesis, air-filled open rectangular waveguides operating in C, X, and

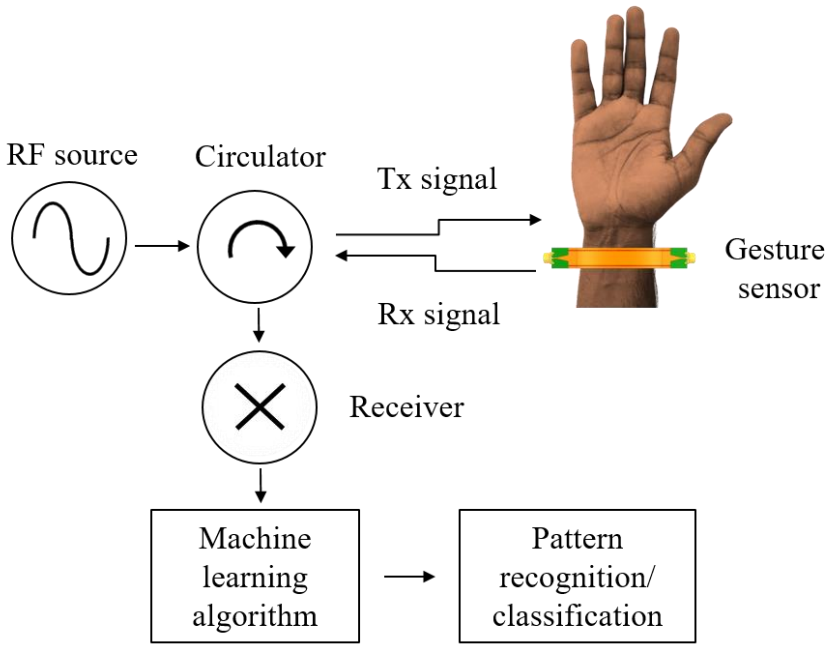

Figure 6.2: Working principle of the proposed gesture sensor.

Table 6.1: Dielectric constants of the wrist anatomy [158]

Component	Blood	Muscle	Tendon	Skin	Nerve	Bone	Fat
ϵ_r	40.2	38.8	25	28.3	21.5	7.3	8.16
σ [S/m]	18.1	15.1	13.6	11.6	8.37	2.77	2.35

Ku bands are used to couple the electromagnetic energy into the wrist. The backscattered signals from various tissues within the wrist are recorded using a circulator and an RF receiver. This data is used as input to a simple gesture classification method that identifies and classifies the gestures. The proposed measurement framework is depicted in Fig. 6.2.

6.2.1 Simulation with a Wrist Model

To understand the near-field radiation behavior of the open waveguide and its sensitivity to various micro-motions of the tissues within the wrist, an approximate wrist cross-section model is developed. The permittivities of different tissues are assigned

following the recommendations in [158]. As seen in Table I, the relative permittivities vary significantly for different tissues. Since the waveguide is air-filled, a poly-vinyl chloride (PVC) matching layer is used to reduce the mismatch loss between the waveguide and wrist. The thickness of the PVC layer was optimized using parametric analysis and found to be approximately 6.5 mm. The designed wrist model along with the waveguide in Ansys HFSS is shown in Fig. 6.3 (a). The S_{11} plots obtained for C, X, and Ku band waveguide probes are shown in Fig. 6.3 (b) which demonstrate a good coupling into the wrist. Further, full-wave simulations were also carried out to verify the coupling into the wrist model and an exemplary comparison at C-band is shown in Fig. 6.3 (c). Similar agreement between simulations and measurements were obtained in all the 3 frequency bands, however, for brevity, only the evaluation results in C-band are presented.

6.2.2 Sensitivity Measurements

Four gestures (labeled G1 to G4), as shown in Fig. 6.4 (a), are used to verify the gesture recognition accuracy of the proposed idea. The measurement setup used to characterize the probe sensitivity is shown in Fig. 6.4 (b). The rectangular waveguide is excited by a continuous wave signal from a vector network analyzer (VNA), and the other end is used to couple the electromagnetic signals into the wrist. The waveguide is mounted on a fixture to keep it steady. As with simulations, a 6.5 mm thick PVC sheet is used to improve the matching between waveguide and skin. The RF signals from the open end of the waveguide illuminate the wrist, and the reflected signals for each gesture are recorded (S_{11} parameter from the VNA). At first, the S_{11} of all the four gestures are recorded which forms the reference gesture data.

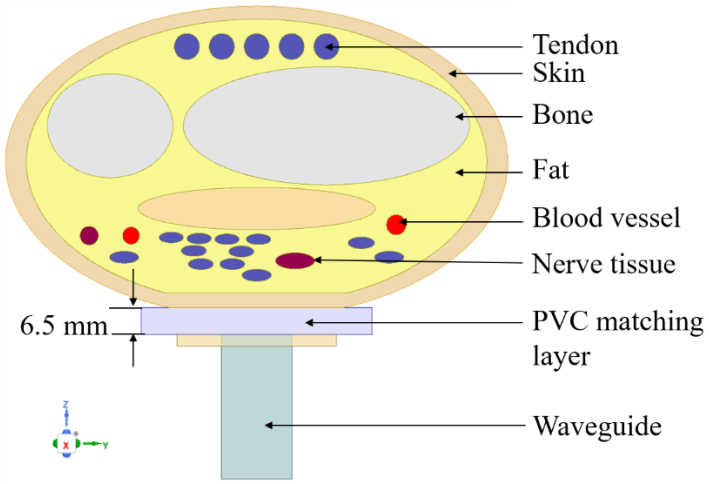

(a)

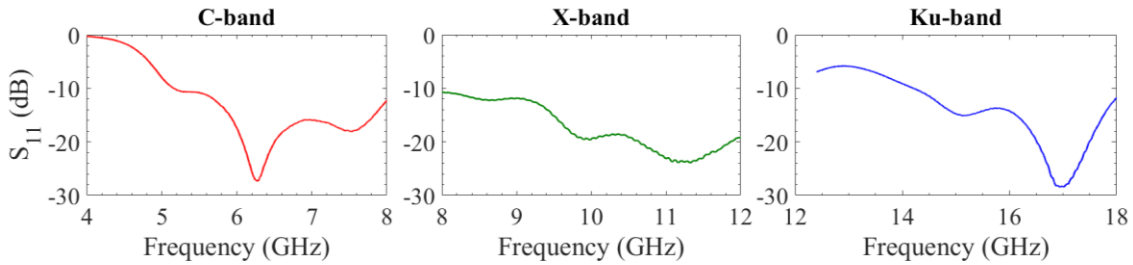

(b)

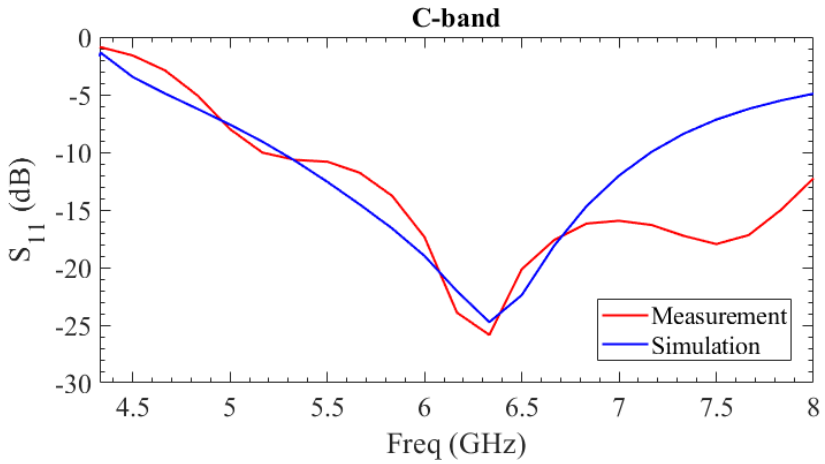

(c)

Figure 6.3: (a) Simulation setup used for verifying the sensitivity of the waveguide to tissue motions, (b) S_{11} plots obtained from real world measurements at C-, X-, and Ku- bands depicting good coupling into the wrist, and (c) S_{11} plots at C-band comparing the simulations results with approximate wrist model to the real-world measurements.

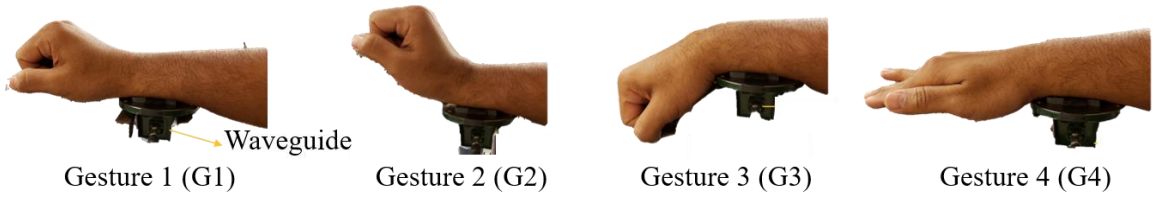

(a)

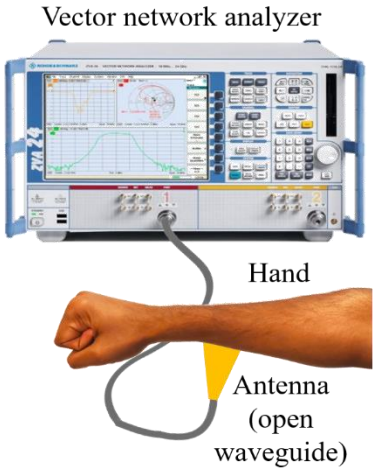

(b)

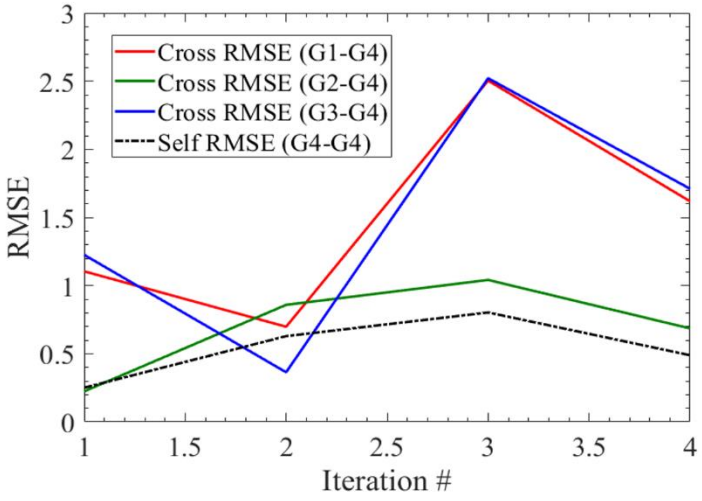

(c)

Figure 6.4: (a) Four different gestures used to validate gesture sensing technique, (b) single antenna measurement setup used for tissue characterization, and (c) RMSE values showing the self-RMSE of gesture 4 to be lower than cross-RMSE values.

For gesture classification, root mean square error (RMSE) is employed as the metric to identify the gesture performed by the user. Every measured gesture G^m is compared with all the reference gestures and the RMSE is calculated using

$$RMSE = \sqrt{\sum_{i=1}^{N} \frac{(G^{p,ref}(i) - G^m(i))^2}{N}} \tag{6.1}$$

where

$G^{p,ref}$ is the p^{th} reference gesture ($1 \leq p \leq 4$) and N is the total number of frequency points

A low value of the resulting RMSE is an indication of a good match between the measured gesture G^m and the corresponding reference gesture. The reference gesture with the lowest RMSE is classified as the hand gesture. Fig. 6.4 (c) shows an example case with the RMSE of gesture 4 across all the 4 iterations, as compared to the reference gestures. In this plot, the RMSE values (G1:G3-G4) are seen to be generally higher than the self RMSE (G4-G4) values. As such, the gesture is classified as G4. Comparable results were obtained for remaining three gestures. Overall, during a series of similar measurements using this simple waveguide-based approach, an average gesture recognition accuracy of about 60 % was achieved.

6.3 Sensitivity Analysis with Substrate Integrated Waveguide Leaky-wave Antenna

Motivated by the positive results obtained from the single probe sensitivity analysis, a more robust sensor was developed based on SIW-LWA. This section presents the design and analysis of SIW-LWA gesture sensor. The LWA is employed to couple the electromagnetic energy into the human wrist. The LWAs are suitable for planar architectures and exhibit inherent frequency scanning capabilities, which form the major motivations for choosing them as the radiating elements of the sensor. Moreover, such sensors can be fully passive with ultra-low power consumption and hyper-compact architectures, making them well-suited for integration with smartwatches and wristbands. On the other hand, the patch and dipole-based array designs would require some active element (PIN diodes, transistors etc.,) to achieve beamscanning. This would increase the size, cost, as well as power requirements, which are extremely important for portable sensor designs.

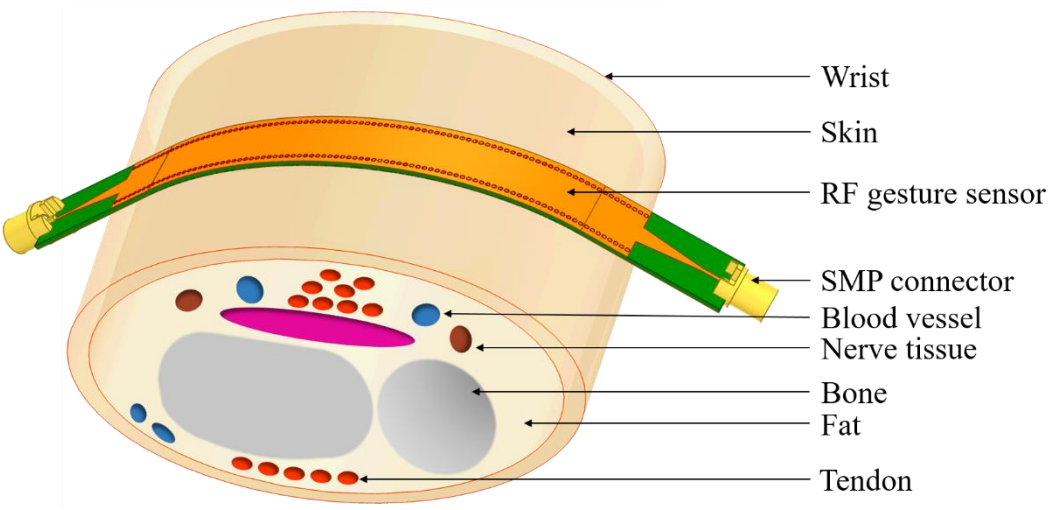

Figure 6.5: Designed SIW-LWA gesture sensor with an approximate model of the wrist anatomy.

The operating principle of the proposed gesture sensor is shown in Fig. 6.2. The SIW-LWA is excited by a continuous wave (CW) RF source through a subminiature push-on (SMP) connector. The RF signals propagate along the SIW and leak into the wrist tissues through the slots along the SIW. The reflected signals from different tissues within the wrist (tendons, blood vessels, nerves, muscles, bones, etc.) are recorded using a coupler and an RF receiver. When a user performs various gestures, the hand and finger motions change the relative positions of the tissues within the wrist, thus providing unique information corresponding to each gesture. The simplified 3D model of the human wrist with representative tissues shown in Fig. 6.3 (a) is again used to carry out the simulations. The cross-section of the human wrist with the sensor mounted on the anterior side (sensor on top with the palm facing up) is shown in Fig. 6.5. The primary goals of this research were to evaluate the ability of the proposed sensor to effectively couple the electromagnetic signal into the human hand as well as to determine the sensitivity improvement that can be achieved when compared to single antenna designs.

6.3.1 Substrate Integrated Waveguide Design

In this work, a substrate integrated waveguide environment is chosen for designing the leaky-wave antenna. The waveguide-based design offers the advantages of broadband operation, low losses, high thermal and power handling capabilities, and isolation. However, the traditional metallic waveguides pose certain challenges in terms of difficulty in integration with planar circuitry and flexible architectures. On the other hand, SIWs are compatible with standard PCB manufacturing processes, while preserving the characteristics of metallic waveguides. Moreover, they are also well-suited for miniaturization at microwave and mmWave frequencies, making them advantageous for compact sensor designs targeted in this work.

The SIW is designed in a $0.508\,mm$ thick flexible Rogers RO3010 substrate ($\epsilon_{r\_sub} = 10.2, tan\delta = 0.0022$). The Rogers RO3010 substrate was selected due to its flexible nature which makes it suitable to be curved and mounted on the wrist (with the proper fixture support). Further, the thickness of the substrate was chosen to be small to ensure that the radius of curvature is within the fracture limits. Since, this SIW utilizes an array of via to create a via wall, large radii of curvature can increase the stress on the metal leading to cracks both along the metal as well as the substrate. The SIW is designed to operate in the dominant TE_{10} mode with a cut-off frequency of 8.2 GHz. The width of the SIW w_{siw}, is obtained using [159]

$$w_{siw} = w_{rwg} + \frac{d^2}{0.95p} \tag{6.2}$$

where

d is the diameter of the vias

p is the spacing between the vias

w_{rwg} is the width of the corresponding rectangular waveguide, which determines the cut-off frequency, f_{c_10} according to

$$f_{c\_10} = \frac{c}{2\pi w_{rwg}\sqrt{\epsilon_{r\_sub}}} \tag{6.3}$$

The SIW was modeled in the 3D electromagnetic solver Ansys HFSS, as shown in Fig. 6.6 (a). At first, perfect electric conductor (PEC) boundary conditions were used to model the metals (top layer, bottom layer and vias) of the waveguide and then the metals were modeled as $1\,oz$ Copper to get a more realistic representation of the SIW performance. The S_{11} and S_{21} are plotted as a function of frequency in Fig. 6.6 (b). The measurement results of Fig. 6.3 (b) show that good signal penetration can be achieved in the $4-18$ GHz band. However, to design the SIW-LWA to be suitable for compact wristband systems, the antenna is targeted to operate in the combined X-band and Ku-band As such, the reflection and transmission behavior of the waveguide are verified in this frequency span. As expected, the dominant TE_{10} mode within SIW starts propagating around the cut-off frequency of 8.2 GHz. Further, the plots also demonstrate good reflection and transmission properties, with the S_{11} staying below -10 dB and S_{21} maintaining a flat response with a magnitude < 2 dB in the entire frequency range of interest. It must also be noted that a slight degradation in S_{21} is observed when going from PEC (-1.31 dB) to $1\,oz$ Copper (-1.79 dB), which is expected due to the finite conductivity of Copper.

(a)

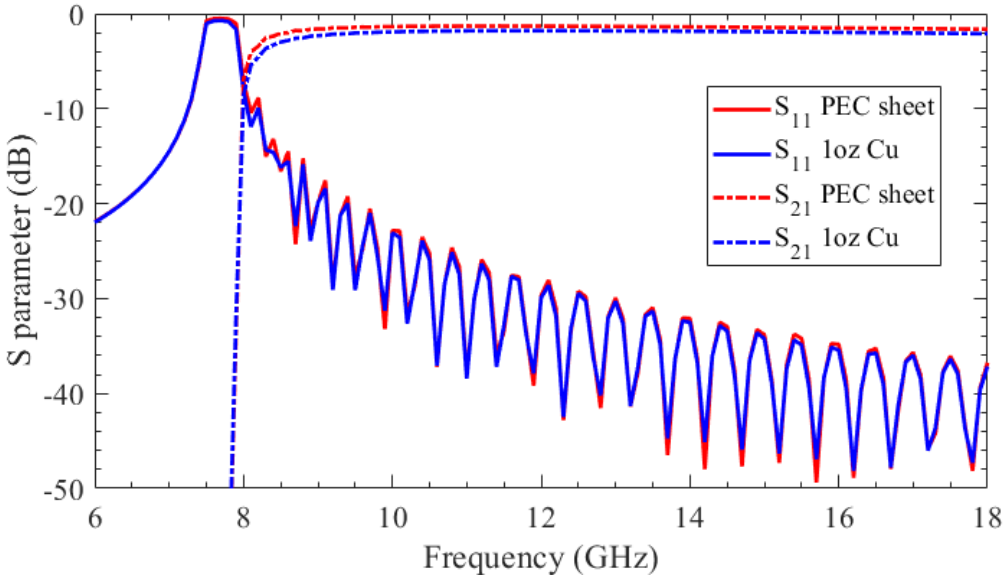

(b)

Figure 6.6: (a) Full wave simulation model of the planar SIW designed in a 3D electromagnetic solver showing top (top) and side (bottom) views and (b) S-parameter plots depicting the performance of the designed SIW.

To characterize the SIW-LWA, it needs to be connected to a VNA, and since coaxial connectors are usually employed for this purpose, a transition needs to be designed to go from SIW to coaxial environment. An SIW to microstrip transition is designed in this work to accomplish this in a planar PCB structure. With the goal of achieving a compact sensor design, SMP connectors were chosen, which offer the advantage of lower space requirement when compared to the conventional SMA connectors. The SIW to MSL transition is designed by modeling the MSL with an equivalent TEM waveguide [160].

The width of the TEM waveguide w_e can be found to be [160]

$$\frac{1}{w_e} = \begin{cases} \frac{60}{\eta_0 h} \ln\left(8\frac{h}{w_{taper}} + 0.25\frac{w_{taper}}{h}\right) & \frac{w}{h} < 1 \\ \frac{120\pi}{\eta_0 h \left[\frac{w_{taper}}{h} + 1.393 + 0.667 \ln\left(\frac{w_{taper}}{h} + 1.444\right)\right]} & \frac{w}{h} > 1 \end{cases} \tag{6.4}$$

where

$\eta = \sqrt{\frac{\mu_0}{\epsilon_0}}$ is the free space intrinsic impedance

h is the substrate thickness

w_{taper} is the width of the tapered transition

Further, curve fitting techniques were used [160] to find the relation between the equivalent MSL width w_e and the SIW width w_{siw} as

$$\frac{1}{w_e} = \frac{4.38}{w_{siw}} e^{-0.627\frac{\epsilon_{r\_sub}}{\epsilon_e}} \tag{6.5}$$

where

ϵ_{r_sub} is the dielectric constant of the substrate, and

$$\epsilon_e = \frac{\epsilon_r + 1}{2} + \frac{\epsilon_r - 1}{2}\left(\frac{1}{1 + \frac{12h}{w_{taper}}}\right) \tag{6.6}$$

By equating (6.5) and (6.6) and solving for w_{taper}, the optimum taper width could be obtained. Although the model does not account for capacitive effects the transition between SIW and MSL taper, it can still be employed to obtain fairly accurate S-parameter results. As such, the dimensions obtained from the analytical equations are used as the starting points for designing the SIW in a 3D electromagnetics solver, and parametric

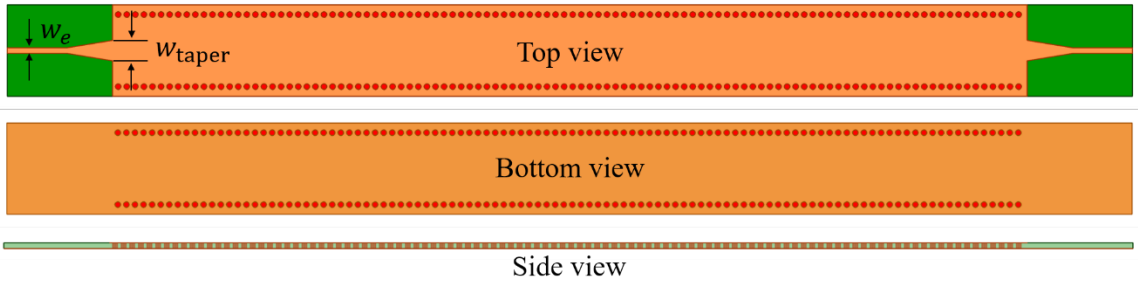

(a)

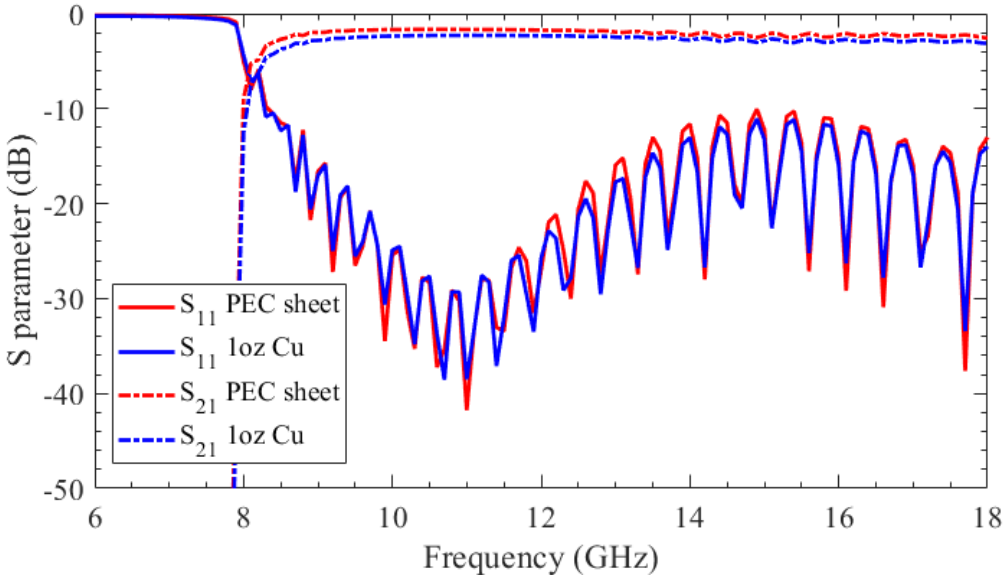

(b)

Figure 6.7: (a) Full wave simulation model of the planar SIW with MSL transition designed in a 3D electromagnetic solver showing top (top) and side (bottom) views and (b) S-parameter plots depicting the performance of the designed SIW.

analysis is utilized to obtain the optimum design parameters. Such an optimized design from Ansys HFSS is depicted in Fig. 6.7 (a), where the top view of the SIW shows the designed transition. Full wave simulation results in Fig. 6.7 (b) shows that the S_{11} stays below -10 dB in $8-18$ GHz frequency range with S_{21} better than -2.5 dB. Moreover, a comparison of the designs with and without the transition reveals that the SIW-to-MSL

transition leads to only about 0.5 dB degradation in the transmission properties of the waveguide (-1.79 dB for SIW with 1 oz Copper but no transition; -2.3 dB for SIW with 1 oz Copper and with transition).

Finally, to evaluate the performance of the curved SIW, the design on conformed to the radius of the wrist model developed in Section 6.2 and simulations are carried out. The curved SIW model is shown in Fig. 6.8 (a). The S-parameters plotted in Fig. 6.8 (b) show that the curvature has minimal impact on the performance of the SIW, with good reflection and transmission properties. In fact, the curved design exhibits slightly better insertion loss as witnessed by S_{21} better then -1.3 dB.

6.3.2 SIW-LWA Design

In this work, two types of LWAs are designed and analyzed – a uniform LWA and a periodic LWA. The uniform LWA is designed with a single long slot as shown in Fig. 6.9 (a) – top. The length of the slot is designed such that it is completely exposed to the skin. The width of the slot is $W \approx \lambda_0/20$, where λ_0 is the wavelength in the radiation medium (wrist). On the other hand, the periodic LWA shown in Fig. 6.9 (a) – bottom, is designed as an array of slots with length, $L \approx \lambda_0/2$ and width, $W \approx \lambda_0/20$. The slots are arranged on either side of the central axis of the waveguide a period p of $\lambda_g/2$ between the slots, where λ_g is the wavelength within the substrate. Again, care is taken to ensure that the radiating aperture is conformal to the surface of the wrist model. The bottom view of both the uniform and periodic LWAs is shown in Fig. 6.9 (b). The SIW-to-MSL transition is moved to bottom surface of the SIW- LWA to avoid any radiation leakage appearing at the transitions from coupling into the wrist. As the tissues within the wrist

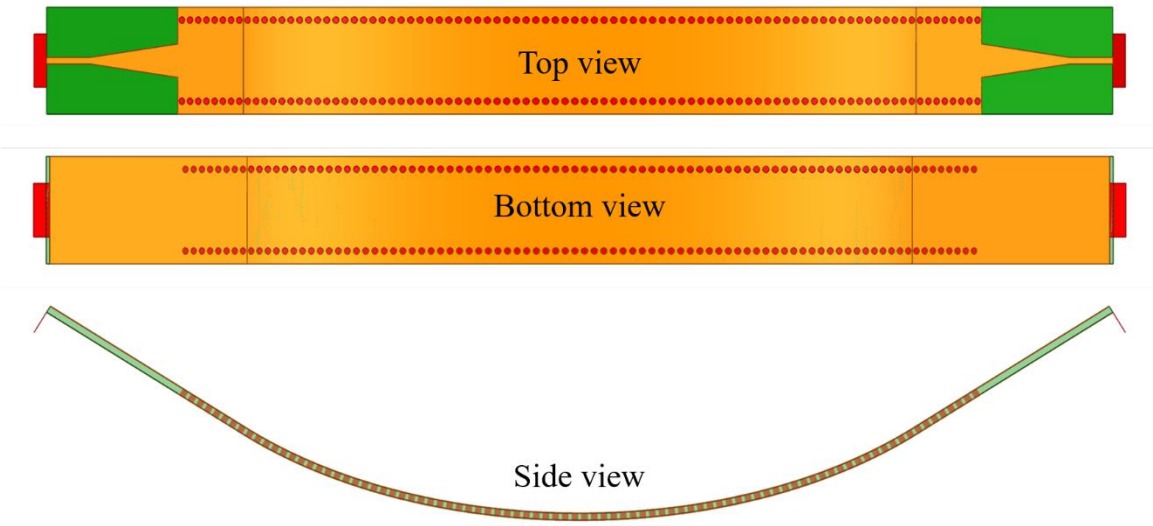

(a)

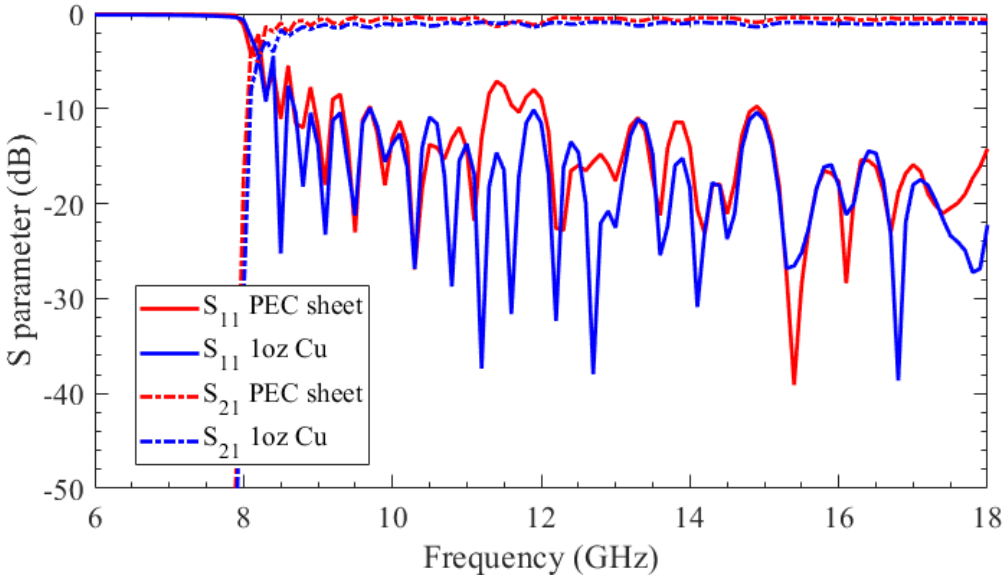

(b)

Figure 6.8: (a) Full wave simulation model of the curved SIW with MSL transition designed in a 3D electromagnetic solver showing top (top) and side (bottom) views and (b) S-parameter plots depicting the performance of the designed SIW.

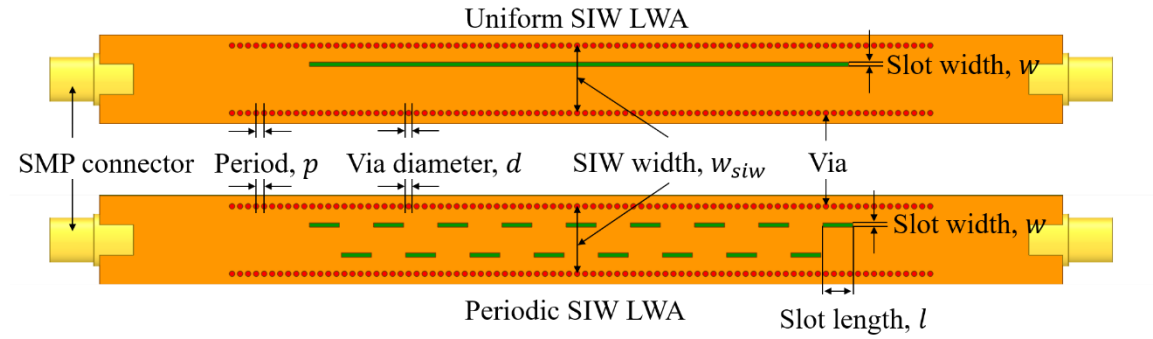

(a)

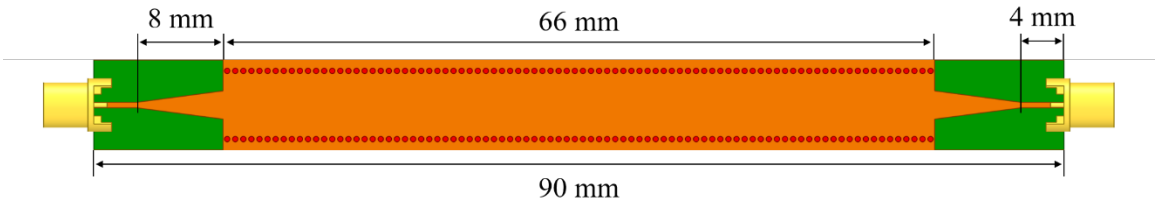

(b)

Figure 6.9: Full wave simulation models of the uniform and periodic SIW-LWAs designed in this research: (a) top view and (b) bottom view.

Table 6.2: Gesture Sensor Design Parameters

Variable	w_{siw}	w_{rwg}	L	W	d	p
Value [mm]	6.3	5.9	2.8	0.4	0.5	0.75

have a wide range of variation ($\epsilon_{r\_medium} = 53$ to 5), an average $\epsilon_{r\_medium} = 25$ is chosen to design the LWA slots. The period, offset, and the length of the slots are optimized using HFFS to achieve the desired radiation performance within the wrist environment and to tailor the attenuation constant along the length of the waveguide. Specifically, the offsets of the slots are adjusted such that about 90 % of the energy is radiated (leaked) before reaching the output port of the SIW-LWA.

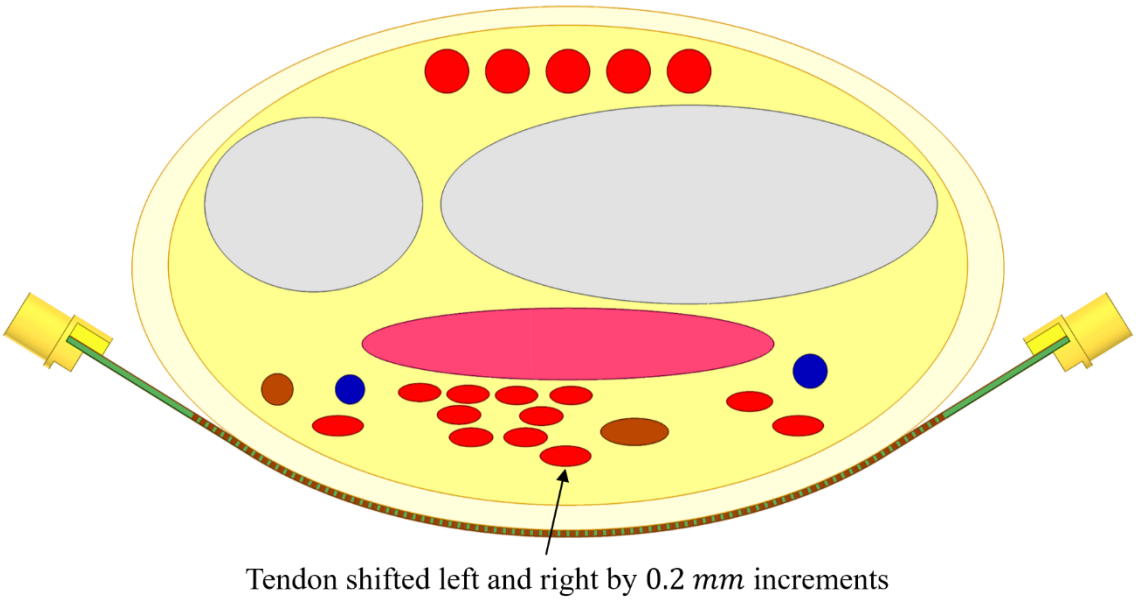

Figure 6.10: Simulation setup used to couple the electromagnetic signal into the wrist and evaluate the sensitivity to tissue motions.

6.3.3 Simulation Results

The SIW-LWA is designed in Ansys HFSS and the optimized design parameters of the antenna are listed in Table 6.2. The gesture sensor and the wrist model are arranged as shown in Fig. 6.10, and simulations were carried out to verify the sensitivity to positional variations of the wrist tissues. An exemplary tendon, as shown in Fig. 6.10, is chosen for verifying the sensitivity. Given that these simulations are extremely resource intensive and since minimal variations were observed between the PEC and 1 oz Copper metallization in the SIW simulations, only simulations with PEC were carried out in this section to reduce the computational resources. A parametric analysis was carried out by varying the position of the tendon. Specifically, the tendon was shifted to the left and right by 0.4 mm, with 0.2 mm increments, and the reflected signals are recorded. The simulations were carried out with both the uniform and periodic SIW-LWAs, and the S_{11} and S_{21} of both the

sensor designs are plotted in Fig. 6.11 (periodic) and Fig. 6.12 (uniform). The plots show the response recorded corresponding to 5 tendon positions: $-0.4\ mm,\ -0.2\ mm,\ 0\ mm,$ $0.2\ mm,\ and\ 0.4\ mm$. The S_{11} plots show that the sensor can detect micromotions of the order of $0.2\ mm$ which are manifested as magnitude and spatial variations in the reflected signal. On the other hand, it is also observed that the S_{21} does not vary much for different tendon positions in the entire frequency band. This could be attributed to the fact that the attenuation constant of the SIW-LWA was optimized such that the antenna radiates more than $90\ \%$ of the signal before reaching the output port to avoid any back reflections. Additionally, the signal that is reflected from the tissues back to the slots could also be re-radiated before reaching the output port of the waveguide. As such, the resulting signal variations could be very minimal to cause any changes to the S_{21}.

Further, to verify the coupling of the electromagnetic signal into the wrist, the electric (E) field distribution inside the wrist was plotted over the entire frequency range of interest. A few representative plots at sample frequencies, 8.5 GHz, 10.5 GHz, 13 GHz, and 16 GHz, are depicted in Fig. 6.13 and Fig. 6.14 respectively, for periodic and uniform SIW-LWA sensors. The field plots show the inherent frequency scanning behavior of the LWA employed as the radiating structure. Consequently, various tissues within the wrist could be illuminated as the frequency is scanned from $8 - 18$ GHz, thus providing unique information corresponding to the spatial variations resulting from the shifting of tissues while performing different gestures. Some amount of back radiation is also observed at the intersection of the SMP connector and the SIW-LWA, which could lead to sensitivity suppression. This will be verified with the measurement results presented in the following sections.

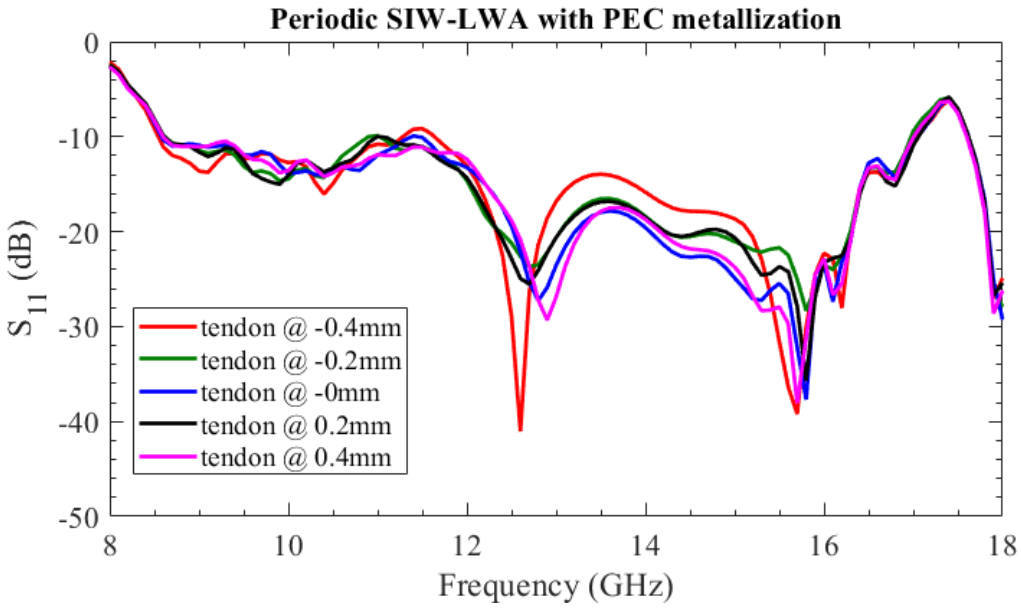

(a)

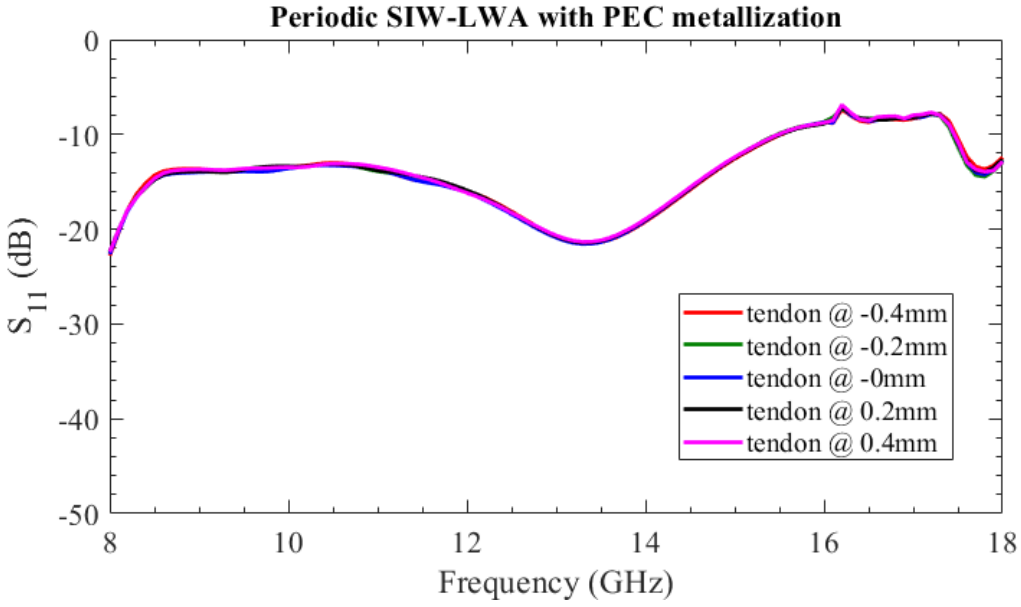

(b)

Figure 6.11: Simulation results of periodic (multi-slot) SIW-LWA: (a) S_{11} plots for different tendon positions showing both magnitude and spatial variations and (b) S_{21} plots for different tendon positions showing almost no variations.

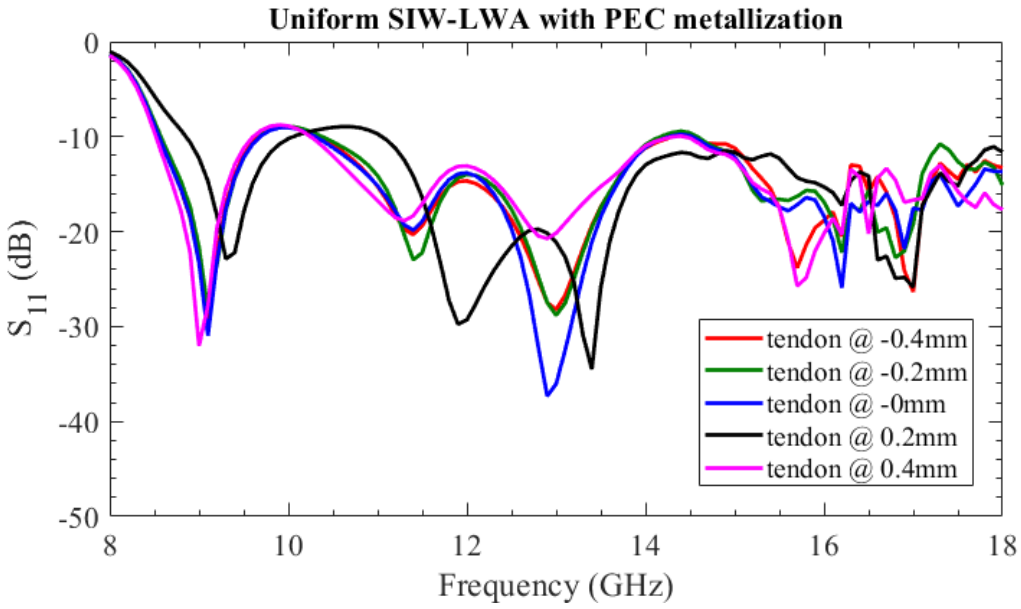

(a)

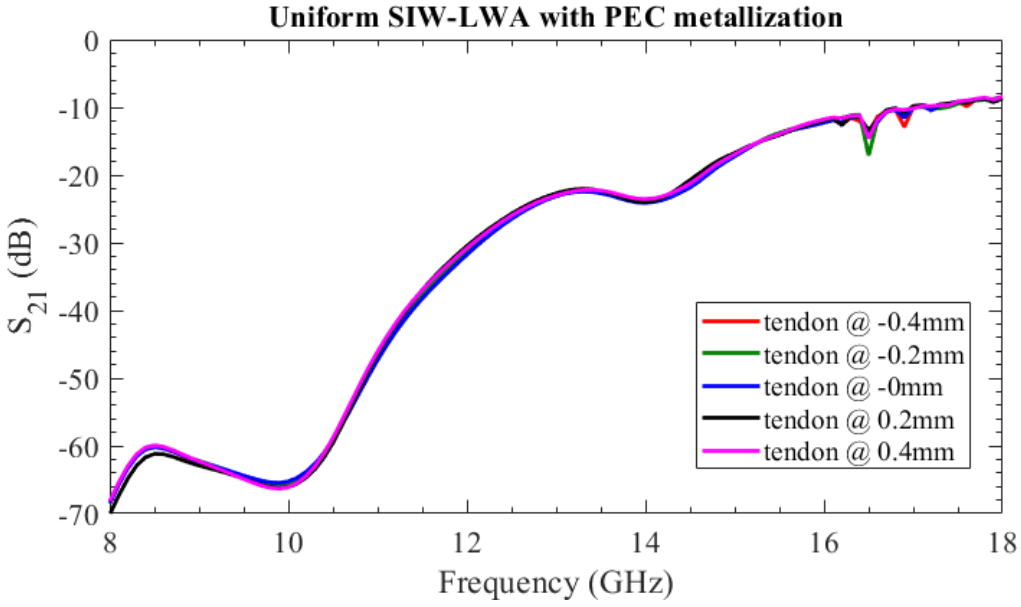

(b)

Figure 6.12: Simulation results of uniform (single-slot) SIW-LWA: (a) S_{11} plots for different tendon positions showing both magnitude and spatial variations and (b) S_{21} plots for different tendon positions showing almost no variations.

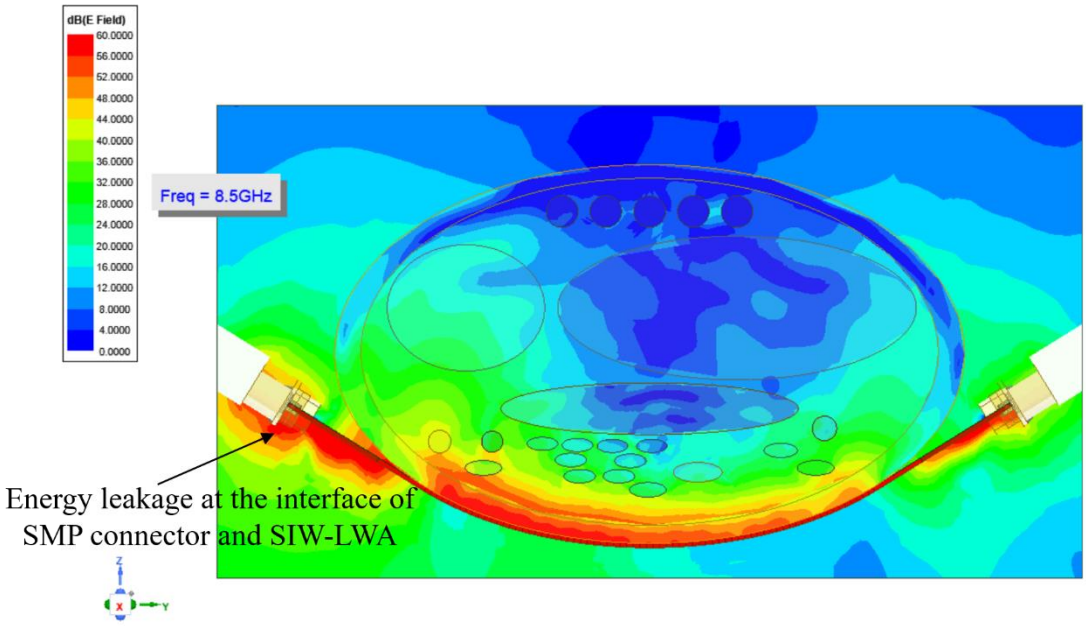
dB(E Field)
60.0000
56.0000
52.0000
48.0000
44.0000
40.0000
36.0000
32.0000
28.0000
24.0000
20.0000
16.0000
12.0000
8.0000
4.0000
0.0000
Freq = 8.5GHz
Energy leakage at the interface of
SMP connector and SIW-LWA

(a)

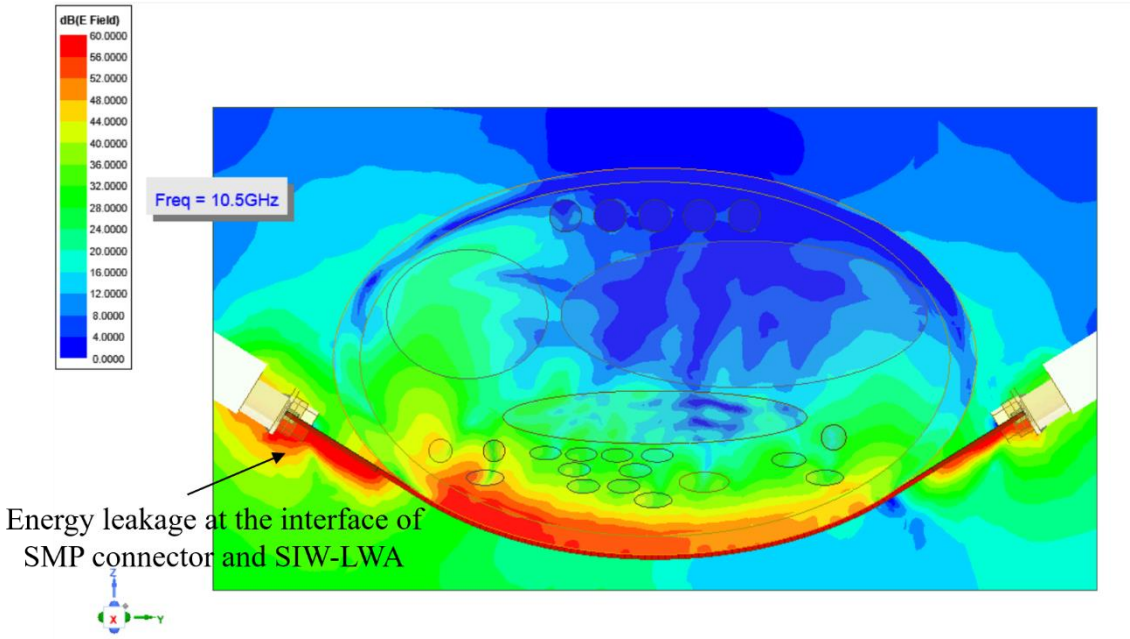
dB(E Field)
60.0000
56.0000
52.0000
48.0000
44.0000
40.0000
36.0000
32.0000
28.0000
24.0000
20.0000
16.0000
12.0000
8.0000
4.0000
0.0000
Freq = 10.5GHz
Energy leakage at the interface of
SMP connector and SIW-LWA

(b)

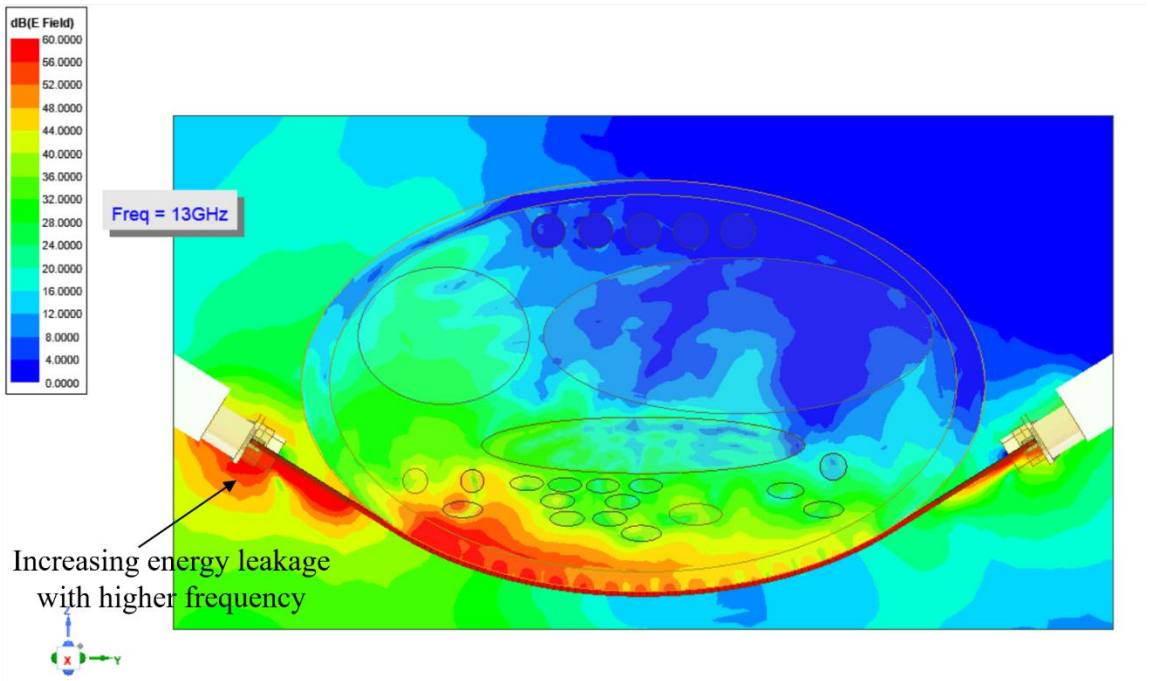

(c)

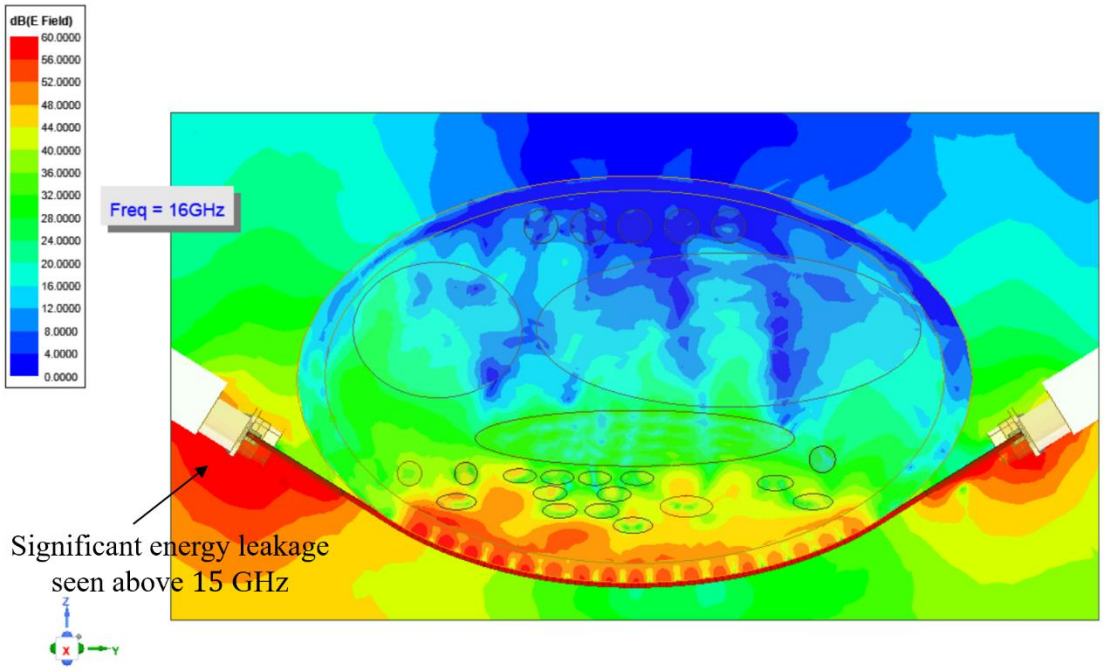

(d)

Figure 6.13: Electric field distribution within the wrist for the periodic (multi-slot) SIW-LWA sampled at a few representative frequencies: (a) 8.5 GHz, (b) 10.5 GHz, (c) 13 GHz, and (d) 16 GHz.

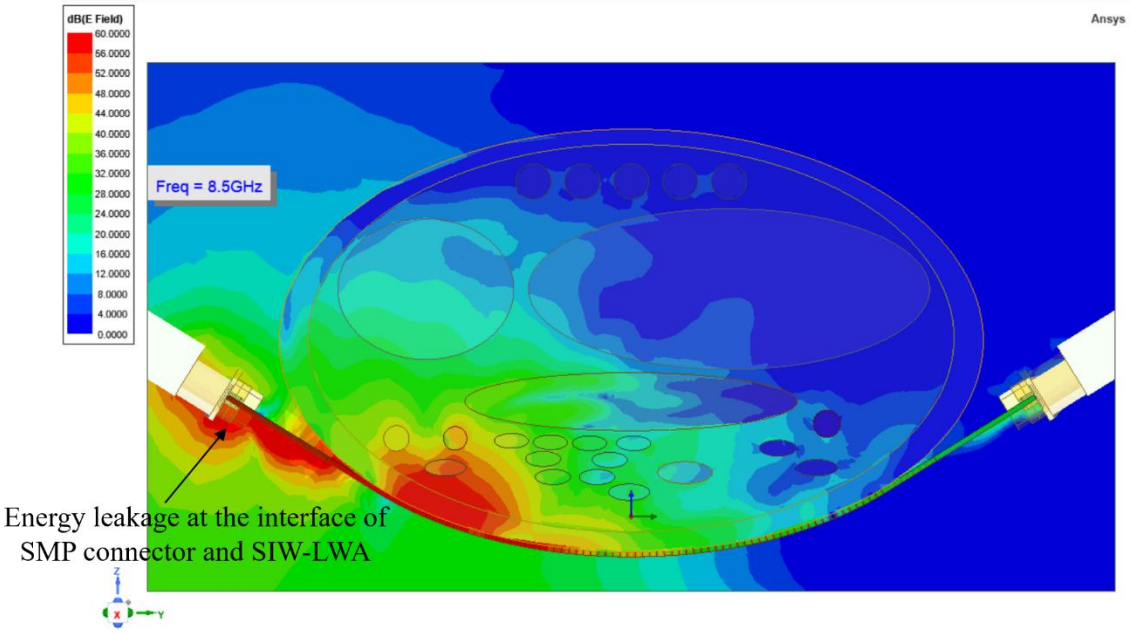
dB(E Field)
60.0000
56.0000
52.0000
48.0000
44.0000
40.0000
36.0000
32.0000
28.0000
24.0000
20.0000
16.0000
12.0000
8.0000
4.0000
0.0000
Ansys
Freq = 8.5GHz
Energy leakage at the interface of
SMP connector and SIW-LWA

(a)

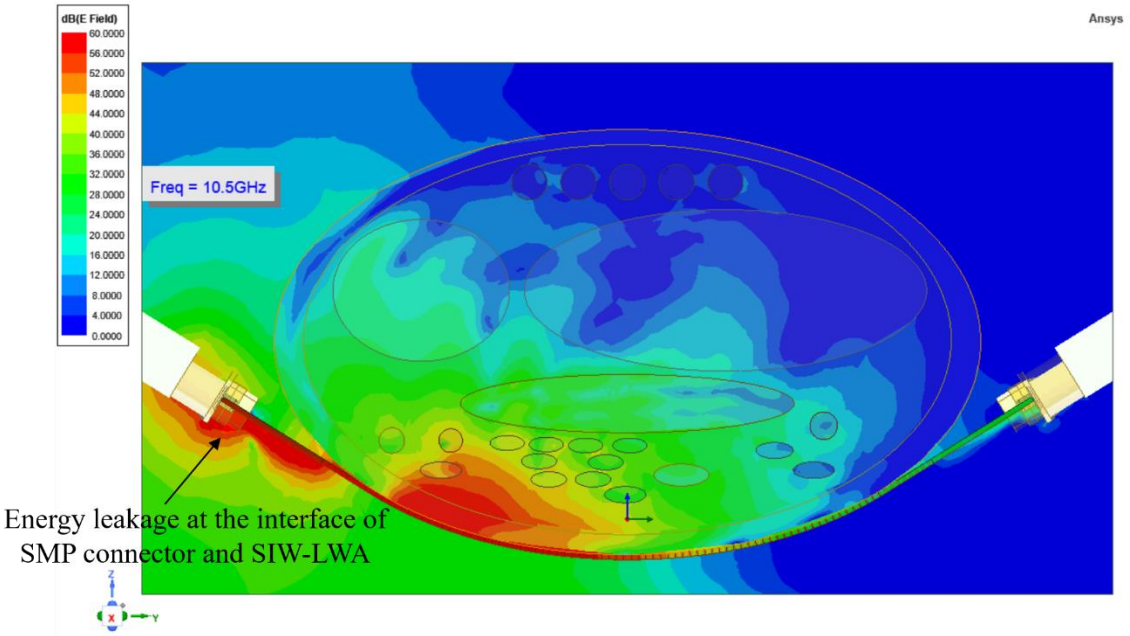
dB(E Field)
60.0000
56.0000
52.0000
48.0000
44.0000
40.0000
36.0000
32.0000
28.0000
24.0000
20.0000
16.0000
12.0000
8.0000
4.0000
0.0000
Ansys
Freq = 10.5GHz
Energy leakage at the interface of
SMP connector and SIW-LWA

(b)

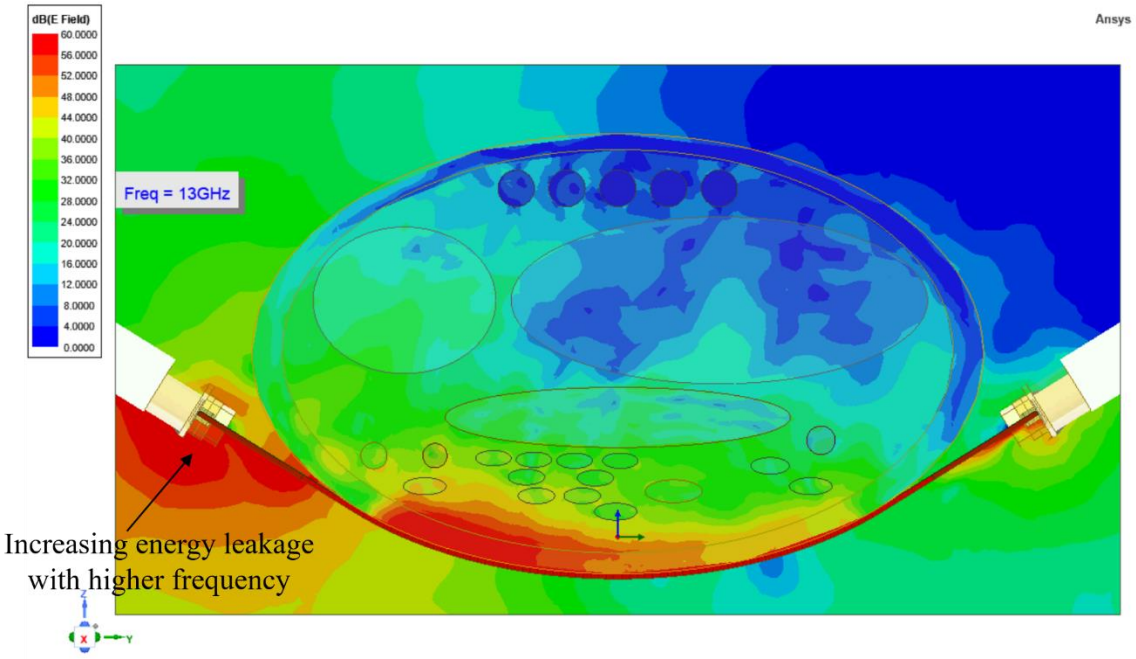

(c)

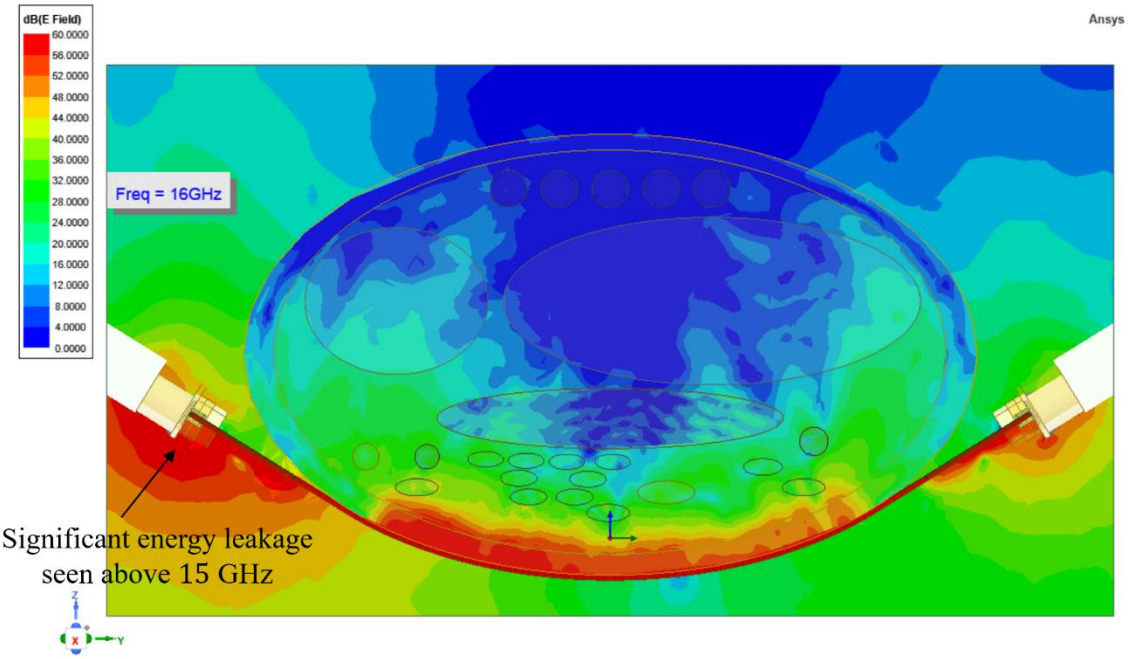

(d)

Figure 6.14: Electric field distribution within the wrist for the uniform (single-slot) SIW-LWA sampled at a few representative frequencies: (a) 8.5 GHz, (b) 10.5 GHz, (c) 13 GHz, and (d) 16 GHz.

6.4 Sensor Characterization

Motivated by the encouraging simulation results, it was decided to fabricate the sensor prototypes to carry out real world measurements. To that end, the sensor designs were exported to Altium Designer and the Gerber files were generated to manufacture both the periodic and uniform LWAs using a standard PCB manufacturing process. A fixture was also designed to mount and fasten the sensor on to the wrist region for carrying out the measurements. The 3D printed fixture is shown in Fig. 6.15 (a). The fabricated sensor prototypes are mounted on the fixture as shown in Fig. 6.15 (b) and (c) and employed for measurements.

The measurement setup used for characterizing the sensitivity of the fabricated sensor prototypes is depicted in Fig. 6.16(a). The sensor is fastened to the anterior side of the wrist of a test user. The coaxial cables from the sensor are connected to the VNA and the S-parameter measurements are carried out in the $8 - 18$ GHz frequency range. The user is asked to perform different hand motions to mimic 5 different gesture postures shown in Fig. 6.16 (b) and the corresponding reflected signals from the wrist tissues for each individual gesture are recorded on the VNA. The measurements are carried out with three different users for each sensor. The magnitude and phase of the reflected signals are plotted in Fig. 6.17 and Fig. 6.18 for the periodic and uniform SIW-LWAs, respectively. Each user is asked to perform all the 5 gestures sequentially from Gesture 1 (G1) to Gesture 5 (G5). The users are then asked to repeat the process and 10 iterations of S-parameter data are collected for each user, with each iteration corresponding to 1 set of all the 5 gestures performed in a sequence.

(a) (b) (c)

Figure 6.15: (a) Prototype of the 3D printed fixture used to mount and secure the sensor on to the wrist and (b)-(c) fabricated prototypes of the SIW-LWA sensors mounted on the fixture: Periodic SIW-LWA (a) and Uniform SIW-LWA (b).

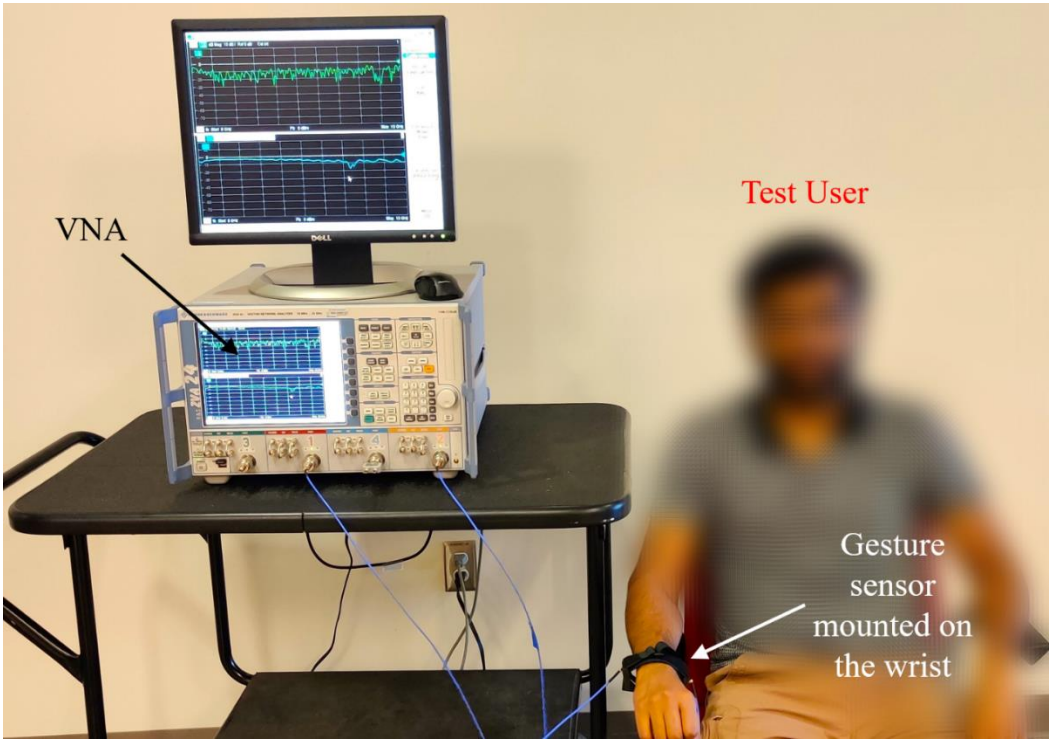

(a)

(b)

Figure 6.16: (a) Measurement setup used to characterize the sensitivity of the designed SIW-LWA gesture sensor prototype and (b) the representative images of the 5 gestures used sensitivity characterization.

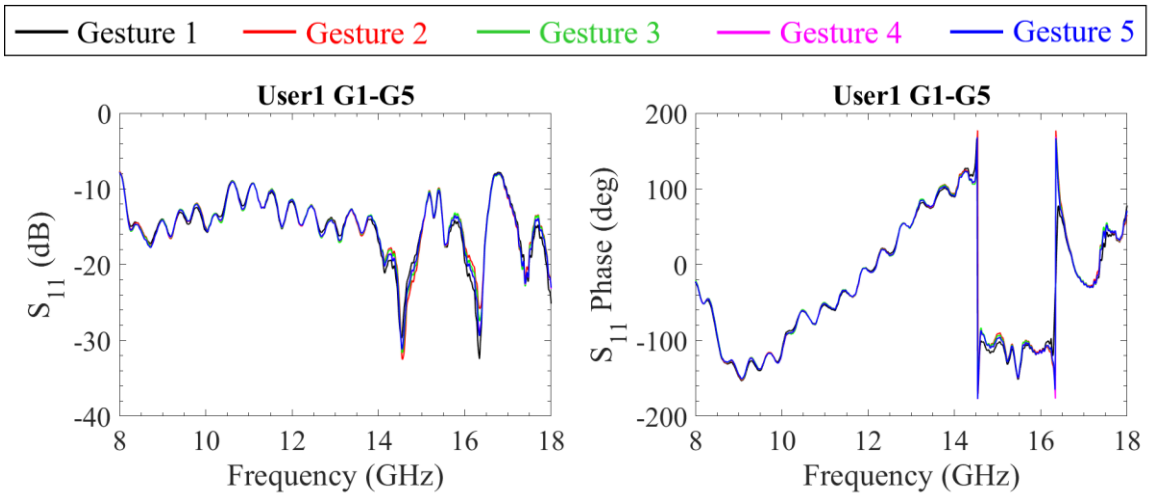

(a)

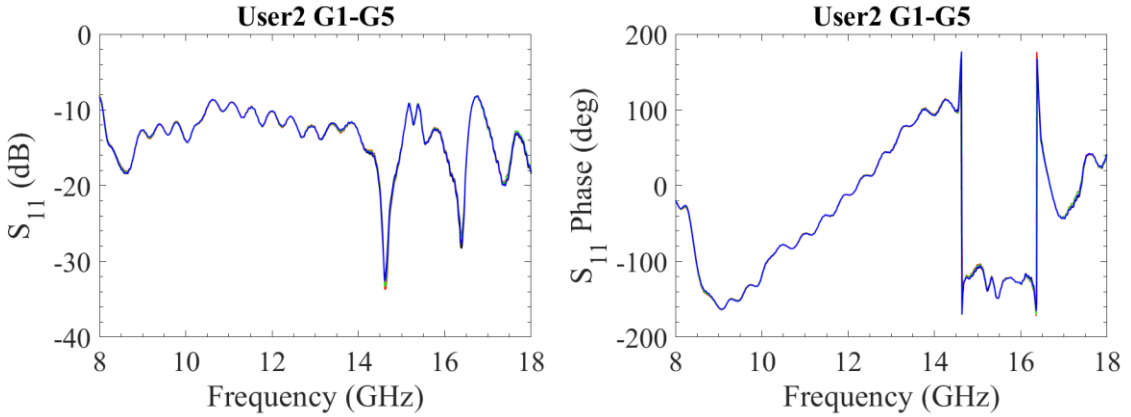

(b)

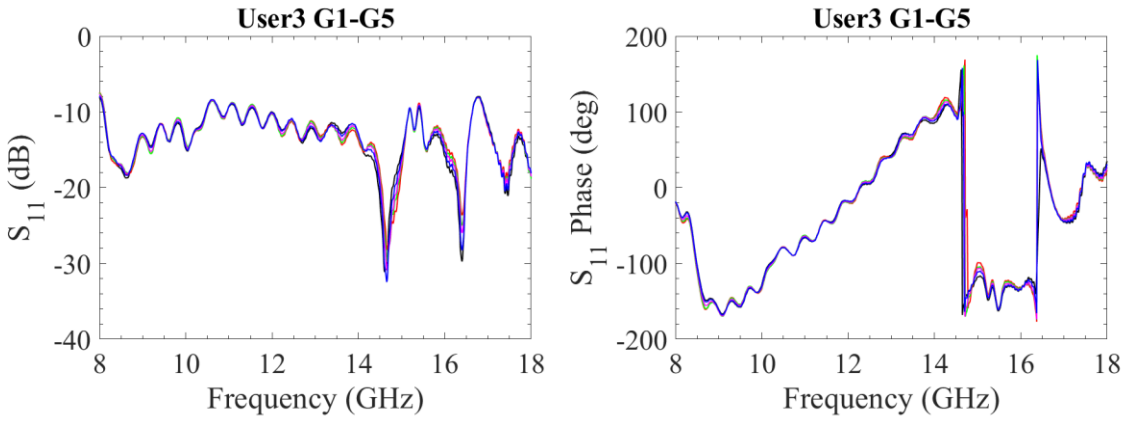

(c)

Figure 6.17: Periodic (multi-slot) SIW-LWA sensitivity measurement results for 3 test subjects showing minimal variations between the gestures (S_{11} magnitude (left) and phase (right)).

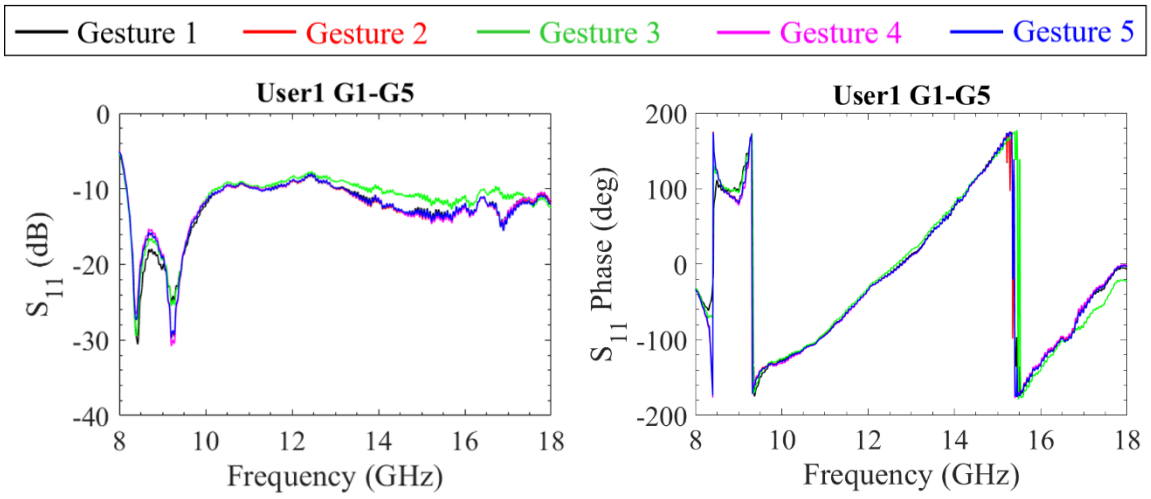

(a)

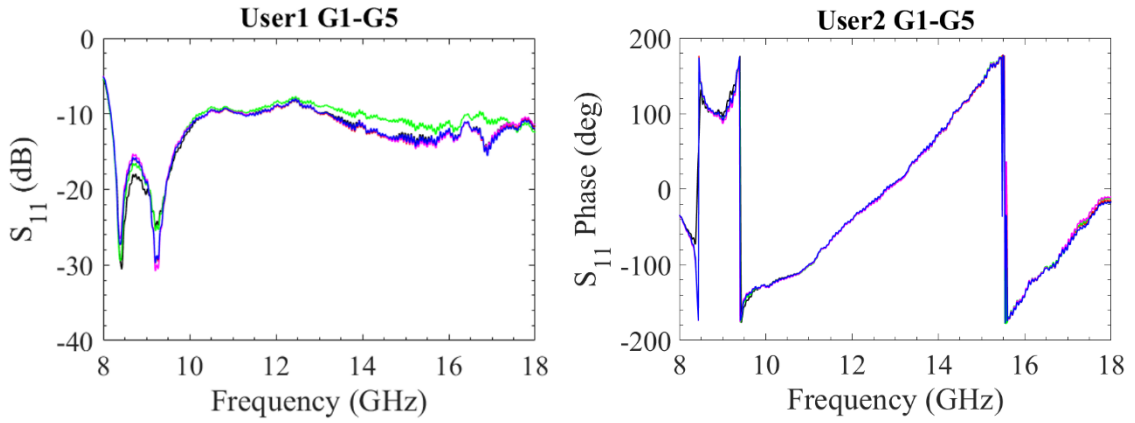

(b)

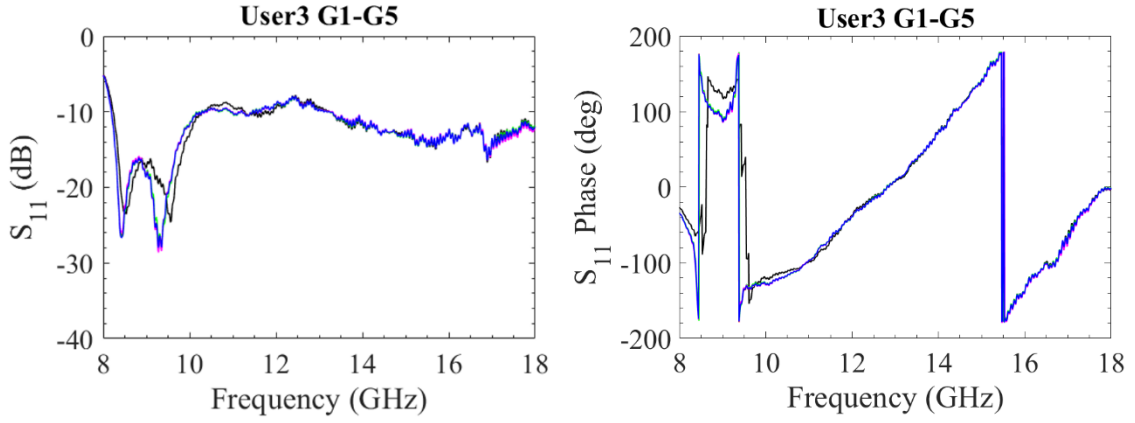

(c)

Figure 6.18: Uniform (single-slot) SIW-LWA sensitivity measurement results for 3 test subjects demonstrating slightly better sensitivity as compared to uniform sensor. (S_{11} magnitude (left) and phase (right)).

Although, good repeatability is observed across different users, the sensitivity is significantly suppressed for all the users when compared to the simulation results. Some of the possible reasons for this could be the fabrication uncertainties or modeling inaccuracies. In terms of fabrication, the assembly of the SMP connector on to the sensors turned out to quite challenging due to a large gap between the bottom metal layer of the SIW-LWA and the GROUND lead of the SMP connector. The gap arises due to the mismatch between the SMP connector's SIGNAL-to-GROUND spacing ($1.8\ mm$) and the substrate thickness ($0.508\ mm$). Consequently, $1.3\ mm$ gap must be efficiently filled with solder which could lead to challenges in terms of radiation losses and signal degradation. Moreover, the S-parameter data was also found to be very sensitive to assembly tolerances. Another critical challenge arises from the limited accuracy of the of the human hand model developed in this work. Particularly, frequency independent material properties were used in the full-wave simulations which could reduce the accuracy. Further, from the wrist cross section in Fig. 6.10, it can be noticed that the permittivities of different tissues vary significantly which can lead to multiple reflections within the wrist before the signal reaches back to the sensor. Additionally, as these tissues are also lossy. As such, the reflected signals could be greatly subdued, thus inherently compromising the sensitivity of the gesture sensor.

The following material outlines the different simulations that were carried out to evaluate the impact of the issues mentioned above. In the simulation results presented in Fig. 6.11 and 6.12, the metals were models as PEC sheets. The thickness of the metal was not included in the simulations to reduce the computational resources. This was prompted by the results of SIW design where it was noticed that the going from sheet to 3D metal

has minimal impact on the obtained results. However, to verify if the thickness of the metal changes the sensitivity, simulations were carried out with 1 oz Copper (same thickness as used in fabrication). The obtained results are plotted in Fig. 6.19 (a) (periodic SIW-LWA) and Fig. 6.19 (b) (uniform SIW-LWA). The plots depict that the sensitivity is significantly suppressed similar to the measurements. Further, it is also observed that the uniform SIW-LWA exhibits slightly better sensitivity compared to the periodic SIW-LWA as was witnessed with the measurement results. Further in Fig. 6.20, a set of comparison plots between simulations and measurements are presented which show a qualitative agreement between the two. The differences are expected due to the variations in the approximate wrist model used for simulations and the actual physical anatomy of the human wrist.

Although this points to the inherent limitation of the lossy multi-dielectric wrist anatomy, to investigate if any sensitivity could be recovered by design modifications, few additional simulations were carried out which are listed below.

1. Analysis without SMP connector:

The E-field plots of Fig. 6.14 and Fig. 6.14 show that there is a significant amount of radiation leakage from the SMP signal pin especially at higher frequencies. This could have an impact on the sensitivity of the signal. To verify this, the SMP connectors were replaced with ideal excitations (wave ports) in the 3D electromagnetic solver and the simulations were repeated. The results for the periodic SIW-LWA are presented here for brevity and similar results were obtained for the uniform SIW-LWA design.

The simulation model with the waveport excitation is depicted in Fig. 6.21. The SMP connectors are replaced with wave ports and the remaining parameters are kept the

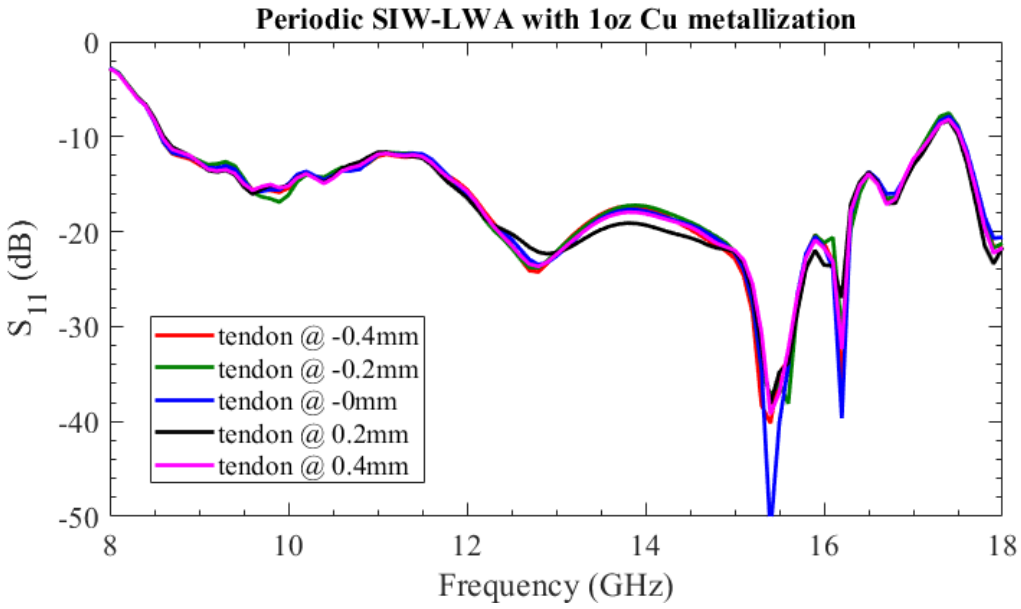

(a)

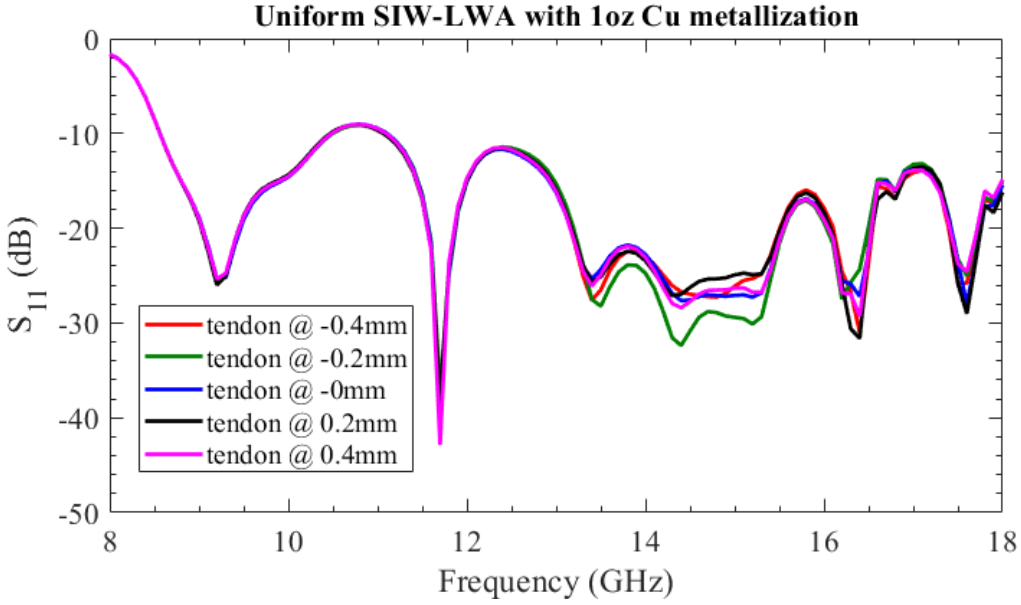

(b)

Figure 6.19: S_{11} plots for different tendon positions showing suppressed sensitivity like the measurements: (a) Periodic SIW-LWA (b) Uniform SIW-LWA.

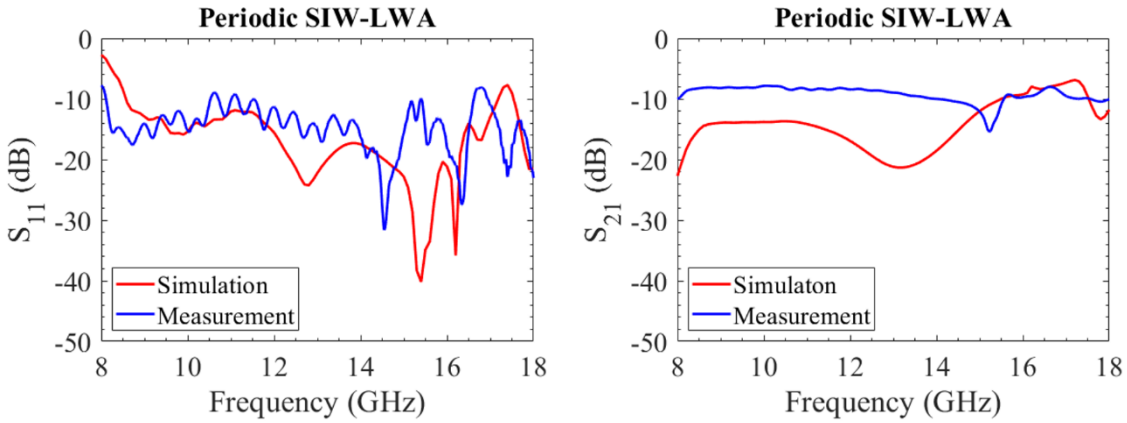

(a)

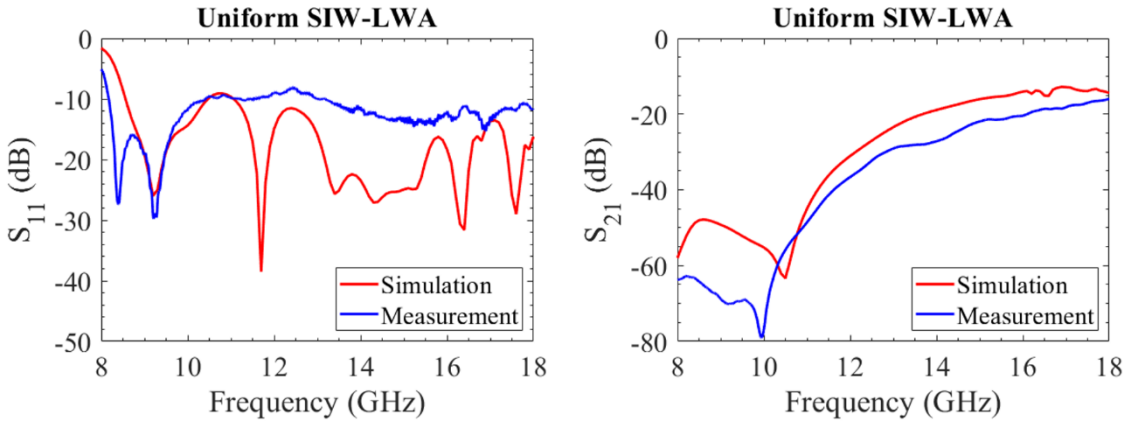

(b)

Figure 6.20: Comparison of simulations (with $1\,oz$ Copper metallization) and measurements for an exemplary gesture. The plots show some qualitative agreement between the simulations and measurements. (a) Periodic SIW-LWA (S_{11} magnitude (left), phase (right)) and (b) Uniform SIW-LWA (S_{11} magnitude (left), phase (right)).

same. A parametric analysis is carried out by moving the same tendon left and right by 0.2 mm increments as before. The obtained S_{11} data are plotted in Fig. 6.22. It shows some sensitivity improvement compared to the model with SMP connectors, thus, indicating that the SMP connectors contribute to the sensitivity degradation. The S_{21} (not

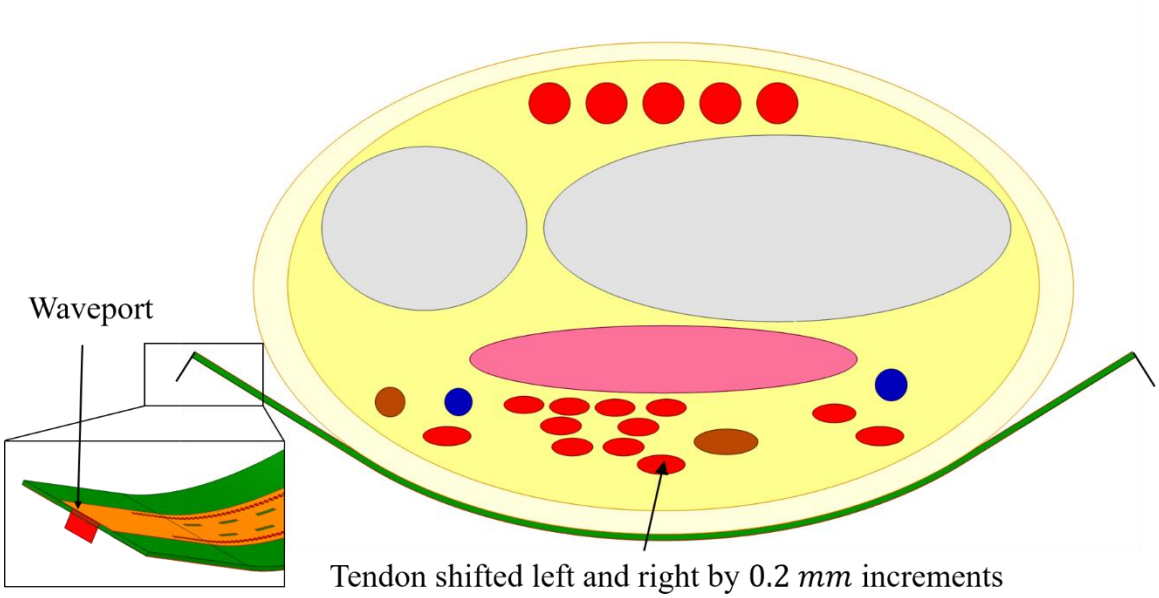

Figure 6.21: Simulation setup with ideal excitation (wave port) used to investigate the sensitivity degradation due to SMP connectors. Inset: Wave port excitation model.

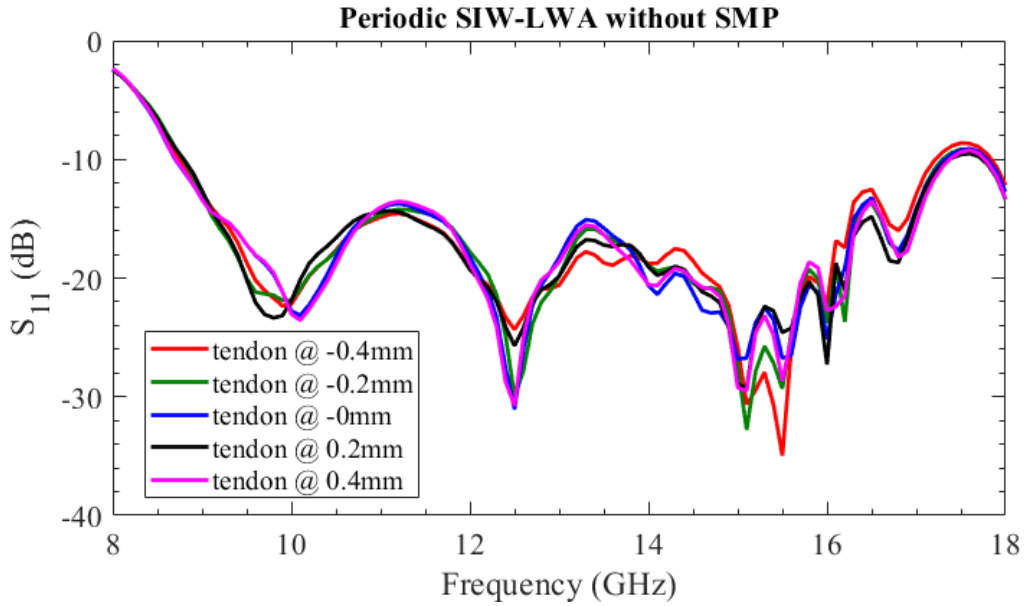

Figure 6.22: Simulation results showing sensitivity improvement for the periodic (multi-slot) SIW-LWA with 1 oz Copper metallization and wave port excitation.

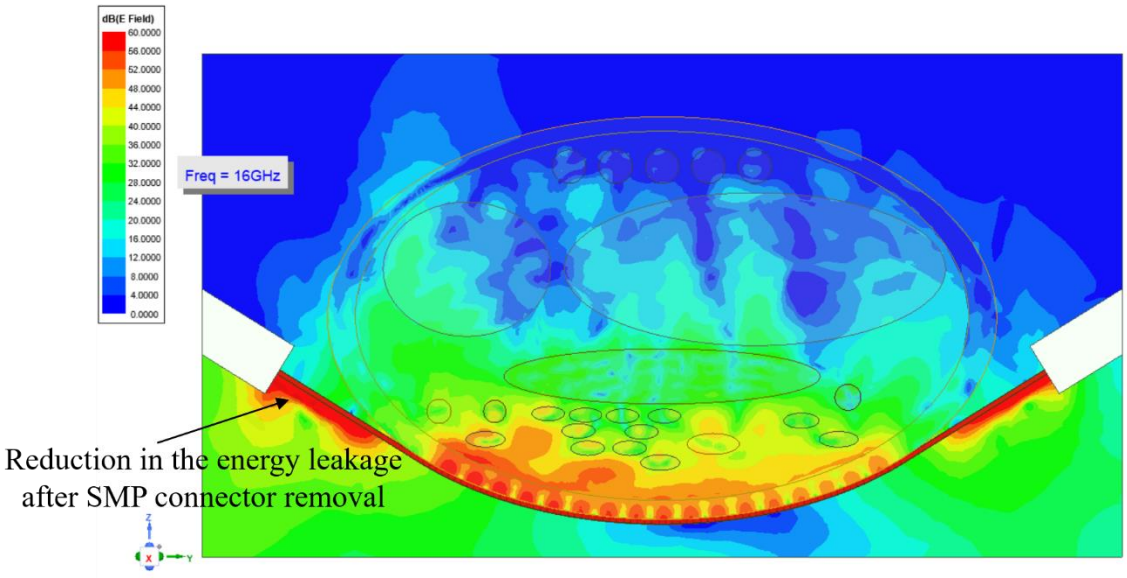

Figure 6.23: Electric field distribution within the wrist depicting the significant reduction in the backward radiated energy after the removal of SMP connector.

shown) is not impacted by the removal of SMP connector. Further, the E-field distribution within the wrist was also plotted and are as shown in Fig. 6.23. Although the radiation leakage is reduced when compared to the design with SMP connector, it is noticed that the SIW-to- MSL transition also leaks some energy, again, significantly, at higher frequencies. This could be attributed to the fact that the MSL is inherently narrow band and thus, leads to radiation leakage at out of band frequencies.

2. Analysis without SMP connector and SIW-to-MSL Transition:

To evaluate, if sensitivity could be further recovered by eliminating the losses due to the SIW-to-MSL transition, simulations were carried out with ideal wave port excitations directly at the input of the SIW-LWA. The simulation model is shown in Fig. 6.24 and the S_{11} data is shown in Fig. 6.25. The results show that by eliminating the SMP connector and the SIW-to-MSL transition, the sensitivity of the SIW-LWA shows further

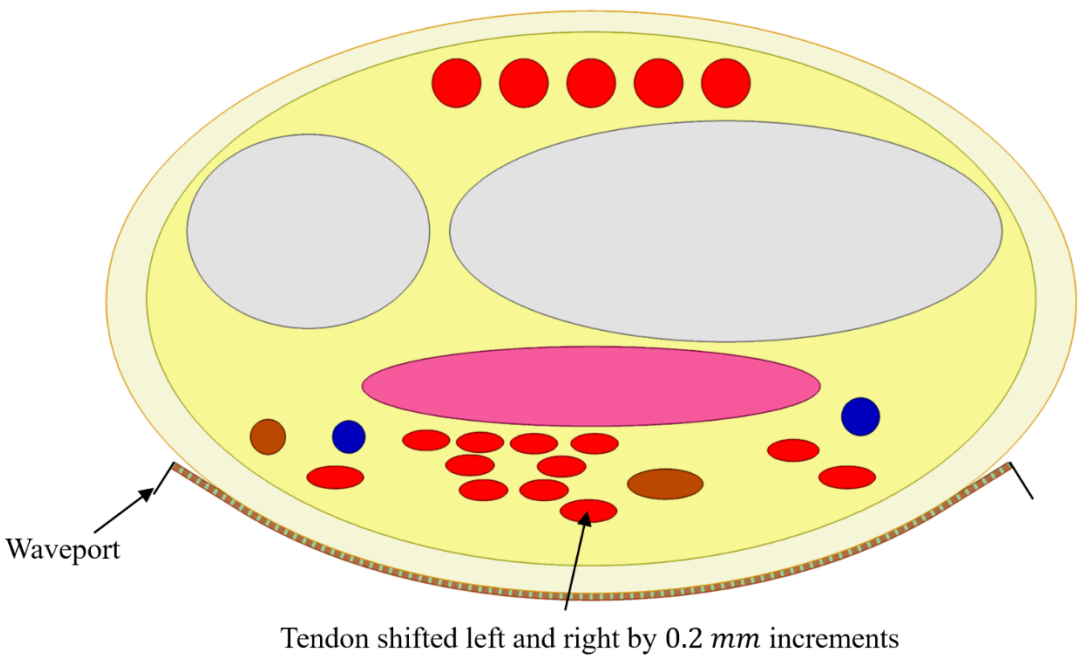

Figure 6.24: Simulation setup of the SIW-LWA with ideal excitation (wave port). No SIW-to-MSL transition employed.

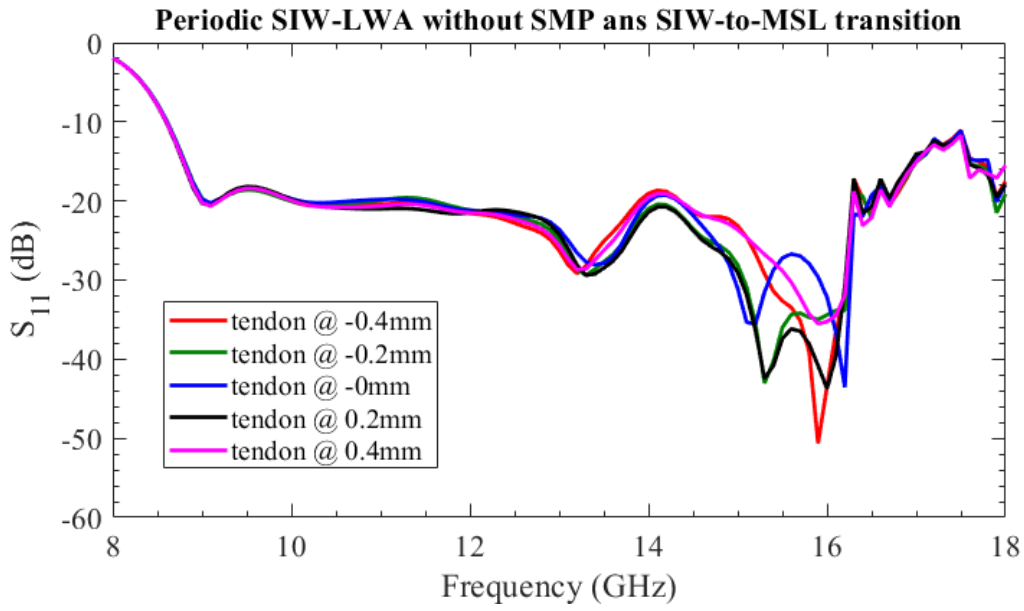

Figure 6.25: Simulation results showing sensitivity improvement for the periodic (multi-slot) SIW-LWA with 1 oz Copper metallization, no SMP, no SIW-to-MSL transition.

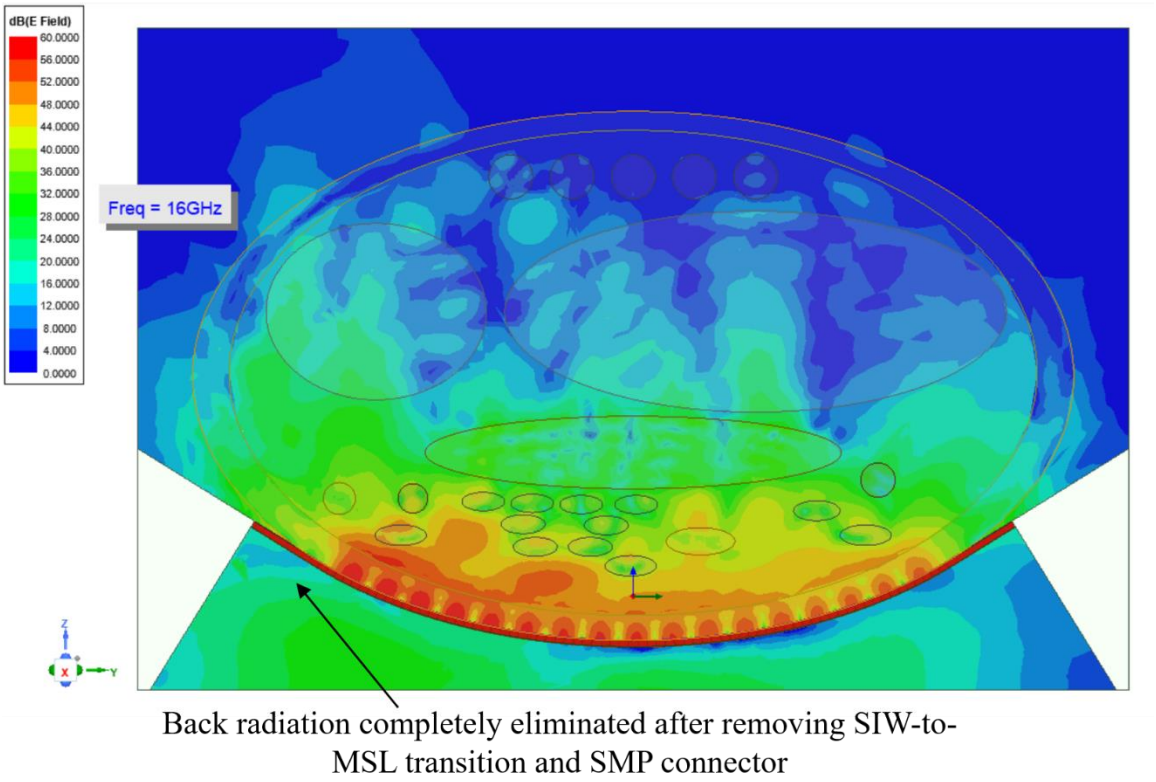

Figure 6.26: Electric field distribution within the wrist showing the complete elimination of backward radiation after the removal of SIW-to-MSL transition and the SMP connector.

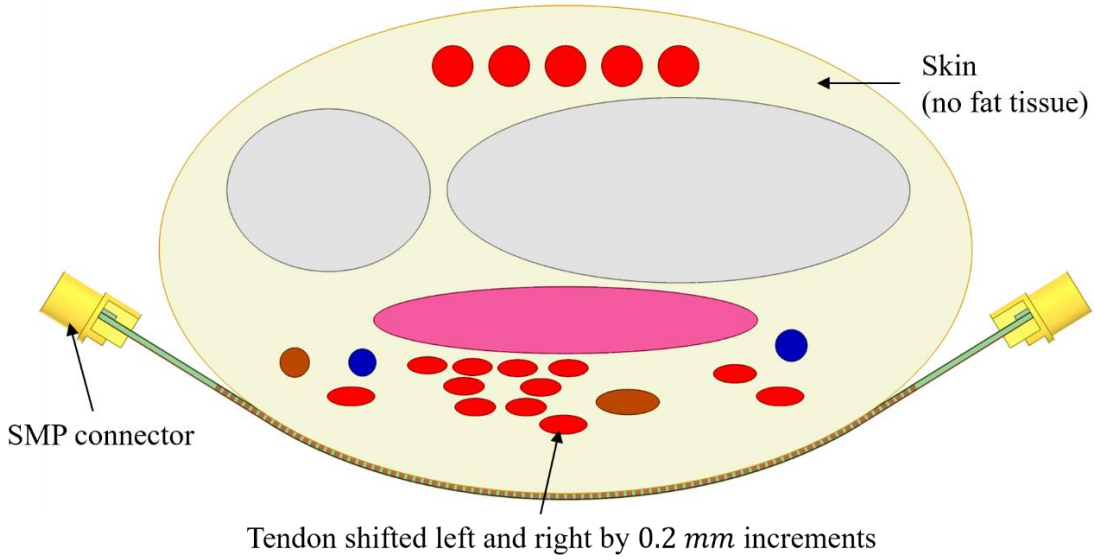

Figure 6.27: Simulation setup of the SIW-LWA without the fat tissue. Tendons, muscles, bones, and other tissues are directly modeled in skin environment.

improvement particularly in the $13 - 17$ GHz frequency range. It should also be noted that a resonance seen around 10 GHz with the previous simulation is lost with the elimination of SIW-to-MSL transition. This could be because the SIW-LWA was optimized for radiating into the wrist in the presence of SIW-to-MSL transition. As such, by re-optimizing the slot dimensions and the offsets, the attenuation constant could be modified, and the lost resonance could be recovered. This needs additional investigation and could be focused in the future works. Moreover, the E-field plots of Fig. 6.26 show that the SIW-LWA has almost no leakage with the current simulation setup. This also opens the doors for utilizing surface mount type connectors instead of edge launch connectors for feeding SIW-LWAs.

3. Analysis without Fat:

As was pointed out earlier, the wrist anatomy consists of multiple lossy dielectric layers which could also adversely affect the sensitivity due to multiple reflections at the interfaces, and this could indicate the limitation of the system. To verify this, the fat layer ($\epsilon_r \approx 8.1, \sigma \approx 2.3$) was removed replaced with the skin tissue ($\epsilon_r \approx 28, \sigma \approx 11.5$). The rest of the tissues were unchanged, and the simulations were carried out. The simulation setup is shown in Fig. 6.27 and the corresponding S_{11} data are plotted in Fig. 6.28.

The plots in Fig. 6.28 show that the sensitivity indeed improves compared to the results in Fig. 6.19. It follows that the sensitivity reduction witnessed in Fig. 6.19 could be due to reduced multiple reflections at the boundaries of lossy dielectrics. Additionally, the impact of the frequency dependent material properties was also verified, and it was found that they do not have noticeable impact on the improvement of sensitivity. This indicates

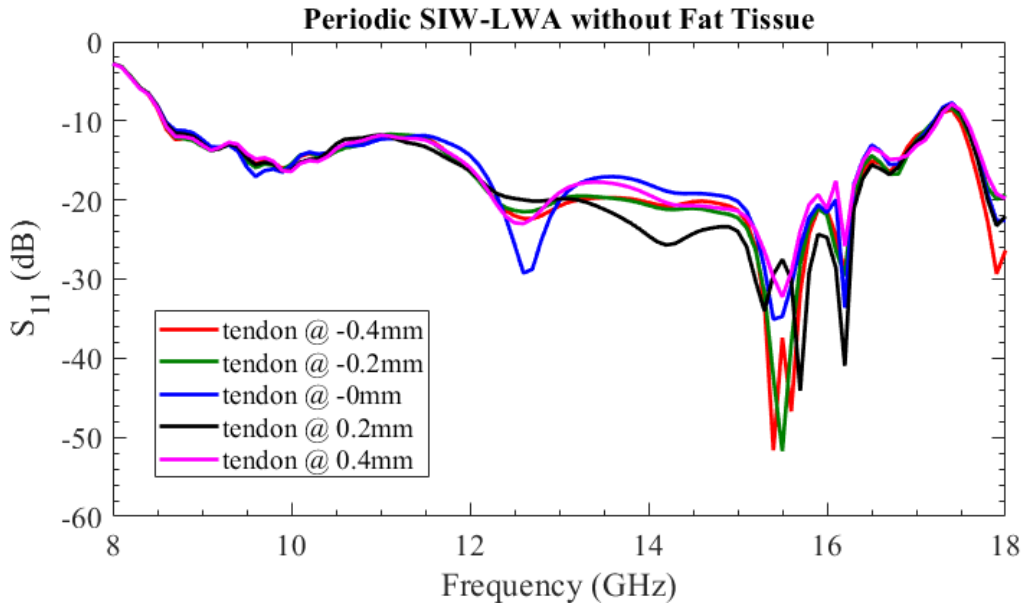

Figure 6.28: Simulation results showing sensitivity improvement for the periodic (multi-slot) SIW-LWA with 1 oz Copper metallization, using a wrist anatomy without fat tissue.

that the system limitations also need to be considered for determining the overall achievable accuracy.

In Fig. 6.29, the sensitivity improvement achieved through various simulation studies is summarized and quantified. The shaded region in the plots show the maximum variations between different gestures across frequencies. Fig. 6.29 (a) shows the default simulation model with SMP connector and SIW-to-MSL transition and has the least sensitivity. When the SMP connector is removed, the sensitivity slightly improves as seen by the plots in Fig. 6.29 (b). The sensitivity further improved when the SIW-to-MSL transition is also removed as seen in Fig. 6.29 (c). Additionally, the plots of Fig. 6.29 (d) indicate that the large variation in the permittivities between the skin and the fat could also be a leading reason to the suppression of sensitivity. As such, by removing the fat tissue, significant sensitivity improvement is noticed.

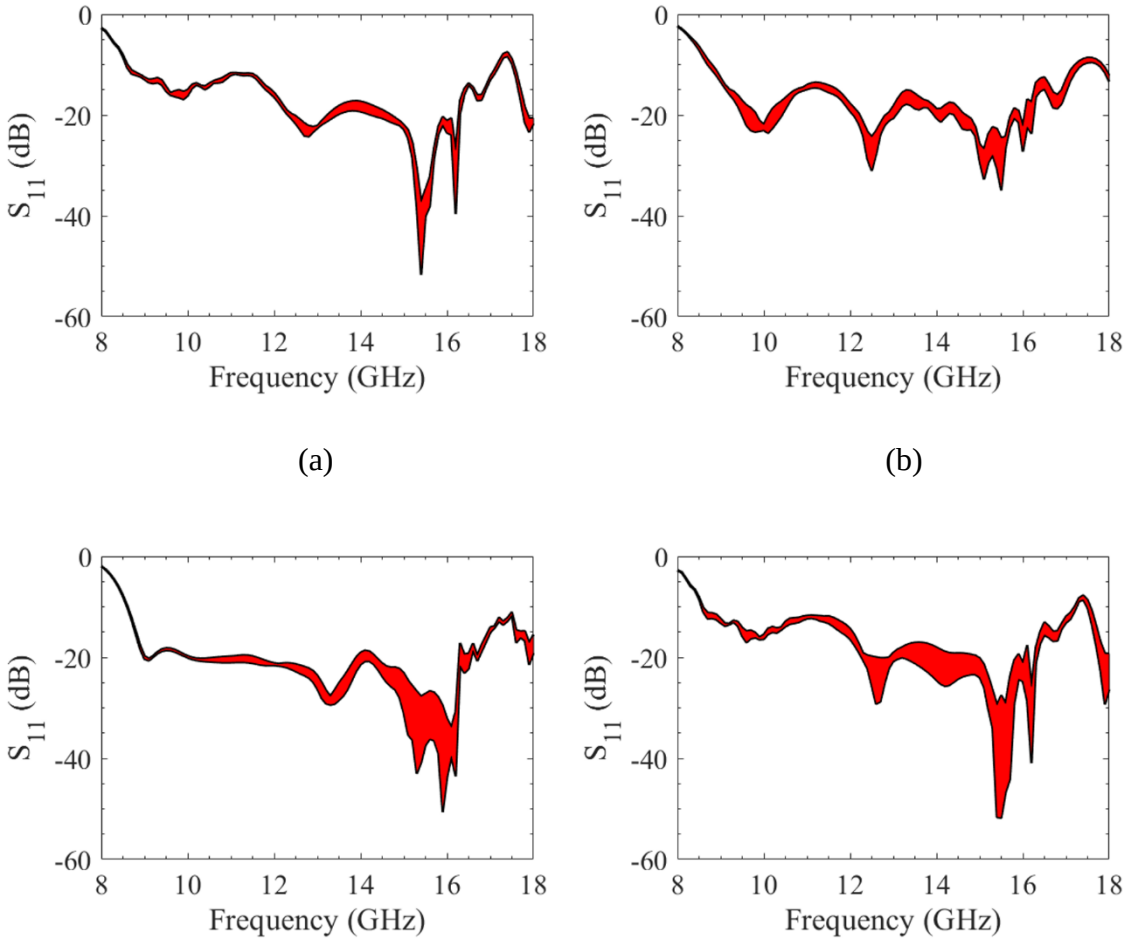

Figure 6.29: Sensitivity improvement characterization with various simulation models studied in this work: (a) Default model with SMP connector and SIW-to-MSL transition (b) model without SMP connector, (c) model without SMP connector and SIW-to-MSL transition, and (d) Default model, but without fat tissue.

6.5 Conclusion

This chapter presented a novel RF gesture sensing technique that can be used to couple microwave signals into the human hand and capture unique gesture related information from the tissues within the arm. Specifically, the design and analysis of an RF

gesture sensor based on SIW-LWAs was outlined. Two LWA configurations were employed for analysis: periodic and uniform. Both the designs were fabricated, and measurements were carried out to evaluate the sensitivity of the proposed LWA based sensors. Although, very good repeatability across users was demonstrated, it was also found that the proof-of-concept gesture sensors developed in this research showed limited sensitivity to different gestures. A comprehensive analysis was carried out to examine the possible reasons for sensitivity degradation. It could be observed that multiple factors lead to a cascading effect and progressively reduce the overall sensitivity of the system. Some of the important reasons for sensitivity degradation were identified as the presence of a lossy multi-layer dielectric anatomy of the wrist and the radiation leakage from the SMP connectors and the SIW-to-MSL transition. Future works could focus on more accurate modeling of the wrist anatomy, optimization of the antenna design and feeding mechanisms to improve the sensitivity to different gestures.

While the sensitivity is suppressed with the current design, the SIW-LWAs exhibit very good coupling into the wrist while also concentrating the radiation close to the surface. Additionally, they also exhibit ultra-wide band performance from $8 - 18$ GHz. As such, they could also find applications in 5G mmWave communications for personal area networks, magnetic resonance imaging (MRI), for monitoring vital signals, and communicating with subdermal implants etc.

CHAPTER 7

CONCLUSIONS AND FUTURE WORK

7.1 Conclusions

This dissertation presented the design and development of reconfigurable metasurfaces that represent a cutting-edge technology with diverse applications across multiple disciplines including 5G communications, radars, and sensing. Metasurfaces offer transformative solutions for the challenges faced by 5G communications. Their ability to manipulate electromagnetic waves with precision not only enhances data rates and coverage but also contributes significantly to the overall efficiency, reliability, and flexibility of 5G networks. The gain and coverage improvement has been demonstrated with a sub-6 GHz RIS prototype in Chapter 3. With a relatively small $160-$ element active RIS, field measurements are carried out, and it is shown that the SNR in the shadow region could be improved by more than 6 dB. The SNR improvement could be further increased by employing larger RISs. In this research, a single bit design is adopted using PIN diodes as switching elements which provides the advantages of ease of fabrication and low power consumption beamforming.

Most of the existing RIS designs suffer from the appearance of quantization lobes in undesired directions when employing plane wave illumination. These unwanted lobes in the radiation pattern are caused by phase rounding quantization errors resulting from limited number of bits used during quantization. These quantization lobes can pose severe security threats as well as lead to interference. Since the RISs are generally targeted towards mmWave or higher frequency communication systems which are severely

interference limited, it is necessary to devise techniques for eliminating the parasitic lobes. To mitigate such quantization lobes, in Chapter 4, a phase randomization technique is outlined. The technique involves randomizing the phase distribution of the surface to break the symmetry of the phase rounding quantization error. This results in a redistribution of the parasitic lobe energy in other directions, thereby eliminating the quantization lobes. The random phases are implemented by using delay lines that are integrated into each unit cell of the RIS. To evaluate the validity of the proposed idea, two passive 1-bit metasurfaces are designed – one at a sub-THz frequency of 222.5 GHz and the second at a mmWave frequency of 28.5 GHz. Both randomized and non-randomized surfaces are designed to carry out a comparative study and it has been demonstrated through both simulations and measurements that a quantization lobe reduction better then 15 dB could be achieved using the proposed phase randomization technique. Ongoing research and development in this area are likely to yield even more sophisticated metasurface-based technologies, further advancing the capabilities of future wireless communication systems.

In Chapter 5, the applications of metasurfaces for low-frequency radar and satellite communications is investigated. Specifically, the advantage of employing metasurface based Rotman lenses is evaluated using a prototype 1D meta-transmission line. Rotman lenses are true time delay beamforming structures that could be employed to eliminate beam squinting issues in phased array systems and extend the operational bandwidth. However, the large size of the Rotman lenses has restricted their usage to microwave and mmWave bands. In this work, a novel technique for miniaturizing the Rotman lenses is proposed. The idea is to replace the Rotman lens wave space with a 2D grid of lumped LC ladder networks. By using lumped networks instead of distributed networks, particularly

since the operation is in low VHF / UHF frequencies, the size of the Rotman lens could be reduced by more than 90 %. Consequently, the group delay of the electromagnetic signal could be increased by about 18 times, thus, achieving hyper compact architectures without the need for extremely high dielectric materials. Further, it is shown that by modifying the conventional TL model to include the mutual inductance effects between the series inductors in the TL, the operational bandwidth could be extended by about 40 %. The prototype developed using the proposed approach has an extremely small formfactor of $200\,mm$ ($\lambda/10$) at the VHF design frequency of 150 MHz and provides similar delay characteristics as that of a $4\,m$ microstrip line. The meta-TL is designed in an FR-4 substrate using standard PCB manufacturing processes, suggesting that it is an excellent candidate for low-cost, large scale solutions.

Finally, in Chapter 6, the application of the metasurfaces in the field of RF sensing is explored. An SIW-LWA based sensor has been developed to couple the electromagnetic signals into the human wrist region and record the responses resulting from the variations of different tissues while performing different hand gestures. An approximate cross section of the wrist is designed and the sensitivity of the LWA based gesture sensor to capture the variations due to tissue motions was recorded. This preliminary analysis demonstrated good coupling into the wrist region along with a qualitative agreement between the simulations and measurements. However, it is noticed that the sensitivity gets damped due to the multi-layer dielectric material configuration resulting from different tissues. The learning from this work on the other hand, provides valuable insight regarding the behavior of electromagnetic signal from the metasurface near human body. This could inspire the design of more sophisticated metasurface based sensors.

7.2 Recommendations for Future Work

The study of metasurfaces has emerged as a transformative area in the realm of electromagnetic wave manipulation. Future research could delve into the development of metasurfaces with enhanced functionalities. Exploring novel materials and structures could lead to metasurfaces with unprecedented properties, enabling applications that were previously deemed unattainable. In this section, the a few recommendations for possible future research are outlined.

7.2.1 Reconfigurable Intelligent Surfaces

The results presented in Chapters 3 and 4 suggest that RISs are perfectly poised to play a pivotal role in the proliferation of mmWave 5G communication systems. By adopting the phase randomization technique single lobe surfaces could be designed for steering the incident signal to desired directions. While the passive RISs designed in this work can redirect the incident plane wave to predetermined fixed direction, by employing active elements, it would be possible to achieve dynamic beam steering capabilities. Specifically, PIN diodes, micro-electromechanical switches (MEMS), varactors, or field effect transistor (FET) based switches could be utilized for designing active RISs in mmWave bands. On the other hand, graphene or vanadium dioxide (VO_2) based switches look to be promising for active RIS implementations at sub-THz frequencies. Care must be taken as the design of active RISs presents additional challenges in terms of biasing network design, increased losses from active devices, as well as higher cost and power consumption issues. Particularly, the integration of active switches can pose difficulties at

the sub-THz frequencies due to the requirements of high manufacturing precision. As such, small errors in fabrication can lead to significant performance degradation.

Additionally, these metasurfaces could be designed as tiles that could be mounted side-by-side, effectively creating a large RIS. Integrated biasing boards could be designed to deploy RISs as standalone architectures on the walls of the buildings for significantly improving SNR and coverage in the shadow regions. Further, the RISs could be combined with the MIMO technology which could be a game changer for the mmWave 5G communications. MIMO technology, when coupled with RIS, can significantly improve spectral efficiency and reduce latency. RIS can help in mitigating multipath interference and enhancing the signal-to-noise ratio, allowing for more efficient use of the available spectrum. The combination of RIS and MIMO technologies opens up a wide range of possibilities, from improving basic wireless communication parameters to enabling advanced applications in diverse fields such as IoT, smart cities, healthcare, and transportation. Continued research and development in this area are expected to unlock even more innovative use cases and benefits for wireless communication systems.

7.2.2 Meta-Transmission Lines

The novel concept of meta-TLs introduced in this research has the potential to revolutionize wideband beamforming techniques for low-frequency, long-range applications. Particularly, when combined with TTD structures like Rotman lenses, they can be used to design wideband hyper compact, low-power consumption and low-cost beam steering solutions. The proof-of-concept 1D prototype designed and evaluated in this research provides an excellent foundation for the development of 2D meta-TL grid that

could be used to replace the Rotman lens wave space and achieve miniaturization. The 2D design however, requires careful modeling as it becomes challenging to model the mutual coupling effects within a two-dimensional lumped element TL network.

7.2.3 RF Sensing Applications

In Chapter 6 a novel RF gesture sensing technique was presented, that couples microwave signals into the human hand to capture unique gesture related information from the tissues within the arm. Although a qualitative agreement was achieved between the simulations and measurements demonstrating the ability of the sensor to effectively couple the signal into the human hand, a significant sensitivity dampening was also observed. The design of the SIW to microstrip transition, use of SMP connector, and the multi-dielectric architecture of the human hand were identified to be the primary contributors for sensitivity degradation. Uniform LWA design was seen to exhibit better sensitivity compared to the periodic LWA. As such, future works could focus on designing and optimizing the uniform LWA sensor. Additionally, alternate leaky-wave architectures could also be explored.

Calibration is an important aspect of the gesture sensing schemes because the sensors can be sensitive to positioning along the wrist, sensor drifting, as well as variations between users. Additionally, the presence of airgaps between the sensor and the skin can also significantly impact the gesture sensing capabilities. As such, future works could also focus on developing efficient and automated calibration and sensing frameworks by employing machine learning algorithms.

LIST OF PUBLICATIONS

The following articles were published as a part of this research. The contents of these publications have been partially used to compile this dissertation.

Journal Articles:

1. **B. G. Kashyap**, P. C. Theofanopoulos, Y. Cui, and G. C. Trichopoulos, "Mitigating Quantization Lobes in mmWave Low-Bit Reconfigurable Reflective Surfaces," in *IEEE Open Journal of Antennas and Propagation*, vol. 1, pp. 604-614, 2020.

2. G. C. Trichopoulos, P. C. Theofanopoulos, **B. G. Kashyap**, *et.al.,* "Design and Evaluation of Reconfigurable Intelligent Surfaces in Real-World Environment," in IEEE Open Journal of the Communications, 2022.

3. **B. G. Kashyap,** R. Diaz, and G. C. Trichopoulos, *"*A Meta-Transmission Line Design for Compact True Time Delay Beamforming," (submitted).

Selected Conference Publications:

1. **B. G. Kashyap**, *et.al.,* "Fabrication and Characterization of a 900-Element 222.5 GHz Single-bit Reflective Surface with Suppressed Quantization Lobes," *2021 United States National Committee of URSI National Radio Science Meeting (USNC-URSI NRSM)*, 2021, pp. 153-154.

2. **B. G. Kashyap**, *et.al.,* "A Reconfigurable Intelligent Surface for 5G Wireless Communication Applications," *IEEE International Symposium on Antennas and Propagation & USNC/URSI National Radio Science Meeting*, 2021.

3. **B. G. Kashyap**, *et.al.,* "Low Sidelobe Level Randomized Reconfigurable Reflective Surfaces under Oblique Incidence," *United States National Committee of URSI National Radio Science Meeting (USNC-URSI NRSM)*, 2022.

4. **B. G. Kashyap,** *et.al.,* "Toward Hyper-Compact Rotman Lenses- A Meta-Transmission Line Wave-space Design," *IEEE International Symposium on Antennas and Propagation & USNC/URSI National Radio Science Meeting*, 2022.

5. **B. G. Kashyap,** *et.al.,* "A Leaky-Wave Antenna Design for RF Gesture Recognition," *IEEE International Symposium on Antennas and Propagation & USNC/URSI National Radio Science Meeting*, 2023.

6. **B. G. Kashyap,** *et.al.,* "Toward Hyper-Compact Rotman Lenses - Meta-Transmission Line Design and Characterization," *IEEE International Symposium on Antennas and Propagation & USNC/URSI National Radio Science Meeting*, 2023.

7. **B. G. Kashyap,** *et.al.,* "A Sub-THz Micro-Doppler Radar for Counter-Surveillance Applications," *IEEE International Symposium on Antennas and Propagation & USNC/URSI National Radio Science Meeting*, 2023.

8. A. S. Shekhawat, **B. G. Kashyap**, *et.al.,* "A Compact Unit-cell Design for mmWave Reconfigurable Intelligent Surfaces," *United States National Committee of URSI National Radio Science Meeting (USNC-URSI NRSM)*, 2022.

9. A. S. Shekhawat, **B. G. Kashyap**, *et.al.,* "Beamforming Characterization of a mmWave Single-bit Reflective Metasurface," *IEEE International Symposium on Antennas and Propagation & USNC/URSI National Radio Science Meeting*, 2022.

REFERENCES

[1] R. J. Mailloux, *Phased Array Antenna Handbook*, 2nd ed. Norwood, MA, USA: Artech House, 2005.

[2] C. Fulton, M. Yeary, D. Thompson, J. Lake, and A. Mitchell, "Digital Phased Arrays: Challenges and Opportunities," in *Proceedings of the IEEE*, vol. 104, no. 3, pp. 487-503, March 2016.

[3] J. S. Herd and M. D. Conway, "The Evolution to Modern Phased Array Architectures," in *Proceedings of the IEEE*, vol. 104, no. 3, pp. 519-529, March 2016.

[4] R. Méndez-Rial, C. Rusu, N. González-Prelcic, A. Alkhateeb, and R. W. Heath, "Hybrid MIMO Architectures for Millimeter Wave Communications: Phase Shifters or Switches?," in *IEEE Access*, vol. 4, pp. 247-267, 2016.

[5] V. Venkateswaran and A. J. van der Veen, "Analog Beamforming in MIMO Communications with Phase Shift Networks and Online Channel Estimation," in *IEEE Transactions on Signal Processing*, vol. 58, no. 8, pp. 4131-4143, Aug. 2010.

[6] K. Spoof, M. Tenhunen, V. Unnikrishnan, K. Stadius, M. Kosunen, and J. Ryynänen, "True-Time-Delay Receiver IC With Reconfigurable Analog and Digital Beamforming," in *IEEE Access*, vol. 10, pp. 116375-116383, 2022.

[7] S. H. Talisa, K. W. O'Haver, T. M. Comberiate, M. D. Sharp, and O. F. Somerlock, "Benefits of Digital Phased Array Radars," in *Proceedings of the IEEE*, vol. 104, no. 3, pp. 530-543, March 2016.

[8] J. A. Nanzer, S. R. Mghabghab, S. M. Ellison, and A. Schlegel, "Distributed Phased Arrays: Challenges and Recent Advances," in *IEEE Transactions on Microwave Theory and Techniques*, vol. 69, no. 11, pp. 4893-4907, Nov. 2021.

[9] A. S. Nagra and R. A. York, "Distributed analog phase shifters with low insertion loss," in *IEEE Transactions on Microwave Theory and Techniques*, vol. 47, no. 9, pp. 1705-1711, Sept. 1999.

[10] A. J. Fenn, D. H. Temme, W. P. Delaney, and W. E. Courtney, ''The development of phased array radar technology,'' *Lincoln Lab. J.*, vol. 12, no. 2, pp. 321–340, Mar. 2000.

[11] R. J. Mailloux, "Array grating lobes due to periodic phase, amplitude and time delay quantization," *IEEE Trans. Antennas Propag.*, vol. AP-32, no. 12, pp. 1364–1368, Dec. 1984.

[12] N. Kurosawa et al, "Explicit Analysis of Channel Mismatch Effects in Time Interleaved ADC Systems," *IEEE Transactions on Circuits and Systems I—Fundamental Theory and Applications*, vol. 48, no. 3, Mar 2003.

[13] U. Nickel, "Fundamentals of radar signal processing for phased array radar," *Res. Inst. High Frequency Phys. Radar Tech.*, Wachtburg, Germany, 2006.

[14] C. T. Lin and H. Ly, "Sidelobe reduction through subarray overlapping for wideband arrays," *in Proc. IEEE Radar Conf.*, May 2001, pp. 228–233.

[15] J. S. Herd, S. M. Duffy, and H. Steyskal, ''Design considerations and results for an overlapped subarray radar antenna,'' *in Proc. IEEE Aerosp. Conf.*, 2005, pp. 1087–1092.

[16] H. Steyskal, ''Digital beamforming,'' *in Proc. 18th Eur. Microw. Conf.*, 1988, pp. 49–57.

[17] E. Carpentieri, U. F. D'Elia, E. De Stefano, L. Di Guida, and R. Vitiello, "Millimeter-wave phased-array antennas," *2008 IEEE Radar Conference*, Rome, Italy, 2008, pp. 1-5.

[18] J. G. Andrews, *et. al.*, "What Will 5G Be?," in *IEEE Journal on Selected Areas in Communications*, vol. 32, no. 6, pp. 1065-1082, June 2014.

[19] T. S. Rappaport, *et. al.*, "Millimeter Wave Mobile Communications for 5G Cellular: It Will Work!," in *IEEE Access*, vol. 1, pp. 335-349, 2013.

[20] Z. Pi and F. Khan, "An introduction to millimeter-wave mobile broadband systems," in *IEEE Communications Magazine*, vol. 49, no. 6, pp. 101-107, June 2011.

[21] M. Agiwal, A. Roy, and N. Saxena, "Next Generation 5G Wireless Networks: A Comprehensive Survey," in *IEEE Communications Surveys & Tutorials*, vol. 18, no. 3, pp. 1617-1655, third quarter 2016.

[22] J. G. Andrews, H. Claussen, M. Dohler, S. Rangan, and M. C. Reed, "Femtocells: Past, Present, and Future," in *IEEE Journal on Selected Areas in Communications*, vol. 30, no. 3, pp. 497-508, April 2012

[23] C. A. Balanis, *Antenna Theory: Analysis and Design*. John Wiley & Sons, 2016.

[24] A. Farago, *et al.*, "Rain effects on 5G millimeter wave ad-hoc mesh networks investigated with different rain models." (2016).

[25] H. Xu, T. S. Rappaport, R. J. Boyle, and J. H. Schaffner, "Measurements and Models for 38-GHz Point-to-multipoint Radiowave Propagation," in *IEEE Journal on Selected Areas in Communications*, vol. 18, no. 3, pp. 310-321, March 2000.

[26] J. Lee, G. T. Gil, and Y. H. Lee, “Exploiting spatial sparsity for estimating channels of hybrid MIMO systems in millimeter wave communications,” *2014 IEEE Global Communications Conference*, Austin, TX, USA, 2014, pp. 3326-3331.

[27] A. Alkhateeb, O. El Ayach, G. Leus, and R. W. Heath, “Channel Estimation and Hybrid Precoding for Millimeter Wave Cellular Systems,” in *IEEE Journal of Selected Topics in Signal Processing*, vol. 8, no. 5, pp. 831-846, Oct. 2014.

[28] S. Rajagopal, S. Abu-Surra, Z. Pi and F. Khan, "Antenna Array Design for Multi-Gbps mmWave Mobile Broadband Communication," *2011 IEEE Global Telecommunications Conference - GLOBECOM 2011*, Houston, TX, USA, 2011, pp. 1-6.

[29] T. L. Marzetta, “Noncooperative Cellular Wireless with Unlimited Numbers of Base Station Antennas,” in *IEEE Transactions on Wireless Communications*, vol. 9, no. 11, pp. 3590-3600, November 2010.

[30] R. Chataut, and R. Akl, “Massive MIMO Systems for 5G and beyond Networks—Overview, Recent Trends, Challenges, and Future Research Direction.” *Sensors*. 20(10): 2753, 2020.

[31] T. S. Rappaport, F. Gutierrez, E. Ben-Dor, J. N. Murdock, Y. Qiao, and J. I. Tamir, “Broadband Millimeter-Wave Propagation Measurements and Models Using Adaptive-Beam Antennas for Outdoor Urban Cellular Communications,” in *IEEE Transactions on Antennas and Propagation*, vol. 61, no. 4, pp. 1850-1859, April 2013.

[32] E. Basar, M. Di Renzo, J. De Rosny, M. Debbah, M. S. Alouini, and R. Zhang, “Wireless Communications Through Reconfigurable Intelligent Surfaces,” in *IEEE Access*, vol. 7, pp. 116753-116773, 2019.

[33] C. Pan, *et. al*., “Multicell MIMO Communications Relying on Intelligent Reflecting Surfaces,” in *IEEE Transactions on Wireless Communications*, vol. 19, no. 8, pp. 5218-5233, Aug. 2020

[34] Q. Wu and R. Zhang, “Intelligent Reflecting Surface Enhanced Wireless Network via Joint Active and Passive Beamforming,” in *IEEE Transactions on Wireless Communications*, vol. 18, no. 11, pp. 5394-5409, Nov. 2019.

[35] C. Huang, A. Zappone, G. C. Alexandropoulos, M. Debbah, and C. Yuen, “Reconfigurable Intelligent Surfaces for Energy Efficiency in Wireless Communication,” in *IEEE Transactions on Wireless Communications*, vol. 18, no. 8, pp. 4157-4170, Aug. 2019.

[36] M. Di Renzo, *et. al*., “Smart Radio Environments Empowered by Reconfigurable Intelligent Surfaces: How It Works, State of Research, and The Road Ahead,”

in *IEEE Journal on Selected Areas in Communications*, vol. 38, no. 11, pp. 2450-2525, Nov. 2020.

[37] W. Tang, *et. al*., "Wireless Communications with Reconfigurable Intelligent Surface: Path Loss Modeling and Experimental Measurement," in *IEEE Transactions on Wireless Communications*, vol. 20, no. 1, pp. 421-439, Jan. 2021.

[38] M. Dohler and Y. Li, *Cooperative Communications: Hardware*, Channeland PHY. Chichester, U.K.: Wiley, 2010.

[39] J. D. Griffin and G. D. Durgin, "Complete Link Budgets for Backscatter Radio and RFID systems," *IEEE Antennas Propag. Mag.*, vol. 51, no. 2, pp. 11-25, Apr. 2009.

[40] B. Singh, O. Tirkkonen, Z. Li, M. A. Uusitalo, and R. Wichman, "Selective multi-hop relaying for ultra-reliable communication in a factory environment," *2016 IEEE 27th Annual International Symposium on Personal, Indoor, and Mobile Radio Communications (PIMRC)*, Valencia, Spain, 2016, pp. 1-6.

[41] K. Ntontin and C. Verikoukis, "Relay-Aided Outdoor-to-Indoor Communication in Millimeter-Wave Cellular Networks," *in IEEE Systems Journal*, vol. 14, no. 2, pp. 2473-2484, June 2020.

[42] D. T. Do, M. S. V. Nguyen, F. Jameel, R. Jäntti, and I. S. Ansari, "Performance Evaluation of Relay-Aided CR-NOMA for Beyond 5G Communications," *in IEEE Access*, vol. 8, pp. 134838-134855, 2020

[43] A. Goldsmith, *Wireless Communications*. Cambridge, U.K.: Cambridge Univ. Press, 2005.

[44] B. Rana, S. S. Cho, and I. P. Hong, "Review Paper on Hardware of Reconfigurable Intelligent Surfaces," in *IEEE Access*, vol. 11, pp. 29614-29634, 2023

[45] S. Basharat, M. Khan, M. Iqbal, U. S. Hashmi, S. A. R. Zaidi, and I. Robertson, "Exploring reconfigurable intelligent surfaces for 6G: State-of-the-art and the road ahead," *IET Commun.* 16, 1458– 1474, 2022.

[46] C. Huang, A. Zappone, G. C. Alexandropoulos, M. Debbah, and C. Yuen, "Reconfigurable intelligent surfaces for energy efficiency in wireless communication," *IEEE Transactions on Wireless Communications*, vol. 18, no. 8, pp. 4157–4170, 2019.

[47] G. Zhou, C. Pan, H. Ren, K. Wang, and K. K. Chai, "RIS-aided mmWave transmission: A stochastic majorization- minimization approach," in *ICC 2021 - IEEE International Conference on Communications*, 2021, pp. 1–6.

[48] J. Ye, S. Guo, and M.S. Alouini, "Joint reflecting and precoding designs for SER minimization in reconfigurable intelligent surfaces assisted MIMO systems," *IEEE Transactions on Wireless Communications*, vol. 19, no. 8, pp. 5561–5574, 2020.

[49] Q. Zhu, H. Li, R. Liu, M. Li, and Q. Liu, "Hybrid beamforming and passive reflection design for RIS-assisted mmWave MIMO systems," in *2021 IEEE International Conference on Communications Workshops (ICC Workshops)*, 2021, pp. 1–6.

[50] A. Taha, M. Alrabeiah, and A. Alkhateeb, "Enabling large intelligent surfaces with compressive sensing and deep learning," *IEEE Access*, vol. 9, pp. 44 304–44 321, 2021.

[51] X. Ying, U. Demirhan, and A. Alkhateeb, "Relay aided intelligent reconfigurable surfaces: Achieving the potential without so many antennas," *arXiv:2006.06644*, 2020.

[52] M. Nemati, J. Park, and J. Choi, "RIS-assisted coverage enhancement in millimeter-wave cellular networks," *IEEE Access*, vol. 8, pp. 188 171–188 185, 2020.

[53] E. Moro, I. Filippini, A. Capone, and D. De Donno, "Planning mm-wave access networks with reconfigurable intelligent surfaces," *arXiv:2105.11755*, 2021.

[54] M. He, W. Xu, and C. Zhao, "RIS-assisted broad coverage for mmWave massive MIMO system," in *2021 IEEE International Conference on Communications Workshops (ICC Workshops)*, 2021, pp. 1–6.

[55] M. Nemati, B. Maham, S. R. Pokhrel, and J. Choi, "Modeling RIS empowered outdoor-to-indoor communication in mmWave cellular networks," *IEEE Trans. Commu*n., vol. 69, no. 11, pp. 7837–7850, Nov. 2021.

[56] X. Mu, Y. Liu, L. Guo, J. Lin, and R. Schober, "Simultaneously transmitting and reflecting (STAR) RIS aided wireless communications," *IEEE Trans. Wireless Commun.*, Oct. 13, 2021.

[57] J. Xu, Y. Liu, X. Mu, and O. A. Dobre, "STAR-RISs: Simultaneous transmitting and reflecting reconfigurable intelligent surfaces," *IEEE Commun. Lett.*, vol. 25, no. 9, pp. 3134–3138, Sep. 2021.

[58] H. Yang, *et.al.,* "A Programmable Metasurface with Dynamic Polarization, Scattering and Focusing control," *Scientific Reports*, vol. 6, no. October, pp. 1–11, 2016.

[59] T. J. Cui, M. Q. Qi, X. Wan, J. Zhao, Q. Cheng, K. T. Lee, J. Y. Lee, S. Seo, L. J. Guo, Z. Zhang, Z. You, and D. Chu, "Coding metamaterials, digital metamaterials and programmable metamaterials," *Light: Science and Applications*, vol. 3, no. 10, 2014. [Online].

[60] X. Wan, M. Q. Qi, T. Y. Chen, and T. J. Cui, "Field-programmable beam reconfiguring based on digitally-controlled coding metasurface," *Scientific Reports*, vol. 6, no. January, pp. 1–8, 2016.

[61] V. Arun and H. Balakrishnan, "RFocus: Beamforming Using Thousands of Passive Antennas," *17th USENIX Symposium on Networked Systems Design and Implementation*, pp. 1047-1061, 2020.

[62] X. Pei, H. Yin, L. Tan, L. Cao, Z. Li, K. Wang, K. Zhang, and E. Bjo¨rnson, "RIS-Aided Wireless Communications: Prototyping, Adaptive Beamforming, and Indoor/Outdoor Field Trials," *arXiv:2103.00534 [cs, math]*, Feb. 2021.

[63] A. Pantelopoulos and N. G. Bourbakis, "A Survey on Wearable Sensor-Based Systems for Health Monitoring and Prognosis," in *IEEE Transactions on Systems, Man, and Cybernetics, Part C (Applications and Reviews)*, vol. 40, no. 1, pp. 1-12, Jan. 2010.

[64] C. Li, V. M. Lubecke, O. Boric-Lubecke, and J. Lin, "A Review on Recent Advances in Doppler Radar Sensors for Noncontact Healthcare Monitoring," in *IEEE Transactions on Microwave Theory and Techniques*, vol. 61, no. 5, pp. 2046-2060, May 2013.

[65] Y. Rong, P. C. Theofanopoulos, G. C. Trichopoulos and D. W. Bliss, "Cardiac Sensing Exploiting an Ultra-Wideband Terahertz Sensing System," *2020 IEEE International Radar Conference (RADAR)*, Washington, DC, USA, 2020, pp. 1002-1006.

[66] P. C. Theofanopoulos and G. C. Trichopoulos, "A Novel Fingerprint Scanning Method Using Terahertz Imaging," *2018 IEEE International Symposium on Antennas and Propagation & USNC/URSI National Radio Science Meeting*, Boston, MA, USA, 2018, pp. 2463-2464.

[67] G. C. Trichopoulos, H. L. Mosbacker, D. Burdette, and K. Sertel, "A Broadband Focal Plane Array Camera for Real-time THz Imaging Applications," in *IEEE Transactions on Antennas and Propagation*, vol. 61, no. 4, pp. 1733-1740, April 2013.

[68] J. Han, L. Shao, D. Xu, and J. Shotton, "Enhanced Computer Vision with Microsoft Kinect Sensor: A Review," in *IEEE Transactions on Cybernetics*, vol. 43, no. 5, pp. 1318-1334, Oct. 2013.

[69] L. Dipietro, A. M. Sabatini, and P. Dario, "A Survey of Glove-Based Systems and Their Applications," in *IEEE Transactions on Systems, Man, and Cybernetics, Part C (Applications and Reviews)*, vol. 38, no. 4, pp. 461-482, July 2008.

[70] X. Zhang, X. Chen, Y. Li, V. Lantz, K. Wang, and J. Yang, "A Framework for Hand Gesture Recognition Based on Accelerometer and EMG Sensors," in *IEEE*

Transactions on Systems, Man, and Cybernetics - Part A: Systems and Humans, vol. 41, no. 6, pp. 1064-1076, Nov. 2011.

[71] G. Marin, F. Dominio, and P. Zanuttigh, "Hand Gesture Recognition with Leap Motion and Kinect Devices," *2014 IEEE International Conference on Image Processing (ICIP)*, Paris, France, 2014, pp. 1565-1569.

[72] Z. Zhang, Z. Tian, and M. Zhou, "Latern: Dynamic Continuous Hand Gesture Recognition Using FMCW Radar Sensor," in *IEEE Sensors Journal*, vol. 18, no. 8, pp. 3278-3289, 15 April15, 2018.

[73] D. Kim and C. Harrison, "EtherPose: Continuous Hand Pose Tracking with Wrist Worn Antenna Impedance Characteristic Sensing," *UIST '22: Proceedings of the 35th Annual ACM Symposium on User Interface Software and Technology*, October 2022.

[74] P. Visconti, F. Gaetani, G. Zappatore, and P. Primiceri, "Technical Features and Functionalities of Myo Armband: An Overview on Related Literature and Advanced Applications of Myoelectric Armbands Mainly Focused on Arm Prostheses," *International Journal on Smart Sensing and Intelligent Systems*, vol.11, no.1, 2018, pp.1-25.

[75] Y. Zhang and C. Harrison, "Tomo: Wearable, Low-Cost Electrical Impedance Tomography for Hand Gesture Recognition," *UIST '15: Proceedings of the 28th Annual ACM Symposium on User Interface Software & Technology*, November 2015, pp.167–173.

[76] R. S. Timsit, "Electrical contact resistance: properties of stationary interfaces," in *IEEE Transactions on Components and Packaging Technologies*, vol. 22, no. 1, pp. 85-98, March 1999.

[77] H. Truong, *et.al.*, "CapBand: Battery-free Successive Capacitance Sensing Wristband for Hand Gesture Recognition," *SenSys '18: Proceedings of the 16th ACM Conference on Embedded Networked Sensor Systems*, November 2018, pp. 54–67.

[78] A. Kadkhodayan, X. Jiang, and C. Menon, "Continuous Prediction of Finger Movements using Force Myography," *J. Med. Biol. Eng.*, vol. 36, no. 4, pp. 594–604, 2016.

[79] N. Friedman, J. B. Rowe, D. J. Reinkensmeyer, and M. Bachman, "The Manumeter: A Wearable Device for Monitoring Daily Use of the Wrist and Fingers," *in IEEE Journal of Biomedical and Health Informatics*, vol. 18, no. 6, pp. 1804-1812, Nov. 2014.

[80] X. Yang, X. Sun, D. Zhou, Y. Li, and H. Liu, "Towards Wearable A-Mode Ultrasound Sensing for Real-Time Finger Motion Recognition," *in IEEE*

Transactions on Neural Systems and Rehabilitation Engineering, vol. 26, no. 6, pp. 1199-1208, June 2018.

[81] J. McIntosh, A. Marzo, M. Fraser, and C. Phillips, "Echoflex: Hand gesture recognition using ultrasound imaging", *Proc. CHI Conf. Hum. Factors Comput. Syst.*, pp. 1923-1934, 2017.

[82] W. Guo, X. Sheng, H. Liu, and X. Zhu, "Mechanomyography assisted myoeletric sensing for upper-extremity prostheses: A hybrid approach", *IEEE Sensors J.*, vol. 17, no. 10, pp. 3100-3108, May 2017.

[83] J. McIntosh, A. Marzo, and M. Fraser, "Sensir: Detecting hand gestures with a wearable bracelet using infrared transmission and reflection", *Proc. 30th Annu. ACM Symp. User Interface Softw. Technol.*, pp. 593-597, 2017.

[84] G. C. Trichopoulos, P. C. Theofanopoulos, B. G. Kashyap, *et.al.,* "Design and Evaluation of Reconfigurable Intelligent Surfaces in Real-World Environment," *in IEEE Open Journal of the Communications*, 2022.

[85] B. G. Kashyap, *et.al.,* "A Reconfigurable Intelligent Surface for 5G Wireless Communication Applications," *IEEE International Symposium on Antennas and Propagation & USNC/URSI National Radio Science Meeting*, 2021.

[86] B. G. Kashyap, P. C. Theofanopoulos, Y. Cui, and G. C. Trichopoulos, "Mitigating Quantization Lobes in mmWave Low-Bit Reconfigurable Reflective Surfaces," in *IEEE Open Journal of Antennas and Propagation*, vol. 1, pp. 604-614, 2020.

[87] B. G. Kashyap, *et.al.*, "Fabrication and Characterization of a 900-Element 222.5 GHz Single-bit Reflective Surface with Suppressed Quantization Lobes," *2021 United States National Committee of URSI National Radio Science Meeting (USNC-URSI NRSM)*, 2021, pp. 153-154.

[88] B. G. Kashyap, *et.al.,* "Low Sidelobe Level Randomized Reconfigurable Reflective Surfaces under Oblique Incidence," *United States National Committee of URSI National Radio Science Meeting (USNC-URSI NRSM)*, 2022

[89] A. S. Shekhawat, B. G. Kashyap, *et.al.,* "A Compact Unit-cell Design for mmWave Reconfigurable Intelligent Surfaces," *United States National Committee of URSI National Radio Science Meeting (USNC-URSI NRSM)*, 2022.

[90] A. S. Shekhawat, B. G. Kashyap, *et.al.,* "Beamforming Characterization of a mmWave Single-bit Reflective Metasurface," *IEEE International Symposium on Antennas and Propagation & USNC/URSI National Radio Science Meeting*, 2022.

[91] B. G. Kashyap, R. Diaz, and G. C. Trichopoulos, *"*A Meta-Transmission Line Design for Compact True Time Delay Beamforming," (submitted).

[92] B. G. Kashyap, *et.al.,* "Toward Hyper-Compact Rotman Lenses- A Meta-Transmission Line Wave-space Design," *IEEE International Symposium on Antennas and Propagation & USNC/URSI National Radio Science Meeting*, 2022.

[93] B. G. Kashyap, *et.al.,* "Toward Hyper-Compact Rotman Lenses - Meta-Transmission Line Design and Characterization," *IEEE International Symposium on Antennas and Propagation & USNC/URSI National Radio Science Meeting*, 2023.

[94] B. G. Kashyap, *et.al.,* "A Leaky-Wave Antenna Design for RF Gesture Recognition," *IEEE International Symposium on Antennas and Propagation & USNC/URSI National Radio Science Meeting*, 2023.

[95] K. Achouri and C. Caloz, *Electromagnetic Metasurfaces: Theory and Applications*. John Wiley & Sons, 2021.

[96] N. Engheta and R. W. Ziolkowski. *Metamaterials: Physics and Engineering Explorations*. John Wiley & Sons, 2006.

[97] J. L. Volakis, *Antenna Engineering Handbook.* McGraw-Hill Professional, 2007.

[98] C. A. Balanis, *Modern Antenna Handbook*. John Wiley & Sons, 2008.

[99] V. G. Veselago, "Electrodynamics of Substances with Simultaneously Negative values of ϵ and μ," *Soviet Physics Uspekhi*, vol. 10, no. 4, 1968 pp. 509-514.

[100] J. B. Pendry, A. J. Holden, D. J. Robbins, and W. J. Stewart, "Magnetism from conductors and enhanced nonlinear phenomena," *IEEE Transactions on Microwave Theory and Techniques*, 47(11):2075-2084, 1999.

[101] D. R. Smith, W. J. Padilla, D. C. Vier, S. C. Nemat-Nasser, and S. Schultz, "Composite Medium with Simultaneously Negative Permeability and Permittivity," *Phys. Rev. Lett*., 84, 2000, pp. 4184-4186.

[102] C. L. Holloway, E. F. Kuester, J. A. Gordon, J. O'Hara, J. Booth, and D. R. Smith, "An Overview of the Theory and Applications of Metasurfaces: The Two-Dimensional Equivalents of Metamaterials," in *IEEE Antennas and Propagation Magazine*, vol. 54, no. 2, pp. 10-35, April 2012.

[103] K. Achouri and C. Caloz, "Design, concepts, and applications of electromagnetic metasurfaces" *Nanophotonics*, vol. 7, no. 6, 2018, pp. 1095-1116.

[104] H. Lamb, "On Group-Velocity," *Proc. London Math. Soc*, Ser. 2, 1, 1904, pp. 473-479.

[105] S. X. Xia, X. Zhai, Y. Huang, J. Q. Liu, L. L. Wang, and S. C. Wen, "Graphene Surface Plasmons with Dielectric Metasurfaces," in *Journal of Lightwave Technology*, vol. 35, no. 20, pp. 4553-4558, 15 Oct.15, 2017

[106] B. Tang, Z. Li, E. Palacios, Z. Liu, S. Butun, and K. Aydin, "Chiral-Selective Plasmonic Metasurface Absorbers Operating at Visible Frequencies," in *IEEE Photonics Technology Letters*, vol. 29, no. 3, pp. 295-298, 1 Feb.1, 2017.

[107] Z. Wang, Y. Dong, Z. Peng, and W. Hong, "Hybrid Metasurface, Dielectric Resonator, Low-Cost, Wide-Angle Beam-Scanning Antenna for 5G Base Station Application," in *IEEE Transactions on Antennas and Propagation*, vol. 70, no. 9, pp. 7646-7658, Sept. 2022.

[108] S. Yin, *et. al*., "Reconfigurable Chiral Metasurface Absorbers Based on Liquid Crystals," in *IEEE Photonics Journal*, vol. 10, no. 6, pp. 1-9, Dec. 2018.

[109] A. Li, Z. Luo, H. Wakatsuchi, S. Kim, and D. F. Sievenpiper, "Nonlinear, Active, and Tunable Metasurfaces for Advanced Electromagnetics Applications," in *IEEE Access*, vol. 5, pp. 27439-27452, 2017.

[110] P. Nayeri, F. Yang, and A. Elsherbeni, *Reflectarray Antennas Theory, Designs and Applications*, Wiley-IEEE Press, 2008.

[111] J. Huang and J.A. Encinar, *Reflectarray Antennas*, Wiley-IEEE Press, 2007.

[112] J. Shaker, M. R. Chaharmir, and J. Ethier, *Reflectarray Antennas: Analysis Design, Fabrication & Measurement*, Artech House, 2013.

[113] P. Nayeri, A. Z. Elsherbeni and F. Yang, "Radiation Analysis Approaches for Reflectarray Antennas [Antenna Designer's Notebook]," in *IEEE Antennas and Propagation Magazine*, vol. 55, no. 1, pp. 127-134, Feb. 2013.

[114] G.W. Pierce, *Electric Oscillations and Electric Waves*. McGraw Hill, 1920

[115] E. A. Guillemin, *Communication Networks*. John Wiley & Sons, 1935.

[116] L. Brillouin, "Electromagnetic Delay Lines," *Symposium on Large-Scale Digital Calculating Machinery*, pp. 110-124, 1948.

[117] W. Hansen, "Radiating electromagnetic waveguide," U.S. Patent 2.402.622, 1940.

[118] M. Wijewardena, T. Samarasinghe, K. T. Hemachandra, S. Atapattu, and J. S. Evans, "Physical Layer Security for Intelligent Reflecting Surface Assisted Two–Way Communications," *IEEE Communications Letters*, vol. 25, no. 7, pp. 2156–2160, Jul. 2021.

[119] I. Rodriguez, H. C. Nguyen, T. B. Sorensen, J. Elling, J. A. Holm, P. Mogensen,

and B. Vejlgaard, “Analysis of 38 GHz mmWave Propagation Characteristics of Urban Scenarios,” in *Proceedings of European Wireless 2015; 21th European Wireless Conference*, May 2015, pp. 1-8.

[120] Y. Zhang, M. Alrabeiah, and A. Alkhateeb, “Reinforcement learning of beam codebooks in millimeter wave and terahertz MIMO systems,” 2021, *arXiv*:2102.11392.

[121] M. Alrabeiah, Y. Zhang, and A. Alkhateeb, “Neural networks-based beam codebooks: Learning mmWave massive MIMO beams that adapt to deployment and hardware,” 2020, *arXiv*:2006.14501.

[122] S. Costanzo, F. Venneri, A. Raffo, and G. Di Massa, "Dual-Layer Single-Varactor Driven Reflectarray Cell for Broad-Band Beam-Steering and Frequency Tunable Applications," in *IEEE Access*, vol. 6, pp. 71793-71800, 2018.

[123] H. Yang *et. al.*, "A Study of Phase Quantization Effects for Reconfigurable Reflectarray Antennas," in *IEEE Antennas and Wireless Propagation Letters*, vol. 16, pp. 302-305, 2017.

[124] M. Smith and Y. Guo, "A comparison of methods for randomizing phase quantization errors in phased arrays," in *IEEE Transactions on Antennas and Propagation*, vol. 31, no. 6, pp. 821-828, November 1983.

[125] S. Liu and T. J. Cui, “Concepts, working principles, and applications of coding and programmable metamaterials,” *Adv. Opt. Mater.*, vol. 5, no. 22, p. 1700624, 2017.

[126] H. Yang, X. Cao, F. Yang, J. Gao, S. Xu, M. Li, X. Chen, Y. Zhao, Y. Zheng, and S. Li, “A programmable metasurface with dynamic polarization, scattering and focusing control,” *Sci. Rep.*, vol. 6, p. 35692, 2016.

[127] M. K. T. Al-Nuaimi, Y. He, and W. Hong, “Design of 1-bit coding engineered reflectors for EM-wave shaping and RCS modifications,” *IEEE Access*, vol. 6, pp. 75 422–75 428, 2018.

[128] J. Yin, Q. Wu, Q. Lou, H. Wang, Z. N. Chen, and W. Hong, "Single-Beam 1 Bit Reflective Metasurface Using Prephased Unit-cells for Normally Incident Plane Waves," in *IEEE Transactions on Antennas and Propagation*, vol. 68, no. 7, pp. 5496-5504, July 2020.

[129] P. C. Theofanopoulos and G. C. Trichopoulos, “Mitigating Quantization Lobes in Reconfigurable Reflective Surfaces,” *2020 IEEE International Symposium on Antennas and Propagation and USNC-URSI Radio Science Meeting*, Montreal, Quebec, Canada, 2020.

[130] P. C. Theofanopoulos and G. C. Trichopoulos, “A Novel 2-Bit Graphene Reconfigurable Reflectarray,” *2020 IEEE International Symposium on Antennas*

and Propagation and USNC-URSI Radio Science Meeting, Montreal, Quebec, Canada, 2020.

[131] G. Zheng, J. Papapolymerou, and M. M. Tentzeris, "Wideband coplanar waveguide RF probe pad to microstrip transitions without via holes," in *IEEE Microwave and Wireless Components Letters*, vol. 13, no. 12, pp. 544-546, Dec. 2003.

[132] P. C. Theofanopoulos and G. C. Trichopoulos, "Modeling of Sub-Millimeter Wave Coplanar Waveguide Graphene Switches," *2019 IEEE International Symposium on Antennas and Propagation and USNC-URSI Radio Science Meeting*, Atlanta, GA, USA, 2019.

[133] Zhuang, *et. al.*, "Flexibility matters: High purity, thin, flexible alumina ribbon ceramic, Ceramic & Glass Manufacturing 1(4)," *ACerS Bulletin 99(7)*: pp. 54–58, 2020.

[134] A. D. Brown, *Active Electronically Scanned Arrays: Fundamentals and Applications*, Wiley-IEEE Press, 2021.

[135] W. Hong, *et.al.*, "Multibeam Antenna Technologies for 5G Wireless Communications," *in IEEE Transactions on Antennas and Propagation*, vol. 65, no. 12, pp. 6231-6249, Dec. 2017.

[136] A. Hassanien and S. A. Vorobyov, "Phased-MIMO Radar: A Tradeoff Between Phased-Array and MIMO Radars," *in IEEE Transactions on Signal Processing*, vol. 58, no. 6, pp. 3137-3151, June 2010.

[137] I. Ahmed, *et. al.*, "A Survey on Hybrid Beamforming Techniques in 5G: Architecture and System Model Perspectives," *in IEEE Communications Surveys & Tutorials*, vol. 20, no. 4, pp. 3060-3097, Fourth quarter 2018.

[138] J. Schoebel, *et. al.*, "Design considerations and technology assessment of phased-array antenna systems with RF MEMS for automotive radar applications," *in IEEE Transactions on Microwave Theory and Techniques*, vol. 53, no. 6, pp. 1968-1975, June 2005.

[139] E. H. Mujammami, I. Afifi, and A. B. Sebak, "Optimum Wideband High Gain Analog Beamforming Network for 5G Applications," *in IEEE Access*, vol. 7, pp. 52226-52237, 2019.

[140] D. I. Lialios, N. Ntetsikas, K. D. Paschaloudis, C.L. Zekios, S. V. Georgakopoulos, and G.A. Kyriacou, "Design of True Time Delay Millimeter Wave Beamformers for 5G Multibeam Phased Arrays," *Electronics* 2020, 9, 1331.

[141] R. Rotman, M. Tur, and L. Yaron, "True Time Delay in Phased Arrays," *in Proceedings of the IEEE*, vol. 104, no. 3, pp. 504-518, March 2016.

[142] W. Rotman and R. Turner, "Wide-angle microwave lens for line source applications," *in IEEE Transactions on Antennas and Propagation*, vol. 11, no. 6, pp. 623-632, November 1963.

[143] T. E. Bogale and L. B. Le, "Beamforming for multiuser massive MIMO systems: Digital versus hybrid analog-digital," *2014 IEEE Global Communications Conference*, Austin, TX, USA, 2014, pp. 4066-4071.

[144] J. Butler and R. Lowe, "Beamforming Matrix Simplifiers Design of Electrically Scanned Antennas," *Electron. Des*. 1961, 9, 170–173.

[145] C. C. Chang, R. H. Lee, and T. Y. Shih, "Design of a Beam Switching/Steering Butler Matrix for Phased Array System," *in IEEE Transactions on Antennas and Propagation*, vol. 58, no. 2, pp. 367-374, Feb. 2010.

[146] J. Blass, "Multidirectional antenna - A new approach to stacked beams," *1958 IRE International Convention Record*, New York, NY, USA, 1960, pp. 48-50.

[147] A. Lambrecht, *et. al.,* "Rotman-lens as a true-time-delay beamformer at low UHF frequencies," 2008 *IEEE Antennas and Propagation Society International Symposium*, 2008, pp. 1-4.

[148] S. Vashist, M. K. Soni, and P. K. Singhal, "A Review on the Development of Rotman Lens Antenna," *Chinese Journal of Engineering*, 2014.

[149] A. Darvazehban, O. Manoochehri, M. A. Salari, P. Dehkhoda, and A. Tavakoli, "Ultra-Wideband Scanning Antenna Array with Rotman Lens," *in IEEE Transactions on Microwave Theory and Techniques*, vol. 65, no. 9, pp. 3435-3442, Sept. 2017.

[150] W. Lee, J. Kim, and Y. J. Yoon, "Compact Two-Layer Rotman Lens-Fed Microstrip Antenna Array at 24 GHz," *in IEEE Transactions on Antennas and Propagation*, vol. 59, no. 2, pp. 460-466, Feb. 2011.

[151] Y. J. Cheng *et. al.,* "Substrate Integrated Waveguide (SIW) Rotman Lens and Its Ka-Band Multibeam Array Antenna Applications," *in IEEE Transactions on Antennas and Propagation*, vol. 56, no. 8, pp. 2504-2513, Aug. 2008.

[152] J. Kim, C. S. Cho, and F. S. Barnes, "Dielectric slab Rotman lens for microwave/millimeter-wave applications," *in IEEE Transactions on Microwave Theory and Techniques*, vol. 53, no. 8, pp. 2622-2627, Aug. 2005.

[153] E. O. Rausch and A. F. Peterson, "Theory and Measurements of a Compact High Dielectric Microstrip Rotman Lens," *1992 22nd European Microwave Conference*, 1992, pp. 876-881.

[154] A. F. Peterson and E. O. Rausch, “Validation of integral equation model with high-dielectric Rotman lens measurements,” *in Proc. 1991 Antenna Applications Symp.*, Monticello, IL, Sept. 1991, pp. 208–229. Rome Lab., Griffiss Air Force Base, NY, Feb. 1992.

[155] E. D. Caswell, (Jul.10, 2008). Artificial Dielectric Rotman Lens, (US Patent US20080165068A1).

[156] G.W. Pierce, (Mar. 9, 1926). Electrical Retardation Line, (US Patent 1576459A).

[157] S. Jiang, *et. al.*, “Emerging Wearable Interfaces and Algorithms for Hand Gesture Recognition: A Survey,” *in IEEE Reviews in Biomedical Engineering*, vol. 15, pp. 85-102, 2022.

[158] C. Gabriel, “Compilation of the Dielectric Properties of Body Tissues at RF and Microwave Frequencies,” (1996).

[159] M. Bozzi, *et. al.*, “Modeling and Design Considerations for Substrate Integrated Waveguide Circuits and Components,” *2007 8th International Conference on Telecommunications in Modern Satellite, Cable and Broadcasting Services*, 2007, pp. P-VII-P-XVI.

[160] D. Deslandes, "Design equations for tapered microstrip-to-Substrate Integrated Waveguide transitions," *2010 IEEE MTT-S International Microwave Symposium*, Anaheim, CA, USA, 2010, pp. 704-707.